

# **A Synchronised Multi-Motor Control System Using Hybrid Sensorless Induction Motor Drives**

**by Gary Turl**

**Thesis submitted to the University of Nottingham for the  
degree of Doctor of Philosophy, May 2002**



## **IMAGING SERVICES NORTH**

Boston Spa, Wetherby  
West Yorkshire, LS23 7BQ  
[www.bl.uk](http://www.bl.uk)

**BEST COPY AVAILABLE.**

**VARIABLE PRINT QUALITY**



---

## Abstract

---

The main aim of this project was to research, develop and test an induction motor drive not requiring a speed encoder, but which could be considered commercially viable by motor drives manufacturers, and which should aim to meet the follow requirements:

- Dynamic torque performance and steady state speed-holding accuracy to be comparable with encoded vector controlled drives
- Extensive and highly accurate knowledge of electrical and mechanical parameters of the motor and load not to be required
- Extensive commissioning from an expert engineer not to be necessary
- Algorithm not to rely on excessive computational capability being available

The drive was to operate, in a stable manner, over speed and load ranges at least comparable with commercially available sensorless induction motor drives. The above requirements were set such that the developed sensorless technique may be considered for synchronised multi-motor process applications, where the advantages of a sensorless system could be exploited for hazardous, damp and hot conditions.

The solution developed consists of a leading model-based sensorless method augmented with a speed estimator that tracks harmonics, seen in the stator terminal quantities, due to rotor slotting. The model-based scheme facilitates field-orientated control for dynamic performance. The slot harmonic speed estimator tunes the model for speed accuracy. Slot harmonics are identified using a recursive signal processing method termed the Recursive Maximum Likelihood – Adaptive Tracking Filter. This work is the first example of the method being developed into a practical sensorless drive system and the complete speed identifier is described, including set-up, pre-filtering and the minimal parameter considerations. Being recursive the method is computationally efficient, yet has accuracy comparable with that of FFT identifiers used in other work.

The developed sensorless strategy was implemented practically on two motor drive systems. The performance of the scheme is shown to give encoder like speed holding

accuracy and field-orientated dynamic performance. The two drives were also configured and tested as a speed synchronised pair, using applicable multi-motor control techniques, themselves compared and contrasted. The sensorless performance is demonstrated, alongside an encoded version acting as a benchmark, and the performance of the two schemes is shown to be highly comparable. The author has found no other example of sensorless techniques considered for use in multi-motor applications. The use of such a technique brings established advantages associated with encoder removal and allows multi-axis electronic synchronisation to be considered for parts of a process where an encoder may not be appropriate.

---

## Acknowledgements

---

As is appropriate, I would like to take this opportunity to thank all the people who have been in some way involved with this project and with my associated time in Nottingham.

I would like to thank my tutors, Dr Mark Sumner and Prof Greg Asher, and all the other members of staff in the Power Electronics, Machines and Control (PEMC) group. A particular thanks to Mark for his constant support, interest and encouragement, letting me ask quite stupid questions and the unbelievably fast turnaround time associated with any proof reading given him.

Thanks to FKI Industrial Drives for their project support and for giving me the opportunity to undertake a short work spell with them in Loughborough.

Finally I'd like to thank Mel, for her constant support, encouragement and positive attitude, my family and friends at home in Devon, all the other PhD students/research assistants involved with the PEMC group, and those others who have made my research more rounded, interesting and enjoyable, are too many to mention, but particularly Steve and Steve.

---

# Contents

---

<b>Contents</b>	<b>iv</b>
<b>List of Figures</b>	<b>x</b>
<b>List of Tables</b>	<b>xvii</b>
<b>List of Symbols</b>	<b>xviii</b>
<b>1 Introduction</b>	<b>1</b>
1.1 Introduction	1
1.2 Vector Control	3
1.3 Sensorless Vector Control	4
1.4 Speed Critical Applications	7
1.4.1 Multi-Motor Applications	8
1.5 Project Motivation, Aims and Objectives	8
1.6 Thesis Organisation	10
1.7 Project Outcomes	12
<b>2 Background</b>	<b>14</b>
2.1 Introduction	14
2.2 Vector Control	15
2.2.1 The Per-Phase Induction Motor Equivalent Circuit	15
2.2.2 Parameter Definition	16
2.2.3 Reference Frames and Transforms	17
2.2.4 Induction Motor Dynamic Equations	19
2.2.5 Flux Orientation	20
2.2.6 Field Weakening Operation	26

2.2.7	Field Orientated Control Block Diagram	27
2.3	Variable Voltage Variable Frequency Supplies	28
2.3.1	The Voltage Source Inverter (VSI)	29
2.3.2	Pulse Width Modulation (PWM)	30
2.3.3	The Non-Ideal Nature of PWM Voltage Construction	35
2.3.4	The Requirement for Deadtime Protection	36
2.4	Sensorless Control	37
2.4.1	Model-Based Sensorless Control	40
2.4.2	Signal-Injection Based Sensorless Control	43
2.4.3	Sensorless Model-Based Control Methods for High Performance	44
2.5	Conclusion	51
<b>3</b>	<b>Experimental Method</b>	<b>53</b>
3.1	Introduction	53
3.2	Experimental System	54
3.3	Motor Drives	55
3.3.1	The ASEA Motor Drive (Rig A)	55
3.3.2	The Brown-Boveri Motor Drive (Rig B)	56
3.3.3	Induction Motor Parameters	57
3.4	Processing Platform	57
3.4.1	Division of Processing Tasks	60
3.5	DSP to Motor Drive Interfacing System	60
3.5.1	Buffering and Interface to the DSPLINK	61
3.5.2	Digital Input/Output	61
3.5.3	Pulse Width Modulation (PWM) Timing	62
3.5.4	Inverter Interface – Incorporating Deadtime Protection	62
3.5.5	Voltage and Current Measurement	63
3.5.6	Analogue Input and Filtering	64
3.5.7	Encoder Interface	64
3.6	High Level Motor Control and Data Capture	65
3.7	Conclusions	66

<b>4</b>	<b>Implementation of the Model-Based Sensorless Control Scheme</b>	<b>68</b>
4.1	Introduction	68
4.2	Sensorless Implementation	69
4.2.1	The Adaptive Flux Observer (AFO)	70
4.2.2	The Adaptive Speed Observer (ASO)	74
4.2.3	Speed and Current Controller Design	76
4.2.4	Design of the AFO and ASO	80
4.3	Sensorless Performance Analysis	82
4.3.1	Results from the AFO	83
4.3.2	Results from the ASO	87
4.3.3	Results from the Fully Sensorless Drive	92
4.4	Model Parameter Variation	97
4.4.1	Resistance Parameter Variation	97
4.4.2	Inductance Parameter Variation	99
4.5	Conclusion	100
<b>5</b>	<b>Rotor Slot Harmonic Speed Estimation and Sensorless Drive Tuning</b>	<b>102</b>
5.1	Introduction	102
5.2	Rotor Slot Harmonics (RSH)	105
5.2.1	RSH Production and Detectability	105
5.2.2	RSH Harmonics in Motor Terminal Quantities	108
5.2.3	RSH Tracking	114
5.3	The Adaptive Tracking Speed Estimator (ATSE)	115
5.3.1	Input Selection	116
5.3.2	Bandpass Pre-Filter	117
5.3.3	Notch Pre-Filtering to Selectively Eliminate PWM Harmonics	119
5.3.4	RML-ATF (RSH Estimator)	120
5.3.5	Calculating the Motor Speed	123
5.3.6	The Complete ATSE System	124
5.4	ATSE Performance Analysis	125
5.4.1	ATSE Steady State Tracking Performance	125

5.4.2	ATSE Speed Transient Tracking Performance	126
5.4.3	ATSE Load Rejection Tracking Performance	129
5.4.4	ATSE Low Speed Tracking Performance	131
5.4.5	Defined Region of ATSE Operation	132
5.5	Sensorless Drive Tuning	133
5.5.1	Considering Direct RSH Speed Estimate Feedback	133
5.5.2	Sensorless Model Based Vector Drive Tuning	135
5.6	Tuning Drive Performance Analysis	137
5.6.1	Sensorless Drive Steady State Performance	137
5.6.2	Sensorless Tuning Drive Transient Performance	139
5.6.3	Sensorless Tuning Drive Load Rejection Performance	140
5.6.4	Sensorless Tuning Drive Low Speed Performance	141
5.6.5	Sensorless Tuning Drive Compensating Temperature Variation	142
5.7	Conclusion	144
<b>6</b>	<b>The Synchronised Sensorless Drive System</b>	<b>147</b>
6.1	Introduction	147
6.2	Electronically Synchronised Control	148
6.3	Methods for Synchronised Control	152
6.3.1	Synchronous Command Generation	153
6.3.2	Master/Slave	154
6.3.3	Cross Coupled Control	156
6.3.4	Virtual Line Shafting	158
6.4	Encoded Bi-Axial Synchronisation Results	159
6.4.1	Synchronous Command Generation	160
6.4.2	Master/Slave	162
6.4.3	Cross Coupled Control	163
6.4.4	Virtual Line Shafting	167
6.5	Sensorless Bi-Axial Synchronisation Results	169
6.5.1	Sensorless Synchronous Command Generation	169
6.5.2	Sensorless Master/Slave	171
6.5.3	Sensorless Cross Coupled Control	172
6.5.4	Sensorless Virtual Line Shafting	173
6.6	Position Synchronisation	175

6.7	Considering Applications and Improving/Extending the Synchronisation Schemes to n Drives	178
6.7.1	Applications	179
6.7.2	Extending the Synchronisation Schemes	182
6.8	Conclusions	183
<b>7</b>	<b>Conclusion</b>	<b>187</b>
7.1	Introduction	187
7.2	Thesis Review	188
7.3	The Sensorless Model-Based Implementation	190
7.4	The Adaptive Tracking Speed Estimator	191
7.5	Speed Synchronisation/Multi-Motor Control	194
7.6	Further Work	196
7.7	Project Outcomes	198
	<b>References</b>	<b>200</b>
	<b>Appendix A Project Resulting Conference Papers</b>	<b>213</b>
A.1	IEE PEVD 2000 – London	213
A.2	IEEE PESC 2001 – Vancouver	219
A.3	EPE 2001 – Graz	225
A.4	IEEE IAS Annual Meeting 2001 – Chicago	234
A.5	IEE PEMD 2002 – Bath	242
	<b>Appendix B Motor Parameter Determination Rig B</b>	<b>248</b>
B.1	No Load Test	248
B.2	Locked Rotor Test	249
	<b>Appendix C Code Listings</b>	<b>251</b>
C.1	Code Listing for Processor A	251
C.2	Code Listing for Processor B	270
C.3	Filter and RSH Tracking Functions	279



<b>Appendix D</b>	<b>Inverter Interface Circuit Diagrams</b>	<b>283</b>
D.1	Eurotherm Inverter – Interface Circuit	283
D.2	Eurotherm Inverter – Trip Circuit	284
D.3	FKI Industrial Drives Inverter – Interface Circuit	285
D.4	FKI Industrial Drives Inverter – Trip Circuit	286
<b>Appendix E</b>	<b>Derivation of the AFO/ASO Equations</b>	<b>287</b>
E.1	The Stator Current Dynamic Equation	287
E.2	The Rotor Flux Dynamic Equation	289
<b>Appendix F</b>	<b>Speed Controller Design</b>	<b>290</b>
F.1	Rig A Speed Controller Design	290
F.2	Rig B Speed Controller Design	292
<b>Appendix G</b>	<b>Current Controller Design</b>	<b>293</b>
G.1	Rig A Current Controller Design	293
G.2	Rig B Current Controller Design	295
<b>Appendix H</b>	<b>AFO Results from Rig B</b>	<b>296</b>
<b>Appendix I</b>	<b>ASO Encoded Results from Rig B</b>	<b>298</b>
<b>Appendix J</b>	<b>ASO Sensorless Results from Rig B</b>	<b>301</b>
<b>Appendix K</b>	<b>Sensorless Master/Slave Cross Coupled Results</b>	<b>304</b>
<b>Appendix L</b>	<b>Encoded Cross Coupled Position Synchronisation Results for Rig B</b>	<b>306</b>
<b>Appendix M</b>	<b>Sensorless Cross Coupled Position Synchronisation Results for Rig B</b>	<b>307</b>

---

## List of Figures

---

1.1	Schematic circuit diagram of the separately excited DC machine	3
2.1	The induction motor per-phase equivalent circuit (squirrel-cage rotor)	15
2.2	Stator, rotor and synchronous reference frames	17
2.3	Direct field oriented control block diagram	27
2.4	Structure of the vector control block for DRFO	28
2.5	Schematic diagram of the voltage source inverter	29
2.6	Example PWM waveform and fundamental component	30
2.7	Asymmetric regular sampling PWM timing	31
2.8	Space vector sector diagram	32
2.9	Space vector timing example	33
2.10	Space vector phase and line voltages with triplen harmonics evident on phase voltages	35
2.11	Division of PWM signals into 2 channels to include deadtime protection delay	36
2.12	Problems with PWM resolution at low voltages	37
2.13	Structure of the V/F control scheme	38
2.14	Structure of the RF-MRAS	45
2.15	Structure of the torque-current MRAS	47
2.16	Structure of the adaptive speed and flux observer	49
3.1	Overall structure of the dual drive rig, with loading systems and control platform	54
3.2	Drive rig A	55
3.3	Drive rig B	56
3.4	The Texas C44 based DSP ISA-bus PC card	58
3.5	Block diagram of the DSP system	59
3.6	The DSP/motor drive hardware interface	61
3.7	The voltage and current transducer systems	61
3.8	The FKI Industrial Drives inverter with interface	63

3.9	An example screen shot of the PC based motor control platform	65
4.1	The induction motor dynamic model in the fixed stator frame	70
4.2	Block diagram of the full-order observer	72
4.3	Block diagram of the speed and flux observer	75
4.4	Structure of the speed control loop	77
4.5	Structure of the current control loop	79
4.6	Measured and observed $\alpha\beta$ currents and observed $\alpha\beta$ flux from the AFO with $k=1.0$ . The drive is operating under encoded IRFO at 100rpm with no load	84
4.7	Imposed rotor flux orientation angle and that measured by the AFO	84
4.8	Measured $\alpha\beta$ stator voltages from the IRFO scheme at 100rpm with no load	85
4.9	Measured and observed $\alpha\beta$ currents and observed $\alpha\beta$ flux from the AFO with $k=3.0$ . The drive is operating under encoded IRFO at 100rpm with no load	86
4.10	Measured speed and ASO speed estimate for $\pm 1000$ rpm no-load speed reversal. Drive running encoded IRFO (rig A)	88
4.11	Measured Speed and ASO speed estimate for 1000rpm no-load speed transient. Drive running encoded IRFO. Start-up conditions – inverter power up (rig A)	89
4.12	Measured Speed and ASO speed estimate for 1000rpm deceleration to standstill. Drive running encoded IRFO – full rated load (rig A)	90
4.13	Measured speed and ASO speed estimate during full-load torque impact at 1000rpm. Drive running encoded IRFO (rig A)	91
4.14	Measured speed and ASO speed estimate during full-load torque impact at 100rpm. Drive running encoded IRFO (rig A)	91
4.15	Measured speed for $\pm 1000$ rpm no-load speed reversal. Drive is running sensorless DRFO (rig A)	92
4.16	Measured speed for 1000rpm no-load speed transient. Drive is running sensorless DRFO. Start up conditions – inverter power up (rig A)	93

4.17	Measured speed during a 1000rpm deceleration to standstill. Drive running sensorless DRFO – full rated load (rig A)	94
4.18	Measured speed during 1000rpm deceleration to standstill – Tr adjusted. Drive running sensorless DRFO – full rated load (rig A)	95
4.19	Measured speed during full-load torque impact at 1000rpm. Drive running sensorless DRFO (rig A)	96
4.20	Measured speed during full-load torque impact at 100rpm. Drive running sensorless DRFO (rig A)	96
5.1	Rotor lamination from a 1.5kW machine with a closed 28- slot rotor	107
5.2	FFTs of $I_a$ , captured from rig A at 100rpm and 1000rpm	110
5.3	FFTs of $ I $ , captured from rig A at 100rpm and 1000rpm	112
5.4	FFTs of $ V $ , captured from rig A at 100rpm and 1000rpm	113
5.5	Block diagram of the Adaptive Tracking Speed Estimator (ATSE)	124
5.6	Encoder (measured), ASO and ATSE (estimated) speeds from both rigs running at a steady 300rpm under $\frac{1}{2}$ rated load. Drives are operating under detuned ASO sensorless control	126
5.7	Encoder, ASO and ATSE speed measures during a 200rpm to 1000rpm speed transient, under $\frac{1}{4}$ rated load, on rig A. The drive is operating in the sensorless ASO mode	127
5.8	Encoder, ASO and ATSE speed measures during a 200rpm to 1000rpm speed transient, under $\frac{1}{4}$ rated load, on rig B. The drive is operating in the sensorless ASO mode	128
5.9	Encoder, ASO and ATSE speed measures during a $\pm 1000$ rpm unloaded speed transient, on rig A. The drive is operating in the sensorless ASO mode	128
5.10	Encoder, ASO and ATSE speed measures during a 1/5 to full rated load torque impact at 600rpm (rig A) and 900rpm (rig B). The drive is operating in the sensorless ASO mode	130
5.11	Encoder, ASO and ATSE speed measures during a full to 1/5 rated load torque removal at 900rpm (rig A) and 600rpm (rig B). The drive is operating in the sensorless ASO mode	130
5.12	Encoder and ATSE speed measures during fully loaded speed deceleration from 300rpm to 30rpm in 30rpm steps. Both drives	

	are operating in the sensorless ASO mode	131
5.13	ATSE suggested operating region, when applied to speed estimation, in the sensorless ASO implementation on the 2 motor drives	132
5.14	RSH based speed estimate as used to provide direct speed feedback in a basic V/F drive. Top trace - full load applied and removed at 750rpm. Lower trace – half rated load applied and removed at 150rpm	134
5.15	Block diagram of the Tr tuning system	136
5.16	Encoder measured speed from both drive rigs, when operating the tuning sensorless control strategy, for a variety of steady state speed and load conditions	138
5.17	Encoder, ASO and ATSE speed measures during a 200rpm to 1000rpm speed transient, under ¼ rated load, on rig A. The drive is operating in the tuning sensorless mode	139
5.18	Encoder, ASO and ATSE speed measures during a 200rpm to 1000rpm speed transient, under ¼ rated load, on rig B. The drive is operating in the tuning sensorless mode	139
5.19	Encoder, ASO and ATSE speed measures during a 1/5 to full rated load torque impact at 600rpm (rig A) and 900rpm (rig B). The drive is operating in the tuning sensorless mode	140
5.20	Encoder, ASO and ATSE speed measures during a full to 1/5 rated load torque impact at 900rpm (rig A) and 600rpm (rig B). The drive is operating in the tuning sensorless mode	141
5.21	Encoder measured speed from both drive rigs, when operating the tuning sensorless control strategy at full load, at low speed. The drives enter and return from the region where tuning is disabled. Speed demand is varied in 30rpm steps, from 150 rpm to 30rpm	141
5.22	Encoder measured speeds, and Tr adjustment values, where the tuning sensorless system is operating at 200rpm, at full load, over a significant time period and from a cold start	142
5.23	Encoder measured speeds, where the ASO sensorless system is operating at 200rpm, at full load, over a significant time period and from a cold start. Tuning is disabled	143
5.24	Encoder measured speeds and Tr adjustment value, where tuning is enabled on the ASO sensorless system shortly after the end of results 5.22	143

6.1	Mechanically synchronised multi-axis system	149
6.2	Electronically synchronised multi-axis system	152
6.3	Synchronous command generation block diagram	153
6.4	Master/Slave synchronisation scheme block diagram	155
6.5	Cross-coupling of the master/slave technique	156
6.6	Parallel cross-coupled system block diagram	157
6.7	Block diagram of the virtual line-shaft system	158
6.8	Response of the encoded synchronous command generation scheme to step changes in reference command	160
6.9	Response of the encoded synchronous command generation scheme to large and sudden variation in load torque – Rig A	161
6.10	Response of the encoded synchronous command generation scheme to large and sudden variation in load torque – Rig B	161
6.11	Response of the encoded master/slave scheme to step changes in reference command	162
6.12	Response of the encoded master/slave scheme to large and sudden variation in load torque – Rig A	163
6.13	Response of the encoded cross-coupled master/slave scheme to step changes in reference command	163
6.14	Response of the encoded cross-coupled master/slave scheme to large and sudden variation in load torque – Rig A	164
6.15	Response of the encoded cross-coupled master/slave scheme to large and sudden variation in load torque – Rig B	164
6.16	Response of the encoded cross-coupled scheme to step changes in reference command	165
6.17	Response of the encoded cross-coupled scheme to an effective step change in the reference command (deceleration), but with reference rate of change limited	166
6.18	Response of the encoded cross-coupled scheme to large and sudden variation in load torque – Rig A	166
6.19	Response of the encoded cross-coupled scheme to large and sudden variation in load torque – Rig B	167
6.20	Response of the encoded virtual line-shaft system to step changes in reference command	167
6.21	Response of the encoded virtual line-shaft scheme to large and sudden variation in load torque – Rig A	168

6.22	Response of the encoded virtual line-shaft scheme to large and sudden variation in load torque – Rig B	168
6.23	Response of the sensorless synchronous command generation system to step changes in reference command	169
6.24	Response of the sensorless synchronous command generation scheme to large and sudden variation in load torque – Rig A	170
6.25	Response of the sensorless synchronous command generation scheme to large and sudden variation in load torque – Rig B	170
6.26	Response of the sensorless master/slave system to step changes in reference command	171
6.27	Response of the sensorless master/slave scheme to large and sudden variation in load torque – Rig A	171
6.28	Response of the sensorless cross-coupled scheme to step changes in reference command	172
6.29	Response of the sensorless cross-coupled scheme to large and sudden variation in load torque – Rig A	173
6.30	Response of the sensorless cross-coupled scheme to large and sudden variation in load torque – Rig B	173
6.31	Response of the sensorless virtual line-shafting system to step changes in reference command	173
6.32	Response of the sensorless virtual line-shafting system to large and sudden variation in load torque – Rig A	174
6.33	Response of the sensorless virtual line-shafting system to large and sudden variation in load torque – Rig B	174
6.34	Structure of the speed/position controller	175
6.35	Modified structure of the parallel cross-coupled scheme, to include relative position correction	176
6.36	Response of the encoded cross-coupling scheme to large and sudden variation in rig A load torque. Relative position error is shown in black and positional correction is not included	176
6.37	Response of the encoded cross-coupling scheme to large and sudden variation in rig A load torque. Relative position error is shown in black and positional correction is included	177
6.38	Response of the sensorless cross-coupling scheme to large and sudden variation in rig A load torque. Relative position error is shown in black and positional correction is not included	178
6.39	Response of the sensorless cross-coupling scheme to large and	

	sudden variation in rig A load torque. Relative position error is shown in black and positional correction is included	178
6.40	Differential speeds to achieve product delivery rate variation	179



---

## List of Tables

---

2.1	Space vector timing distributions according to sector	34
2.2	Sensorless drive applications and required performance	39
3.1	Specifications of the 2 induction machines	57
4.1	Speed controller specifications	78
4.2	Current controller specifications	79
4.3	AFO implementation specifications	80
4.4	ASO implementation specifications	81
4.5	Key to speed and current measurements/estimates in figures in sections 4.32 and 4.33	87
5.1	Key to the marking of the FFT plots of motor terminal Quantities	110
5.2	Where RSH harmonics for $\kappa = -1$ and $+3$ coincide with next lowest PWM harmonics	111
5.3	Where RSH harmonics coincide with next lowest PWM Harmonic	113
5.4	Key to speed measures/estimates shown in figures (unless otherwise stated)	125
5.5	Tuning specification implementation	137
6.1	Colour key to the speed and position measures shown in the following results	160

---

## List of Symbols

---

This is a list of the principal symbols used with regard to describing induction motor operation throughout the text.

$i_a, i_b, i_c$	induction motor 3-phase line currents (A)
$v_{ab}, v_{bc}, v_{ca}$	induction motor 3-phase line voltages (V)
$i_\alpha, i_\beta$	induction motor currents in the 2-axis fixed stator frame (A)
$v_\alpha, v_\beta$	induction motor voltages in the 2-axis fixed stator frame (V)
$i_d, i_q$	induction motor currents in the 2-axis synchronous frame (A)
$v_d, v_q$	induction motor voltages in the 2-axis synchronous frame (V)
$\underline{i_s}$	induction motor stator current vector (A)
$\underline{i_r}$	induction motor rotor current vector (A)
$\underline{v_s}$	induction motor stator voltage vector (V)
$\underline{v_r}$	induction motor rotor voltage vector (V)
$\underline{\lambda_s}$	induction motor stator flux vector (Wb)
$\underline{\lambda_r}$	induction motor rotor flux vector (Wb)
$\omega_e$	synchronous (stator applied/flux) frequency (rad/s)
$\omega_r$	rotor (speed) frequency (rad/s)
$\omega_{slip}$	slip frequency (rad/s)
$\theta_e$	angle between synchronous frame and fixed stator frame (radians)
$\theta_r$	angle between rotor frame and fixed stator frame (radians)
$T_e$	induction motor electromagnetic torque (Nm)
$J$	motor rig inertia ( $\text{kgm}^2$ )
$B$	motor rig friction ( $\text{kgm}^2/\text{s}$ )
$p$	number of motor pole pairs

$R_s, R_r$	stator and rotor resistances ( $\Omega$ )
$l_s, l_r$	stator and rotor leakage inductances (H)
$M$	stator-rotor mutual inductance (H)
$L_s, L_r$	stator and rotor self-inductances (H)
$\sigma$	inductance leakage coefficient
$T_r$	rotor time constant (s)

The  $\alpha, \beta, d, q$  subscripts are used, as defined for current and voltage above, to define aligned and orthogonal components of the various vector quantities, in the fixed stator and synchronous rotating frames respectively, in various parts of the dynamic equation analysis throughout the text.

In other sections, particularly those regarding voltage source inverter operation and rotor slot harmonic tracking, various other symbols are defined locally for use in the presented analysis.

---

# CHAPTER 1 Introduction

---

## 1.1 Introduction

The control of electrical machines forms a fundamental part of industrial manufacture and process control in most developed countries. Applications range from simple fixed speed drives for pumps, fans, conveyors, etc, through to more advanced motion control problems associated with robotics, machine tools and complex manufacturing processes. Power requirements range from Watts (disk drives) through to Megawatts (steel plants, traction) and it is estimated that 70% of all the electricity utilised in the EU and Japan involves electric motor drives of some form [1]. Indeed, over the last few years, a renewed interest in clean energy sources and associated technology, such as the electric car, has led to an upsurge in interest in electric motor control and in improving motor drive efficiency [2, 3]. Although many types of electric motor are available, ranging from the traditional brushed DC machine through to more recent developments in permanent magnet and reluctance motors, the induction motor still remains the most popular choice for many industrial applications.

The induction motor was developed in the late 1800s, principally by Nikola Tesla [4]. Operating from an alternating current (AC) electrical source, power is transferred from the stator to the rotor through electromagnetic induction, rather like the action of a transformer, and this alleviates the need for any sliding contacts to the moving component of the machine. In contrast, the direct current (DC) motor requires sliding brushes to facilitate an electrical connection directly to the rotating armature. The advantages of the induction motor are related to this lack of sliding contacts, and include lower manufacturing and maintenance costs, increased robustness and power for a given volume, and elimination of any sparking hazard associated with the sliding brushes. These considerations have long established the induction motor as the most suitable choice for fixed speed operation in industrial processes and the development of distribution systems as we know them has been tailored to their requirements [4]. An estimated 22 million three-phase induction motors in the UK are thought to utilise around 43% of the generated electricity [5].

In applications where variable speed and/or high dynamic performance are required the DC motor has traditionally been the machine of choice. Although the DC machine has a more complex construction, and hence is at a disadvantage compared to the induction motor in many respects (as previously described), the control requirement for its high performance operation is straightforward. Hence the power processing electronics required for its high performance/variable speed operation are simple and thus both inexpensive and reliable.

There are two main types of power converter used to provide DC motor control. Voltage must be controllable to perform current control, thus DC-DC converters (choppers) can be used. This type of converter controls the average voltage applied to the motor from a fixed DC supply, through high frequency modulation of power electronic switches. Alternatively, and more often used at higher power levels, a controlled rectifier can be used to provide a controllable DC voltage. The different configurations offer various advantages/disadvantages and topologies can be arranged to provide various speed (forward/reverse) and torque (motoring/regenerating) control modes. DC converters are very well described by Mohan, Undeland and Robbins [6].

Variable speed operation using the induction motor is now more readily achieved since the advent of the power electronic inverter, although this is somewhat more complex a power converter than the DC converters. The variable speed is achieved by control of the stator voltage and excitation frequency using a Volt/Hertz (V/F) control scheme. In the scheme the ratio of output voltage/frequency is held constant in an attempt to maintain a constant flux in the machine. Both V/F control and the operation of the power electronic inverter are also well covered in textbooks [6-8]. The dynamic performance of V/F control is poor however, because the validity of the voltage/frequency relationship only holds in the steady state. More recently high performance operation was proposed, for the induction motor and other AC machines, through the application of vector control. The pioneering work in this area was carried out in Germany in the late sixties/early seventies [9, 10]. The power converter requirement is similar here to that used in the V/F scheme, but additional sensors, as well as increased control computational capability, are required.

Power and control processing technologies (power semiconductors and microprocessors) are continuously advancing. Improving manufacturing processes

and increased product demand results in the relative cheapness of these products. Vector controlled high performance AC motor drives are now a realistic financial proposition in industrial applications. The advantages gained by the cheaper manufacturing costs, increased robustness and lesser maintenance requirements of the induction motor outweigh the increased costs associated with the power converter technology.

### 1.2 Vector Control

In the separately excited ideal DC machine, flux and torque can be regulated independently. Flux is regulated by controlling the current flowing in the field winding  $I_f$ , whilst torque is controlled by regulating the current flowing in the armature winding  $I_a$ . The current control is achieved through independent control of  $V_f$  and  $V_a$ . Figure 1.1 shows the schematic circuit diagram of the separately excited DC motor and the independence of the field and armature circuits is evident.

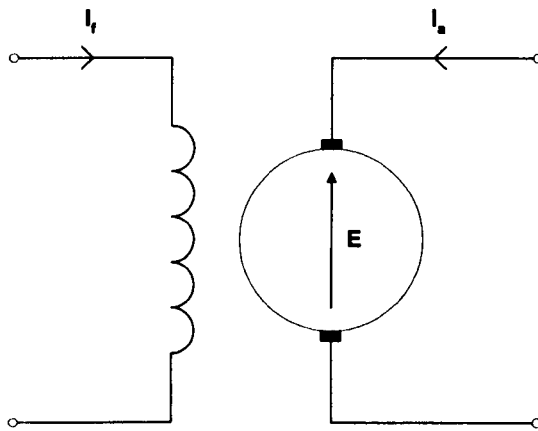


**Figure 1.1. Schematic circuit diagram of the separately excited DC machine**

Things are not so simple in an induction motor, but vector control is the method by which the torque and flux related quantities are decoupled for independent control. Application of this method allows high dynamic performance to be obtained, comparable to that of the DC machine. The direct control of torque is no longer affected by the slow magnetic time constant of the machine, as would be the case under V/F control for example, where flux and torque control will be coupled.

The construction of the simple squirrel cage induction motor incorporates no direct connection to the rotor and hence the current flowing in the rotor bars, that will be

related to torque, cannot be directly regulated or measured (this being unlike the armature current in the ideal DC machine). Control of the induction motor must be achieved through regulation of stator quantities. Torque and flux must both be regulated by control of the 3-phase stator currents, which form a balanced set.

The three measured instantaneous stator currents can be transformed to a single current vector, with an associated amplitude and phase, referenced to a fixed position [11]. It is now reasonable to assume that part of this current vector is responsible for flux production and part solely for producing torque. Vector control is the means by which these components are decoupled and controlled. It must be appreciated that vector control is by no means as simple as DC motor control, because it both deals with rotating (AC) quantities and must determine robust reference information for decoupling. In effect the removal of rotating terminal quantities and the decoupling of flux and torque components in a DC machine is inherent in its construction.

The most straightforward implementation for decoupled vector control is termed rotor flux orientation. If the rotor flux vector, which rotates in the same co-ordinate system as the transformed current, can be determined (directly or indirectly) and the transformed current is split into components that are aligned to and orthogonal to this rotor flux vector, it is found that the aligned component is responsible for flux production and the orthogonal component is responsible for torque production. In essence, if reference is correctly made with the rotor flux vector, the transformed current components ( $I_d$  is the aligned flux related component,  $I_q$  is the orthogonal torque related component) are controlled as DC values, analogous to  $I_f$  and  $I_a$  in the DC machine.

A mathematical analysis for vector control is presented in chapter 2. Vector control is also often termed flux (or field) oriented control. The principles of electrical motor control are most excellently and thoroughly covered in the work of Leonhard [12].

### 1.3 Sensorless Vector Control

Having established that decoupled control of flux and torque can be achieved with knowledge of the rotating rotor flux vector, it is necessary to obtain a measure/estimate of this quantity. Early implementations were based on direct measurement through the use of hall probes (or search coils) mounted in the motor air gap [9, 13]. The solution of direct measurement is considered somewhat impractical

however, because the fitting of the measurement devices obviously negates many of the practical and cost associated advantages related to induction motor use.

In practice the simplest means of establishing vector control is termed Indirect Rotor Flux Orientation (IRFO). This method takes advantage of the following electrical equations (equation 1.1 and equation 1.2) to force orientation. Equation 1.1 is in its simplest form, ignoring transient field effects, and equation 1.3 is included to show how electrical and mechanical frequencies (in this example speeds) are related by the motor pole pair number.

$$\omega_{slip(elec)} = \frac{I_q}{I_d T_r} \quad (1.1)$$

$$\omega_{e(elec)} = \omega_{r(elec)} + \omega_{slip(elec)} \quad (1.2)$$

$$\omega_{r(mech)} = \frac{\omega_{r(elec)}}{p} \quad (1.3)$$

Here  $\omega_e$  is the excitation (stator applied) frequency,  $\omega_r$  is the speed,  $\omega_{slip}$  is the slip frequency (and is imposed),  $I_d$  is the aligned axis current component,  $I_q$  is the orthogonal axis current component,  $T_r$  is the rotor time constant (a motor electrical model parameter defined in the following chapter) and  $p$  is the number of motor pole pairs. Essentially the voltage amplitude and phase, applied to the induction motor by the power electronic inverter, are controlled to maintain suitable  $I_d$  and  $I_q$  currents for flux and torque control and the  $\omega_e$  frequency for orientation. Hence the control satisfies the induction motor dynamic equations, from which it is derived, and unlike V/F control is valid under transient conditions. This is made clear in the analysis presented in chapter 2.

The important aspect to note, from the above equations, is that knowledge of speed is required for this (IRFO) implementation. High performance induction motor drives are thus mainly associated with the requirement for a high precision optical shaft-mounted speed encoder. An implementation incorporating such measurement of speed is thus termed encoded (or sensed) control.



The addition of a speed encoder is considered a disadvantage in terms of robustness, practicality and cost, and especially if this is simply only to facilitate decoupled flux/torque control. Again the fitting of such a device certainly negates the advantages associated with the use of an induction motor and the cost, for lower power drives, can form a large proportion of the overall expenditure. The desired elimination of such a transducer has resulted in the development of so called sensorless techniques. Thus, for the purposes of this work, sensorless control is defined as that control not requiring a transducer directly measuring speed or position.

Whilst the high performance control of induction machines, through the implementation of encoded IRFO vector control, is an established technique, the manner by which sensorless control is achieved varies widely through many different methods. A thorough review of this area is therefore presented in the following background chapter.

As a more general overview, sensorless techniques obtain both speed and flux information, for vector control, from measured electrical terminal quantities. Many techniques, and certainly those that have mainly impacted into commercial products, rely on knowledge of the machine electrical parameters. Speed and flux information is obtained through application of the induction motor dynamic equations and this is again considered further in chapter 2. The problem with this type of method is that performance is dependent upon the accurate knowledge of motor electrical parameters. Even if the parameters are determined accurately at start-up, resistance parameters will vary greatly with operating condition (temperature) and inductance parameters will also be subject to variation (with flux). In these schemes, under conditions where parameters are subject to inaccuracy/drift, both speed and torque performance will be compromised. Whilst tuning schemes have been proposed, based on electrical characteristic measurement (see next chapter), to correct individual model parameters, parameter interdependency ensures that high accuracy speed and/or torque regulation cannot be guaranteed.

More recently techniques have been introduced that exploit mechanical/electrical saliencies in the machine to extract flux and/or speed/position information. A more detailed account can again be found in chapter 2. Very often these techniques use specially modified machines and/or signal injection techniques. Such techniques have yet to significantly impact in industry, because a great deal of engineering is

required to make them wholly viable. Use of signal injection methods, for example, may increase drive torque ripple, power losses, acoustic noise, etc and may only be appropriate over a small speed range, in the low speed region. These techniques have been demonstrated to offer excellent performance however, as speed and flux information can be obtained, the accuracy of which is independent of operating condition.

Previous work, based on saliency in the induction machine rotor, due to necessary rotor slotting, has provided a speed estimate that does not require the use of signal injection. Slotting harmonics in terminal quantities are related to the applied stator frequency and the number of rotor slots per pole pair and thus can provide a speed estimate that does not vary with electrical parameters. Speed signals have been extracted using analogue techniques, but with performance compromised by analogue circuit tolerances and drift, and using digital methods, such as the FFT, but these have high computational requirements and have thus not had commercial impact. More recently recursive techniques have been proposed and tested, but have yet to be developed into a sensorless system. The work presented here exploits and extends these methods and, as such, a thorough background and review is presented in chapter 5.

### 1.4 Speed Critical Applications

Encoded induction motor drives have now impacted into the range of applications previously considered the domain of DC drives. Sensorless induction motor drives however, have not replaced encoded systems in particular application areas. One such significant area is based around those applications that rely on highly accurate speed holding capability.

In an IRFO encoded drive, referring back to equation 1.1 and 1.2, the criteria for field orientation depends on knowledge of motor speed and the machine rotor time constant  $T_r$ . Inaccurate knowledge of  $T_r$  and/or an associated variation with operating condition will therefore affect the decoupled (dynamic) performance of the drive. However, the measurement of speed driving the speed control loop ensures that the speed holding capability of the drive is not compromised. Of course this assumes that the drive is operating within its rated conditions and that orientation (decoupling) inaccuracy does not cause substantial instability. Unlike model-based sensorless techniques, where performance with parameter inaccuracy/variation will affect speed

holding, a drive based on this method will be suitable for speed critical processes and this would include multi-motor speed synchronised applications.

### **1.4.1 Multi-motor applications**

Many mechanisms, in manufacturing processes for example, require that multiple axes be controlled relative to each other. These processes would include the manufacture or handling of sheet material. Co-ordinated control is generally achieved by connection of the various elements, through mechanical linkages and gearing, to a common source of mechanical power.

More recently mechanisms have been produced where constituent components are driven independently. Here the synchronisation is achieved electronically and control is often designed to emulate mechanically coupled performance. The advantages associated with electronically coupled control certainly includes an increase in flexibility: gearing ratios can be adjusted in software and machinery can be quickly set-up to vary product specification with a minimum of downtime, or even on-line. The reduction in mechanical component count may also serve to reduce the size of the overall system and increases the robustness and reliability, whilst reducing maintenance requirements.

Use of encoded induction motor drives in multi-axis machinery provides the advantages associated with the use of an induction machine, over the use of DC machines, as previously described. The use of sensorless techniques would hence bring further advantages in terms of practicality and cost, given that their range of applicability were extended, to include the capability of accurate speed holding. Indeed, in applications such as paper production, where parts of a process may be subject to damp/wet conditions, and steel manufacture, where extremes of temperature may be encountered, it may not be possible to use an encoder. In rolling road applications a shaft-mounted encoder may be difficult to fit. These are certainly applications where electronic multi-motor control can be applied. This area is more fully considered in chapter 6.

## **1.5 Project Motivation, Aims and Objectives**

The overall aim of this project is as follows:

*To develop and demonstrate a fully sensorless induction motor drive that has sufficient speed holding capability to make it suitable for industrial processes where multi-motor control is required.*

Primarily the work of this project concentrates on the engineering of a sensorless drive that will display encoder like speed holding accuracy in the steady state. Secondly the validity of the engineered sensorless algorithm is tested for its use in multi-motor applications. By applying the algorithm to a second motor drive, the speed holding sensorless algorithm is tested on an alternative system and the two sensorless drives are combined, to form a dual-axis speed synchronised arrangement.

This project is supported by FKI Industrial Drives and the general push from industry is such that sensorless methods are developed using standard power electronics and do not rely on non-standard or modified machines. It would also be preferred that methods do not rely on signal injection, which may increase power losses and acoustic noise. Nor should a method require such high a processing requirement that it would be considered impractical or uneconomical. The developed system should also operate over the majority of the rated speed and load range, having an operating region and performance at least comparable with existing model-based sensorless solutions. Ideally the developed scheme will have minimal set-up requirements, not requiring extensive knowledge of machine and plant characteristics.

This work introduces a sensorless algorithm developed for speed holding accuracy, in the form of a new hybrid system, with the above criteria in mind. A parameter dependent model-based vector control algorithm (for decoupled dynamic performance) is combined with a motor speed estimator that exploits natural motor saliency (for speed accuracy). The accurate speed estimate is used for tuning of the motor model and is extracted using recursive signal processing techniques, from the spectral information seen naturally in terminal quantities due to rotor slotting. Unlike previous works, the speed estimator, because of the recursive nature of the technique, has a sufficiently low computational overhead so as to have commercial validity. This is the first time the slot harmonic identifying method has been developed into a fully functional sensorless practical system, a full technique suitably described and full testing performed. The solution is tested on two developed test rigs and compared to encoded vector schemes run on the same. The rigs both use standard commercial power electronic inverters and standard unmodified induction machines.

The developed tuning mechanism is intended to account for error and variation in motor model parameters, such that speed-holding accuracy is not compromised.

The engineered sensorless solution is tested for use in multi-motor speed synchronised applications. As previously established, this is an area that would typically require the use of an encoded solution. Various multi-motor algorithms are tested for use with the sensorless implementation described. Results obtained are compared and contrasted with those obtained from a fully sensed solution. It is the intention of this project that fully practical solutions are obtained and this work is therefore highly biased towards experimental results.

### 1.6 Thesis Organisation

As previously alluded to, chapter 2 takes a more in-depth look at the background to the project than has been provided in this introduction, with a detailed literature review. The principles and necessary theory for vector control are presented. As well as IRFO control, other appropriate methods will be discussed. The chapter then looks at the operation of the power electronic inverter and particularly at how the AC output produced, whilst of variable voltage and phase, is non-ideal. This is of concern and will be picked up again when the model-based sensorless method and the rotor slotting speed estimator are practically considered in subsequent chapters. Finally chapter 2 goes on to review the area of sensorless induction motor control in some depth, considering the merits of particular algorithms and techniques. The review forms the basis on which a suitable model-based method is chosen for implementation and this is discussed and more fully presented in chapter 4.

As it was the intention that this project should have a heavy practical bias and commercial validity, both the development of the sensorless algorithm and the multi-motor testing have been performed on a practical dual motor drive system. The system was developed as part of the project and consists of a Digital Signal Processing (DSP) platform housed in a host PC. The DSP is interfaced, through data measurement and acquisition, control and digital input-output circuitry, to commercial power electronic inverters and 4kW induction motors. The DSP is used for real-time control, with the PC performing overall high-level command control and drive data capture functions. The induction motors are each connected to DC machines that act as load. As is appropriate for a practical/experimental thesis, the system is documented and described in chapter 3.

In chapter 4 the model-based sensorless algorithm forming the foundation of the sensorless strategy is fully considered and described. The reasons for its selection are discussed, based on the sensorless review of chapter 2 and other testing work. The chapter introduces tests that demonstrate the performance of the sensorless drive. Results are obtained for both encoded and sensorless schemes running the prescribed tests and the two compared. The chapter continues by considering the implications and effects of parameter detuning in the sensorless scheme, showing that the most significant speed accuracy deterioration is related to a detuning of the rotor time constant  $T_r$ .

Chapter 5 discusses the production and tracking of rotor slot harmonics. Spectral estimation techniques previously presented to obtain speed estimation from slot harmonic effects are reviewed, as well as previous examples where the estimate is used to tune  $T_r$ . These examples are however, based mainly on highly computationally intensive algorithms. The chapter goes on to present the technique used in this instance: a recursive digital filtering technique called the Recursive Maximum Likelihood – Adaptive Tracking Filter (RML-ATF). Using this method, a high bandwidth, highly accurate speed estimate is obtained. The estimate, through its comparison with the sensorless model-based speed measure, is used to drive a tuning mechanism for  $T_r$ . The tuning scheme is presented and discussed. Finally, results are presented that demonstrate the performance of the practical sensorless tuning drive, with a particular view to demonstrating its speed holding performance in the steady state. The engineered solution is shown to display encoder like speed holding accuracy. It is believed that this is the first time the algorithm has been presented in a PhD thesis relating to its use as a speed estimator in motor drives, and the first time it has been demonstrated in/developed into a fully sensorless system.

In chapter 6, speed synchronisation of multiple machines is considered. The advantages associated with replacing a mechanically coupled multi-axis system (partly or completely), with individually driven axes that are speed synchronised electronically, are considered. Applications where this would be/is applicable are given and these include printing, sheet material production, etc. The algorithms presented that enable such synchronisation are described and firstly results are presented that demonstrate the encoded practical system running these schemes for dual drive synchronisation. The chapter then presents results obtained, under similar test conditions, with the developed sensorless tuning drives running the speed-

synchronised control. In the conclusion of the chapter the results obtained in the encoded and the sensorless modes are compared, with the sensorless scheme being considered to have fulfilled its desired design criteria: to provide encoder like speed holding accuracy, and hence synchronisation, in the steady state. The validity of using the sensorless speed estimate to provide some degree of positional error correction (that incurred during transient conditions) is also tested. The relative merits of the various synchronisation schemes are discussed. The author has been unable to find any other work specific to the use of sensorless motor drives in this application area.

Conclusions are drawn together in chapter 7 and ideas for further work are presented. Particularly this chapter reviews the demonstrated performance of the work. It discusses the possibility of commercial implementation of the RML-ATF algorithm to tune sensorless schemes, integration of the method with signal injection methods for improved low speed performance, improving the scheme through appropriate motor choice and application of sensorless techniques to further application areas.

### 1.7 Project Outcomes

With particular regard to emphasising the novel areas of this work, the outcomes of the project are:

- A viable sensorless drive algorithm has been practically engineered, as an extension to model-based methods, for accurate encoder-like speed holding
  - The RML-ATF frequency identifier has now been developed into a complete speed identifier, with new pre-filtering methods applied
  - New inputs have been tested that improve the speed identifier performance, using measured current and reference voltage
  - The algorithm is developed into a true sensorless system, tuning a model-based method, and encoder-like speed accuracy practically demonstrated
  - The validity of the algorithm has been demonstrated, by its application to a second induction motor drive system with minimal modification

- The slot harmonic based speed measurement has been considered for direct feedback and a simple scheme, based around V/F control, demonstrated
- A review of multi-motor synchronisation schemes has been undertaken, with the practical performance of each scheme demonstrated
- Electronic bi-axial speed synchronisation in the sensorless mode has been considered. Synchronised operation of the engineered sensorless tuning drive has been shown practically to be highly comparable to an encoded version.
- The developed bi-axial sensorless scheme has shown the ability to compensate somewhat for relative position error accumulated during fast load transient conditions
- Areas for further work, in order to allow sensorless techniques to further impact into non-standard sensorless application areas, have been highlighted

Interest in the sensorless tuning scheme is being shown by two UK drives companies. The work has resulted in five conference papers [14-18], and these are included as Appendix A.



---

## CHAPTER 2 Background

---

### 2.1 Introduction

Chapter 1 introduced the concept of vector control. The concept relies on the decoupling of flux and torque producing components of measured induction motor stator current. Decoupling enables control to be established for high dynamic performance capability. The following section develops the theory behind the method that achieves decoupled control, termed vector control or flux (field) orientation.

The per-phase electrical equivalent circuit of the induction motor is firstly considered, in section 2.2. The resistance and inductance parameters contained in the circuit are defined for use in the analysis of the motor dynamic equations. Rotating reference frames are also discussed, as the equations must be defined in a rotating frame, such that flux and torque currents can be controlled as DC values. The section goes on to present the dynamic equation derivations for rotor and stator flux orientation. The various methods of achieving orientation are considered, as is the operation of the induction motor in field weakening.

Having established that controlling the instantaneous stator current of the induction motor can facilitate vector control, it is necessary to understand how this can be achieved in practice. Here use is generally made of the Voltage Source Inverter (VSI) type power converter. The VSI provides a magnitude and phase controllable 3-phase voltage output, applied to the induction motor stator terminals. The vector scheme current controllers drive the voltage vector demanded from the VSI. The topology for this type of converter is presented and discussed in section 2.3. The section goes on to present and analyse the way in which the VSI is controlled using Pulse Width Modulation (PWM) techniques. The PWM method used in this work is termed Space Vector Modulation (SVM). The theory of SVM is presented and the associated discussion centres on the non-ideal nature of the voltage waveforms produced by any PWM method. Also considered is the necessity for inverter switch deadtime as this contributes to the non-ideal nature of the VSI output.

Section 2.4 outlines the motivational criteria for achieving vector control without the use of a shaft-mounted speed encoder. It goes on to provide the background of sensorless vector control and presents an overview of the leading methods that achieve this, based on the machine dynamic equations considered in section 2.2. These methods are facilitated through measurement of stator terminal quantities and are termed ‘model-based’ techniques.

In the conclusion of this chapter the motivational criteria for this work will be reinforced and it is hoped that sufficient theory will have been imparted to allow full understanding of the remaining work.

## 2.2 Vector Control

Vector control of the induction motor is achieved through control of flux and torque related components of the stator currents. In order to achieve this the full dynamic model of the induction motor must be considered.

### 2.2.1 The Per-Phase Induction Motor Equivalent Circuit

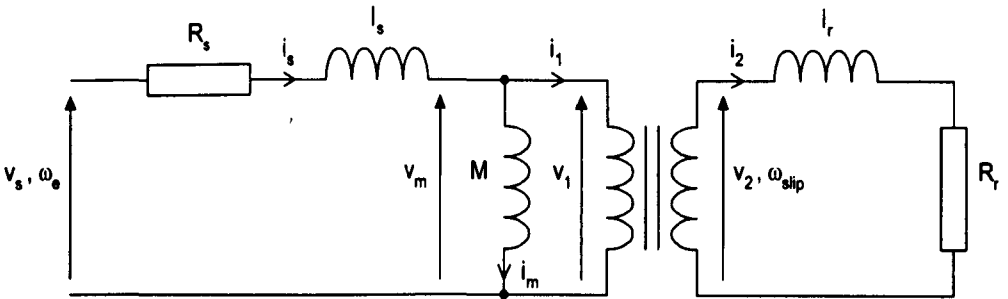


Figure 2.1 The induction motor per-phase equivalent circuit (squirrel-cage rotor)

The per-phase equivalent circuit of the squirrel cage induction motor is shown in figure 2.1. The circuit is similar to the equivalent circuit for a transformer and the analysis is not far removed. In the case of the induction motor however, the rotor/secondary circuit frequency ( $\omega_{slip}$ ) is dissimilar from that at the stator/primary ( $\omega_e$ ) and this is due to the rotation of the rotor. Note also that the resistance shown on the secondary side is that of the rotor circuit ( $R_r$ ) only. With the transformer there would be secondary and load resistances. The load resistance is absent here because the squirrel cage configuration of the rotor is effectively a short-circuited secondary.

Various circuit voltages are labelled, although, as with other circuit quantities, it is only the motor terminal voltage ( $v_s$ ) that is directly obtainable.

Analysis of the circuit allows for simplification. The ideal transformer can be removed if the rotor side parameters are referred to the stator side. The simplified circuit will include a speed related voltage source. If the motor is operating in the steady state the circuit can be simplified further by removal of this additional voltage source. The value of rotor resistance must then be modified to  $R_r/s$ , where  $s$  is motor slip [ $s = (\omega_e - \omega_r)/\omega_e$ ]. The simple steady state circuit is used to determine the electrical circuit parameters shown in the figure, using no-load and locked rotor tests [19]. These tests are the equivalent to the open and short circuit tests used to characterise a transformer [19].

Derivation and simplification of the equivalent circuit is well described in [12]. The equivalent circuit is directly related to the dynamic equation analysis that will be presented in the following sections. Here the circuit is presented only in its general form to enable the definition of the parameters used in such analysis

The equivalent circuit is utilised in Appendix B to calculate motor parameters for one of the induction motors used in this work.

### **2.2.2 Parameter Definition**

Referring back to the equivalent circuit (figure 2.1), the motor electrical parameters are defined as

$R_s, R_r$	-	Stator and Rotor Resistances ( $\Omega$ )
$l_s, l_m$	-	Stator and Rotor Leakage Inductances (H)
$M$	-	Stator-Rotor Mutual Inductance (H)
$L_s = l_s + M$	-	Stator Self Inductance (H)
$L_r = l_r + M$	-	Rotor Self Inductance (H)
$\sigma = \frac{L_s L_r - M^2}{L_s L_r}$	-	Leakage Coefficient
$T_r = \frac{L_r}{R_r}$	-	Rotor Time Constant (s)

(2.1)

### 2.2.3 Reference Frames and Transforms

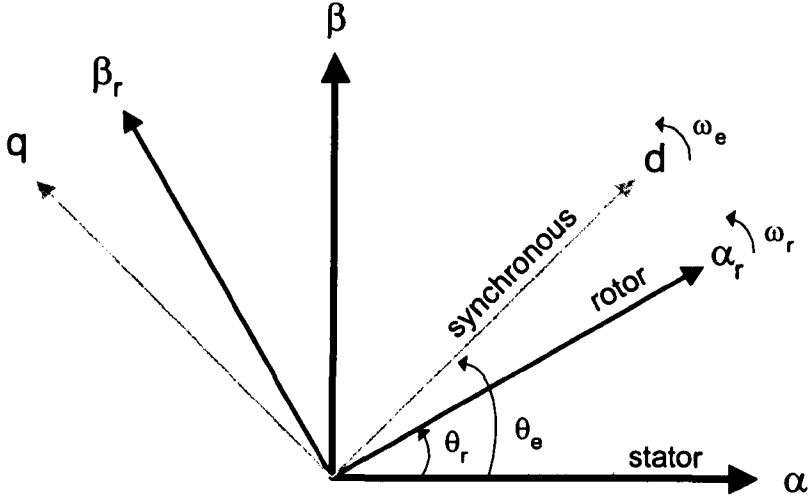


Figure 2.2. Stator, rotor and synchronous reference frames

Figure 2.2 shows the reference frames used to develop the vector control theory/dynamic equation analysis. The 2-axis stator frame is fixed (as is the physical stator) and the 3-phase terminal quantities (voltage and current) can be expressed as individual vectors rotating in this frame, by applying the Clark transform [11]. The  $\alpha$ -axis of the 2-axis stator frame is aligned with the a-phase of the 3-phase system. The 3-phase to 2-phase current and voltage transforms are shown in the equations below.

$$\begin{pmatrix} i_\alpha \\ i_\beta \end{pmatrix} = \frac{2}{3\sqrt{3}\sqrt{2}} \begin{pmatrix} 3/2 & 0 & 0 \\ 0 & \sqrt{3}/2 & -\sqrt{3}/2 \end{pmatrix} \begin{pmatrix} i_a \\ i_b \\ i_c \end{pmatrix} \quad (2.2)$$

$$\begin{pmatrix} v_\alpha \\ v_\beta \end{pmatrix} = \frac{2}{3\sqrt{2}} \begin{pmatrix} \sqrt{3}/2 & 0 & -\sqrt{3}/2 \\ 0 & 3/2 & 0 \end{pmatrix} \begin{pmatrix} v_{ab} \\ v_{bc} \\ v_{ca} \end{pmatrix} \quad (2.3)$$

The measured variables ( $i_a$ ,  $i_b$ ,  $i_c$ ,  $v_{ab}$ ,  $v_{bc}$ ,  $v_{ca}$ ) are 3-phase line quantities. For delta connected loads, as used in this work, line voltages and phase voltages are the same. Line to phase current scaling is incorporated in equation 2.2. Both sets of equations account for a  $3/2$  scaling factor introduced by the  $\alpha\beta$  transformation and appropriate

RMS scaling is applied. Therefore the dq quantities represent the machine currents as RMS values, providing a direct relation to machine ratings.

It is a necessity to measure and transform the current for use in the fast current control loops of any vector control scheme. The voltages are not always measured: reference values could be used, as long as any low-voltage non-linear relationship between  $V_{\text{reference}}$  and  $V_{\text{measured}}$  is calibrated.

Again referring to figure 2.2, the 2-axis rotor frame rotates with the rotor at rotor speed ( $\omega_r$ ). This frame is used to define the rotor dynamic equation prior to us introducing the synchronous frame. Use of this frame allows the rotation of the rotor to be neglected in the analysis, apart from where stator quantities are used.

The synchronous frame is the frame that will enable us to demonstrate the principles of vector control. The synchronous frame rotates at the stator excitation frequency ( $\omega_e$ ), as do the various flux vectors. The induction motor dynamic equations will be transformed to this frame and current quantities controlling flux and torque appear as DC values (in this frame) in the steady state.

Transformation from the fixed stator frame to any rotating frame makes use of the rotating vector angle within the fixed frame, through application of the Park transform [11]. The equations shown below, as an example, are for transformation of  $\alpha\beta$  currents to the synchronous dq frame.

$$\begin{pmatrix} i_d \\ i_q \end{pmatrix} = \begin{pmatrix} \cos \theta_e & \sin \theta_e \\ -\sin \theta_e & \cos \theta_e \end{pmatrix} \begin{pmatrix} i_\alpha \\ i_\beta \end{pmatrix} \quad (2.4)$$

Prior to the analysis of the induction motor dynamic equations, frequency and phase relationships are defined below.

$$\begin{array}{ll} \omega_e = \frac{d\theta_e}{dt} & - \quad \text{Synchronous (Excitation) Frequency (rad/s)} \\ \omega_r = \frac{d\theta_r}{dt} & - \quad \text{Rotor (Electrical Speed) Frequency (rad/s)} \\ \omega_{slip} = \omega_e - \omega_r & - \quad \text{Slip Frequency (rad/s)} \end{array} \quad (2.5)$$

As outlined in chapter 1, electrical and mechanical frequencies are simply related by the motor pole pair number ( $p$ ), as shown in equation 2.6. The relationships outlined in the set of equations 2.5 hold if referring to only electrical or only mechanical frequencies. Primarily we are concerned with electrical quantities.

$$\omega_{x(mech)} = \frac{\omega_{x(elec)}}{p} \quad (2.6)$$

It is also appropriate to define the subscript terminology, used here to represent reference frames, and this is given below, with flux as an example variable.

$\lambda_s$	-	Stator Flux in Synchronous Frame (Wb)
$\lambda_r$	-	Rotor Flux in Synchronous Frame (Wb)
$\lambda_{ss}$	-	Stator Flux in Stator Frame (Wb)
$\lambda_{rr}$	-	Rotor Flux in Rotor Frame (Wb)

#### 2.2.4 Induction Motor Dynamic Equations

The induction motor equivalent circuit can now be used to develop the induction motor dynamic equations using the concept of reference and rotating frames.

The stator dynamic equation for the induction motor in the stator reference frame [12]

$$\underline{v}_{ss} = R_s \underline{i}_{ss} + L_s \frac{d \underline{i}_{ss}}{dt} + M \frac{d (\underline{i}_{rr} e^{j\theta})}{dt} \quad (2.7)$$

The rotor dynamic equation in the rotor reference frame [12]

$$\begin{aligned} \underline{v}_{rr} &= 0 \\ &= R_r \underline{i}_{rr} + L_r \frac{d \underline{i}_{rr}}{dt} + M \frac{d (\underline{i}_{ss} e^{-j\theta})}{dt} \end{aligned} \quad (2.8)$$

The electromagnetic torque ( $T_e$ ) can be defined, and is that produced by the induction motor to provide a total force: the mechanical load torque plus windage, friction, etc associated with the motor itself. As torque is essentially a mechanical quantity, it must

be related to electrical quantities using an expression involving the motor pole pair number. Hence the induction motor equation for electromagnetic torque [12]

$$\begin{aligned} T_e &= 3 p \operatorname{Im}(\underline{i}_{ss} \underline{\lambda}_{sr}^*) \\ &= 3 p M \operatorname{Im}(\underline{i}_{ss} (\underline{i}_{rr} e^{j\theta})^*) \end{aligned} \quad \begin{array}{l} \text{where } \underline{\lambda}_{sr} = \text{rotor flux linkage} \\ \text{in the synchronous frame} \end{array} \quad (2.9)$$

If the stator, rotor and torque equations are transformed to the synchronously rotating frame, using an  $e^{j\theta_e}$  phase relation, equations 2.5 to 2.7 become

$$\underline{v}_s = R_s \underline{i}_s + L_s \left( \frac{d \underline{i}_s}{dt} + j \omega_e \underline{i}_s \right) + M \left( \frac{d \underline{i}_r}{dt} + j \omega_e \underline{i}_r \right) \quad (2.10)$$

$$0 = R_r \underline{i}_r + L_r \left( \frac{d \underline{i}_r}{dt} + j \omega_{slip} \underline{i}_r \right) + M \left( \frac{d \underline{i}_s}{dt} + j \omega_{slip} \underline{i}_s \right) \quad (2.11)$$

$$T_e = 3 p M \operatorname{Im}(\underline{i}_s \underline{i}_r^*) \quad (2.12)$$

## 2.2.5 Flux Orientation

### Rotor Flux Orientation

The general synchronous frame equations shown in 2.10 to 2.12 are modified to include only those quantities of interest. In the case of rotor flux orientation, this is the measurable stator current vector and the rotor flux vector.

The following relationship is used to substitute for  $\underline{i}_r$  in equations 2.10 to 2.12 [12]

$$\underline{\lambda}_r = L_r \underline{i}_r + M \underline{i}_s \quad (2.13)$$

Using the definition of the leakage coefficient ( $\sigma$ ), equations 2.10 to 2.12 become

$$\underline{v}_s = R_s \underline{i}_s + \sigma L_s \frac{d \underline{i}_s}{dt} + j \omega_e \sigma L_s \underline{i}_s + \frac{M}{L_r} \frac{d \underline{\lambda}_r}{dt} + j \omega_e \frac{M}{L_r} \underline{\lambda}_r \quad (2.14)$$

$$0 = -\frac{M}{L_r} R_r \underline{i_s} + \frac{R_r}{L_r} \underline{\lambda_r} + \frac{d \underline{\lambda_r}}{dt} + j \omega_{slip} \underline{\lambda_r} \quad (2.15)$$

$$T_e = 3 p \frac{M}{L_r} \text{Im}(\underline{i_s} \underline{\lambda_r}^*) \quad (2.16)$$

It is equations 2.15 and 2.16 that provide the important information for rotor flux oriented vector control. The equations are expressed in real and imaginary components below.

$$0 = -\frac{M}{L_r} R_r i_{sd} + \frac{R_r}{L_r} \lambda_{rd} + \frac{d \lambda_{rd}}{dt} - \omega_{slip} \lambda_{rq} \quad (2.17)$$

$$0 = -\frac{M}{L_r} R_r i_{sq} + \frac{R_r}{L_r} \lambda_{rq} + \frac{d \lambda_{rq}}{dt} + \omega_{slip} \lambda_{rd} \quad (2.18)$$

$$T_e = 3 p \frac{M}{L_r} (i_{sq} \lambda_{rd} - i_{sd} \lambda_{rq}) \quad (2.19)$$

The synchronous frame is aligned with the rotor flux vector and hence the q components of rotor flux in the above equations are eliminated. Using the previous definition of the rotor time constant ( $T_r$ ), and rearranging each equation in turn, the fundamental rotor flux orientation equations are formed.

$$\frac{d \lambda_{rd}}{dt} + \frac{1}{T_r} \lambda_{rd} = \frac{M}{T_r} i_{sd} \quad (2.20)$$

$$\omega_{slip} = \frac{M}{T_r \lambda_{rd}} i_{sq} \quad (2.21)$$

$$T_e = 3 p \frac{M}{L_r} i_{sq} \lambda_{rd} \quad (2.22)$$

Equation 2.20 shows that the  $i_{sd}$  component can be used to directly regulate flux. Below base speed, after initial fluxing at start-up, the rotor flux is held constant with a constant 'magnetising' value of  $i_{sd}$ . In other words we can ignore the derivative term



in the equation within this speed range. Above base speed the region of field weakening is entered and the full equation must be considered.

From equation 2.22 and again appreciating that flux is held constant within the rated speed range, it is clear that the induction motor torque can be directly regulated by  $i_{sq}$ . Equations 2.20 and 2.22 together show the flux and torque decoupling effect when orientation is made with the rotor flux vector. The operation of the induction motor can be likened to that of the separately excited DC machine using this scheme.

Equation 2.21 can be exploited to achieve the orientation with rotor flux that is required for the above analysis to hold. Using equation 2.21 in this way is termed Indirect Rotor Flux Orientation (IRFO), but firstly Direct Rotor Flux Orientation (DRFO) is considered.

### *Direct rotor flux orientation (DRFO)*

Direct methods of achieving rotor flux orientation rely on either direct measurement or estimation of the rotor flux vector [9, 13]. Direct measurement techniques are considered somewhat impractical, outside of a research environment or specialised application, requiring hall probes or search coils to be fitted in the machine air gap. The fitting of such transducers has associated cost and reliability issues that are typically avoided. Also, such a configuration may actually measure air-gap flux, with parameter knowledge (dependency) required to estimate the rotor flux vector.

Methods of estimating the rotor flux include signal injection techniques, with subsequent tracking of magnetic saturation affects. Such methods are reviewed in [20], and discussed further in section 2.4. Other methods further exploit dynamic equation analysis (model-based) [21-23]. Both method types rely on measurement of electrical terminal quantities and/or knowledge of electrical/mechanical parameters. Speed sensorless techniques are often extensions of these algorithms and therefore more depth is given to the review and analysis of such methods in section 2.4. In the model-based methods, if speed is not simultaneously estimated with rotor flux (speed being measured), many of these algorithms can be used to account for parameter inaccuracy and variation in the estimate of rotor flux [23]. Again this is considered further in section 2.4.

### *Indirect Rotor Flux Orientation (IRFO)*

Indirect rotor flux orientation is a common and robust means of establishing vector control, given that an accurate instantaneous measurement of speed is available. Most often this is from a shaft mounted optical encoder. The method exploits equation 2.21, presented previously, to force an orientated condition. The IRFO vector control method is now a feature of many electrical drive products available. Sensorless techniques that obtain only a measure of speed will often use the same technique to force orientation.

Equation 2.21 gives an expression for the motor slip frequency that applies only if orientated with rotor flux. In the IRFO method, this value of slip is imposed on the motor. Given that the motor speed is known, through measurement, an excitation frequency can be imposed on the machine, where this is the addition of the motor speed and imposed slip frequencies.

As the rotor flux vector rotates at the excitation frequency, this vector can be established (arbitrarily at start up), about which measured values of current can be transformed for use in d and q current control loops. Voltage references from the current controllers are transformed, using the same vector, back to 3-phase commands for control of the power converter (see section 2.3).

Below base speed, where the flux magnitude is held at the constant rated value, equation 2.21 is dependent only on the rotor time constant ( $T_r$ ). This reliance on a single motor parameter is the reason for the robustness of this technique. Other vector control methods rely on the knowledge of more motor parameters. Tuning techniques for  $T_r$  in an encoded drive are detailed in various examples [23-25].

### **Stator Flux Orientation**

Field orientated control taking alignment with the various flux vectors (rotor, stator and air-gap) is considered in [26]. For the purposes of this work it is also useful to consider stator flux orientation.

Following a similar method as before, taking equations 2.10 and 2.11 and expressing in terms of stator current and stator flux, the equations for stator flux orientation are obtained.

Using the following relationship to modify equations 2.10 and 2.11 [12]

$$\underline{\lambda}_s = L_s \underline{i}_s + M \underline{i}_r \quad (2.23)$$

The induction motor dynamic equations become

$$\underline{v}_s = R_s \underline{i}_s + \frac{d \underline{\lambda}_s}{dt} + j \omega_e \underline{\lambda}_s \quad (2.24)$$

$$0 = -L_s \underline{i}_s - T_r \sigma L_s \frac{d \underline{i}_s}{dt} - j T_r \sigma L_s \omega_{slip} \underline{i}_s + \underline{\lambda}_s + T_r \frac{d \underline{\lambda}_s}{dt} + j T_r \omega_{slip} \underline{\lambda}_s \quad (2.25)$$

Again the above equations, 2.24 and 2.25, are expressed in their d and q components. Here alignment is made with stator flux and therefore the q-axis component of this quantity is eliminated.

$$v_{sd} = R_s i_{sd} + \frac{d \lambda_{sd}}{dt} \quad (2.26)$$

$$v_{sq} = R_s i_{sq} + \omega_e \lambda_{sd} \quad (2.27)$$

$$0 = -L_s i_{sd} - T_r \sigma L_s \frac{d i_{sd}}{dt} + T_r \sigma L_s \omega_{slip} i_{sq} + \lambda_{sd} + T_r \frac{d \lambda_{sd}}{dt} \quad (2.28)$$

$$0 = -L_s i_{sq} - T_r \sigma L_s \frac{d i_{sq}}{dt} - T_r \sigma L_s \omega_{slip} i_{sd} + T_r \omega_{slip} \lambda_{sd} \quad (2.29)$$

Rearranging equation 2.28 gives an expression for stator flux

$$\lambda_{sd} + T_r \frac{d \lambda_{sd}}{dt} = L_s i_{sd} + T_r \sigma L_s \frac{d i_{sd}}{dt} - T_r \sigma L_s \omega_{slip} i_{sq} \quad (2.30)$$

This equation alone shows that orientation with the stator flux vector does not allow a similar decoupling of flux and torque as that of rotor flux orientation. It is clear that the stator flux is dependent upon both d and q axis currents, as will be the torque. It is

possible to derive a decoupling term using equations 2.28 and 2.29 [27, 28], but this is sensitive to errors in the stator leakage inductance term ( $\sigma L_s$ ) [28].

### *Direct Stator Flux Orientation (DSFO)*

The apparent advantage of stator flux orientation is that the flux vector is simply measured/estimated, as shown in equation 2.31 below, obtained from the stator voltage equations above.

$$\underline{\lambda}_s = \int (\underline{v}_s - R_s \underline{i}_s) dt \quad (2.31)$$

This is not quite as practical as it may seem. The required direct integration will be very sensitive to any DC offsets that will be present in a measured quantities system. For this reason the integral function is often replaced with a filter function (such as band-pass) [28]. Combined with the reliance of this equation on the stator resistance ( $R_s$ ), a parameter that will vary significantly with operating condition, use of the high-pass/band-pass filter degrades the performance of such a scheme at low speed. As speed increases, so will the stator voltage and any resistance error will lessen in significance. Equation 2.31 can be likened to the back emf equation of the DC machine.

The main advantage of this scheme is that flux regulation/orientation can be obtained without a measure of speed. Operation in the region of field weakening is more appropriate using this scheme and this is considered further shortly. Ultimate decoupling of torque and flux will still be dependent on several motor parameters however, where they are used in the compensation terms [27, 28].

### *Indirect Stator Flux Orientation (ISFO)*

ISFO holds no significant advantages over any of the previously considered orientation methods [28], as the stator flux is simply measured for DSFO and IRFO requires only knowledge of the rotor time constant ( $T_r$ ).

### **Other Orientation Schemes**

The induction motor dynamic equations can be analysed through alignment with the air-gap flux vector, but this is similar to stator flux orientation, in that flux and torque are not fully decoupled. It is considered to offer no particular practical advantage over

either of the previously considered methods and is not considered further. As previously mentioned, the various types of flux orientation are further considered in [26], as well as [28].

Other methods of controlling induction motor flux and torque include Direct Self Control (DSC) [29], Direct Torque Control (DTC) [30], and Direct Flux Control (DFC) [31]. These methods compare demanded flux/torque to values estimated from measured terminal quantities using motor primary variables (so still parameter dependent). The error is used to directly optimise the inverter switching pattern, without the use of current controllers. Very fast torque response is hence facilitated, as there are no current control dynamics. These techniques were originally developed for high power applications, such as traction, where low switching frequencies were used for high power devices. They can also effectively utilise variable switching frequency, which is not appropriate for this project.

In this work the concern is primarily with the outer (speed control) loop, engineering a drive with true sensorless speed holding accuracy, rather than with the inner orientation/torque control loop. This work therefore restricts itself to the more standard field orientation methods (vector control).

### 2.2.6 Field Weakening Operation

As with the DC machine, it is possible to operate the induction motor above base speed using field weakening [7]. The field weakening region is entered into when the maximum voltage output of the power converter feeding the motor is reached. The region of operation below base speed is termed the constant torque region, where the power converter will provide whatever voltage necessary to fully flux the machine and provide up to the rated current (rated torque). Operation above base speed is in the constant power region. Operation in this region is still to the limit of rated voltage and rated current, but rated current does not correspond to rated torque, because the motor is operating with reduced flux (the majority of the voltage limit is overcoming the motor back emf).

Unfortunately induction motor operation in field weakening is not as straightforward as that of the separately excited DC machine. It is found that motor inductance parameters will vary with flux [32], due to magnetic effects such as saturation, and these variations must be known. It is also shown that the effects are particularly

significant in closed-slot machines [27]. It is possible that auto-commissioning tests may go some way to predicting these effects however [33].

The operation of an IRFO scheme in field weakening depends on the full evaluation of the equations presented previously (equations 2.20 to 2.22). Orientation can now not be forced with only knowledge of  $T_r$  (and  $T_r$  will vary with flux anyway) and thus the performance of an IRFO scheme is compromised in field weakening. The flux can be estimated for DRFO in an open loop fashion with an equation similar to that for DSFO (equation 2.31), but the equation will contain and be highly sensitive to inductance parameters [27]. The DSFO scheme is perhaps the most appropriate for induction motor operation in field weakening. The flux is estimated with only sensitivity to  $R_s$ , which will have little significance at high speed. Although decoupling compensation will be sensitive to inductance parameters, this has been shown to be applicable only in the transient state [27].

2.2.7 Field Orientated Control Block Diagram

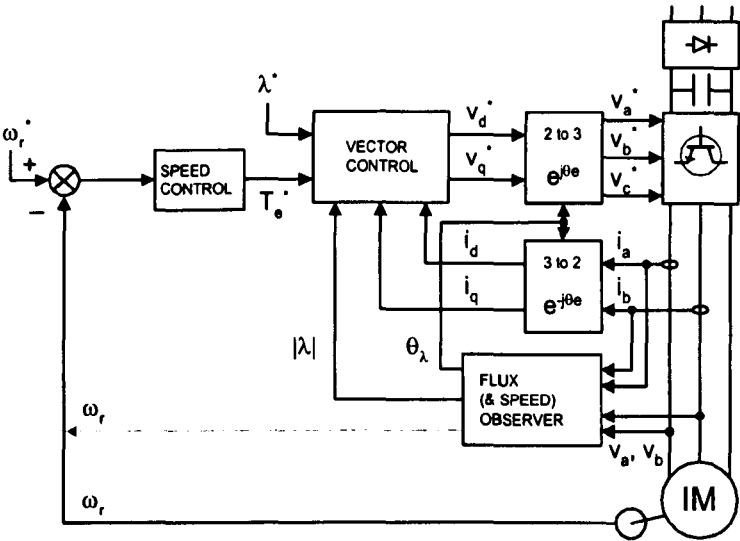


Figure 2.3. Direct field orientated control block diagram.

The control block diagram for direct field orientated control is shown in figure 2.3. Flux estimation is obtained from a model-based observer using measured currents and voltages. Currents must be measured for vector control, but voltages are often obtained from reference values. The vector control block will include d and q axis current controllers, decoupling if a DSFO scheme is used, and field weakening control.

The vector control block is expanded in figure 2.4 for a DRFO implementation, without decoupling compensation terms, showing d and q current controllers driven by flux current and torque current errors. The figure simply shows current PI controllers, with the  $I_q$  command coming from the speed controller torque command, suitably modified by the torque constant scaling.  $I_d^*$  is set at a constant magnetising value within the base speed region and hence no field controller is shown.

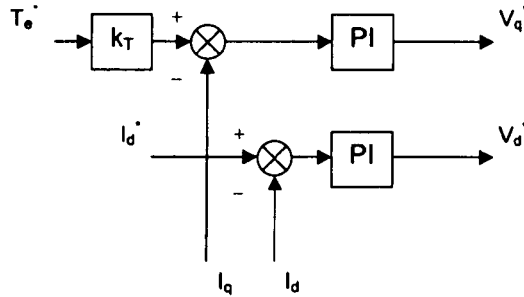


Figure 2.4. Structure of the vector control block for DRFO

### 2.3 Variable Voltage Variable Frequency Supplies

As has been shown in all the above theory, vector control relies on tight control of current with respect to an appropriate flux vector. In order to achieve this, current controllers must drive the reference demand for a quantity that can affect changes in current and this is the applied stator voltage vector.

Considering the applied stator voltage as an instantaneously controllable vector puts considerable pressure on power supply requirements. For vector control operation the induction motor must be supplied from a variable magnitude, variable phase (and therefore frequency) supply. The instantaneous control requirement limited the scope of vector control for some time and is why induction motors were limited to fixed frequency application in the past.

Prior to the advent of power electronics and the development of variable voltage variable frequency converters, variable speed operation of AC machines was limited by practicality and cost considerations. Although speed variation can be achieved, with pole changing schemes and wound rotor machines [7], these are neither high bandwidth nor wholly practical options in many circumstances; they certainly can't be compared with the separately excited DC machine. Nowadays voltage source inverters

(VSI) allow power-processing capability that can be used to directly feed induction motors.

The coupling of power converter and machine is termed a motor drive. The current direction of research in this area includes direct AC to AC conversion, using the matrix converter concept and the combination of power converter and motor into an integrated drive product [34, 35].

This project uses standard VSI technology, in the form of 2 modified commercial products (see next chapter) and the remainder of this section is devoted to describing the operation of this technology.

2.3.1 The Voltage Source Inverter (VSI)

It is not the purpose of this work to rigorously analyse the operation of VSIs, but their operation must be understood in order to practically implement a vector drive and their limitations, primarily the non-ideal nature of the AC voltage produced, must be appreciated and understood for later in this work.

Figure 2.5 shows the common configuration for a variable-voltage variable-frequency inverter. A 3-phase 50Hz mains supply is rectified at the input to create an approximately 600V DC link, with suitable energy storage and smoothing. The magnitude and phase of output voltage is controlled via the modulation of 6 power electronic switches.

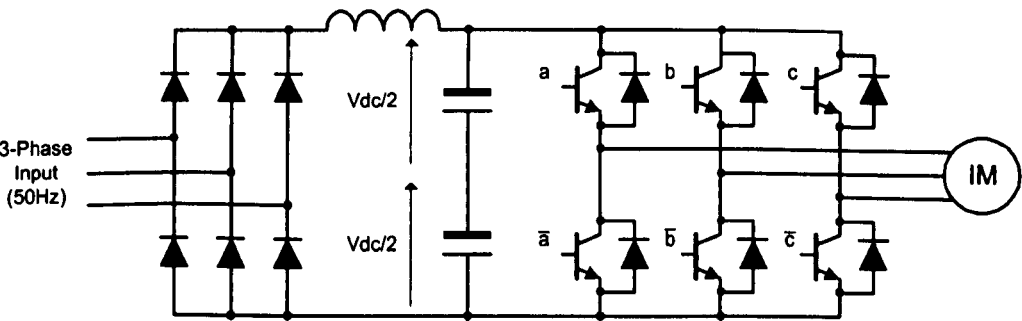


Figure 2.5. Schematic diagram of the voltage source inverter

The configuration shown is that utilised by both systems in this work. The power electronic switches in both inverters are Insulated Gate Bipolar Transistors (IGBTs).



Other converters may make use alternative devices (MOSFETs in a lower power application for example). Other configurations include single-phase inputs for low power level drives and active front ends (6 controlled power electronic switches at the input) to handle regenerative loads.

In order to cope with braking and short periods of regeneration, the systems used in this work include dynamic braking. The brake consists of a suitably sized resistor, in series with a power electronic switch (another IGBT), both connected across the inverter DC link. Regenerative energy is dissipated in the resistance with the switch acting as a chopper; turning on when the DC link voltage rises above a predetermined operating point. The control of the brake circuit is part of the manufacturers hardware control. Without any form of regenerative power handling, the capacitors would be asked to dissipate energy and this would not be appropriate, creating over-voltage conditions.

### 2.3.2 Pulse Width Modulation (PWM)

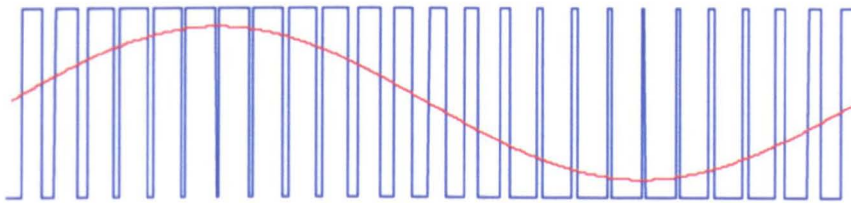


Figure 2.6. Example PWM waveform and fundamental component

Pulse Width Modulation (PWM) techniques are used to produce a voltage output from the inverter. Referring back to figure 2.5, and considering the 3 pairs of switches connected across the DC link at the output, it should be appreciated that these 3 pairs are complementary: for each pair, one transistor will be on, whilst the other is off. Each pair of switches is modulated to produce an appropriate AC voltage waveform at the output (switch midpoint), with respect to the DC link capacitor midpoint. The voltage waveforms produced will certainly not be sinusoidal, they will be squarewave in nature, but will have strong fundamental components at the desired frequency. Due to the highly inductive nature of the motor, the current waveform will be near sinusoidal, as will be the fluxes created in the machine. Figure 2.6 shows the principle of PWM, displaying the switching waveform (blue) and its associated fundamental component (red).

In order to produce the desired voltage output it is necessary to calculate and control the switching instants of each pair of switches and one of the simpler techniques used for this is termed asymmetric regular sampling. Here the switching control, operating at a fixed interrupt frequency of  $2 \times$  the desired switching frequency, compares the desired output fundamental waveforms (sinusoidal) with a switching frequency triangular waveform. If the intersections of the two waveforms can be calculated, with respect to the interrupt point, switching times are calculated and are timed on appropriate PWM circuitry, updated at the beginning of each interrupt cycle. The circuitry feeds the gate drives of the power electronic switches. The instantaneous 3-phase references must be calculated from the overall rotating voltage vector and this ensures that a tightly coupled 3-phase set is produced, as necessary to drive a balanced 3-phase load.

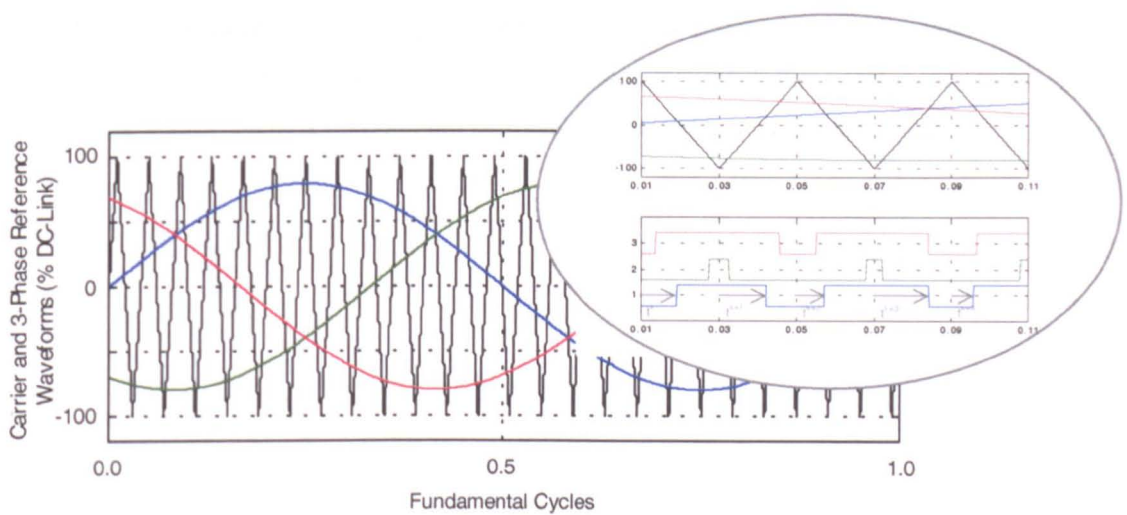


Figure 2.7. Asymmetric regular sampling PWM timing

The principle of asymmetric regular sampling is shown in figure 2.7. Note that for simplicity this figure shows steady state 3-phase voltages as an example. The triangular carrier waveform shown is at a rather low frequency, compared with the reference waveforms, and this is for illustrative clarity. In practice the carrier waveform frequency (the switching frequency) will be many times larger than the maximum inverter output frequency. The ratio of these 2 frequencies will determine output voltage quality, but also switching losses. Quality considerations are discussed further in section 2.3.3.

Advantage is gained by considering the desired voltage output as a vector, as it is considered in the vector control theory, and use of a scheme termed Space Vector Modulation (SVM) to calculate switching times directly [36]. SVM better utilises the voltage capacity of the inverter and is the technique used in this work (as well as being the method of choice in many commercial systems).

Remembering that there are 3 pairs of switches, it is clear that there are therefore  $2^3$  possible switching states, these are shown in the logic expression below (equation 2.32).

$$sw(k) = \overline{a}\overline{b}\overline{c} + \overline{a}b\overline{c} + \overline{a}bc + a\overline{b}\overline{c} + a\overline{b}c + ab\overline{c} + abc + \overline{a}\overline{b}c \quad (2.32)$$

These states can be shown on a vector diagram, as can be seen in figure 2.8. Position 1 corresponds to switch a on only, position 2 switches a and b on, position 3 switch b on only, etc (as defined in the above logic expression). If all upper switches are either on or off (remembering that the lower switches are complementary), this corresponds to a zero voltage vector: there is no potential difference between any of the three phases.

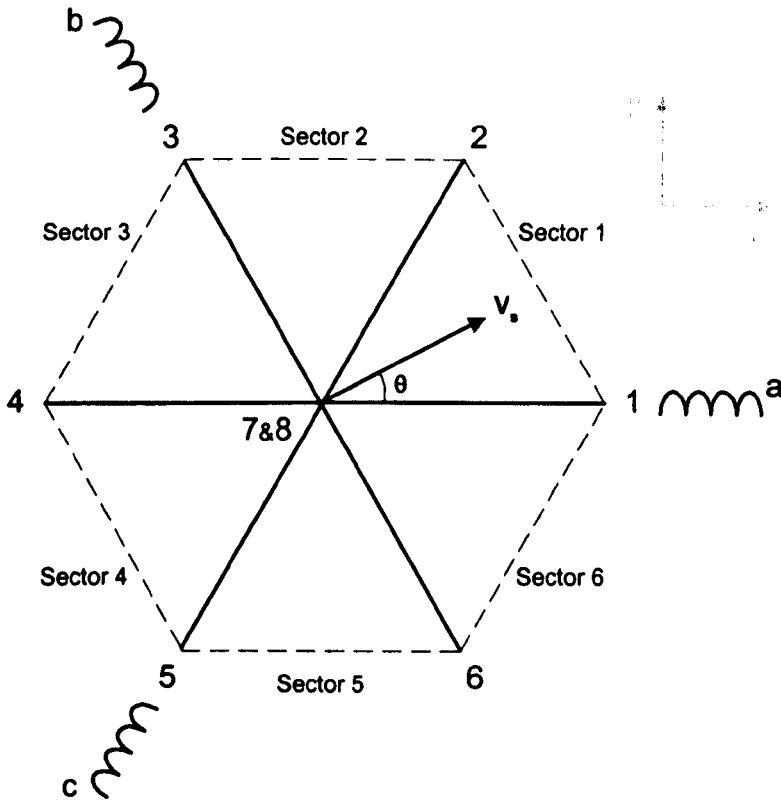


Figure 2.8. Space vector sector diagram

The desired overall voltage vector  $v_s$  is constructed by spending an appropriate fraction of time at each adjacent state, depending on which sector the desired vector is in, over an interrupt period, along with time at the zero states. As an example, the vector  $v_s$  shown in figure 2.8 (in sector 1) would be created by dividing the interrupt time between switch states 1, 2, 7 and 8. The ratio of time spent in state 1 compared with state 2 determines the resultant vector phase within the sector. The ratio of time spent in states 1 and 2 compared with that spent in 7 and 8 will determine the vector magnitude.

A modulation index is defined as the ratio of desired line voltage to DC link voltage, as shown in equation 2.33, where  $\hat{V}_{line}$  is the maximum value (or magnitude) of the desired line voltage and  $V_{DC}$  is the DC-link voltage. The DC link voltage may be assumed, or may be measured (it will normally be measured for dynamic braking).

$$m = \frac{\hat{V}_{line}}{V_{DC}} \quad (2.33)$$

Three timing values ( $t_1$ ,  $t_2$  and  $t_0$ ) are calculated as follows, where  $t_s$  is the switching sample time

$$t_1 = m t_s \sin(60^\circ - \theta) \quad (2.34)$$

$$t_2 = m t_s \sin \theta \quad (2.35)$$

$$t_0 = t_s - t_1 - t_2 \quad (2.36)$$

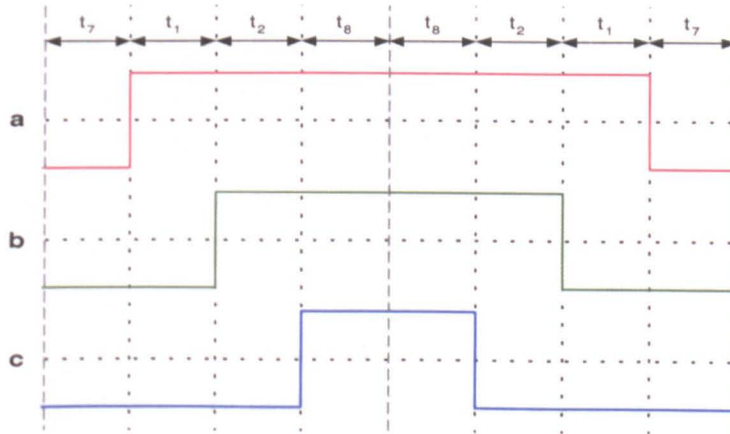


Figure 2.9. Space vector timing example

Time spent in states 7 and 8 will both be  $\frac{1}{2} t_0$  and the results from the above timing calculations are combined to produce the appropriate switching waveforms, as shown in figure 2.9. For the example vector shown in figure 2.8, time spent in state 1 is  $t_1 + t_2 + \frac{1}{2}t_0$ , time in state 2 is  $t_2 + \frac{1}{2}t_0$ . The figure shows the timings over 2 interrupt periods. Similarly to asymmetric natural sampling, the switching frequency is half that of the interrupt frequency and the drive signals toggle between positive and negative switching edges every other interrupt period.

Timings are calculated in the same way for a vector in each sector. The PWM logic code must decide which sector the desired vector is in and then pass the timing data, as combinations of  $t_1$ ,  $t_2$  and  $\frac{1}{2} t_0$ , to the correct switches according to the sector. This is shown in table 2.1.

Sector	$t_a$	$t_b$	$t_c$
1	$t_1 + t_2 + \frac{1}{2}t_0$	$t_2 + \frac{1}{2}t_0$	$\frac{1}{2}t_0$
2	$t_2 + \frac{1}{2}t_0$	$t_1 + t_2 + \frac{1}{2}t_0$	$\frac{1}{2}t_0$
3	$\frac{1}{2}t_0$	$t_1 + t_2 + \frac{1}{2}t_0$	$t_2 + \frac{1}{2}t_0$
4	$\frac{1}{2}t_0$	$t_2 + \frac{1}{2}t_0$	$t_1 + t_2 + \frac{1}{2}t_0$
5	$t_2 + \frac{1}{2}t_0$	$\frac{1}{2}t_0$	$t_1 + t_2 + \frac{1}{2}t_0$
6	$t_1 + t_2 + \frac{1}{2}t_0$	$\frac{1}{2}t_0$	$t_2 + \frac{1}{2}t_0$

**Table 2.1. Space vector timing distributions according to sector**

The advantage of this scheme is in its utilisation of the available voltage capacity of the inverter. It can be shown that the scheme is similar to asymmetric regular sampling, described previously, but with a triplen harmonic waveform added to the sinusoid references [36]. The harmonic addition allows a maximum output voltage approaching the value of the DC link voltage (unlike the 0.866 limit associated with standard regular sampling) [36]. The extra triplen harmonic addition can be shown to cancel between phases in a balanced  $\Delta$ -connected 3-phase system [36]. Figure 2.10 shows phase voltages generated within the DC link limits and the full 600V line voltages that are produced. The figure is for operation with a full modulation index value at 50Hz output frequency.



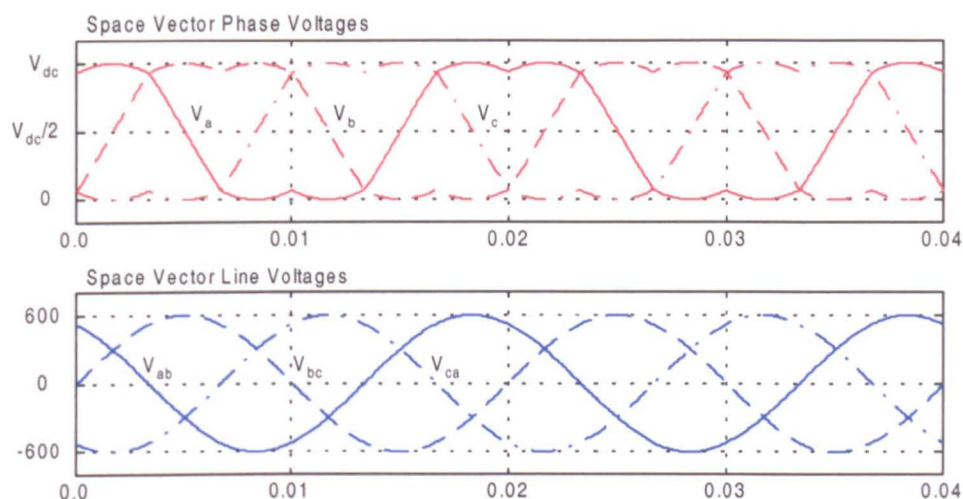


Figure 2.10. Space vector phase and line voltages with triplen harmonics evident on phase voltages

### 2.3.3 The Non-Ideal Nature of PWM Voltage Construction

The switching or squarewave nature of the voltage output of a VSI, generated by the PWM method, is certainly not ideal considering that the desired waveform is sinusoidal. Whilst some form of smoothing would be appropriate in many applications, in this instance, where the magnitude and phase of the output voltage vector must be instantaneously variable, this would introduce inappropriate delays.

The output voltage will in practice include the higher order harmonics associated with a squarewave, but without the triplen harmonics that naturally cancel in a balanced 3-phase system: leaving 1<sup>st</sup>, 5<sup>th</sup>, 7<sup>th</sup>, 11<sup>th</sup>, 13<sup>th</sup>, 17<sup>th</sup>, etc. The magnitude of these harmonics will depend on the PWM technique used and the switching frequency [6]. PWM techniques that minimise selected components can be used, but this will be at the expense of an increase in others [6].

In practice the choice of switching frequency will be determined by a number of considerations. Many of the techniques used to minimise harmonics will make use of variable switching (as DSC, DTC, etc) and this may not be suitable for control purposes. If control and PWM generation are carried out using the same control processor, sufficient interrupt time must be allowed for both aspects. This consideration may limit the maximum switching frequency, yet the control scheme would benefit from high switching frequencies that provide superior quality output

waveforms. Other considerations include acoustic noise, switching losses (which will be higher at higher frequencies) and torque ripple that low order harmonics may inflict on a motor drive. This topic will be addressed further in chapter 5 where machine rotor slot harmonics are considered.

### 2.3.4 The Requirement for Deadtime Protection

Again referring back to the schematic of a 3-phase inverter presented in figure 2.5, consider 1 pair of the complementary power switches at the output. In practice the 2 switches are not perfectly complementary. The conducting switch must be turned off slightly before switching its complementary partner on. Doing this avoids the situation of shoot-through: this is the case where an effective short circuit is placed across the DC link. If the conducting devices survive switching for any time without the incorporation of deadtime, the lifetime of the devices will drastically be reduced.

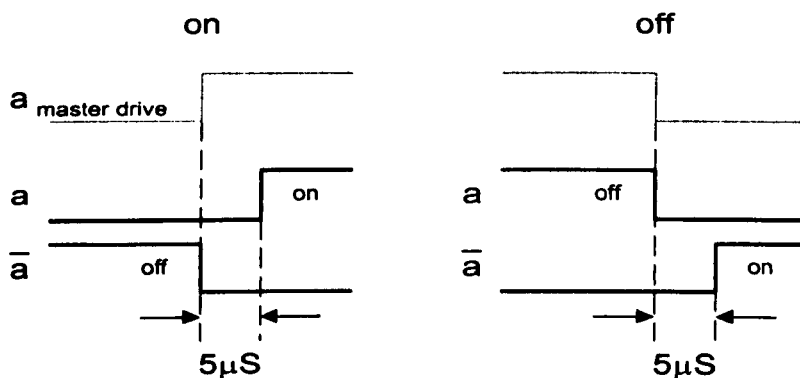


**Figure 2.11. Division of PWM signal into 2 channels to include deadtime protection delay**

Figure 2.11 shows how the master drive signal for phase-a is divided into 2 channels, one control signal for each switch, to include deadtime. Hence the 3-phase control signals arriving at the power converter, from the PWM circuitry, are divided into 6 channels for inclusion of the delay. In this work this is achieved on an inverter interface board using Schmitt triggers and RC timing circuits. The experimental system is more fully described in the next chapter. Like the squarewave nature of the PWM voltage representation, deadtime effects contribute to the non-ideal nature of the produced voltage [37].

Other important effects that contribute to distortion when operating at low voltage (low speed), which will be highly non-linear, include switching imbalance. This may be introduced by differences in deadtime circuit delays, gate drive circuit delays, power device turn-on/turn-off characteristics, etc. The effects will be influenced by current

direction and compounded by the resolution in PWM generation circuits. As shown in figure 2.12, the motor applied voltages are not directly determined by individual phase timings.  $V_{ab}$  in the illustrated example is dependent on the timing of the a-channel and b-channel signal edges relative to each other. In truth, it is dependent not on the timing edges, but rather the switching edges of the power devices. All of the above mentioned effects are at their most significant at low voltage outputs. Remember that for a zero voltage PWM output, all of the gate drive signals are the same, at 50% duty cycle (or the time passed to each gate drive is equal to half the sample time).

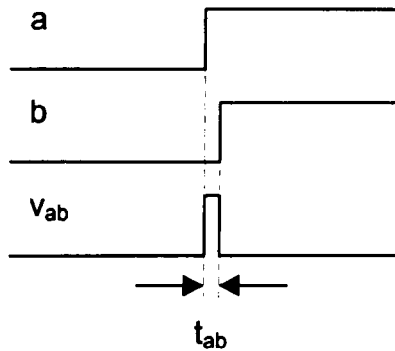


Figure 2.12. Problems with PWM resolution at low voltages

## 2.4 Sensorless Control

Fitting an optical encoder to the shaft of any rotating machine in order to obtain an instantaneous and accurate measure of speed has several drawbacks. These are with regard to cost, reliability and practicality and are outlined below.

### Cost Issues:

- The encoder cost may be a large percentage of the overall drive price
- The encoder will require fitting and incur additional cabling costs

### Reliability Issues:

- The encoder will be considerably more fragile than any other drive part
- The encoder must be robustly fitted to the machine
- Additional cabling will be susceptible to damage and electrical noise

### Practicality Issues:

- Not all applications will allow fitting of an encoder
- Generally a motor shaft end must be made available



- An encoder will increase the volume of the overall drive product

Reliability issues will of course also appear as practicality and cost considerations, perhaps resulting in increased process ‘down time’. The performance of an unreliable encoded solution, with a poorly fitted/slipping encoder for example, would not be tolerated in any application and may have damaging consequences.

For all the above reasons the requirement for an accurate measurement of speed in order to obtain high dynamic performance from an induction motor drive (IRFO) is considered undesirable. Sensorless control is now, and has been for some time, a major research area that aims to overcome this problem. The earliest reference the author has found pertaining to induction motor speed control without a shaft encoder is from 1975 [38].

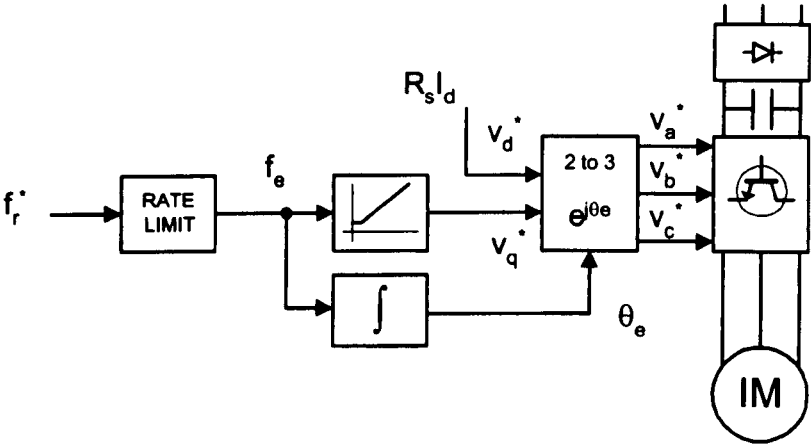


Figure 2.13. Structure of the V/F control scheme

A block diagram of the simple (low performance) open loop Volt/Hertz (V/F) control method is shown in figure 2.13. The stator excitation frequency is adjusted such that it is equal to the desired speed. The voltage applied is proportional to the frequency, with a d-axis voltage boost to account for the stator resistance drop. The scheme is based on the induction motor steady state equations, such that variations in speed must be rate limited, because flux is not controlled. Where dq terminology is used this cannot assume orientation with a particular flux vector and the torque regulation at low speed is poor.

Sensorless algorithms obtain information required for improved torque and/or speed control through measurement of motor terminal quantities and knowledge of electrical and/or mechanical characteristics. The many techniques presented range from simple

extensions to the V/F method, for improved speed holding performance [38, 39], through to sophisticated signal injection methods that facilitate low/zero speed position control (see section 2.4.2). The algorithms thus vary in their requirements for computational power, electrical sensing/measurement hardware and the knowledge of machine parameters/characteristics. Some of the methods rely on specific/modified machines such that particular machine characteristics are promoted (section 2.4.2).

In the work of Campbell [40], the requirements of a range of applications are considered. The demands of the application, with regard to the sensorless performance requirement (sensorless classification), are defined. With his kind permission, the table is repeated here as table 2.2

<b>Application</b>	<b>Torque/Speed Control Requirements</b>	<b>Sensorless Classification</b>
Fans	Torque – no closed loop control required Speed – no closed loop control required	Low
Pumps, compressors	Torque – reasonably accurate torque control, particularly in starting Speed – no closed loop control required	Medium
Conveyors	Torque and speed control required, accuracy not always essential	Medium
Winches, hoists	Torque and speed control essential and demanding – e.g. full control of torque at zero speed	High
General traction – trains, trams	Good torque response required Speed measurement to detect slippage, but not usually for feedback	Medium/High
Electric Automobiles	Good torque response required Speed measurement used for visual feedback and maybe for synchronised drive (e.g. a differential axis)	Medium/High
Dynamometers, rolling roads	Good torque and speed control essential over the full operating range	High
Strip rollers (steel, paper mills)	Demanding torque and speed control required over significant parts of the operating region	Medium/High
Machine tools	Torque and speed control essential and demanding – e.g. full controlled torque at zero speed	High

**Table 2.2. Sensorless drive applications and required performance**

For low performance applications V/F control may be appropriate. Sensorless strategies implemented in commercial products tend to sit, in terms of sophistication and performance, somewhere between V/F control and the leading algorithms based on the machine dynamic equations (model-based). For example, knowledge of motor parameters may be used to facilitate improved speed holding under load, through an estimation of slip/speed [38, 39]. These implementations can generally be regarded as low/medium performance.

### 2.4.1 Model-Based Sensorless Control

The majority of algorithms presented to establish sensorless vector control rely on the induction motor model and measurement of motor terminal quantities to provide flux and speed estimates. The flux estimate facilitates decoupled flux and torque control and many of the techniques, on which speed sensorless methods are based, make use of or exploit redundancy in flux observer methods [21-23]. These methods produce flux estimates for use in encoded drives or applications requiring only torque control. Such work is not the prime focus of this project, but typified in various examples [21-23]. As alluded to in section 2.2, and more fully examined when Model Reference Adaptive System (MRAS) techniques are considered shortly, flux estimates can be obtained by directly solving the presented dynamic motor equations. If more than one independent estimate for flux, or indeed another quantity, can be obtained, seemingly unobservable motor parameters can be determined. Observer techniques are used to alleviate the dependency of IRFO drives on the rotor time constant for example [23, 25].

Methods that obtain speed and flux estimates (or simply speed for IRFO), are again utilising the dynamic induction motor model. Given that the model parameters are known, and terminal quantities measured with sufficient accuracy, the performance of the leading schemes can be compared with encoded IRFO over the majority of the speed and load range. The leading schemes are presented, reviewed and tested in [39, 41-44] and can be regarded as offering medium/high performance. These schemes are somewhat more computationally intensive than simple extensions to the V/F scheme, but, with increased processing power becoming ever more affordable, they are now commercially viable.

There are two particularly significant considerations with regards to the practicality of sensorless implementations based on motor parameters and these are model parameter

determination and model parameter variation. The variability of drive performance due to parameter inaccuracy, particularly speed accuracy, is what currently stops sensorless drives impacting into particular sectors. Inaccuracy in the rotor time constant ( $T_r$ ) will affect the performance of the encoded IRFO scheme [24, 25], but the measured speed will ensure the speed accuracy is not compromised.

Good motor characterisation can be obtained from no load and locked rotor tests [19], for a given motor under a particular set of operating conditions, should this be practicable when (or prior to) a motor drive is installed. In many cases this will not be desirable and parameter auto-commissioning tests have been developed that estimate some of the induction motor parameters [45-47]. Combined with motor nameplate data, this allows a reasonable set-up to be obtained prior to running a sensorless algorithm. Controller self-tuning schemes have also been proposed [45-47], as speed and current controller design specifications also rely on drive parameters. It should be noted that where a complete motor drive product is obtained from a single manufacturer, motor parameter base information could perhaps be embedded into a control algorithm at the end of the manufacture process.

Parameter variation is the major factor influencing the applicability of model-based sensorless drives to particular applications [40]. Even if parameters are accurately obtained at start-up, changes in operating condition will result in variation of the nominal parameters. Resistance variation is the major effect, as stator and rotor resistances will vary with temperature (ambient and load influenced heating) and this variation will be difficult to predict [28, 40, 48]. Stator resistance ( $R_s$ ) variation has been shown to particularly affect the stability of sensorless algorithms and is most significant at low speed [48]. Rotor resistance ( $R_r$ ), and hence rotor time constant ( $T_r$ ), variation significantly affects speed estimation accuracy throughout the speed range [28, 40, 49]. Inductance variation also contributes to degradation in performance. Although less significant than resistance variation (in the below base speed region), the nominal inductance parameters will vary with magnetising condition, as the orientation is affected by the resistance parameters for example, and with magnetising effects that may alter with speed and load condition [28, 40, 48]. Sensorless and encoded schemes would both require extended inductance parameter information for operation in field weakening and it has already been established in this chapter that the encoded IRFO scheme does not generally offer good performance in this region. Various works look at sensorless operation in the field weakening region [50, 51]. It is considered beyond the scope of this work, but will be discussed for further work in the

final chapter. Parameter variation in sensorless methods is looked at again in chapter 4.

Various parameter-tuning schemes have been proposed in order to negate the performance deterioration that sensorless drives are subject to due to parameter variation [50-60]. Considering resistance parameters, Bose looks at estimating resistance change using a thermal type model, estimating resistance change as a function of measurable drive variables and time [52]. Neural network approaches exist that attempt to compensate against error in all parameters [53, 54]. The majority of schemes attempt to correct the resistance parameters individually however [55-60].  $R_s$  estimation can be achieved by applying a DC voltage component to the machine and measuring the associated current [55], but this disturbs normal drive operation and more sophisticated methods exploit motor model equations [56-58]. The use of neural networks for  $R_s$  estimation is proposed/described in [40, 59].  $R_r$  estimation is difficult to separate from speed estimation in a sensorless drive [28], but Kubota obtains an independent estimate through the sinusoidal disturbance of the magnetising current [60]. These schemes are however, dependent on the accurate knowledge of the other motor parameters. Such schemes can succeed in improving both the torque performance and speed accuracy of the sensorless model-based drive [60]. However, unless an independent accurate measure of speed is obtained, tuning is effectively compensating, with respect to speed holding accuracy, in an open loop fashion. Where the use of artificial neural networks has been proposed to compensate for all parameter variation [53, 54], this too cannot guarantee speed holding accuracy, because again, with respect to speed, compensation is effectively open loop.

The region of operation where sensorless model-based performance is particularly compromised is for a stator applied frequencies below 1Hz to 2Hz. Without persistent natural excitation, and at zero speed, rotor information is not seen on the coupled stator side [41]. Where high performance torque and/or speed control are required, at and around standstill, in applications such as machine tools, these sensorless methods will not be appropriate.

Problems caused by the non-ideal nature of inverter voltage representation, discussed earlier in this chapter, and measurement offset/error, are at their most significant at low speeds. This further compounds the problems of model-based operation in this region and is also a consideration for signal injection methods (see next section) [20]. Advanced deadtime compensation techniques have been considered in [61], and with a

view to improving signal injection techniques in [62]. Holtz considers use of a non-linear model to compensate model-based techniques at low speed [63]. Various other works consider model-based performance in this region [41-44].

### **2.4.2 Signal-Injection Based Sensorless Control**

More recently high sensorless performance at low speed has been demonstrated in the research environment, by schemes employing PWM disturbance/high frequency signal injection. Injected signals superimposed on the natural PWM, for example, produce harmonic components in the stator terminal quantities that have been modulated by saliency effects in the rotor. The first works, based on such mechanisms, obtained flux information for field orientation, through tracking of localised saturation effects within the rotor [20, 64-67]. These schemes can be extended to estimate speed, by estimating slip, as the excitation frequency is effectively being tracked [20, 67]. Positional information can be more directly extracted, for position/speed control, by tracking rotor saliency effects such as rotor eccentricity, anisotropy in rotor laminations, rotor resistance or inductance variation around the rotor circumference and rotor slotting [20, 68-74]. A thorough review of such methods can be found in the work of Teske, who has demonstrated excellent closed loop induction motor position control in the low speed range (around standstill and up to 150rpm for a 4-pole machine) [20, 74].

There are drawbacks associated with these methods however, and these include high computational (processing) requirements, a possible increase in torque pulsations, increased motor losses, decreased drive lifetime and increased acoustic noise. Much of the published work makes use of modified machines [20], where a particular rotor saliency effect has been promoted, and this may not be viable. Also the voltage capacity of the inverter is reduced, where the signal injection voltages must overcome the natural back emf of the machine, and hence these techniques are perhaps restricted to the low speed region about zero speed [20]. In many schemes drive characterisation is highly important, such that an inverter/control unit may only realistically be used with an associated machine and harmonic effects are thus predictable/known [20]. This is because, saturation effects can hinder sensorless position/speed control and must be known and/or eliminated [20].

The motivation behind signal injection techniques is in improving sensorless drive performance at low speed/low excitation frequencies and removing dependence on variable electrical parameters. The supplementary injected signals ensure that

flux/position information exists independently of the stator excitation and rotor speed frequencies. As rotor saliency effects are exploited, the schemes are not dependent on the absolute values of electrical parameters. It is considered that these methods are the methods of the future for applications requiring accurate torque and/or speed control about standstill. Lorenz recently suggested and discussed the application of these techniques to electrically assisted power steering in production motor cars [75]. It is considered however, that the region in which a signal-injection mode of operation should be applied would desirably be limited, due to the drawbacks described. Many of the leading researchers in sensorless control are continuing to improve these techniques, but much engineering is required before the methods have a significant commercial impact. For the remaining region of operation, high performance model-based methods remain the most suitable candidates for implementation. For applications where drives are not required to operate for extended periods about standstill, or where the performance in this region is not critical, the model-based methods will alone suffice.

### **2.4.3 Sensorless Model-based Control Methods for High Performance**

This section outlines the leading candidates for a sensorless vector control implementation that are based on the motor dynamic equations, such that a method can be chosen for implementation in chapter 4.

#### **The Rotor Flux - Model Reference Adaptive System (RF-MRAS)**

The RF-MRAS system operates by obtaining estimates of the rotor flux vector, using terminal quantities and motor model parameters, from two independent induction motor dynamic equations. It exploits the fact that one of the rotor flux estimates is obtained without the requirement of a speed measurement to adaptively drive the speed value required in the second equation, such that the rotor flux estimates converge. The technique is attributable to Schauder [76], and Tamai [77]. Considering the operation of the RF-MRAS also allows the general MRAS concept to be understood and demonstrates how rotor flux estimation can be directly obtained from the motor dynamic equations.

The rotor flux vector can be estimated in an open-loop manner by using the machine voltage model equation, shown as equation 2.37. Like the equation for stator flux, it allows a rotor flux estimate to be obtained without a speed measurement and could be used directly for sensorless torque control. Also as stator flux estimation, it is

particularly dependent on stator resistance ( $R_s$ ) accuracy at low speed and requires a direct integration that will be sensitive to DC components of voltage and current measurement. Unlike the stator flux equation, it also depends on accurate knowledge of the inductance parameters.

$$\underline{\lambda}_r = \frac{L_r}{M} \left( \int (\underline{v}_s - R_s \underline{i}_s) dt - \sigma L_s \underline{i}_s \right) \quad (2.37)$$

The rotor flux can also be estimated using the current model, using equation 2.38. Note that speed is required in this equation and if it were used for orientation in an encoded system it would provide performance akin to IRFO, primarily requiring knowledge of the rotor time constant ( $T_r$ )

$$\frac{d \underline{\lambda}_r}{dt} = \frac{M}{T_r} \underline{i}_s - \frac{1}{T_r} \underline{\lambda}_r + j \omega_r \underline{\lambda}_r \quad (2.38)$$

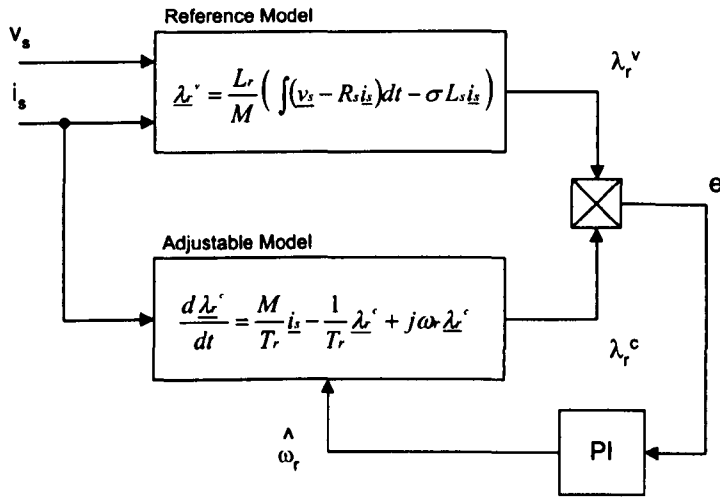


Figure 2.14. Structure of the RF-MRAS

The structure of the RF-MRAS is shown in figure 2.14. Note that the voltage equation is termed the reference model and the current equation is termed the adjustable model. This is the general structure of an MRAS system: a reference model and an adjustable model both provide estimates of an error vector. The adjustable model depends on the unknown parameter of interest. An adaptation mechanism is constructed that adjusts the unknown parameter, such that the error vectors converge. In the case of the RF-



MRAS the rotor flux vector is the error vector and the rotor speed is the unknown parameter adjusted in the adjustable model.

The adaptation mechanism in the RF-MRAS is a PI controller, the output of which is the speed estimate used in the current model equation. The error that drives the PI controller is the cross product of the two rotor flux vector estimates, such that the speed estimate is used to drive the phase error to zero. The RF-MRAS speed estimate can thus be used for speed feedback and the flux vector angle can be used to achieve direct orientation (DRFO).

The disadvantages of the scheme are those described in relation to the use of the voltage model equation for flux estimation in an encoded system. The current model is forced to follow the voltage model, and in the region that the voltage model performance degrades, speed and flux estimates will be compromised. The requirement of a direct integration in the voltage model is in practice facilitated with a high pass filter, so as to ignore DC components.

The basic MRAS method is improved in the low speed region by using an MRAS - closed loop flux observer (MRAS-CLFO) [78]. The CLFO was proposed by Jansen and Lorenz and combines the above method with a mechanical model of the plant. In the scheme the rotor flux is determined only from the current model at low speed. Combined with a measurement of stator current, the flux estimate is used to gain a measure of torque fed into the mechanical model of the machine, providing a speed estimate in the low speed region. Whilst this method relies on both accurate knowledge of electrical parameters and mechanical plant parameters, it provides superior performance, even with some parameter inaccuracy, than the simple MRAS implementation [28, 78]. In a practical scenario however, the method is unattractive due to it requiring robust mechanical plant information; in some applications the plant parameters may not be constant. Also, for sustained operation at low speed it is suggested that the scheme may still lose orientation, and thus speed holding capability, due to drift.

### **The Back-EMF MRAS and The Reactive Power MRAS**

Two alternative MRAS schemes have been suggested by Peng [79]. Making use of alternative error vectors, the systems attempt to overcome some of the problems associated with the RF-MRAS.

The back-emf MRAS is proposed, as two independent estimates of the back-emf can be obtained without the need for a direct integration [79]. Knowledge of  $R_s$  is still required however, so the use of reactive power is also suggested as an error vector, where  $R_s$  is not needed [79].

In the work of Cilia the relative performance of these two MRAS schemes was considered, along with that of the RF-MRAS [80]. The work was undertaken with a particular view to comparing the low speed performance and the design of the adaptation mechanism. In conclusion it considered that neither of the proposed schemes offered any particular advantage, or significant improvement, over the RF-MRAS. Both the alternative error vectors tend to zero as the speed nears standstill, thus not overcoming the problems at low speed. The adaptive controllers for the back emf and reactive power systems contain highly non-linear gains, making their design more difficult for robust performance. In the work then carried out, use was made of the RF-MRAS as this has the advantage of offering a fast flux estimate for DRFO.

### The Torque Current - Rotor Flux System

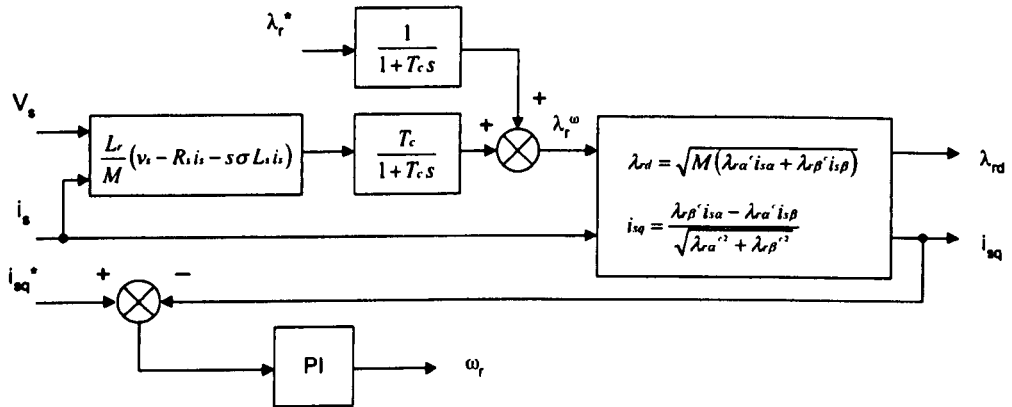


Figure 2.15 Structure of the torque-current MRAS

The system presented by Ohtani [81], and developed by Ohyama [82], makes use of torque current comparison to estimate motor speed and achieve rotor flux orientation. It has a claimed high performance, approaching that of an encoded solution [41]. It is often termed the torque current MRAS or  $i_{sq}$ -MRAS, but differs slightly from the traditional MRAS structure described above. The scheme achieves orientation with rotor flux indirectly, by imposing rotor flux orientated conditions on the machine. The system is shown in block diagram format in figure 2.15.

The rotor flux is calculated using the voltage model equation seen in the RF-MRAS scheme. The value of the rotor flux is then used, with the measured stator current, to estimate  $i_{sq}$  (the torque current) given that the system is orientated with the rotor flux. The difference between the  $i_{sq}$  estimate and the reference value from the speed controller indicates reference frame misalignment. The error is thus used to drive a PI controller whose output is an estimate of speed. The speed is used as sensorless speed feedback and, together with an estimate of slip obtained from the rotor flux oriented slip equation (using flux and  $i_{sq}$  reference values), allows an estimate of the stator excitation frequency that is integrated for orientation.

The scheme relies on suitably high dynamic current control and requires integration in evaluation of the voltage model equation. At low speed the scheme suggests use of the reference value for rotor flux and thus the flux control is open loop in this region, but this may be preferable to integration of measured variables. Band-limited integration handles the smooth changeover from reference to estimated rotor flux at a frequency dependent on the value of  $T_c$  (shown in the figure). Thus this is equivalent to combining low and high pass filters with similar cut-off frequencies.

As the scheme is inherently indirect, it does not lend itself to straightforward implementation: it, unlike the RF-MRAS and the following scheme (based on a rotor flux observer) cannot be used as open loop flux and speed observers. As this is the case, when being developed on a research system where an encoded mode of operation is available, sensorless speed and flux estimates cannot be compared with encoded versions, to verify the algorithm operation, prior to the sensorless speed loop being closed.

### **The Adaptive Observer**

The operation of an adaptive observer can often be considered as similar to that of an MRAS where the reference model is the real plant. Whilst distinction is made in some comparative papers, others will present such an adaptive observer and call it an MRAS.

The implementation considered here is based on a full-order observer of rotor flux. An adaptive mechanism is employed to adjust for speed as an unknown quantity. The method is attributable to Kubota [83] and Yang [84].

In the full-order flux observer structure, dynamic equations for stator current and rotor flux (current model) are implemented, where stator voltage and speed are measured. The stator current estimate is used in obtaining the rotor flux estimate and vice-versa. The error between measured and estimated stator current is used to drive state feedback that can be used to define flux estimation dynamics and correct some degree of parameter inaccuracy, account for initial conditions, etc.

The structure is modified to estimate both rotor flux and speed simultaneously. The simplest form, where the state feedback is ignored, is shown in figure 2.16. The cross product of the current error and the rotor flux estimate provides an estimate of the torque error in the model. The error drives a PI controller, the output of which is the speed estimate fed back into the model.

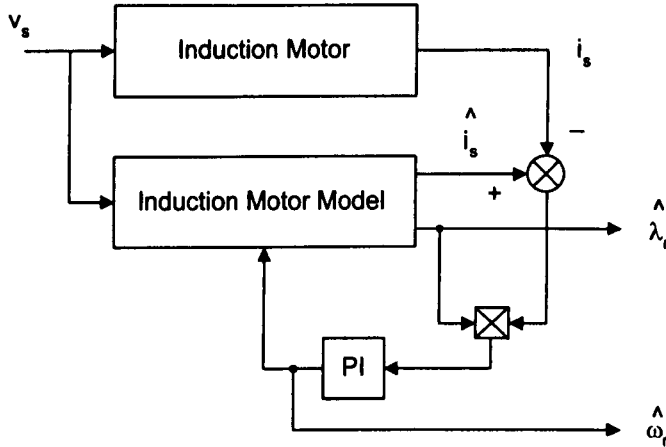


Figure 2.16 Structure of the adaptive speed and flux observer

In the work of Kubota adaptation mechanisms for  $R_s$  and  $R_r$  are presented. The adaptation of  $R_r$  calls for a sinusoidal disturbance on the flux command that thus has no net effect [60]. The paper also analyses the torque error due to  $R_s$  and  $R_r$  error.

For reasons that will be established at the beginning of chapter 4, this is the sensorless method used in this project. A more detailed description of its operation is therefore presented in that chapter.

### **Sensorless Stator Flux Orientation**

A stator flux orientated sensorless approach has been proposed by Xu [85]. In the review of sensorless techniques by Holtz [41] the method is given a high performance grading and is used in further tuning work by the author [86].

Having already seen that stator flux regulation/orientation is readily implemented using the stator back-emf equation, the proposed scheme calculates the motor speed in an open loop fashion. The stator excitation and slip frequencies are calculated and used to obtain the motor speed, assuming stator flux orientation. The scheme hence requires fast current control and a suitable decoupling law is proposed [85].

The scheme offers the previously established advantages of stator flux orientation at high speed and thus particularly in field weakening, where flux regulation is more easily achieved without steady state error [27, 85]. The speed estimate is heavily dependent upon the flux regulation/orientation however, and this is a significant drawback at low speed. The scheme requires implementation of direct integration again and is heavily dependent upon  $R_s$ . Suitable parameter knowledge must be available for robust decoupling and this will affect the speed estimate.

Whilst this scheme may offer improved operation at high speed, it is considered that the previously discussed methods would offer a more robust performance below base speed. The open loop calculation of speed in this scheme is non-ideal and it is suggested that it would be subject to heavy parameter/decoupling error and noise.

### **Other Methods**

Other methods for obtaining a speed/flux estimate that are high performance and use the induction motor state equations include those based on Extended Kalman Filtering [87-89], and Neural Networks [90]. In [88] the stator and rotor temperatures are also estimated. Whilst these algorithms may optimise the performance of the model-based type algorithms already discussed, they are still parameter dependent and additionally are computationally intensive. Some of the methods may require sophisticated set-up procedures. Although perhaps improving the torque performance, noise immunity and/or parameter tolerance, like the tuning algorithms previously mentioned, none are considered to fully achieve the desired encoder like speed holding accuracy that is the stated aim of this work. These methods may not be wholly suited to a general practical implementation and are thus not considered further for this work.

## **2.5 Conclusion**

This chapter has presented analysis of the induction motor dynamic equations, such that the principle of decoupled control through field orientation could be shown. The induction motor model has been introduced, and its associated parameters defined, for use in the analysis presented here and in subsequent chapters. Both rotor flux and stator flux orientation have been considered, along with methods of achieving these conditions, and the relative advantages of each of these techniques discussed. Operation of the induction motor in the field weakening region has also been considered.

Vector control calls for fast current control and this is generally provided, as in this work, by the use of a Voltage Source Inverter (VSI). The VSI is driven by the vector control demand for an instantaneously variable voltage vector (controlling currents). This chapter has presented analysis of VSI operation, including Space Vector Modulation (SVM), and has considered the non-ideal nature of the voltage waveform produced, as well as the need for deadtime. The following chapter further describes the inverters used in this project, such as the way they have been modified for microprocessor control and for the inclusion of switch deadtime. The non-ideal nature of the voltage waveform produced will be picked up again in chapter 5, where speed measurement using rotor slot harmonics is addressed.

The motivation for removing the speed sensor in an induction motor drive has been established. Model-based methods can provide decoupled control without a shaft sensor, but ultimately the performance is dependent upon accurate motor parameter knowledge and is compromised at low speed. Commercial products that provide a higher performance than V/F control will rely on the motor model. Signal injection methods have been shown in the research environment to overcome some of the problems associated with model-based methods. The push from industry however, is to achieve improved sensorless performance without using modified machines or power electronics. Many of the signal injection techniques use machines that have been modified, and/or the algorithm may need advanced knowledge of the machine characteristics. It is desirable not to inject signals that might produce torque ripple effects, increase losses, produce significant noise (be this acoustic or electrical) and the methods may only be applicable over a small low speed region.

It is considered that model-based methods provide wholly adequate performance for a majority of applications, facilitating field orientated control for dynamic performance. For applications requiring highly accurate closed loop speed holding performance model-based methods fail, due to the effects of parameter variation. In the main, tuning schemes presented cannot guarantee speed accuracy unless an accurate independent speed estimate is obtained. As outlined in the previous chapter, this work proposes the combination of a model-based algorithm, for dynamic performance, with a Rotor Slot Harmonic (RSH) speed estimator, for speed accuracy. As such, ideally the work will be suitable for augmentation with existing sensorless techniques that exist in commercial products. Background regarding RSH type speed estimators and resulting tuning has been reserved until chapter 5, where the mechanism of RSH production is more appropriately firstly considered.

Finally in this chapter, the sensorless review was extended with the leading candidate algorithms for model-based control outlined in more depth. In chapter 4 one of the presented algorithms is chosen, based on previous research comparing the relative performance of sensorless techniques. The experimental implementation is then explained in more depth and results presented. The chapter also goes on to further explore the effects of parameter variation in the model-based system.

Further to chapter 4 this work concentrates on improving the speed holding performance of a sensorless model-based technique. Whilst the tuning techniques discussed may improve the overall performance, this work tackles the problem of drive detuning with a particular view to improving the speed holding. Commercially viable sensorless techniques to date fail to suit applications requiring highly accurate speed holding and the goal of this project is to develop a sensorless algorithm for multi-motor applications. This is an area requiring encoded speed holding performance and is further considered, along with the presentation of sensorless speed synchronised results, in chapter 6.

---

## CHAPTER 3 Experimental Implementation

---

### 3.1 Introduction

This chapter describes the hardware and software solutions that were used to develop and test the algorithms presented in the following chapters. As the work is concerned with the performance of both stand-alone and combined sensorless drives, two development rigs were constructed. The first rig (hereafter termed rig A) was originally used in projects by both Sumner and Blasco [91, 28], whilst the second (rig B) is of similar ratings and was used in other development work within the PEMC group at Nottingham [92].

Both test rigs utilise standard squirrel-cage 4kW induction machines and 7.5kW IGBT inverters, although these are all from different manufacturers. Each induction machine is coupled to a DC machine, with associated converter of higher power rating, and these act as loading devices. The DC converters are run under their own control and are set-up to provide variable torque demands.

The IGBT inverter of each rig is modified to allow access to the gate drive circuitry of the power devices. The modification is achieved whilst still retaining manufacturer safety and protection functionality. The gate drive circuitry is interfaced to PWM timing circuits and these circuits are themselves interfaced to a processing platform running motor control code. Measurement, signal-acquisition, signal-conditioning and digital input/output circuitry also connect the processing hardware to the motor drive.

Processing capability is provided by a platform housed in a host PC and based on the Texas TMS320C4x family of Digital Signal Processors (DSP). A carrier board connected to the ISA bus has room for four TIM-40 modules<sup>1</sup>. These modules could be processor based and/or contain input/output devices (A/D converters and the like). In this case two processor modules occupy the first two slots. The board communicates with the PC, for the downloading of real-time control code, data

<sup>1</sup> TIM-40 module – *Texas Instruments Module for C4 family DSP architecture* 53



capture and overall motor control functionality, via the ISA bus and with the interface circuitry for the motor drives via a mapped section of the primary DSP memory map. The mapped area is termed the DSPLINK and results in all input/output devices being written to or read from specific predetermined addresses.

The following sections contain converter and motor specifications and go on to detail the processing platform, development of measurement and interface circuitry and development of real-time DSP motor control software and high-level PC interface motor control software.

3.2 Experimental System

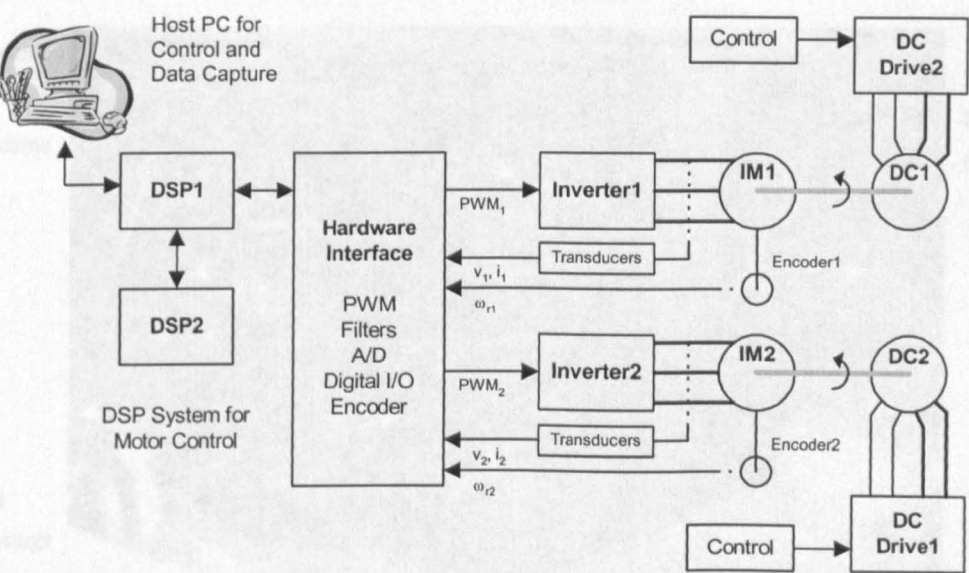


Figure 3.1. Overall structure of the dual drive rig, with loading systems and control platform

The overall structure of the drive rigs and control platform is shown in figure 3.1. Note that two independent motor test rigs are controlled using a single PC and DSP platform. Connection is made to the test rigs through a common hardware interface. Although two DSP processors are shown, only DSP 1 can communicate with the PC and hardware interface.

Evident in both the rigs is a direct measurement of speed. This measure is provided by the inclusion of incremental position encoders. The encoder fitted to rig A produces 10,000-pulses/revolution, compared to that of rig B which produces 2,500-pulses/revolution. These provided speed measurement during development of vector

and multi-motor schemes, to which sensorless results could be compared, and measurement of speed and position to verify the accuracy and performance of the developed sensorless techniques.

The developed system is capable of running what would be considered high performance AC motor control and the DSP and host PC set-up is such as to provide a highly flexible experimental research platform.

3.3 Motor Drives

3.3.1 The Asea Motor Drive (Rig A)

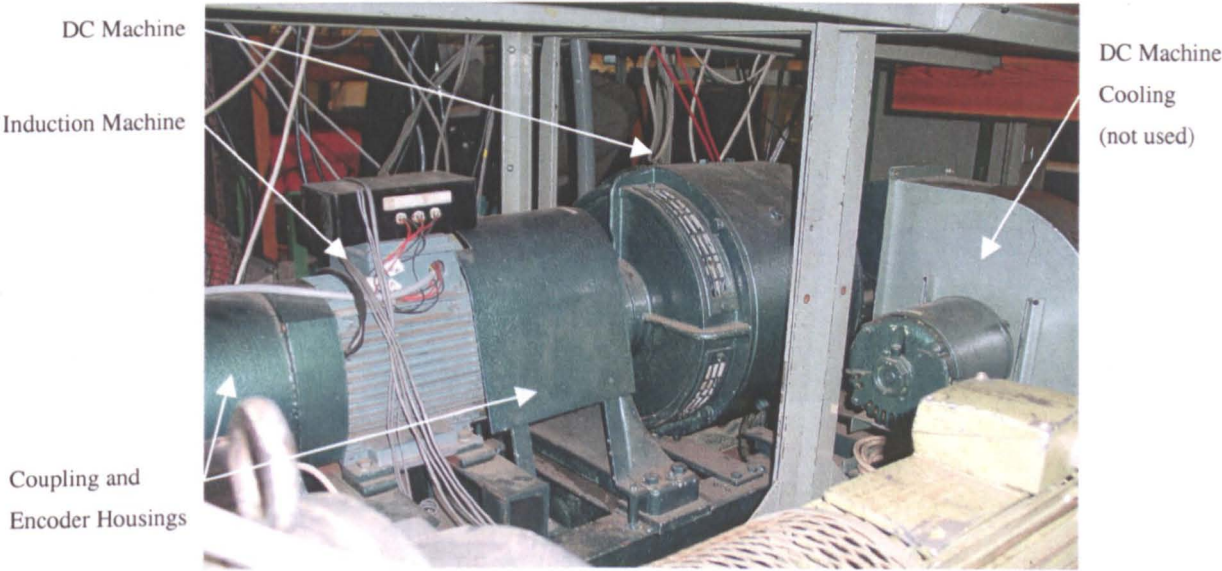


Figure 3.2. Drive rig A

Motor drive rig A consists of a delta connected, 4-pole, 4kW, closed and skewed slot, squirrel cage induction motor, manufactured by Asea. This machine is fed by a 7.5kW Eurotherm IGBT inverter and fitted with the 10,000-line encoder. The inverter has an external dynamic braking resistor fitted, suitable to dissipate energy due to deceleration. The motor test bed is shown in figure 3.2.

Information about the motor, such as the number of rotor slots and motor electrical/mechanical parameters, is known from the works of Blasco and Sumner [91, 28]. The specifications are presented in table 3.1 at the end of this section.

The load DC machine is rated at 10kW and fed by a Control Techniques 4-quadrant converter. Being an older machine, its inertia is several times larger than the induction machine alone and larger than either machine in the rig B configuration. An external control box varies the torque demand to the DC drive by varying a fed back reference voltage.

### 3.3.2 The Brown-Boveri Motor Drive (Rig B)

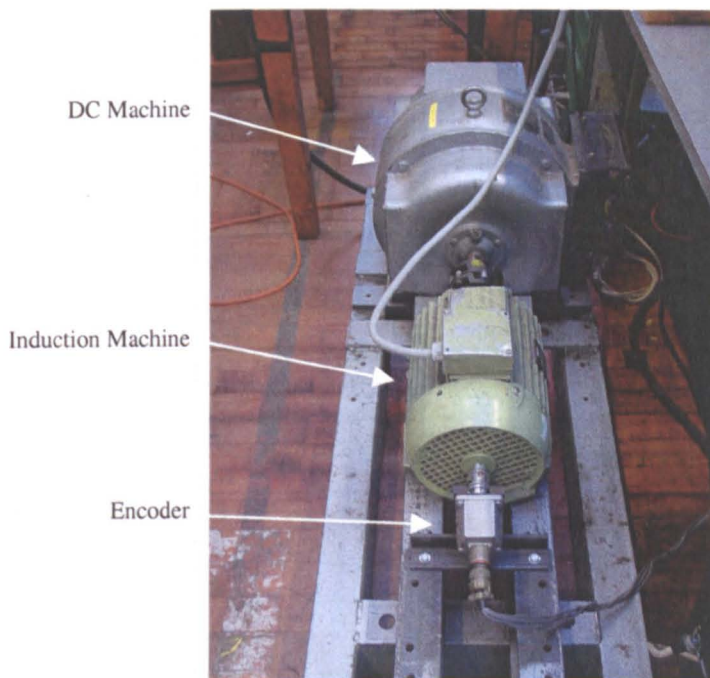


Figure 3.3. Drive rig B

Motor rig B is similar to rig A and the motor test bed is shown in figure 3.3. It consists of a delta connected, 4-pole, 4kW, closed and skewed slot, squirrel cage induction motor, manufactured by Brown-Boveri. This machine is fed by a 7.5kW FKI Industrial Drives IGBT inverter and fitted with the 2,500-line encoder. The inverter has an integral dynamic braking resistor fitted suitable to dissipate energy due to deceleration.

The number of rotor slots for this machine was determined through spectral analysis of stator current. The motor electrical parameters were determined through no load and locked rotor tests, as defined in Appendix B. These are also presented in table 3.1.

The load DC machine is rated at 10kW and fed by a Eurotherm 4-quadrant converter. It is approximately 1/3 the inertia of rig A. Similarly to rig A, the DC drive is configured to operate under its own control. Again an external control box varies the torque demand to the drive by varying a fed back reference voltage.

## 3.3.3 Induction Motor Parameters

	Rig A	Rig B
<b>Rated Power</b>	4kW	4kW
<b>Rated Speed</b>	1420rpm	1420rpm
<b>Rated Torque</b>	26.9Nm	26.9Nm
<b>Rated Voltage</b>	415V	415V
<b>Rated Current</b>	8.4A	8.42A
<b>No. Poles</b>	4	4
<b>Rated Phase <math>I_d</math></b>	2.2A	2.3A
<b>Rated Phase <math>I_q</math></b>	4A	4A
<b><math>R_s</math></b>	5.32 $\Omega$	5.9 $\Omega$
<b><math>T_r</math></b>	0.168s	0.14s
<b><math>L_s</math></b>	0.64H	0.56H
<b><math>L_r</math></b>	0.633H	0.56H
<b>M</b>	0.6H	0.53H
<b><math>\sigma</math></b>	0.11	0.12
<b>J</b>	0.3kgm <sup>2</sup>	0.12kgm <sup>2</sup>
<b>B</b>	0.02kgm <sup>2</sup> /s	0.01kgm <sup>2</sup> /s
<b>No. Rotor Slots</b>	28	28

Table 3.1 Specifications of the 2 induction machines

## 3.4 Processing Platform

Digital Signal Processing (DSP) techniques are now used in a variety of applications, replacing analogue techniques and extending their range of operation. Generally, applications are those that involve complex mathematical functions and/or real-time operation. In filtering applications for example, where analogue methods would have been employed in the past, the big advantage of a digital implementation is an increase in flexibility and accuracy. Function specifications can be varied on-line in software (adaptively) and results (output) will not be subject to error associated with analogue methods, such as component inaccuracy, tolerance, drift, etc. The digitisation of the previously analogue methods requires computational capability that allows functions to be performed whilst sampling at a suitably high rate, so as to offer similar functionality to analogue methods.



The processors developed for these mathematical and real-time problems (Digital Signal Processors or DSPs) are eminently suitable for, and now widely used in, motor control applications. The requirement of sensorless control in induction motor drives is for both high mathematical and real-time processing capability. DSPs are optimised for such applications, offering the possibility for high-speed connection to external circuitry and performing multiply and accumulate (MAC) functions often in a single processor cycle.

This work uses a system based on the Texas TMS320C4x family of processors. A Blue Wave Systems carrier board is installed in a standard desktop PC and has the capacity for up to four DSP units, this is shown in figure 3.4. Two of these slots are utilised and contain C44 floating-point processing modules. According to manufacturer data these processors are capable of executing 30 million instructions/second (MIPS) and have a peak arithmetic performance of 330 million operations/second (MOPS) [93].

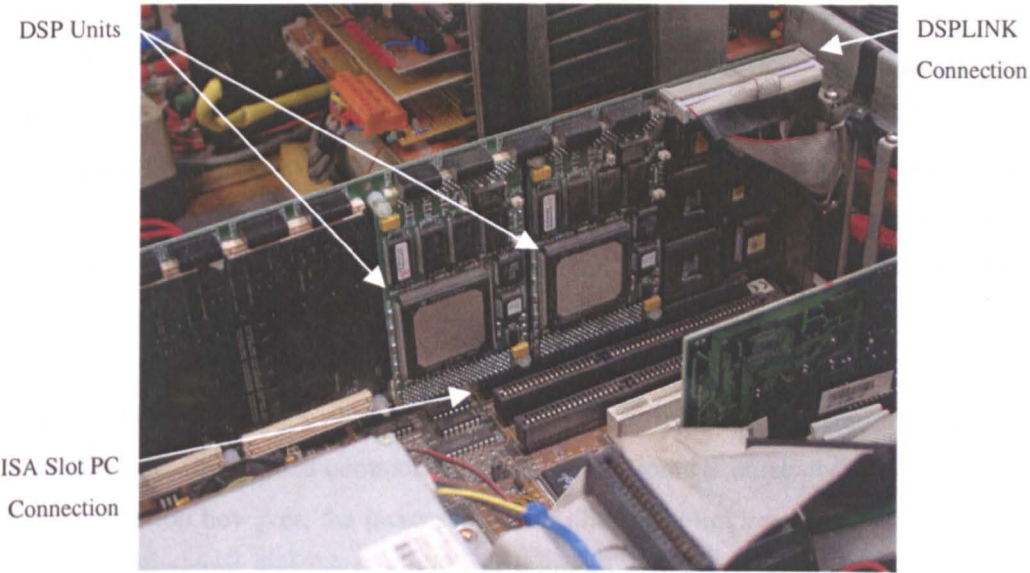


**Figure 3.4. The Texas C44 based DSP ISA-bus PC card**

A functional block diagram of the system is shown in figure 3.5. Note that processor A can communicate with the PC via both an 8kB block of Dual Port Ram (DPRAM) and a high speed parallel communications port, and with interfaced memory-mapped external devices via the DSPLINK Adaptor. The external devices include all necessary interface and measurement hardware required to control the motor drives.

The communication with the host PC enables data capture and overall motor control programs to be implemented (see section 3.6). The second processor (processor B) is in communication with processor A, as well as other processors that could be added, via serial communication ports and a 1kB block of shared memory. This processor has no direct means of communication with either the host or outside world.

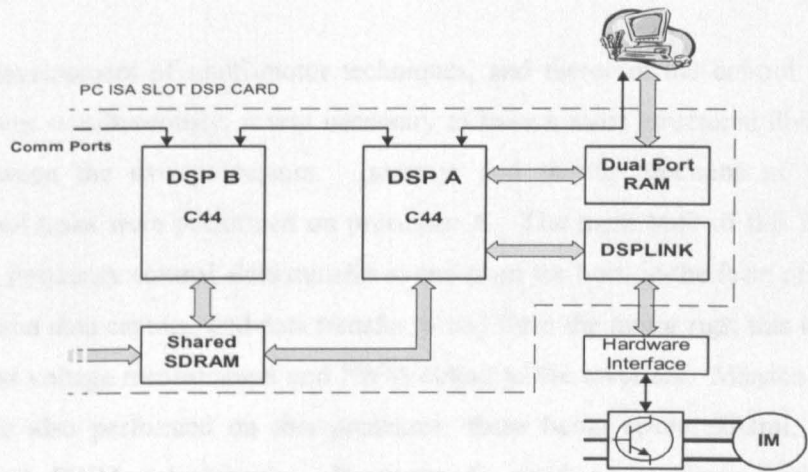


Figure 3.5. Block diagram of the DSP system

Software for the 2 processors was written in the C programming language and compiled using a Texas C compiler specific to the processor type. It is also possible to program parts or all of the code in assembly language, but this functionality was not used. The nature of the processor architecture incorporates parallelism to give high-speed performance and this would be difficult to optimise if programming at this low level.

It should be noted that the above described DSP platform is somewhat more powerful than that typically used in commercial motor drive products currently. As a research implementation however, the increased power allows the implementation and test of complex algorithms and the flexibility to program mathematical functions at a high level (i.e. without time consuming optimisation). These considerations allow the many and varied program modifications and improvements that are associated with a research/development project. The solution was also found to be capable of running all control and PWM generation code for simultaneous operation of both motor drives.

### 3.4.1 Division of Processing Tasks

For the majority of work involving the development of individual stand-alone sensorless drive algorithms, it was only necessary to use a single processor. For the more advanced slot harmonic tracking and tuning algorithms, use was sometimes made of the second processor, simply to perform background tasks.

For the development of multi-motor techniques, and therefore the control of both motor drives simultaneously, it was necessary to have a more structured division of tasks between the two processors. Interrupt and timing functions as well as input/output tasks were performed on processor A. The main bulk of this includes switching frequency control, data transfer to and from the host, in the form of control variables and data capture, and data transfer to and from the motor rigs, this includes current and voltage measurement and PWM output to the inverters. Mission critical tasks were also performed on this processor; these being speed control, current control and PWM calculations. Processor B acted as a slave device and synchronisation was performed in the communication structure at the beginning of each interrupt. Sensorless speed and flux observers, speed estimation from rotor slot harmonics and parameter tuning were executed on this processor.

Two code listings for the dual-drive speed synchronised sensorless solution are included in Appendix C, one for each processor. As well as showing coding of the algorithms that will be described in the following chapters, they illustrate how processing tasks were divided between the two processors. The listings are included as reference for others who may use the DSP system and/or work with the presented algorithms and do not include the more trivial processing functions; these are hidden in associated header files.

### 3.5 DSP to Motor Drive Interface System

This section details the connection of the motor drives to the DSP control platform and it was the development of this system that took up much of the first half of the project duration. Figure 3.6 shows the system rack containing all the interface boards and figure 3.7 shows the transducer systems. Specifications for the development of equipment interfaced to the DSPLINK are contained in the DSPLINK System Expansion Interface Guide, available from Blue Wave Systems [94]. The component parts of this hardware interface are outlined in the following sections.



3.5.1 Buffering and interface to the DSPLINK

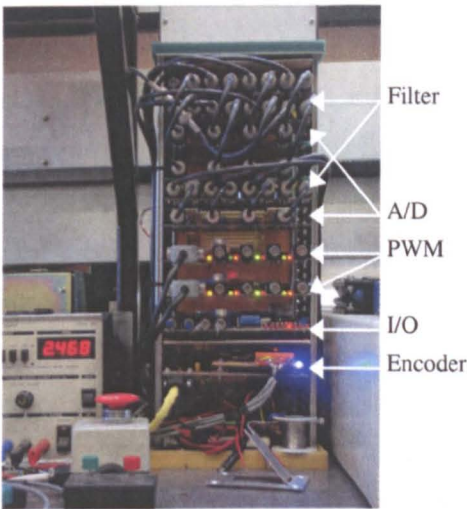


Figure 3.6. The DSP/motor drive hardware interface

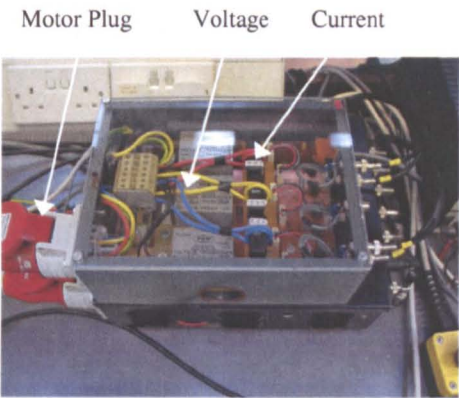


Figure 3.7. The voltage and current transducer systems

Connection is made to the DSP board via a 50-way IDC header. A short section of ribbon cable joins this header to a similar connector, on an interface and buffering PCB, at the bottom and back of the hardware interface racking. The cable contains 16-bit address bus and 16-bit data bus signals for the DSPLINK interface, as well as associated control signals. This board also facilitates connection of logic level (5V) and analogue ( $\pm 15V$ ) power supplies. All digital signals are passed through HCT family logic buffers, with  $100\Omega$  series resistors, to protect the DSP board. The DSP board power supply is therefore decoupled from the hardware interface. Address, data and control signals and power supply lines then travel up a back-plane PCB spurring off connections for auxiliary boards. Address decoding is performed on each auxiliary board and these boards are described in the following sections.

3.5.2 Digital Input/Output

Digital input/output is provided on an auxiliary board via a 4-channel 12-bit DAC, input option switches, signal LEDs and TTL input/output pins. Many of these options are not continuously required, but are of use in a development system and are employed as diagnostic input/output for functions such as interrupt and data capture timing, etc.



### 3.5.3 Pulse Width Modulation (PWM) Timing

As this project uses a more powerful DSP platform than that generally utilised in commercial motor control applications, and is therefore not specifically aimed at this market, PWM timing registers and output pins are not provided on chip. Two boards were constructed to provide this functionality for the two AC drives.

Based around the 8254 timer chip, each board receives 3-phase timing values and control information from the DSP and, by counting pulses from a 10MHz oscillator, produces timed 3-phase switching waveforms. These waveforms are at the DSP controlled switching frequency. In order to produce this output, as explained in the previous chapter, the DSP must send information to these boards at twice the desired switching frequency, changing the output switch edge polarity on each occasion. Therefore the DSP must have an interrupt frequency of twice the switching frequency. **In this work the switching frequency was set at 4kHz.**

The outputs from this board are configurable and can be either voltage level or current mirror signals. A watchdog circuit is also provided and this issues a trip signal if the 8254 timer does not receive an update every DSP interrupt cycle. These are all considerations when designing the inverter interface.

### 3.5.4 Inverter Interface – Incorporating Deadtime Protection

The output from the PWM board is fed to the inverter interface as 3-channel, corresponding to the three motor phases, current level gate drive signals. This has suitably higher noise immunity, in what is quite an electrically noisy environment, than sending voltage level signals and the signals are eminently suited to driving opto-coupler inputs (for isolation). The signals are not suitable to directly drive the power devices and must first be separated into six channels for the inclusion of deadtime delays, as noted in the previous chapter. **In this work the deadtime delay was set at 5 $\mu$ S.** The minimum and maximum pulse time were set to be 10 $\mu$ S and 115 $\mu$ S.

The interface circuit also includes necessary protection functionality. The board fitted to the FKI inverter is shown in figure 3.8. The watchdog signal from the PWM board is logically ORed with hardware over-current and over-voltage protection trip signals from the inverter. Any of these trip conditions disables the PWM signals applied to the inverter switching devices.

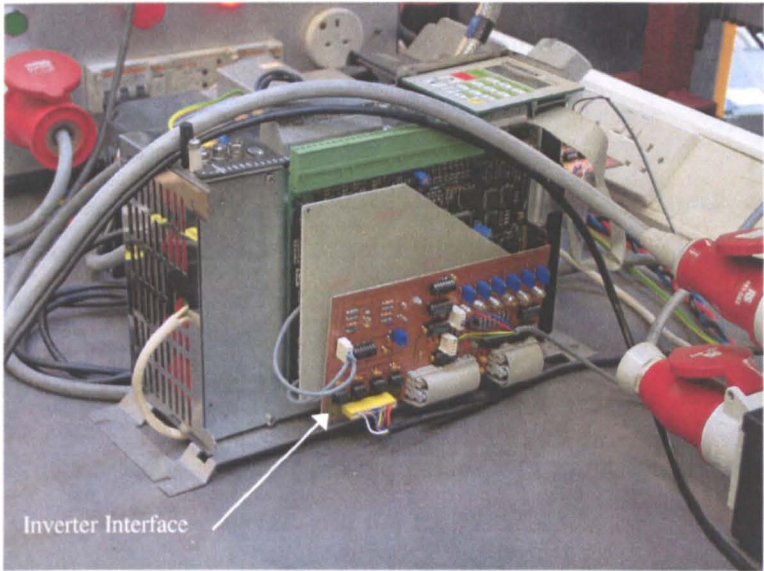


Figure 3.8. The FKI Industrial Drives inverter with interface

The PWM and watchdog inputs to the circuit are in the form of opto-couplers and this provides necessary isolation for safety. The supply for this circuit is derived from the inverter's own. Outputs from the circuit are designed to interface directly to the manufacturer gate drivers. Circuit diagrams for the two circuits used in this project are provided in the Appendix D.

**3.5.5 Voltage and Current Measurement**

Line-to-line voltages and line currents are measured, in both motor rigs, by suitable transducers placed between the inverter output and the motor input terminals.

Current measurement is required for the current controllers in vector control and for drive protection in commercial products. Generally two currents are measured but, in the case of this project, provision is made to measure all three currents on each rig. The transducers used are LEM hall-effect devices.

Voltage measurement is not always utilised in commercial products. Voltage quantities are often required for sensorless control methods, but, as the inverter can be considered a voltage source, sometimes reference values will be used. In other cases a measurement of the dc link voltage is obtained, as this may be used in braking and protection circuitry, and this may help to improve the estimate, through using the

measured value when considering the switching pattern of the PWM. If either of these methods is used, performance will be dependent upon how accurately reference values represent real ones. In this work, similarly to the currents, all three voltages are measured, again for the flexibility and accuracy required in a research implementation.

Outputs from the transducers are passed through necessary signal conditioning circuitry (amplifiers with gain and offset adjustment). Connection is made to the interface system using screened cable and BNC type connections.

### 3.5.6 Analogue Input and Filtering

The outputs of the transducer systems are passed, via the screened cable, through filters and on to the A/D converters in the hardware interface. The filters are 2<sup>nd</sup> order low-pass butterworth type, with a cut-off frequency of around 720Hz, and are used to prevent anti-alias effects associated with a digitally sampled system [95].

The A/D converters are 16-bit and there is a total of three boards, each of four channels. This is sufficient capacity to measure the six channels of voltage and current data coming from each rig. The conversion and acquisition time of these devices is in the order of 10 $\mu$ S. Acquisition is aligned with the PWM, such that measurement is obtained not immediately following a switching edge. Aligned acquisition alleviates the possibility of error and noise pick up associated with the switching edges.

### 3.5.7 Encoder Interface

Both of the encoders used in this work are of a similar type. Neither are of the quadrature type now used commonly, for which decoder integrated circuits can be readily obtained. Each has three outputs channels; one channel provides a pulse train if rotating in one direction; the 2<sup>nd</sup> channel provides a similar pulse train if rotating in the opposite direction; the 3<sup>rd</sup> channel provides a reset pulse. The reset pulse is a single pulse per revolution marking a particular fixed position.

After the signals are received, by a differential input stage, the pulse trains feed binary up/down counters (one for each encoder). One channel feeds the up count input, whilst the other feeds the down count input. The reset pulse feeds the reset (or zero) input and the counters are therefore set to zero once per revolution. The

counters are multiples of 4-bits, such that a maximum count is equal to or greater than the number of encoder lines.

Software routines that read in what is effectively an incremental position count, obtain a speed measure by comparing the new count value with the previous one. This measurement runs with the speed control loop every 0.01secs. The code must account for the reset nature of the count circuitry, where an overflow may occur, causing a reset, between samples.

As on all of the previously described boards, data to be read from or written to the data bus goes through suitable tri-state buffer circuitry. This provides isolation for unused devices.

3.6 High Level Motor Control and Data Capture

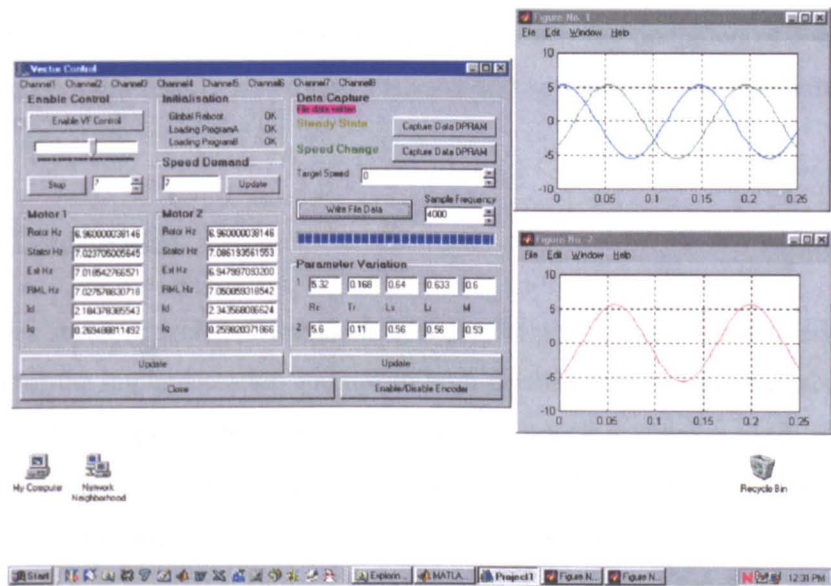


Figure 3.9. An example screen shot of the PC based motor control platform

High-level motor control and data capture is facilitated through PC based software developed using Borland C++ Builder. The DSP board is supplied with library functions that allow communication, between the DSP and PC, to be programmed in such an environment. The communication is achieved by utilising the DSP comm ports and the Dual Port RAM (DPRAM). These resources are memory mapped into PC address space. Memory arbitration is controlled by hardware, but must be appreciated, particularly when considering DSP code timing.

A typical host program screen shot is shown in figure 3.9. Note that the role of the host program includes downloading and booting DSP code, enabling inverter control (current and speed controllers), communicating options and parameters (changes of speed, etc) and capturing online variables and block data.

Similar functionality could be achieved using a DOS based PC environment, but this windows based alternative was found to be eminently suitable for this type of application. Captured data was written to file and then read and interpreted by suitable analysis programs (such as MATLAB).

PC based control and data analysis, using methods such as that presented, and the implementation of induction motor control, using the PC based DSP card and developed communications interface, would not be appropriate in many commercial applications. In this case however, the developed system is a most flexible and powerful research and development tool. PC communication options are now becoming available on commercial products, such that the operation of a particular drive can be more readily tested and analysed and so that set-up and options can be varied.

### 3.7 Conclusions

The drives system developed for use in this project provides a powerful and flexible solution for the implementation and test of high-performance induction motor control strategies. It is appropriate to the environment in which it is being used, this being research and development. The system can be operated over the full rated speed range of the induction machines and the speed demand can be instantaneously varied. The independent loading system of each rig allows developed schemes to be tested over the full rated load range and the load condition is also instantaneously variable. Fitting of speed encoders and current and voltage transducers allows encoded and sensorless algorithm to be readily developed, tested and compared.

The powerful floating-point DSP-based platform, used for the real-time motor control, allows advanced control methods to be implemented quickly, without the need for much time-consuming code optimisation. In a commercial product the emphasis would be on reducing both cost and size, but in real-terms the price of processing hardware is ever decreasing. Similar processors to those used here are

now within the realms of possible use in commercial products. The accuracy of the floating point system and the use of high precision measurement is necessary for much of the sensorless speed estimation techniques described in the following chapters.

Designing and building the system has been a most worthwhile part of this project and a deeper understanding of power electronic motor drives has certainly been gained during its development.

---

## **CHAPTER 4    Implementation of the Model-Based Sensorless Control Scheme**

---

### **4.1 Introduction**

The leading candidates for the implementation of a model-based sensorless vector drive were highlighted in chapter 2. This chapter is devoted to presentation of the chosen algorithm and a full test of the practical system.

In the following section, section 4.2, the implemented sensorless technique, as first proposed by Kubota et al [83], will be fully detailed. The reasons for choosing this algorithm will be explained. Designs for speed and current controllers are presented and the design of the adaptive speed estimator is considered. Information regarding the discretisation of the controllers and observer is also given, so as to provide a full specification for the practical system.

Section 4.3 examines the experimental performance of the sensorless scheme on both motor drive rigs. Results are presented confirming the operation of the Kubota method as a flux observer in an encoded IRFO solution. The section considers and defines test criteria, so that speed sensorless operation can be analysed. The tests are based on those set out by Campbell [40] and are firstly carried out on the encoded IRFO solution to provide a benchmark. Results are presented for the sensorless system with nominal parameters, after first operating the drive under full load, at low speed, to achieve a realistic operating temperature. Results from the encoded and sensorless schemes are compared and contrasted.

In section 4.4 the mechanisms causing parameter variation are considered. Analysis and discussion is centred around how this parameter variation affects the performance of a model-based system. This is an area much studied in relation to both encoded and sensorless induction motor drives [23-25, 28, 39, 40, 48-60, 96].

The chapter concludes with section 4.5, where the performance of the developed sensorless system is further considered. Suggestions are made as to the best means of tuning the system for high accuracy speed-holding, for continuation of the work in the following chapters.

## **4.2 Sensorless Implementation**

Previous sensorless drive implementations in PhD projects undertaken at Nottingham [28, 40, 80] have used the RF-MRAS [76, 77], or its extended version - the MRAS-CLFO [78]. More recent comparative assessment, undertaken by Ohyama et al [43, 44], reviewed the practical performance of the MRAS-CLFO [78], the Ohtani Isq-MRAS [81] and Kubota ASO [83], all briefly described previously in chapter 2. The three of these methods are generally accepted to give high sensorless performance, particularly in terms of dynamic performance and low speed operation. The conclusions of the work indicated that, whilst the performance of all three schemes was comparable, the Isq-MRAS and the ASO were 'both proving superior to the MRAS-CLFO in respect of robustness to  $R_s$  and performance on no-load' [44].

As a result of Ohyama's work, it was decided that this project would use the Kubota ASO as the chosen model-based sensorless implementation. Both the Isq-MRAS and the ASO benefit from not requiring knowledge of the drive mechanical parameters (inertia, etc). The ASO does not require a direct integration in its estimate of  $\lambda_r$  and the suggested configuration for the Isq-MRAS (chapter 2) is such that a direct integration is avoided in the problematic low speed region. The ASO algorithm however, allows for an online estimation of  $R_s$ , as first reported in [97]. Unlike the Isq-MRAS, it can also firstly be set-up as an open loop speed and flux observer in an encoded system and thus its operation can be tested, in this instance, prior to the sensorless loop being closed. It must of course be remembered that the further work in this thesis is aimed at tuning the model-based system for accurate speed holding capability and this would be appropriate to most other model-based methods.

The remainder of this chapter is devoted to a full presentation and review of the Kubota method of sensorless control, as implemented on the two motor drives used in this work.



### 4.2.1 The Adaptive Flux Observer (AFO)

Kubota et al presented the adaptive rotor flux observer, where speed is a measured variable, in 1990 [97]. Based on a full-order observer [98], observing stator current and rotor flux for use in an encoded DRFO vector implementation, schemes are presented to adaptively update stator and rotor resistances [97]. The observer algorithm is presented in this section. The final part of the paper goes on to present an adaptive scheme, using the same basic observer structure, for simultaneous speed and flux estimation and a simulation result is provided. The speed sensorless scheme is more fully presented, reviewed and extended in further papers [60, 83, 99, 100], and will be detailed in section 4.2.2.

The induction motor equivalent circuit in the stationary frame is shown in figure 4.1. Note that this is a variation of the circuit presented in chapter 2. The ideal transformer is now removed, with the rotor quantities now referred to the stator side [12].

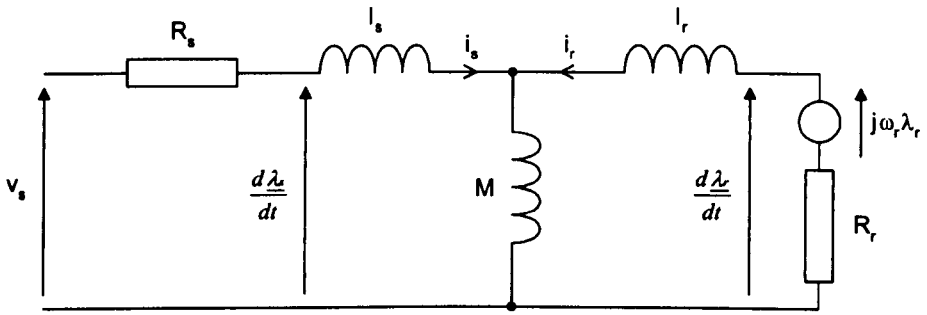


Figure 4.1. The induction motor dynamic model in the fixed stator frame

From this circuit the dynamic equation for stator current, in terms of appropriate variables, can be derived

$$\frac{d i_s}{dt} = -\frac{R_s}{\sigma L_s} i_s - \frac{(1-\sigma)}{\sigma T_r} i_s + \frac{M}{\sigma L_s L_r T_r} \lambda_r + \frac{1}{\sigma L_s} v_s - j \frac{M}{\sigma L_s L_r} \omega_r \lambda_r \quad (4.1)$$

The dynamic equation for rotor flux can also be derived

$$\frac{d \lambda_r}{dt} = \frac{M}{T_r} i_s - \frac{1}{T_r} \lambda_r + j \omega_r \lambda_r \quad (4.2)$$

The full derivation of these equations is shown in Appendix E. Note that the equation for rotor flux, equation 4.2, is the ‘Current-Model’ equation. As shown in the review of sensorless methods (chapter 2), this can be used as an open-loop estimator of rotor flux in an encoded drive, to provide performance akin to IRFO, and is also used in the RF-MRAS structure [76, 77].

The equations can be expressed in matrix form, in  $\alpha\beta$  co-ordinates, as follows

$$\begin{aligned} \frac{d}{dt} \begin{pmatrix} \underline{i}_s \\ \underline{\lambda}_r \end{pmatrix} &= \begin{pmatrix} A_{11} & A_{12} \\ A_{21} & A_{22} \end{pmatrix} \begin{pmatrix} \underline{i}_s \\ \underline{\lambda}_r \end{pmatrix} + \begin{pmatrix} B_1 \\ 0 \end{pmatrix} v_s \\ &= A \underline{x} + B \underline{v}_s \end{aligned} \quad (4.3)$$

$$\underline{i}_s = C \underline{x} \quad (4.4)$$

where

$$\underline{i}_s = [i_{\alpha s} \quad i_{\beta s}]^T \quad \underline{\lambda}_r = [\lambda_{\alpha r} \quad \lambda_{\beta r}]^T \quad \underline{v}_s = [v_{\alpha s} \quad v_{\beta s}]^T$$

$$A_{11} = -(R_s/(\sigma L_s) + (1-\sigma)/(\sigma T_r)) I = a_{r11} I$$

$$A_{12} = M/(\sigma L_s L_r)((1/T_r)I - \omega_r J) = a_{r12} I + a_{i12} J$$

$$A_{21} = (M/T_r) I = a_{r21} I$$

$$A_{22} = -(1/T_r) I + \omega_r J = a_{r22} I + a_{i22} J$$

$$B_1 = 1/(\sigma L_s) I = b_1 I$$

$$C = [I \quad 0] \quad I = \begin{bmatrix} 1 & 0 \\ 0 & 1 \end{bmatrix} \quad J = \begin{bmatrix} 0 & -1 \\ 1 & 0 \end{bmatrix}$$

Given that equations 4.3 and 4.4 describe the real induction motor, with the measurable output  $\underline{i}_s$ , a full order observer can be constructed, as shown in figure 4.2, to estimate  $\underline{\lambda}_r$ . The block G, shown in the figure, is the observer feedback matrix.

The observer equations are as follows (where ^ indicates estimated values)

$$\frac{d \hat{\underline{x}}}{dt} = A \hat{\underline{x}} + B \underline{v}_s + G (\hat{\underline{i}}_s - \underline{i}_s) \quad (4.5)$$

$$\hat{\underline{i}}_s = C \hat{\underline{x}} \quad (4.6)$$

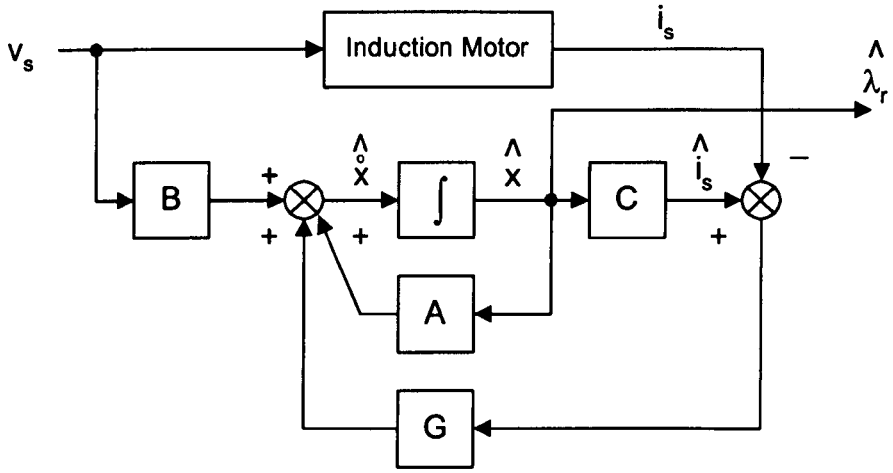


Figure 4.2. Block diagram of the full-order state observer

Substituting equations 4.4 and 4.6 into 4.5 gives

$$\frac{d \hat{\underline{x}}}{dt} = A \hat{\underline{x}} + B \underline{v}_s + G C (\hat{\underline{x}} - \underline{x}) \quad (4.7)$$

Subtracting 4.3 from 4.7 gives an equation defining the error dynamics and allows  $G$  to be designed

$$\frac{d \underline{e}}{dt} = (A + G C) \underline{e} \quad (4.8)$$

where

$$\underline{e} = (\hat{\underline{x}} - \underline{x}).$$

In [97] a design solution for matrix  $G$  is presented such that the poles/dynamics of the observer are made proportional to those of the induction motor. This is for a proportional constant  $k > 0$  and is as shown below.

$$G = \begin{bmatrix} g^1 & g^2 & g^3 & g^4 \\ -g^2 & g^1 & -g^4 & g^3 \end{bmatrix}^T \quad (4.9)$$

where

$$\begin{aligned} g_1 &= (k-1)(-a_{r11} - a_{r22}) \\ g_2 &= (k-1)(-a_{i22}) \\ g_3 &= (k^2-1)(c a_{r11} - a_{r21}) + c g_1 \\ g_4 &= c g_2 \\ c &= -(\sigma L_s L_r)/M \end{aligned}$$

Practical implementation of the observer is achieved by discretisation of the observer dynamic equations using a suitable technique, such as the Euler method [98].

The paper [97], goes on to look at the influence of variation in both stator and rotor resistance to the performance of the observer when used for encoded DRFO. The ratio of produced to desired torque is analysed, when errors in these parameters persist, and this analysis is performed with various values of  $k$ . At low speed the system is sensitive to errors in  $R_s$ , as this is included in the stator current dynamic model. Variation in  $R_r$  is also more significant at lower speeds, but the structure, because the estimation of rotor flux is obtained with an estimation of stator current, performs better than IRFO with a similar detuning of  $R_r$ , even in open loop mode ( $k=1.0$ ). This indicates that the scheme should perhaps perform better in the high speed region than IRFO, but it would of course still be sensitive to inductance parameter variation in field-weakening.

It is shown that particular values of  $k$  can restrain the influence of inaccurate parameters, whilst also varying the dynamic performance of the rotor flux estimate. Design of  $k$  to correct parameter influence, particularly that of  $R_s$  and  $R_r$ , would be difficult, due to parameter interdependency and the amount by which the parameters may vary. The paper [97] therefore goes on to present schemes for adaptive adjustment of  $R_s$  and  $R_r$ . The  $R_s$  adjustment law is shown in the paper to be stable, using Lyapunov's theorem [98], for  $k=1.0$  and is presented below.

$$\frac{d \hat{R}_s}{dt} = -\lambda_1 (e_{i\alpha s} \hat{i}_{\alpha s} + e_{i\beta s} \hat{i}_{\beta s}) \quad (4.10)$$

where  $\lambda_1$  is an arbitrary positive gain and  $e_{i\alpha s}$  and  $e_{i\beta s}$  are the  $\alpha\beta$  current errors. Simulation results are presented to verify the method [97].

The adaptation law for  $R_r$  shown in the paper [97] is not considered here, because it is only suitable where an independent measure of speed is available (in an encoded drive). The following section will present the speed and flux estimator based on the above observer and here the  $R_s$  adaptation method is still applicable.

Section 4.3.1 shows some experimental results with the AFO used to provide an estimate of rotor flux, through the estimation of stator current, in an encoded IRFO drive solution running on the project rigs. A DRFO implementation, using this flux estimate, was run on the rig and gave similar performance to the IRFO implementation. The sensitivity to parameter inaccuracy and the high speed performance of the technique was not tested and compared with the IRFO method. This is tested by Kubota [97], and this work is concerned with obtaining a speed sensorless implementation, not optimising an encoded solution.

#### 4.2.2 The Adaptive Speed Observer (ASO)

The authors of the AFO paper go on to more fully present the flux observer used to measure flux and speed together in [83]. The structure was presented at a similar time by Yang and Chin [84]. In this project the algorithm will be termed the adaptive speed observer (ASO). Extending the simulation result from [97], practical results are presented in [83]. The paper assumes that the matrix  $A$  is an estimation. It is anyway, because it contains estimated model parameters, but now also includes an unknown value for speed. An adaptation mechanism for speed estimation is proposed and is implemented in practice uses a PI controller (like MRAS schemes [76, 77]) to provide a speed estimate in the model. This is shown in the following equation

$$\hat{\omega}_r = K_p (e_{ias} \hat{\lambda}_{\beta r} - e_{i\beta s} \hat{\lambda}_{\alpha r}) + K_i \int (e_{ias} \hat{\lambda}_{\beta r} - e_{i\beta s} \hat{\lambda}_{\alpha r}) \quad (4.11)$$

where

$$e_{ias} = i_{as} - \hat{i}_{as} \text{ and } e_{i\beta s} = i_{\beta s} - \hat{i}_{\beta s}.$$

From inspection it is evident that the error function, used to drive the speed estimate, is proportional to the instantaneous torque error in the model (see equation 2.12 in chapter 2). The rotor flux orientation vector, obtained from the observer, is effectively applied to the real machine to decouple current components. Estimated and applied rotor flux are ideally the same, so the stator current error can be used to

obtain the torque related error. Again, the stability of the scheme is analysed in the paper, using Lyapunov's theorem [98] for  $k=1.0$ .

The modified structure, outputting speed and flux estimates, is shown in figure 4.3. The implementation presented in the Kubota paper [83] sets the  $G$  matrix proportional constant  $k$  to 1.0 ( $G = 0.0$ ), such that the  $G$  matrix feedback can be removed from the figure.

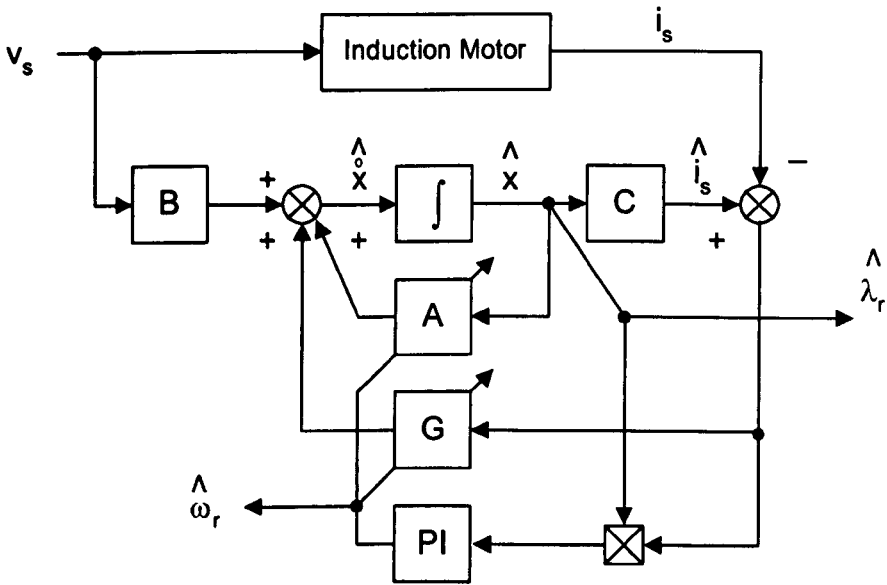


**Figure 4.3. Block diagram of the speed and flux observer**

In [83] PI gains for the adaptive speed estimator are selected experimentally. The estimator must have sufficient bandwidth to drive the speed control loop and this is suggested, in papers on MRAS techniques, to be at least 2 times that of the speed loop [76]. This may limit the maximum speed loop bandwidth of the sensorless drive, due to noise constraints, and this will be discussed in the following section, where speed, current and estimator controller designs are considered.

Practical results presented in the paper are for no-load operation at zero speed, large and unloaded forward-reverse speed transients and a single load impact test with the drive running at 100rpm. More challenging criteria for the test of sensorless drives, including results obtained from an ASO, are presented in [43, 44]. This is discussed further in the results section of this chapter, where the performance of the practical implementation developed for this project is fully tested.

The performance of the speed sensorless scheme will of course be sensitive to errors in machine model parameters. Values of  $k$  may improve performance, in terms of speed accuracy and flux estimation dynamics, but may also degrade it. As mentioned, with regard to the observer, it would be difficult to choose the correct value of  $k$  for parameter tuning, due to parameter interdependency. Simulation results are included in [83] to show how speed accuracy will vary with  $R_r$  (the primary source of speed error) and how speed accuracy and torque vary with errors in  $R_s$ .  $R_s$  remains significant at low speed and differing values of  $k$  are shown to both improve and reduce the speed accuracy when the error due to this quantity is fixed.

The  $R_s$  adaptation technique presented previously is still relevant in the speed sensorless scheme.  $R_r$  cannot be readily adapted, because its effect cannot easily be distinguished from speed [28]. In a third paper by the authors [60], a method is presented for  $R_r$  adaptation that involves superimposing an ac signal on the field current command. This is not considered further here, because it is not believed that the adaptation of resistances will be sufficiently accurate, together with the fact that errors will exist in other parameters, to provide the encoder like speed-holding accuracy that is the requirement of this project.  $R_s$  adaptation is still highly relevant, as this has a large influence on sensorless stability, as shown in [48]. It is suggested that the method presented in [59], based on the use of neural networks, would offer perhaps the best adaptation of the  $R_s$  parameter.

More recent work by the authors includes a paper on improving the low speed performance of the ASO, by offset compensation of the stator voltages [99]. Also a paper was presented very recently, at the 2001 Industry Applications Society Annual Meeting, on improving the stability of the algorithm in the low speed regenerative region, by correct choice of feedback proportional constant  $k$  [100]. This area of operation was also considered and shown to give some instability problems in [101].

This project considers the use of the basic algorithm ( $k=1.0$ ) where tuning is developed to provide accurate speed holding. A scheme to provide much improved  $R_s$  estimation for model-based methods, as previously mentioned, is presented in [59].

### **4.2.3 Speed and Current Controller Design**

Speed and current controllers were designed for this work using s-domain techniques and the values of inertia, friction (speed loop), stator resistance and stator leakage

inductance (current loop) presented in chapter 3. The designs are relevant for sensorless and encoded implementations and are presented below. The general principles and design methods for cascaded control of motor drives are further presented in [12].

### Speed Controller

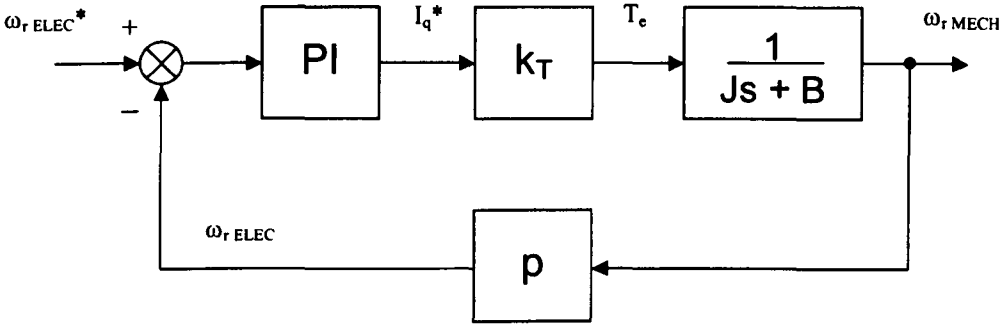


Figure 4.4 Structure of the speed control loop

The structure of the speed controller is shown in figure 4.4. It assumes correct field orientation, such that  $I_q$  is directly torque producing. The s-domain transfer function of the PI control block is defined as

$$\begin{aligned} \frac{\text{output}}{\text{input}} &= \frac{k_c(s + a_c)}{s} \\ &= k_p + \frac{k_i}{s} \end{aligned} \quad (4.12)$$

The controller output is a quantity that can influence torque and, as can be seen in the figure, this is a demand for  $i_q$ . The value of  $i_q$  is limited in practice depending on inverter and motor ratings. Generally the limiting will be 1-2 times the rated motor current as long as the inverter limit is not exceeded [7]. Anti-windup must be included in the controller to disable the integrating term when limiting is active [98].

Design of the controller to provide the desired bandwidth and damping relies on the knowledge of inertia  $J$ , friction  $B$  and the torque constant  $k_T$  (relating torque to  $i_q$ ). The dynamics of the current control can be neglected as they are sufficiently higher than those of the speed loop [12]. Values of inertia and friction for the 2 motor rigs in



this project were shown in chapter 3.  $k_T$  can be derived from motor specifications and is shown for each rig in table 4.1. The table shows the designed specifications of the speed control loops.

Full design of the speed control parameters for the two motor rigs is shown in Appendix F. The derived s-domain transfer-functions were discretised using the bilinear transform [98]. This is applicable if the control loop sample frequency is sufficiently larger than the control bandwidth: generally at least 20 times larger is suggested [98]. From the table it can be seen that the speed loop sample time is 10ms (100Hz or 628.32rad/s), some 60+ times faster than the speed control bandwidth of 10rad/s.

	$k_T$	Bandwidth	Damping	Sample Time	$k_p$	$k_i$
Rig A	7.1	10 rad/s	0.707	10 ms	0.28	2
Rig B	6.9	10 rad/s	0.707	10 ms	0.16	0.9

**Table 4.1 Speed controller specifications**

The maximum speed control bandwidth of an encoded drive is determined by the maximum acceptable torque ripple. The torque ripple will be determined primarily by the inertia of the system and the encoder resolution for a given sample time [28]. The maximum bandwidth of a sensorless system is not often tested and often the bandwidth used in research papers is not defined. The work of Blasco looked at comparing encoded solutions with sensorless MRAS solutions [28, 48, 49]. It was concluded that the maximum bandwidth attainable from a sensorless solution will depend on stability considerations. Oscillations will exist in the speed estimation signal due to parameter inaccuracy and sensitivity will increase with an increasing estimation bandwidth. The estimation bandwidth must however, be suitably higher than the speed loop bandwidth so as not to directly affect its design. Bandwidths in excess of 20 rad/s can be obtained for the speed loop from the encoded implementations on the practical rigs used here. The chosen sensorless bandwidth is similar to that used by Blasco [28] (although he tested various designs) and the same as that used by Ohyama (in his comparative studies) [43, 44], in their work on rigs of a similar power level.

Current Control

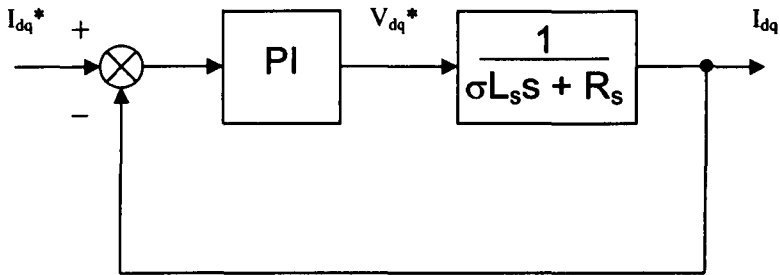


Figure 4.5 Structure of the current control loop

The reduced structure of the current control loop is shown in figure 4.5. Two similar controllers exist in the vector scheme: one for  $i_q$  and the second for  $i_d$ . The s-domain transfer function of the PI control block is as before and defined in equation 4.12 in the previous section.

Here the controller output is a quantity that can influence current directly: this being voltage. Design of this controller relies on the knowledge of stator resistance  $R_s$  and stator leakage inductance  $\sigma L_s$ . The nominal values, shown in chapter 3, were used in the design (presented in Appendix G). Table 4.2 shows the designed specifications of the current control loops.

	Bandwidth	Damping	Sample Time	$k_p$	$k_i$
Rig A	628.32 rad/s	0.707	250 $\mu$ s	57.23	27800
Rig B	628.32 rad/s	0.707	250 $\mu$ s	53.8	26530

Table 4.2 Current controller specifications

Again the controllers were designed in the s-domain and discretised using the bilinear transform [98]. In this case the sample time is some 40 times that of the designed controller bandwidth. Note that  $k_p$  and  $k_i$  gains for the 2 rigs are not dissimilar and this is because motor electrical specifications are alike (unlike mechanical specifications), as the machines are similarly rated.

It is considered that the designed current control bandwidth is typical for a machine of this size and similar to commercial implementations. Higher bandwidth control may be necessary in some of the advanced signal injection techniques mentioned in chapter 2, but then design would be undertaken in the z-domain (to account for inverter, sampling and processing delays) and may require a higher switching

frequency control of the inverter. Current control bandwidth is also a consideration in the slot harmonic tracking algorithm and is considered in the next chapter.

#### **4.2.4 Design of the AFO and ASO**

The specifications for the AFO implementation are shown in table 4.3 in relation to the DSP interrupt timing and switching frequency. The specifications shown are the same for both rigs.

Interrupt Frequency	Switching Frequency	AFO Discretisation Frequency	AFO Discretisation Method
8kHz	4kHz	4kHz	Euler

**Table 4.3. AFO implementation specifications**

Reference can be made to the software listings contained in Appendix C, which contains coding for both the AFO and ASO. The difference equations that form the calculation of  $\alpha\beta$  stator current components and rotor flux components can be seen.

Implementation of the ASO is less straightforward and some consideration must be given to the design of the adaptive speed estimation mechanism. The estimation bandwidth must be sufficiently higher than that of the speed control loops, so as not to interfere with or limit their dynamics [28, 48, 76]. The estimator design might, however, limit the maximum speed loop bandwidth [28, 48]. The work of Blasco found that the sensorless drive is more sensitive to parameter error the higher the estimator bandwidth is set [48]. Large proportional gains may be necessary to give the estimator sufficient bandwidth, for a particular speed loop specification, and this may introduce excessive noise on to the speed estimate. The speed loop will be sensitive to large noise levels in much the same way that it is sensitive to encoder resolution.

In the Kubota papers [60, 83, 99, 100], a formalised design approach for the adaptive speed loop is not specified. In [83] the authors show the transient performance of three different sets of PI controller gains, where the speed observer is enabled whilst an encoded drive runs at a steady state 100rpm. In this work, because an encoded mode of operation could be used, the estimator was set up in much the same way. With the drive running encoded IRFO, the ASO was implemented as an observer. The IRFO drive was operated under transient (speed and load) and steady state

conditions and PI controller  $k_p$  and  $k_i$  gains were chosen, such that the ASO gave suitable tracking performance. The PI gains are shown in table 4.4.

	Sample Time	$k_p$	$k_i$	Approximate Speed Estimator Bandwidth
Rig A	2 ms	3.75	250	25.13 to 37.7 rad/s
Rig B	2 ms	4.25	750	28.27 to 40.84 rad/s

**Table 4.4. ASO implementation specifications**

Also shown in table 4.4 is an approximation of the speed estimator bandwidth. A formalised design procedure was not heavily investigated in this work, although this has been considered for other model-based techniques [28, 76, 80], as it was not considered the primary focus of the work. This was geared more towards simply engineering a working sensorless method and, given that an encoded mode of operation was available, the estimator could be adequately set-up/tested as an observer of motor speed before closing the sensorless loop. In any case, the tuning system to be developed is aimed at being applicable to a majority of model-based approaches and aims to provide improved speed-holding performance to a non-optimised solution.

The estimator bandwidth approximations should only be taken as a guide. They were obtained by varying the reference command fed to the encoded drives in a sinusoidal manner. This was about various fixed operating points (speeds and loads), and studying the phase difference between measured and estimated speed. It must be noted that such a disturbance is heavily filtered by the closed-loop dynamics of the drive and the captured information is difficult to analyse, due to the encoder resolution and noise on the estimate. It can be seen however, that for both drives it is considered that the estimator bandwidth is in the region of some 2.5 to 4 times the designed speed loop bandwidth and thus appropriately faster.

Were the Kubota algorithm to be used for a general sensorless implementation, in a commercial product for example, then a more rigorous design procedure would be necessary for the adaptive speed estimator. As mentioned, various works analyse the dynamics of speed estimator in model-based sensorless algorithms and often the design is operating point and parameter dependent and rather involved [28, 48, 76, 80].

### **4.3 Sensorless Performance Analysis**

The performance of both the Adaptive Flux Observer (AFO) and the Adaptive Speed Observer (ASO) is reviewed in this section.

In section 4.3.1 results are presented that demonstrate the operation of the AFO providing estimates of stator current and rotor flux. The results are presented simply to illustrate the flux estimation operation and the analysis allows the discussion of effects such as deadtime, which produce evident distortion. The primary focus of section 4.3 is in analysing and reviewing sensorless speed operation.

Section 4.3.2 examines the performance of the ASO used as a speed estimator in an encoded IRFO implementation (similarly to how estimator gains were determined). Results are obtained for a series of tests and this provides a benchmark for comparison with sensorless results. Results, for the same series of tests, are provided in section 4.3.3 from the fully sensorless system.

Various authors have looked at testing sensorless induction motor drives [39, 41-44], although in many research papers implementations are not rigorously tested. The effect of parameter variation on sensorless performance is given more consideration in section 4.4, but the main areas and modes of operational interest are:

- Steady State Speed Accuracy
- Drive Stability
- Speed Transient Performance
- Load Rejection Performance
- Low Speed Performance

Speed accuracy and stability will be mainly functions of model parameter accuracy, depending primarily on accurate knowledge of resistance parameters [48, 49], but good design of the adaptive speed loop is also important with regard to stability [48]. It is important that the sensorless scheme be suitably stable, but speed accuracy is not expected to be encoder like without a suitable tuning mechanism and this is the aim of this work.

It is primarily the transient and load rejection performance that must be tested at this stage, because one of the aims of this work is to obtain 'encoded IRFO-like

dynamic performance' and the results of these tests give an indication of the orientation quality of the algorithm – the torque response. The performance at low speed, although generally compromised in model-based methods, must provide at least functional operation and is therefore a worthwhile test.

In the recent work of Campbell [40], five performance tests were proposed that assess the performance of a sensorless drive in the proposed areas, these being:

- Large Scale Speed Reversal under No Load
- Large Scale Acceleration from Standstill under No Load
- Large Scale Deceleration to Standstill under Full Load
- Load Rejection at High Speed
- Load Rejection at Low Speed

These are the tests performed, for the results in sections 4.3.2 and 4.3.3, to test the encoded drive performance, and the ASO performance as both an observer of speed and as a closed loop sensorless drive. Effectively the test criteria and the five tests are a measure of the sensorless speed and orientation quality. The information that can be obtained from each test will be outlined in the following results sections, but firstly the operation of the AFO is briefly considered.

### 4.3.1 Results from the AFO

Results are presented in this section to verify the operation of the AFO. This is when operating as an observer of rotor flux, in an encoded IRFO scheme that is running on experimental rig A. Results obtained from rig B are included in Appendix H for similar operating conditions.

The upper trace in figure 4.6 shows measured  $\alpha\beta$  currents and observed  $\alpha\beta$  currents from the AFO. The drive is operating under encoded IRFO control, at 100rpm and with no load. The observer is running in open-loop mode ( $k=1.0$ ) and no attempt has been made to optimise motor model parameters for the particular operating condition. That is, whilst the drive has been run up to an approximate nominal operating temperature, model parameters have not been characterised or adjusted. The lower trace shows the estimated  $\alpha\beta$  components of rotor flux.

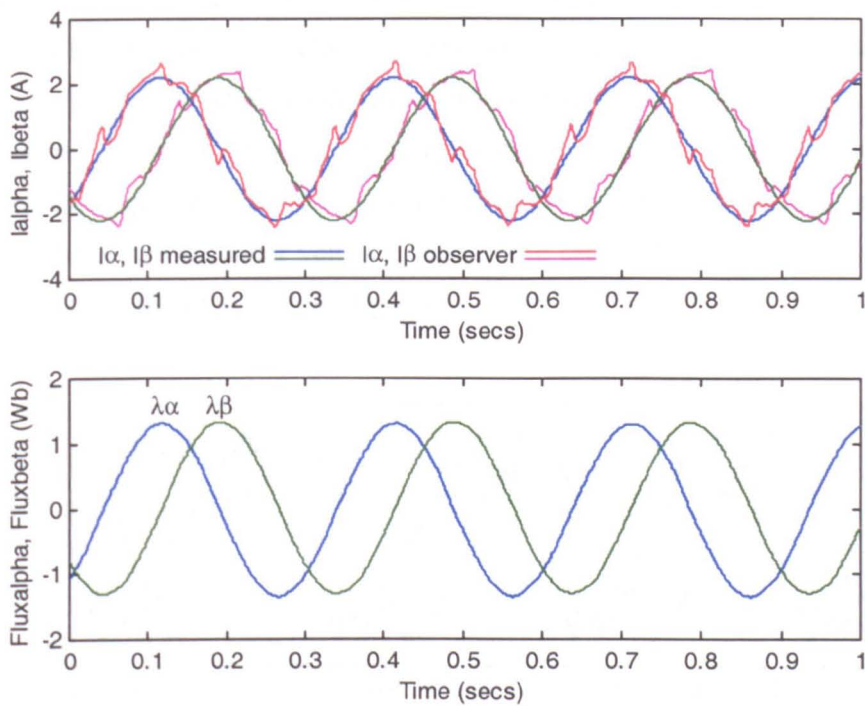


Figure 4.6 Measured and observed  $\alpha\beta$  currents and observed  $\alpha\beta$  flux from the AFO with  $k=1.0$   
The drive is operating under encoded IRFO at 100rpm with no load

In figure 4.7 the rotor flux angle obtained from the  $\alpha\beta$  flux components of figure 4.6 is compared with the imposed flux angle in the IRFO scheme. Note that little difference is observed. The scheme is shown to give a good estimation of flux for orientation.

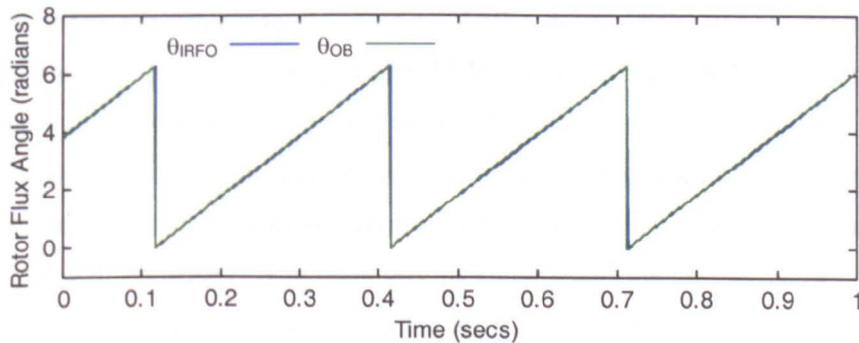


Figure 4.7 Imposed rotor flux orientation angle and that measured by the AFO

Note that there is distortion evident on the observed  $\alpha\beta$  currents in figure 4.6. This distortion appears at the zero crossing points of the 3-phase line currents

(remembering that  $I_\alpha$  is in phase with  $I_a$ ). This distortion is due to the deadtime effects in the inverter, as discussed in chapter 2. The fast acting current controllers in the vector scheme negate the effects of deadtime in the measured current, but, as is shown in figure 4.8, significant deadtime distortion therefore appears on the voltage waveforms. These voltages are an input to the equation for stator current in the observer (see equation 4.1). The waveforms shown in figure 4.8 are measured  $\alpha\beta$  components of applied stator voltage. These were captured under similar operating conditions to those of the previous figures.

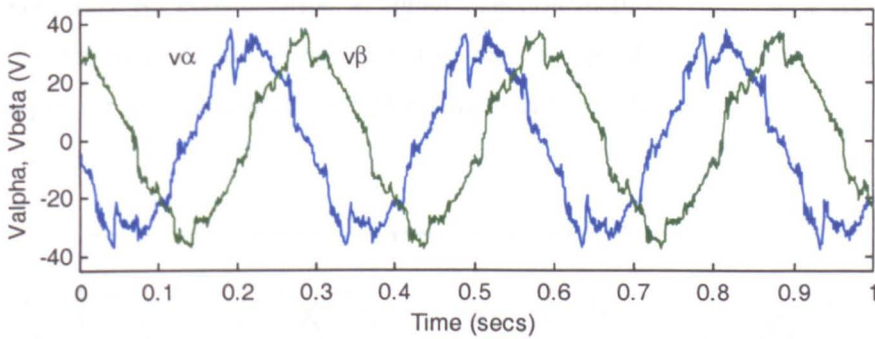


Figure 4.8 Measured  $\alpha\beta$  stator voltages from the IRFO scheme at 100rpm with no load

The distortion in the observed current is more significant at low speed, where the motor back emf is smaller, and at low load, where the current and voltage are smaller than with load. An improvement may perhaps be possible if reference voltages were used to drive the observer, but account must then be made for processing delays, as well as still accounting for deadtime effects, and this is not trivial. Using measured currents and voltages in an observer does not require knowledge of these delays, as both quantities are subject to the same or similar delay. Schemes are proposed to compensate for deadtime [61, 62], where PWM timings are adjusted to suitably move (compensate) the switching edges. A simple scheme was implemented during development of the drive algorithms. One of the drawbacks however, is in the requirement for a high-resolution current measurement (which is not a problem in this case), but with no offset. It is necessary to know when the current passes through zero with some accuracy. Other drawbacks are that full appreciation must be given to processing delays for this method, this is with regard to the measurement of current and switching actuation, and that a good scheme increases processing overheads. Whilst the simple implementation, which didn't consider the delays, much improved the voltage waveforms in an open-loop V/F scheme, some stability problems were encountered with the current controllers when the compensation was included in the



vector schemes. Also, as this project has a commercial impact, it was considered that a complex compensation solution would not generally be found in a commercial product, so one was not included here.

From the lower trace of figure 4.6, note that distortion effects are not clearly evident in the flux estimations. This is due to the differing time constants between the dynamic equation for current and that for flux: that for flux is much longer and thus serves to further filter the distortion. These effects however, are one of the reasons for model-based techniques failing at very low speed [63]. The deadtime problem is also necessary for consideration in signal injection methods [62]. In a very recent paper Holtz considers the improvement of the low speed operation of model-based techniques through the use of a non-linear inverter model [63].

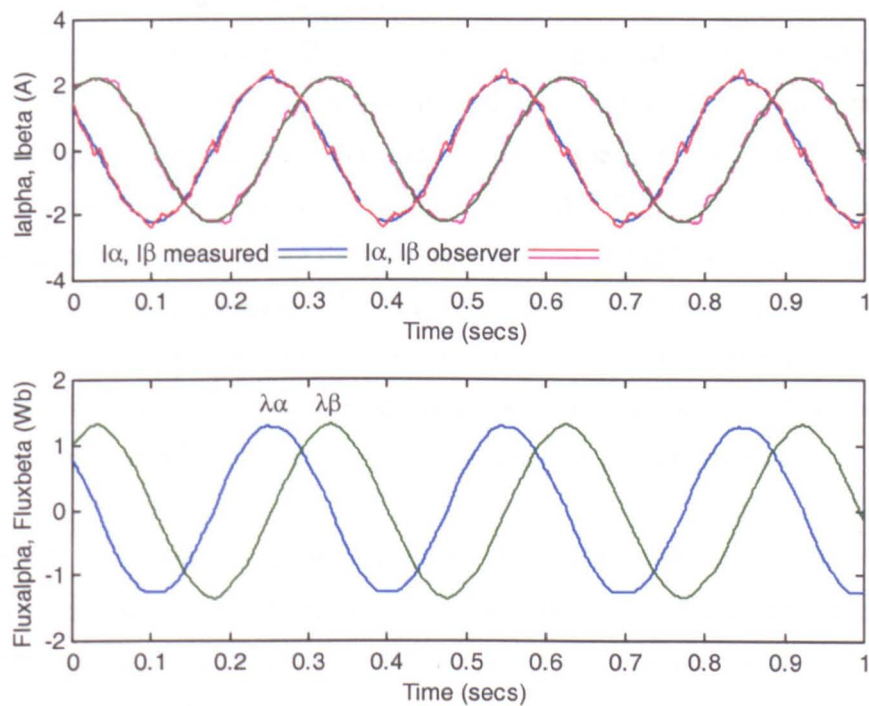


Figure 4.9 Measured and observed  $\alpha\beta$  currents and observed  $\alpha\beta$  flux from the AFO with  $k=3.0$   
The drive is operating under encoded IRFO at 100rpm with no load

Figure 4.9 shows similar observer results to those shown in figure 4.6, but with  $k$  now set to 3.0 and therefore with some feedback forcing measured and estimated currents together. Note that the deadtime distortion is now much less evident in the estimated current waveforms. The dynamics of the feedback is such that the distortion is reduced. The feedback is also applied to the dynamic equation for flux however, and

increased distortion may be seen in the flux estimates: some flattening on the waveform peaks. The flux estimate is more sensitive to the feedback correction terms than to the original error in the observed current. Larger values of  $k$  cause increased distortion in the flux estimate, whilst reducing that seen in the estimated current, and it is suggested that excessively high values of  $k$  would cause problems in an encoded DRFO scheme. In the Kubota AFO paper  $k$  values tested are 0.5, 1 and 1.5. The value must be set  $k > 1$  to improve the flux estimation dynamics and  $k > 0$ , but not  $= 1$  to have any parameter correction capability [83]. The scheme was used to provide orientation in an encoded DRFO scheme on the motor rigs with  $k = 2.0$  and performance was not noticeably different to that of IRFO.

4.3.2 Results from the ASO

Results to verify the operation of the speed observer are presented in this section. The tests carried out were as suggested in the work of Campbell [40] and outlined at the beginning of section 4.3. These are shown for rig A and again the results for rig B are contained in an appendix (Appendix I). In all of the results presented, the drive is operating under encoded IRFO control and the speed measured by the encoder can be compared with that estimated by the ASO. The drive was operated for approximately a ½ hour before the tests, at rated load and at low speed, to achieve a realistic operating temperature. The parameters used in the model are those shown in chapter 3. The results presented in this section will of course serve to demonstrate the performance of the encoded solution and hence act as a benchmark, by which to compare and contrast the sensorless results presented in the following section.

Table 4.5 shows the key used to interpret the results contained in this and the following section, 4.3.3. In section 4.3.3 only the encoded measured speed is shown in the results, although this plays no part in the control. Measured  $I_d$  and  $I_q$  waveforms are unfiltered.

Encoder Measured Speed	_____
ASO Estimated Speed	_____
Measured $I_d$	_____
Measured $I_q$	_____

Table 4.5 Key to speed and current measurements/estimates in figures in sections 4.32 and 4.33

Figure 4.10 shows the encoded IRFO drive performing the first test, a  $\pm 1000\text{rpm}$  speed reversal. The speed estimate can be seen to track the measured speed well in terms of both dynamic response and accuracy. Some oscillation can be seen on the speed estimate as the speed passes through zero and this is due to the ‘low speed problems’ of model-based methods discussed in chapter 2: loss of rotor information in stator quantities and high sensitivity to any  $R_s$  error. Note that the speed estimate is soon regained as the speed increases and this is the important test to ensure that the algorithm is stable.

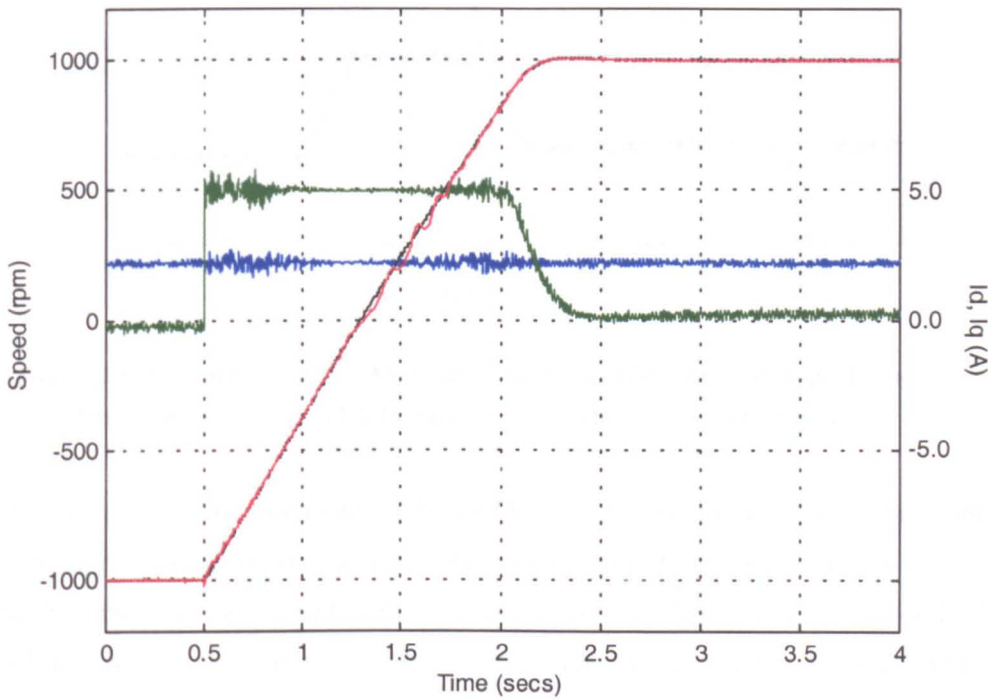


Figure 4.10. Measured speed and ASO speed estimate for  $\pm 1000\text{rpm}$  no-load speed reversal  
Drive running encoded IRFO (rig A)

The result in figure 4.11 shows a speed transient to  $1000\text{rpm}$  from standstill. The inverter was switched on just prior to  $t=0\text{secs}$  and speed and current controllers enabled. Note that the estimator successfully tracks the real speed with good dynamic performance and accuracy and that the system is very stable in the steady state. Again oscillations can be seen as the speed increases from zero, for the same reasons as mentioned previously. A speed estimation offset is noticeable at zero speed and this is again due to the high parameter dependency at low speed.

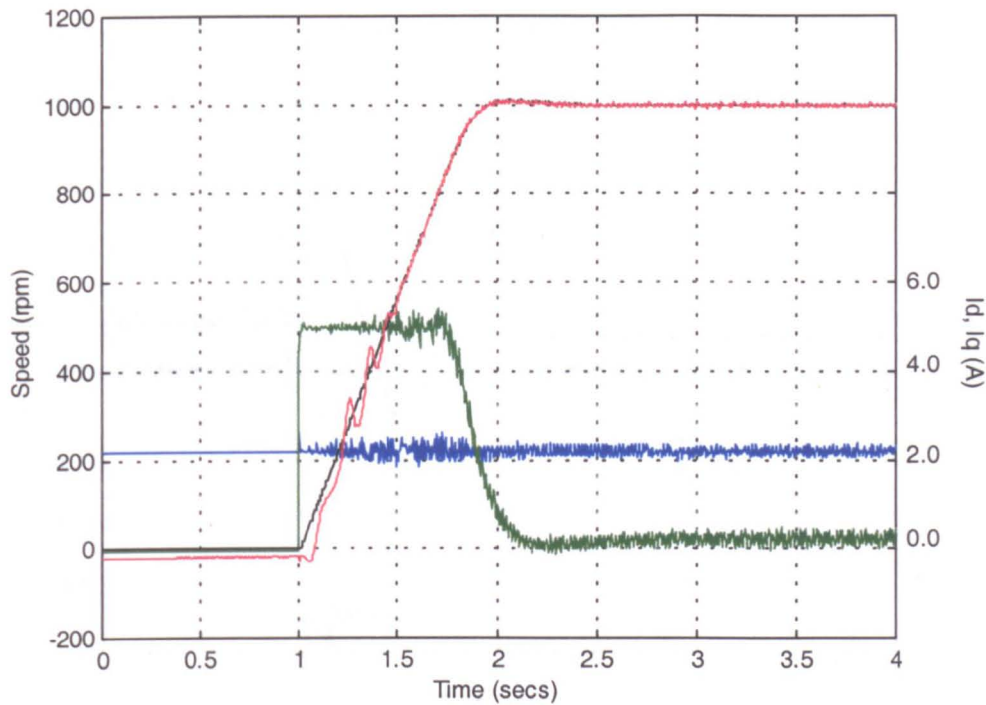


Figure 4.11. Measured Speed and ASO speed estimate for 1000rpm no-load speed transient  
Drive running encoded IRFO. Start-up conditions – inveter power up (rig A)

A deceleration to zero speed under full rated load is shown in figure 4.12. This is the fastest large-scale speed transient the observer is likely to encounter and it is clear that the observer has tracked well. Although the transient for this type of load condition is fast, the torque, and hence rotor and stator currents are high, more information is therefore effectively available to the observer algorithm. The speed estimate at standstill is reasonable. There is some noticeable offset and noise. At this speed any parameter inaccuracy is at its most significant. The noise is due to the significance of deadtime effects that were discussed in the AFO section. A fully loaded condition is preferred at standstill however, because the stator frequency will be higher in this case [50]. Again this is a combination of the amount of rotor information available at the stator, the significance of parameter error and the significance of measurement error and noise. Perhaps the worst-case operating scenario for model-based sensorless methods would be at low speeds with light active (i.e. not purely inertia and friction) generating loads.



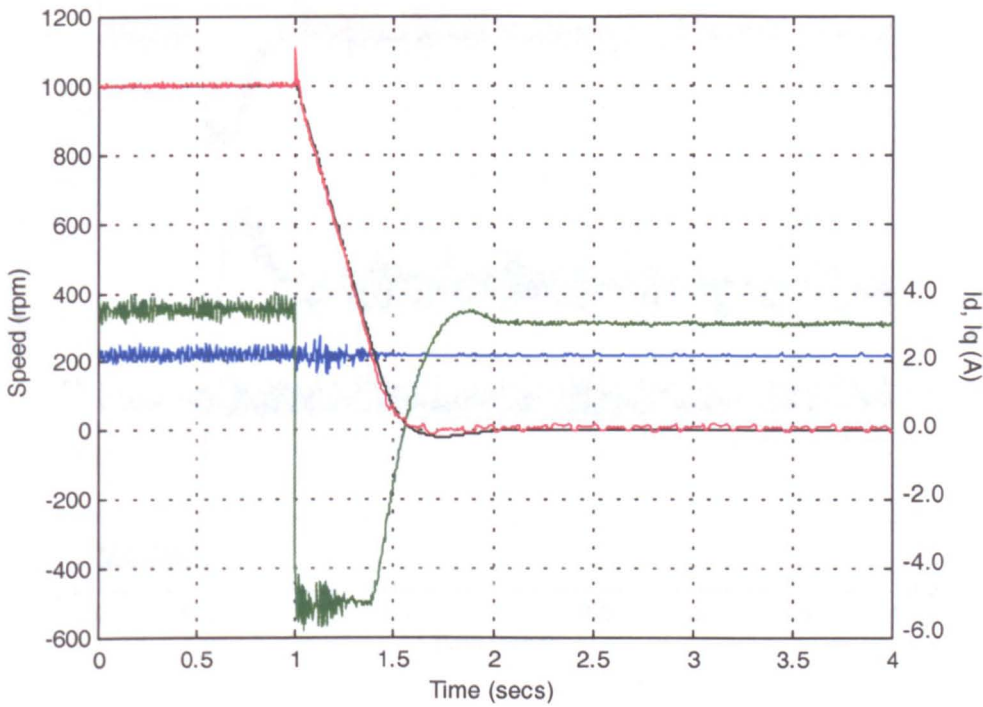


Figure 4.12. Measured Speed and ASO speed estimate for 1000rpm deceleration to standstill  
Drive running encoded IRFO – full rated load (rig A)

The observer load impact performance is shown in figures 4.13.and 4.14 at 1000rpm and 100rpm respectively. These figures more clearly show the noise present on the estimation signal, as the graphing scale is smaller. Oscillations at the excitation frequency occur due to differing inverter switching characteristics between phases and offsets on measured quantities. A similar effect was also observed by Blasco, particularly at low speeds, in model-based MRAS techniques with an error in  $R_s$  estimation [48]. Noise at six times the excitation frequency occurs due to the inverter deadtime effects. Similarly to the AFO it is now the speed estimator that responds to the differences between measured and observed currents, in its attempt to adaptively adjust for speed in the model. Less significant sources of noise will of course also be present: that of quantisation effects in measured signals, etc. The 100rpm impact response on rig B, as shown in Appendix I, shows more sign of oscillations on the speed estimate due to inverter imbalance and these problems are associated with the gate drives of the FKI inverter. The real performance of the ASO will be assessed in the following section when the drive is operated in the fully sensorless mode.

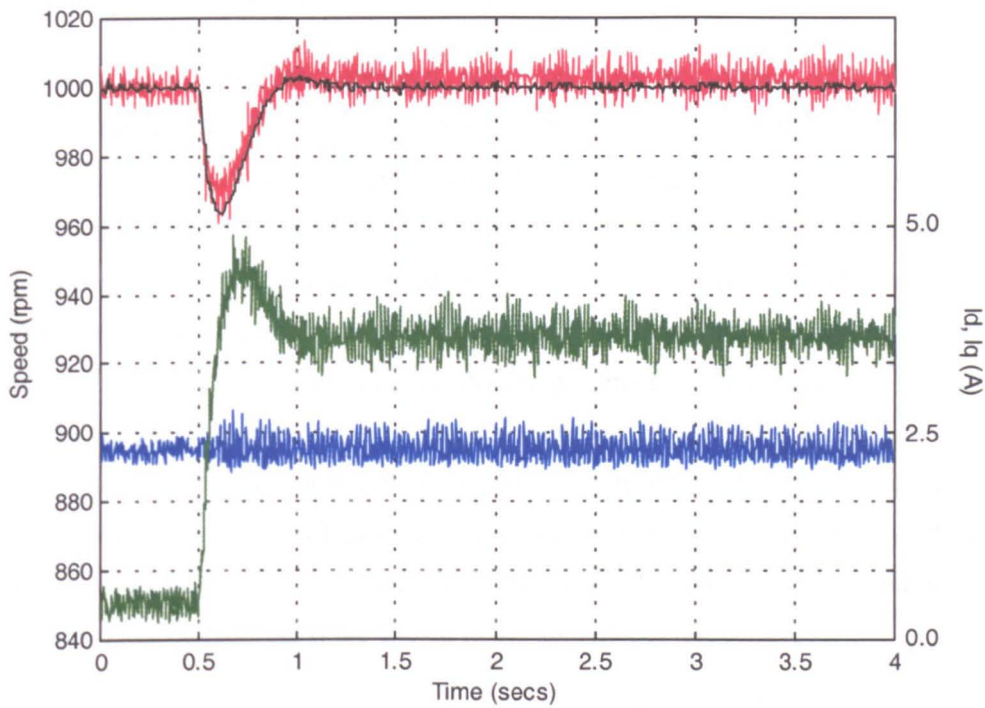


Figure 4.13. Measured speed and ASO speed estimate during full-load torque impact at 1000rpm  
Drive running encoded IRFO (rig A)

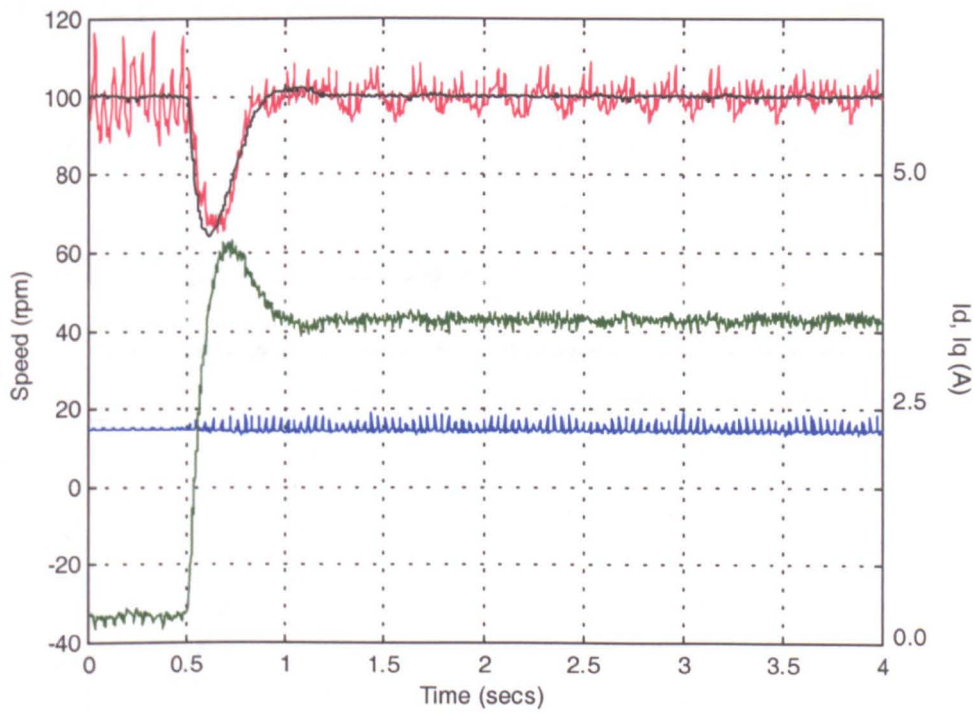


Figure 4.14. Measured speed and ASO speed estimate during full-load torque impact at 100rpm  
Drive running encoded IRFO (rig A)

4.3.3 Results from the Fully Sensorless Drive

The following results were obtained from the fully sensorless ASO solution. Estimated speed is used to drive the speed loop and the rotor flux angle, obtained from the  $\alpha\beta$  flux estimates, is used to provide decoupling for vector control. The scheme is therefore sensorless DRFO. A low pass filter of 12Hz bandwidth filters the sensorless speed fed back in the speed loop to reduce the noise effects seen in the ASO results. The unfiltered sensorless estimate is still used in the observer model that provides the flux estimate. Five results are presented, for the same five tests as shown in the previous section, and these can therefore be compared to the previous results obtained under encoded IRFO control. Again the results are obtained after running the drive for approximately a ½ hour before the tests, from a cold start, at rated load and at low speed. The sensorless results are obtained from rig A and again the results obtained from rig B are shown in the appendices (Appendix J).

Figure 4.15 shows the sensorless scheme performing the  $\pm 1000\text{rpm}$  speed reversal test. Note that the estimated speed is not shown in these results, as the concern is now with what the real speed is doing under sensorless operation. The measured speed plays no part in control of the drive.

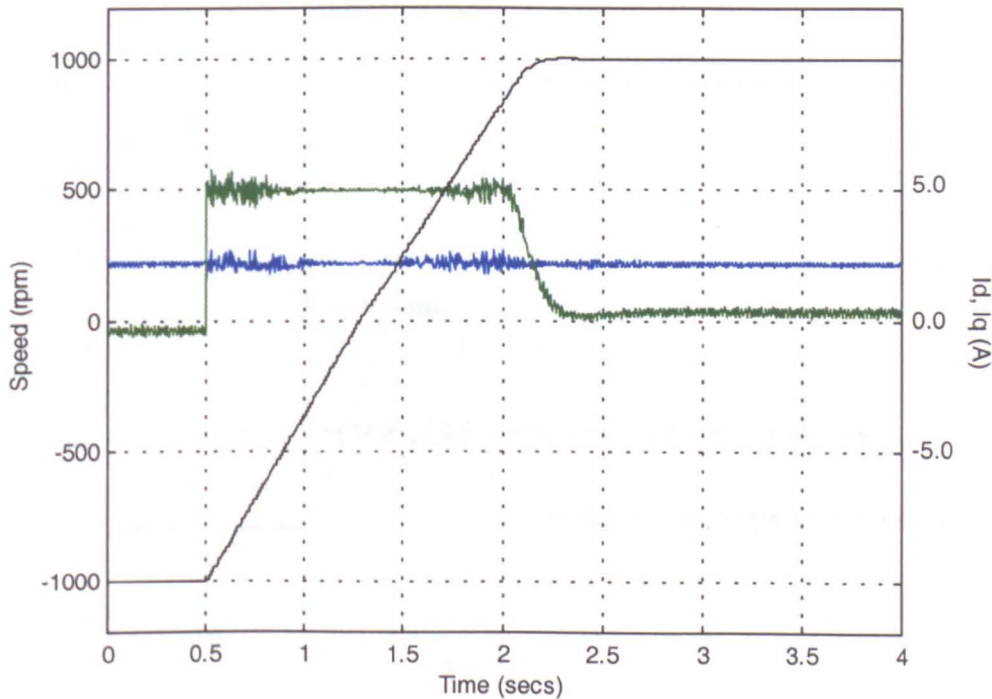


Figure 4.15. Measured speed for  $\pm 1000\text{rpm}$  no-load speed reversal  
Drive is running sensorless DRFO (rig A)



The speed reversal performance shown is akin to that obtained with the encoded solution. Operation in the steady state is stable and noise free and the transient is similar to that obtained and shown in figure 4.10. The speed during the transient is perhaps not as highly linear as that obtained from the encoded drive, with maybe a little noticeable deviation as the speed passes through zero, but this causes no real degradation in performance. Note that the transient performance in a test such as this is effectively open loop with respect to the operation of the speed controller, as the demand for  $i_q$  is saturated at a limited value. It can be seen that the settling is comparable between figures 4.10 and 4.15, where the speed controller is regaining regulation of the drive speed.

The performance of the drive when accelerating from standstill is shown in figure 4.16 and this can be compared with the encoded result in figure 4.11. Again the sensorless performance is very like the encoded, with the drive giving stable speed holding operation in both steady states and similar performance during the transient, even when looking particularly at the settling response of the speed. The noise, speed oscillations and offset in the speed estimation at standstill, seen when using the ASO as a speed observer in figure 4.11, cause no problems in the closed-loop sensorless drive.

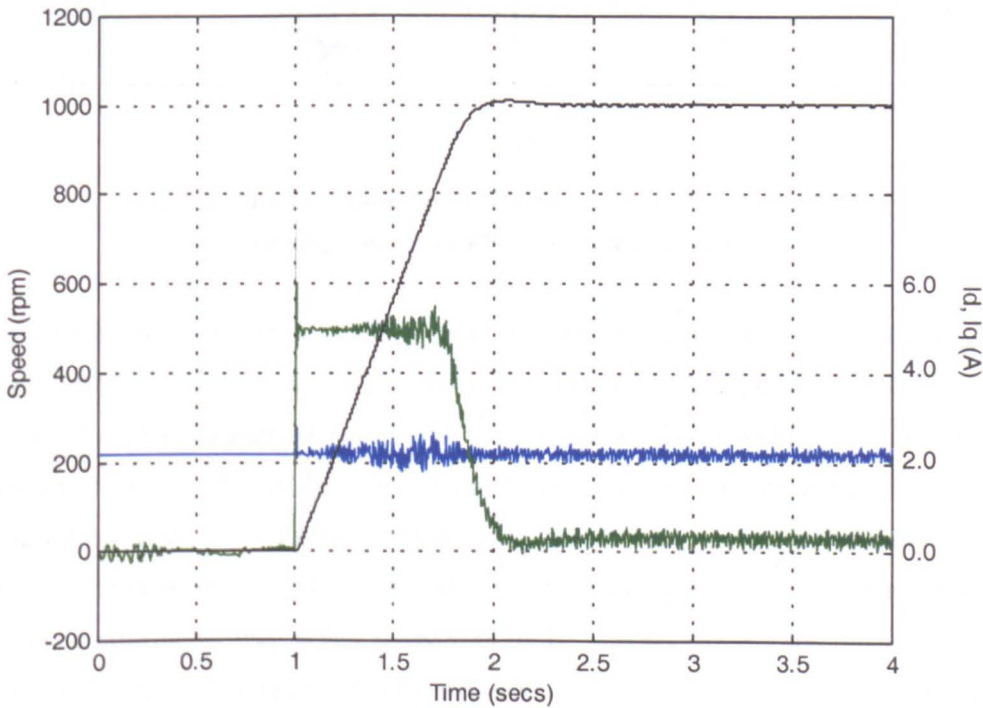


Figure 4.16. Measured speed for 1000rpm no-load speed transient  
Drive is running sensorless DRFO. Start up conditions – inverter power up (rig A)



Figure 4.17 demonstrates the performance of the sensorless scheme when decelerating from 1000rpm to standstill under full load. Note that the result shows the drive losing orientation at low speed and hence both speed and torque regulation fail. This is, as previously discussed, the operating range in which model-based sensorless techniques struggle, being particularly sensitive to system noise, measurement error, parameter error, etc. Speed control to and around zero speed will also involve some operation in the state of zero excitation frequency and in this state rotor side parameters, such as speed, will not be observable [41].

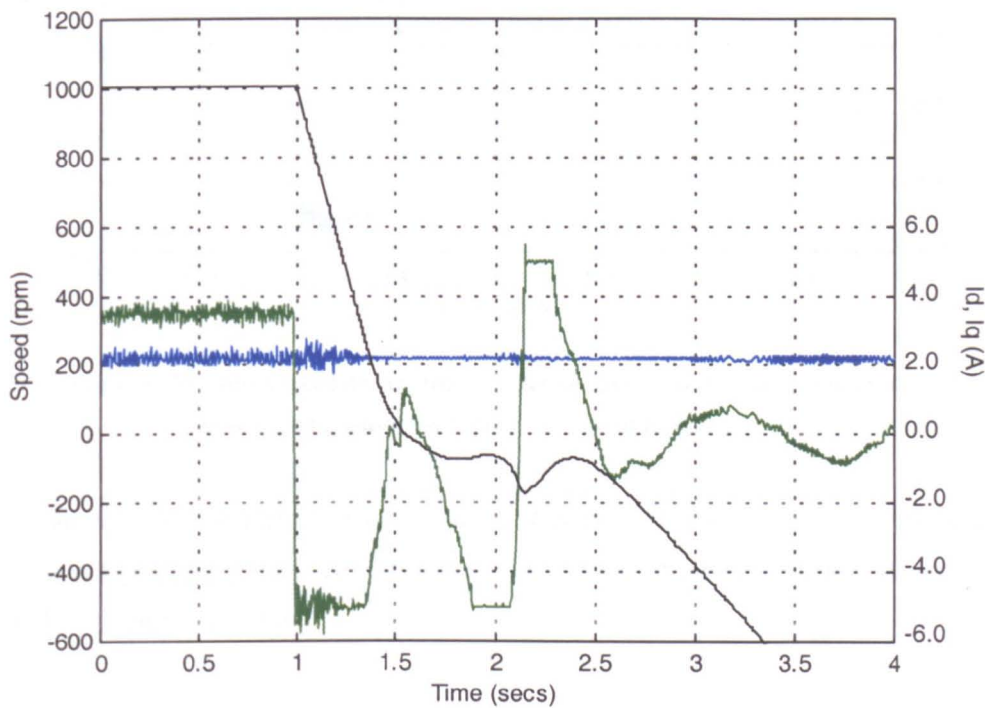


Figure 4.17. Measured speed during a 1000rpm deceleration to standstill  
Drive running sensorless DRFO – full rated load (rig A)

Performance is improved with the manual adjustment of the  $R_s$  and  $T_r$  values by approximately 10%. Figure 4.18 shows that the same test performed with the adjusted motor parameters is successful and this shows the importance of updating parameters online. It can be seen, in the second figure, that the performance at standstill is particularly sensitive. The noise on measured  $I_q$  contains significant noise due to inverter deadtime. It was found that rig A was possibly more sensitive to parameter error under load at low speed than rig B. It is considered that this is due to the higher inertia resulting in a slower transition through the low speed region. Some increased tolerance of parameter error may be obtained by the adjustment of  $k$  values in the observer feedback matrix, but this has yet to be extensively investigated in research literature.

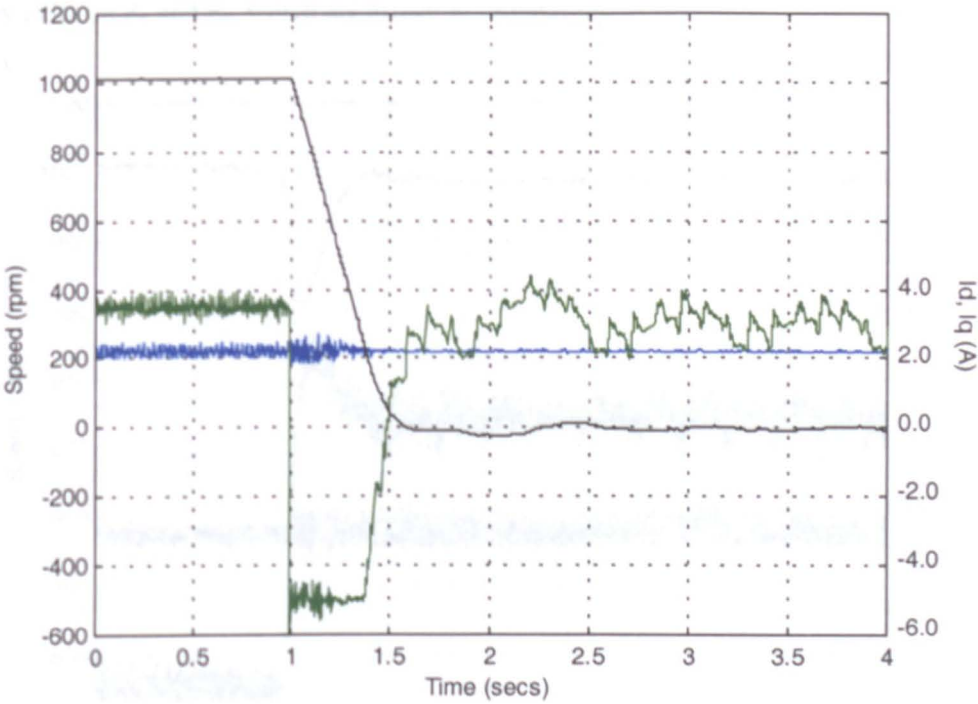


Figure 4.18. Measured speed during 1000rpm deceleration to standstill – Tr adjusted  
Drive running sensorless DRFO – full rated load (rig A)

The load rejection performance of the sensorless drive is shown for 1000rpm and 100rpm in figures 4.19 and 4.20 respectively. The drive parameters are maintained at their slightly adjusted values.

The performance of the drive can be seen to be very similar to the encoded solution. The dynamic response of the sensorless drive is similar to that shown in figures 4.12 and 4.13, with maybe just a little more speed lost during the torque impact at 100rpm on the sensorless drive, but this is only in the order of 3-4rpm. It is clear that the  $I_q$  current waveform for 100rpm operation is noisier in the sensorless mode and again the noise frequencies are that of the excitation and deadtime, due to non-ideal inverter operation. Noise due to deadtime can certainly also be seen in the encoded operation result in figure 4.14, but is less significant.

An important consideration in both results is that, although the speed regulation is good, there is evident speed error when operating in the sensorless mode and this varies depending on the load condition, due to parameter variation with load. The work of Blasco picked up on such variation and attributed it to the effects of

saturation on the value of inductance parameters [28], but this is as well as errors that may exist on  $R_s$  and  $R_r$ , which are affecting orientation.

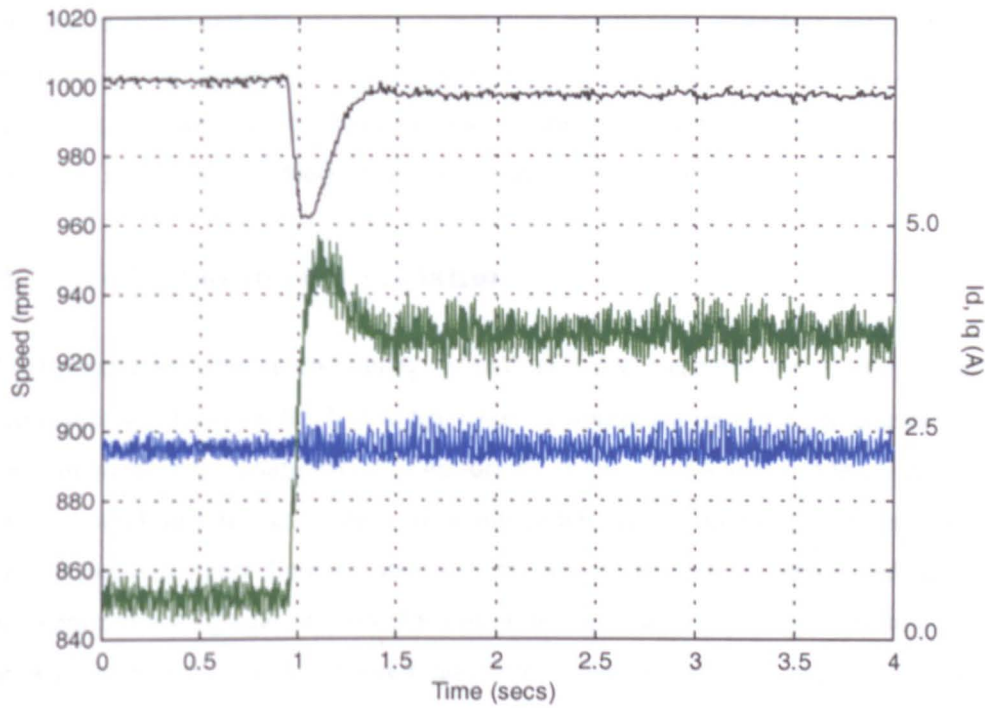


Figure 4.19. Measured speed during full-load torque impact at 1000rpm  
Drive running sensorless DRFO (rig A)

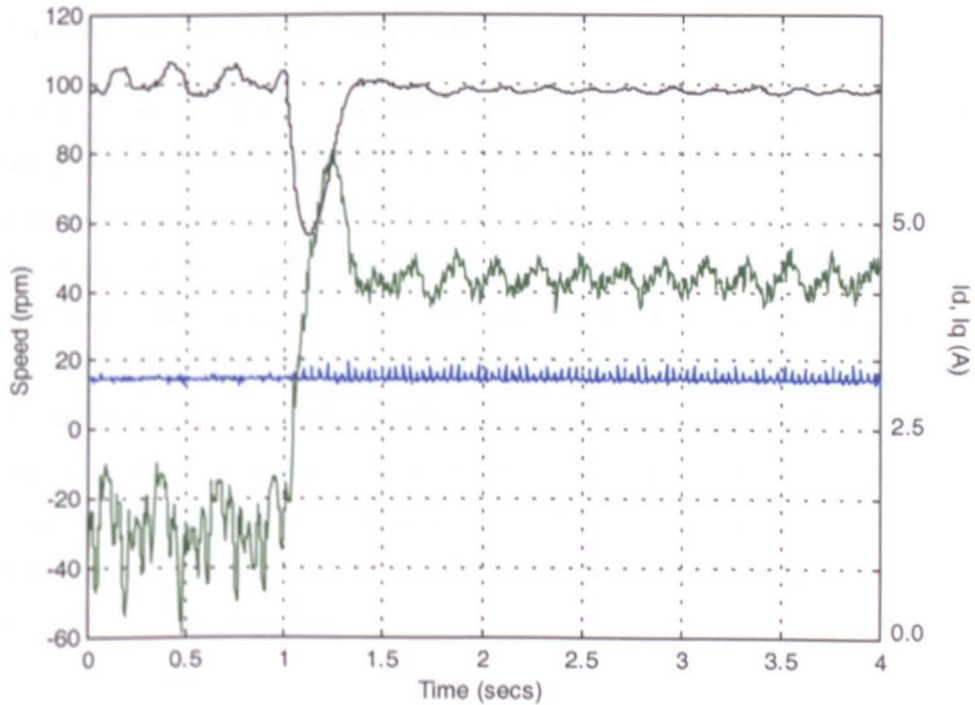


Figure 4.20. Measured speed during full-load torque impact at 100rpm  
Drive running sensorless DRFO (rig A)

The results for rig B, in Appendix J, show similar performance to those shown for rig A in this section. Due to the lower inertia of rig B, the performance at zero speed seems more stable and less sensitive to errors in parameters. However, operation at low speed, due to the poorer inverter performance, shows more excitation (inverter imbalance) and deadtime frequency noise in the decoupled currents. Due to the lower inertia this also has more effect on the drive speed ripple/variation.

## **4.4 Model Parameter Variation**

Whilst parameter variation and tuning, of both encoded and sensorless drives, was briefly mentioned in chapter 2, it is necessary to appreciate the primary causes and effects of parameter variation in the sensorless drive. This section thus presents a review of work in this area. The goal of this project is the tuning of the sensorless drive for accurate speed holding, such that the tuning mechanism introduced in the next chapter is tuning against a small variation in combined effects of all parameters. The way in which this is achieved however, is in choosing to tune the motor parameter that most affects speed accuracy ( $T_r$ ) and significant variation in other parameters, which is not considered in this work, must be appreciated (particularly  $R_s$ ).

### **4.4.1 Resistance Parameter Variation**

The most significant parameter variation effects in motor drives, certainly for those operating over a great range of speed and load conditions, will be due to temperature (resistance) change. Even if parameters are well known at start-up, detuning of the resistance parameters  $R_s$  and  $R_r$  (and hence  $T_r$ ) will be most evident. A change in ambient temperature will of course affect the resistance parameters, but in the majority of environments this change is likely to be small and often the ambient temperature will be reasonably regulated. By far the most significant factor influencing motor temperature will be the motor operating condition. Often the effectiveness of motor cooling is speed related and motor heating effects are due to inevitable motor losses [7, 40]. An excellent account of motor heating processes is given in [40].

Motor temperature variation and nature of the heating effects will be highly non-linear and hence very difficult to predict and compensate for [40]. Heating effects may be somewhat counteracted by forced cooling techniques and suchlike, but this

will not always be practical, or wholly effective with regard to minimising parameter variation. For the variable speed operation of many machines, perhaps designed for fixed speed operation, heating is an important consideration. Sufficient cooling must be provided, bearing in mind that effective natural 'fan' cooling will be speed related [7]. Often a motor must be de-rated for variable speed operation [7].

Significant temperature variation will be apparent in many applications, where a motor drive will be operated from a cold start and then run at around its rated load. In this instance a large variation in the resistance parameters will be apparent between the starting state and the nominal operating temperature state. Depending on whether the resistance values used in the control algorithm are the cold starting values or the hot rated values, different problems will be experienced. For optimal operation, drive resistances should be accurately known, but, particularly for stable operation, an underestimate is perhaps preferred to an overestimate [28, 48].

The variation of  $R_s$  has already been discussed in chapter 2, due to its significance in the back-emf equation. In the sensorless drive  $R_s$  accuracy has been shown to heavily influence drive stability [48]. The effect on drive stability also depends on the adaptive speed loop dynamics [48]. The significance of  $R_s$  error in speed estimation can be high at low speed, but its influence becomes increasingly less significant as the speed rises above only a few hertz. This is certainly the case in the Kubota scheme [83]. For the purposes of this work tuning of  $R_s$  is not implemented, but in practice, for algorithm stability and particularly improved low speed performance, some adaptation scheme would be appropriate. The mechanism proposed by Kubota [83, 60], or the application and measurement of a dc voltage/current component could be used, although the neural network approach would be considered superior [40, 59].

Variation of  $R_r$  and hence the variation of  $T_r$  has been shown to most greatly influence the speed accuracy of a sensorless drive throughout the speed range [28, 83]. Its effect is difficult to ascertain in a speed sensorless system, because it is directly related to speed, being proportional to slip. It cannot be readily obtained, from dynamic equation analysis, unless the system is excited by more than one frequency [28]. A simple form of compensation can be implemented where  $R_s$  variation is tracked, by assuming that  $R_r$  varies in proportion. Such compensation is of course open-loop with respect to absolute speed holding accuracy and  $T_r$  will also vary with any variation in  $L_r$ .  $T_r$  is the parameter most suitably adjusted to correct for speed error, if possible, so ultimately this should account for resistance and



inductance variation. If inductance effects can be distinguished,  $R_s$  could then be assumed to vary in proportion, instead of vice-versa.

#### **4.4.2 Inductance Parameter Variation**

The inductance parameters in the induction motor model will vary with flux condition [32, 33, 50, 51]. As such they may vary slightly with the quality of orientation, as may be affected by resistance parameter variation. The most significant inductance parameters variation (below base speed) will, however, be due to saturation variation caused by current (load) change [48].

Where inductance is related to a current carrying coil, its value is related to the number of turns. The relationship between flux and current is assumed linear, given that the coil is operated below its rated value of current and hence not in saturation. The inductance is therefore considered constant. When operating in and around saturation, a variation in current has less of an effect on flux and hence the inductance is effectively not constant.

Unfortunately inductance parameters, as related to the induction motor model, are not straightforwardly defined. The work of Sokola and Levi deals with the modification of the motor equivalent circuit with regard to field strength variation [32]. The construction/geometry of the induction motor leads to inductance effects that are difficult to define, where, for example, parts of the motor will be subject to saturation effects, due to operating condition, before others. The effects will be highly difficult to characterise and, where the motor model control is based on the presented equivalent circuit, will result in changes of the various inductance related parameters [32, 33, 50, 51].

Fortunately however, inductance parameter variation is shown to have less effect on sensorless drive performance, both in terms of stability and speed accuracy, than resistance variation, below base speed [28]. In field weakening, robust inductance parameter knowledge is critical however [32, 33, 50, 51]. For the purposes of this work, where adjustment of  $T_r$  is proposed (in the next chapter) to achieve steady state speed accuracy, this allows adjustment against  $R_r$  variation due to thermal effects and  $L_r$  variation due to saturation, load, etc. This mechanism is therefore artificially adjusting  $T_r$  slightly to account for minor variation in the other inductance parameters.

## **4.5 Conclusion**

Following on from the review of leading model-based sensorless methods, presented in chapter 2, this chapter has presented the Kubota Adaptive Speed Observer (ASO) in somewhat more detail. The reasons for choosing the ASO over the CLFO-MRAS and the Isq-MRAS have been detailed.

As the Adaptive Speed Observer (ASO) scheme is based on an Adaptive Flux Observer (AFO) structure, this scheme was presented, so as to allow the derivation of the dynamic equations for stator current and rotor flux, upon which the method is founded. The AFO can be used in an encoded drive for flux estimation and uses a state feedback mechanism to drive estimated and measured stator currents together. The state feedback was examined and an  $R_s$  adaptation mechanism presented.

The full ASO system has been detailed, where the AFO structure is modified to include speed adaptation, the speed in the model being provided by a PI mechanism. The mechanism is driven by the instantaneous rotor flux orientated torque error in the model. Design of speed, current and speed adaptation controllers is considered. The ASO is used in its simplest form, where state feedback is not used.

Results have been presented that demonstrate the performance of the AFO operating in the encoded system. The system is shown to provide a sound flux estimate that is suitable to provide orientation in an encoded DRFO system. The discussion presented centres on evident distortion due to deadtime in the practical system. Whilst deadtime compensation techniques exist, an implementation must be highly robust and not create instability problems relating to the current control loops, etc. In this work a simple compensation algorithm was tested, and, although improving the voltage waveforms, caused current controller instability problems and was thus not utilised. The exact nature of the instability was not investigated, nor the work extended to a more advanced implementation, because such an implementation is not considered to be practically/commercially typical.

Results have been presented for the ASO operating in two modes, running five similar tests in each. Firstly the ASO acted as a speed observer in an IRFO encoded implementation. Results obtained acted as a benchmark, for comparison with fully sensorless results, and good tracking performance was demonstrated. When the fully sensorless speed loop was closed, performance obtained from the drive was highly

comparable with the encoded solution. Some problems were evident at low speed under high load conditions, but these were overcome with slight tuning of the model resistance parameters and were only experienced in the high inertia system. The low speed region had been anticipated to display poorer performance with a model-based, and in this case un-optimised, system. In a commercial product, operation in this region would benefit from online  $R_s$  adaptation and perhaps advanced field control [50, 59]. Field control where the field is weakened at low speed maximises the applied frequency and makes as much information as possible available to the model [50]. Interest in this mode of operation has also been shown, because it can provide efficiency gains [50, 51]. As was suggested in chapter 2, operation in the low speed region would best be guaranteed with application of signal injection methods.

The intended field orientated dynamic performance of the sensorless system was demonstrated with the first three tests, involving speed transient operation, and then the final two tests, where the load rejection performance was demonstrated. On the tighter scale used for the latter two tests however, it was plain to see that speed holding accuracy of the model-based system was lacking. The effect varied with load, although it is questionable as to whether this relates to a varying significance of detuning (with load), or indeed actual parameter variation with load. The presence of this speed error is evidence of the problem tackled by this project: tuning against a single effect will not guarantee speed-holding accuracy. The solution proposed is demonstrated in the next chapter. After presenting the sensorless results, this chapter went on to discuss the causes and effects of parameter variation in model-based sensorless drives in more detail, based on the research of other authors.

Whilst  $R_s$  variation has been discussed with regard to improving drive stability/low speed performance, the parameter most significantly affecting speed accuracy is the rotor time constant ( $T_r$ ).  $T_r$  varies significantly with rotor resistance, due to temperature variation, but also somewhat with rotor inductance, due to non-linear field effects (saturation, etc) that will be difficult to predict. The contribution of the  $T_r$  error to speed error is difficult to establish, unless an independent measure of speed is available and this is the topic addressed in chapter 5, where  $T_r$  adjustment is used to provide accurate sensorless speed holding capability.



---

## CHAPTER 5 Rotor Slot Harmonic Speed Estimation & Sensorless Drive Tuning

---

### 5.1 Introduction

As has been established in the previous chapters, for high performance operation of an induction motor, based on knowledge of the motor model and measurement of motor terminal quantities, model parameters must be ‘tuned’. Particularly,  $R_s$  must be tuned for low speed performance and stability, this is considered in [48], and  $T_r$  is most appropriately tuned for speed holding accuracy [49]. The engineering of an induction motor control strategy for highly accurate speed holding capability is the motivation of this project.

To separate  $T_r$  information from speed information (to gain an independent estimate of  $T_r$ ) the sensorless induction motor must be excited by more than a single frequency [28]. However, whilst most significantly improving the sensorless speed accuracy, estimating/correcting  $T_r$  in this way will only truly minimise speed error if all other motor parameter estimates exactly represent practical values. Alternatively, if a second and highly accurate, sensorless speed estimate can be obtained, then speed error can be minimised by tuning  $T_r$  [28]. This ensures high speed-accuracy, but now  $T_r$  can only be considered highly robust if all the others parameters estimates exactly represent the real values. The advantage with the second method is that  $T_r$ , the parameter most affecting speed accuracy [28] is purposefully also used to account for speed error attributable to error in other parameter estimates. It must be remembered that false adjustment of  $T_r$  to correct such speed error will be minimal, because  $T_r$  is the significant parameter affecting precise speed estimation [28]. Such a technique is truly fulfilling the aim of the work – tuning for speed holding accuracy. It should of course be noted, that if an accurate knowledge of speed is available, then this could be used for feedback to facilitate IRFO. However, this would require a highly robust and high dynamic estimate. This is considered further later in the chapter.

This work makes use of the fact that speed information is naturally available in the induction motor terminal quantities due to the effects of rotor slotting. Harmonics can be observed in measured terminal quantities, the frequency of which are related to the number of rotor slots, the rotor speed and the stator excitation frequency. Through tracking the frequency of these Rotor Slot Harmonics (RSH) a highly accurate measurement of speed can be obtained, which is not dependent on the electrical parameters of the machine. It is dependent on a constant mechanical parameter (the number of rotor slots) and is, as such, not sensitive to the parameter variations discussed in the previous chapter. It is of course a requirement that the number of rotor slots (per pole pair) is known and this could be determined by commissioning tests [102, 103]. The stator excitation frequency must also be available for an estimate of speed to be established from an estimate of slot harmonic frequency. In some schemes this can be obtained directly, in others through differentiating the flux angle.

Various methods have been proposed to obtain a measurement or estimate of the RSH frequency through sampled measurement of stator quantities [28, 102-114]. Batch-processing methods, such as the FFT, can provide high resolution and accuracy, but it should be noted that this is at the expense of dynamic performance [113]. The resolution of such methods is proportional to the record length (number of samples required) and this seriously limits the dynamic capability, as well as incurring a high processing overhead. The work of Ferrah et al proposed the Recursive Maximum Likelihood – Adaptive Tracking Filter (RML-ATF) algorithm to be perhaps the most practically viable solution for speed tracking in motor drives [113]. The recursive nature of the RML-ATF allows for high dynamic tracking performance, whilst high steady-state resolution and accuracy can also be obtained, similar to that available from a practical FFT implementation [113]. The speed estimate is updated on a per-sample basis and, as well as improving the dynamic performance, this means the algorithm is not so highly computationally intensive as to necessitate unrealistic real-time processing capability.

Whilst the RML-ATF algorithm, as an RSH identifier, was investigated in the research of Ferrah, it was not developed into a practical drive system. In this project the RML-ATF work is developed and extended. It is developed into a practical speed estimator and used to tune the model-based method presented in the previous chapter. Similar implementations using other RSH derived speed estimates are discussed. It is

considered however, that the RML-ATF forms the most practically viable solution. It can be implemented on a DSP platform along with full drive control, PWM, etc.

Firstly in this chapter the mechanisms that give rise to RSH effects are considered, in section 5.2, along with a background review of work related to tracking. When considering the production of RSHs, results are presented to illustrate the harmonic make-up of various stator quantities. RSHs are related to and exist with inverter and other machine harmonics and this requires consideration, as the various components must not be confused by the RSH identification scheme. This work has found that the current controller bandwidth, as well as the more obvious inverter harmonics, can affect the tracking ability of the RML-ATF and a new method is suggested to alleviate these problems. The interaction of rotor slotting with higher order machine and inverter harmonics can be used to improve the robustness of the tracking algorithm and this is shown.

In section 5.3 development of the RML-ATF algorithm, into a full RSH based speed estimator, is fully described and speed estimation/tracking results are presented in section 5.4. Previous work by Ferrah et al tested the RML-ATF algorithm on a variety of different machine configurations, including machines similar to those used here (with closed and skewed slots), to verify the method [114].

Section 5.5 fully presents the method by which the ATF speed measure is used to provide a correction term for  $T_r$  in the Adaptive Speed Observer (ASO) sensorless scheme. As was seen in the previous chapter,  $T_r$  is the parameter that most significantly affects speed-holding accuracy in the model-based solution. As mentioned, it can however, also be artificially adjusted to account for small variations in the other parameters that are degrading the speed accuracy. Whilst this may compromise the field orientated performance slightly it fulfils the motivation of the work - to produce a sensorless drive whose prime interest is speed holding accuracy, and can be likened to the effects of  $T_r$  detuning in an IRFO drive. Results from the tuning sensorless scheme are included in section 5.6, to demonstrate the ability of the developed method to maintain encoder like speed holding accuracy where parameters vary, and this is for both motor drive rigs. Conclusions are drawn together in section 5.7.

## **5.2 Rotor Slot Harmonics (RSH)**

In this section, the mechanisms that lead to RSH effects being seen in terminal quantities are discussed. The fact that they exist with PWM harmonics causes practical problems, with regard to tracking, and this is picked up in the second part of the section. New input quantities are suggested, in which the RSH frequency information exists, for use in a robust speed estimator.

### **5.2.1 RSH Production and Detectability**

It is not the purpose of this work to explicitly define and analyse the mechanisms that give rise to rotor slot harmonics. An overview will suffice to allow an understanding of their existence and how they can be used for speed tracking. Whilst machine design may be carried out in an attempt to minimise unwanted effects that are due to rotor slotting, such as crawling, cogging and acoustic noise, and this may minimise RSH amplitude, they are unlikely to be completely eliminated [28, 103]. Of course their detectability is dependent upon their amplitude and given that the criteria for their existence in 3-phase terminal quantities is met (see later). For a more rigorous analysis of RSH production reference can be made to work and texts that look more particularly at machine design [115].

The operation of the induction machine relies on the discrete, regularly separated, current carrying rotor bars. It is the stator generated flux linking with the rotor that induces current in the rotor bars, producing torque (and hence rotation). Iron laminations form the bulk of the rotor and this is the material that separates the rotor conductors. In practice the airgap flux contains harmonics that are due to this rotor slotting. Hence, these harmonics will be seen in the stator flux and therefore stator terminal quantities. Principally, RSH effects will depend on the following processes [103]:

- Rotor slot permeance harmonics will exist due to the variation in permeability of rotor bar/rotor slot material to iron lamination material
- Rotor and stator MMF harmonics will interact, where the rotor MMF is produced by the torque current flowing in the rotor bars
- Saturation will affect both processes

Whilst the analysis of RSH production is somewhat involved with regard to harmonic amplitude, it is only the frequency of these harmonics that conveys speed information. Considering firstly the fundamental machine properties and quantities, the process is effectively the amplitude modulation of the fundamental frequency, imagining the flux vector as it travels around the machine relative to the stator, with the passing rotor slot frequency, as the slots move relative to the fundamental flux vector. The fundamental forward and backward RSH frequencies are defined in equation 5.1. It is clear that this is an amplitude modulation process involving the fundamental machine MMF frequency and the fundamental rotor slot passing frequency. The equation is dependent upon the number of rotor slots ( $z$ ) and the number of motor pole pairs ( $p$ ).

$$\begin{aligned} f_{sh} &= \frac{z}{p}(f_e - f_{slip}) \pm f_e \\ &= \frac{z}{p}f_r \pm f_e \end{aligned} \tag{5.1}$$

The existence of RSH components in stator terminal quantities is dependent upon a machine having an **even number of rotor slots per pole pair** (or odd slot harmonic pole numbers  $[z/p \pm 1]$ ). A machine with an even or fractional slot harmonic pole numbers will induce zero average slot harmonic currents at the stator [103]. Where the number of rotor slots per pole pair is an even multiple of 3, both positive and negative sequence components will be detectable. In cases for even values that are not multiples of 3, only one fundamental RSH component will be detectable: the slot harmonic pole number that is divisible by 3 will induce RSH effects that have no path in a balanced 3-phase system. Fortunately, due to various design constraints, a detectable RSH should exist in a majority of inverter fed, squirrel cage machines [103]. Note that the two 4kW machines used in this work were not specifically chosen, but both have the same number of rotor slots per pole pair and produce detectable RSH components.

With regard to RSH amplitude, the consideration is whether or not the harmonics can be detected when there is significant noise present. Common rotor design practices include methods that reduce the harmonic amplitude and hence reduce crawling, cogging, etc. Methods include closing and skewing the rotor slots. Closing the slots means effectively burying the rotor bars in the laminated iron rotor. A lamination from a closed slot rotor is shown in figure 5.1. It is clear that a material variation is

not apparent at the surface of the rotor. The harmonics however, should still be seen in the flux. Permeance effects will be less significant and the harmonic amplitude will increase with load, due to the MMF interaction effects. Skewing results in rotor bars not being parallel to the machine shaft and introduces a phase shift into the flux density distribution. Again, both machines used in this work were chosen to be practically typical and not to maximise RSH trackability, both having closed and skewed slots.

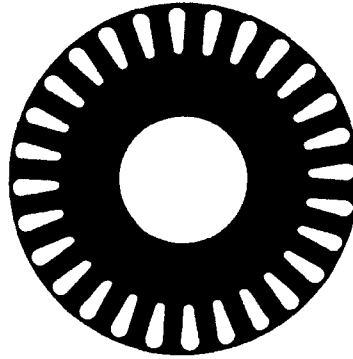


Figure 5.1. Rotor lamination from a 1.5kW machine with a closed 28-slot rotor

Other speed related harmonics will exist, due to rotor eccentricity for example, and are used to obtain speed information in [108]. These effects are not considered in this work, as it is believed that the best natural speed estimate will be obtained from RSH effects. This is unless methods such as signal injection are used to particularly promote other harmonics, as eccentricity effects tend to require some form of excitation to improve the signal to noise ratio.

When feeding the induction motor from an inverter, frequencies that are harmonics of the fundamental will be applied to the machine, due to the non-ideal nature of the supply. Higher order time harmonics are produced in the airgap flux, together with space harmonics that are due to machine design, saturation effects, etc. PWM frequencies exist according to equation 5.2.

$$f_{pwm} = f_e + \sum_{k=1,2,..} (6k \pm 1) f_e \quad (5.2)$$

Rotor slotting is also discrete (squarewave) in nature and thus higher order RSH components will exist. Equation 5.1 is modified to include these considerations, as is

shown in equation 5.3. The  $\nu$  and  $\kappa$  terms are used to show that higher order slotting effects and higher order MMF effects appear in terminal quantities.

$$f_{sh} = \nu \frac{z}{p} f_r \pm \kappa f_e \quad (5.3)$$

where  $\nu = 1, 2, 3 \dots$

$\kappa = 1, 2, 3 \dots$  (although not all effects will be present/detectable)

The higher order slotting effects will be low in magnitude and  $\nu=1$  will therefore be assumed from this point on. The higher order MMF effects will be due to machine design, magnetic saturation and inverter harmonics, as previously mentioned. RSH harmonics due to  $\kappa>1$  are exploited in this work.

### 5.2.2 RSH Harmonics in Motor Terminal Quantities

As well as producing other RSH frequencies, the PWM harmonics of equation 5.2 must be considered with regard to RSH tracking. Measured stator quantities will contain PWM harmonic components and RSH components. Both obey similar existence criteria:

- PWM harmonics exist for odd, non-triplen, multiples of  $f_e$
- RSH components exist for odd, non-triplen, values of  $z/p \pm \kappa$

The RSH equation, 5.3, can be re-written as shown in equation 5.4.

$$f_{sh} = \left( \frac{z}{p} \pm \kappa \right) f_e - \frac{z}{p} f_{slip} \quad (5.4)$$

At low-loads, where the motor slip is small (approaching zero), a particular RSH harmonic will exist in close proximity to an inverter harmonic. In the case of the closed and skewed slot motors used in this work, the RSH will also be low in amplitude at this low load. A robust/reliable RSH estimation technique must therefore be able to resolve between these two components for correct estimation. As an example, where  $f_e=50\text{Hz}$  and the motor is running at synchronous speed (slip=0), the most significant slot harmonic, corresponding to  $\kappa=-1$ , will exist at 650Hz for

both machines used in this work. Slot harmonic effects follow the same existence criteria as the inverter harmonics and thus the RSH is aligned with the 13<sup>th</sup> inverter harmonic.

At high-loads, where the motor slip is larger, the RSH will have increased in amplitude and have moved away from the associated inverter harmonic. However, as the RSH moves it may then contact lower order PWM harmonics. Note that, for a particular value of slip, the RSH will always be a particular distance away from (and lower than for motoring operation) the associated no-load PWM harmonic and this does not vary with  $f_e$ . This 'contact' problem is therefore more significant at low speed/low excitation frequency, when the PWM harmonic spread is tighter. Again the robustness and reliability of a tracking algorithm may be compromised where the RSH is in close proximity to a PWM harmonic. Two examples help to illustrate these points. Again, if the induction motor is running with  $f_e=50\text{Hz}$  and fully loaded (say slip=1.5Hz), then the RSH associated with  $k=-1$  exists at 629Hz, as opposed to the 13<sup>th</sup> inverter harmonic, which is still at 650Hz. However, for  $f_e=10.5\text{Hz}$  the full load slip is still 1.5Hz, the RSH exists at 115.5Hz and this is the same frequency as the 11<sup>th</sup> inverter harmonic.

Some help can be given to the algorithm by appropriately choosing an input quantity. Equation 5.4 can be rearranged and, by dividing both sides by  $f_e$ , can be used to determine at what speed the RSH will contact the next lowest PWM harmonic at full load. At higher speeds the RSH will not contact any PWM harmonics over the full rated load range. At lower speeds the RSH will, of course, contact the PWM harmonic at a lower load than fully rated.

### **RSH and PWM Components in $I_a$**

Figure 5.2 shows the frequency spectrum of a single measured line current ( $I_a$ ), from rig A, for four operating conditions. A suitable batch of data was captured from the rig, whilst running encoded IRFO, and an FFT performed off-line in Matlab. The batch corresponds to 1000 samples captured over 10 complete cycles of the fundamental frequency. The FFT therefore has a resolution of  $1/10 f_e$  and data is illustrated in terms of the fundamental harmonic number (0 to 20).

In all the spectral figures the key shown in table 5.1 indicates how the inverter and RSH harmonics are distinguished.



Inverter Harmonic	-----
Rotor Slot Harmonic	-----

Table 5.1 Key to the marking of the FFT plots of motor terminal quantities

The four operating conditions are 100rpm with a small load, 100rpm fully loaded, 1000rpm with a small load and 1000rpm fully loaded. The small load value was set such that the RSH could just be distinguished from the associated no load PWM harmonic at 1000rpm, with the particular FFT resolution used. The same value of load torque was used at the lower speed also.

The expected inverter harmonics can be clearly observed in all four plots, up to and including the 19<sup>th</sup>. RSH components are clearly evident on the two 1000rpm plots, where the  $\kappa = -1$  and  $+3$  components are observed to be particularly strong and of a larger amplitude than the associated 13<sup>th</sup> and 17<sup>th</sup> PWM harmonics.

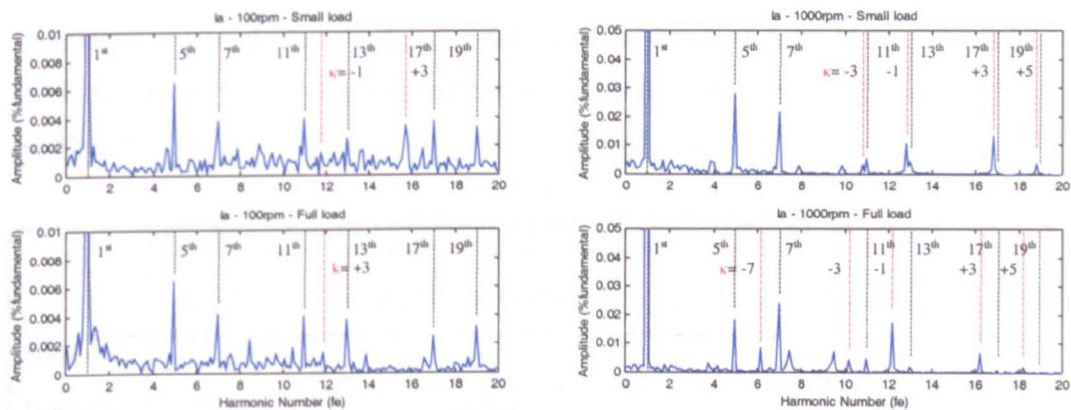


Figure 5.2. FFTs of  $I_a$ , captured from rig A at 100rpm and 1000rpm

The RSH components in the lower speed plots are very difficult to spot relative to the associated noise, even at higher loads. Principally this is due to the action of the current controllers. In a V/F drive, where there are no controllers, the RSH effects should always be more strongly noticeable in stator current. Here the V/F scheme imposes stator voltages in an open-loop fashion and, as the inverter output impedance will be low, slot harmonic effects will mainly affect the stator currents. Where current controllers are present, the RSH effects seen in the stator currents will be acted on (attenuated) by the current controllers. The result will be an increase in RSH amplitude in stator voltages. The inverter is now considered as a current source. At higher speeds the RSH frequencies encountered, in the drive rigs used in this project,

are higher than the designed current controller bandwidth. At lower speeds the RSH components, when within the controller bandwidth, are severely attenuated. At these lower speeds it would perhaps be beneficial to track RSH components in measured voltage. However, it must be remembered that PWM components in voltage are somewhat more severe, as the induction motor filters the PWM effects in current. Note that the current controllers cannot act to reduce PWM harmonic effects, because it is the action of the current controller output quantity (voltage  $V^*$ ) that creates them. PWM effects would be reduced with a higher switching frequency, but here the switching frequency was chosen to be practically typical and to allow the control of both motor drives on the particular processing platform used.

As previously mentioned, it is also a concern as to how much frequency space the RSH has in which to travel, as the machine is loaded, before contacting the next lowest inverter harmonic. This can be calculated by rearranging equation 5.4 and is shown in table 5.2 for the 2 drives. If the  $\kappa = -1$  RSH (aligned with the 13<sup>th</sup> inverter harmonic at no load) is tracked in each drive, the 11<sup>th</sup> harmonic will be next contacted, at a particular speed and at full load, and this is shown. If the 17<sup>th</sup> related RSH is tracked, then more frequency space is available before the RSH comes into contact with the 13<sup>th</sup> PWM harmonic ( $4f_c$  as opposed to  $2f_c$ ).

	Full-Load Slip	Speed $\kappa = -1$ RSH Coincides with 11 <sup>th</sup> PWM Harmonic	Speed $\kappa = +3$ RSH Coincides with 13 <sup>th</sup> PWM Harmonic
Drive A	1.72Hz	310rpm	129rpm
Drive B	2.16Hz	389rpm	162rpm

Table 5.2 Where RSH harmonics for  $\kappa = -1$  and  $+3$  coincide with next lowest PWM harmonics

It can be seen that, although the  $\kappa = +3$  RSH is a higher order than the fundamental  $\kappa = -1$  RSH, it offers the advantage of possibly being tracked to a lower speed, before becoming confused with the lower order PWM harmonics.

**RSH and PWM Components in  $|I|$**

Manipulated quantities that are used within the vector control scheme also contain RSH information. Most notably, the rotating current vector magnitude can be used. Although perhaps not calculated for control purposes,  $|I|$  is simply evaluated from

measured  $I_d$  and  $I_q$ , as shown in equation 5.5. Also, the square root does not require to be evaluated if the quantity is used for spectral information only.

$$|I| = \sqrt{I_d^2 + I_q^2} \quad (5.5)$$

The frequency spectrum plots are repeated, for the same speed and load conditions as previously shown, for the quantity  $|I|$  in figure 5.3.

Being a vector magnitude,  $|I|$  is a dc quantity in the steady state. The plots show the harmonic content and have been normalised to the dc average (not shown). The PWM harmonics appear in this quantity at multiples of 6 times the fundamental. RSH harmonics exist in similar positions at no load, again moving away from the PWM harmonics as load increases. The fundamental RSH component in this quantity is associated with the 12<sup>th</sup> PWM harmonic ( $\kappa = -2$ ).

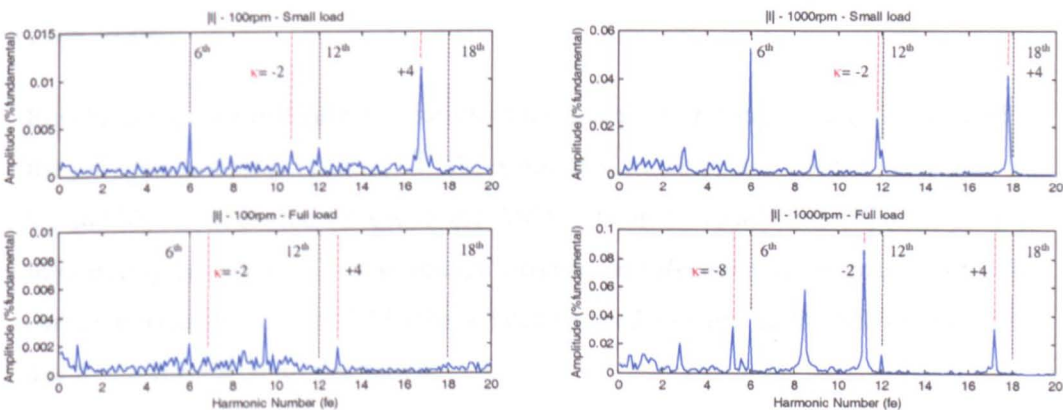


Figure 5.3. FFTs of  $|I|$ , captured from rig A at 100rpm and 1000rpm

At the higher speed, the  $\kappa = -2$  and  $+4$  RSH components are clearly seen and are suitably high in amplitude to be distinguished from the PWM effects. At low speed the RSH components are certainly more evident than they were in  $I_a$ , but are still difficult to pick out from harmonic noise. At low load the  $\kappa = +4$  harmonic is surprisingly evident however. A similar effect was seen in figure 5.2, where the 17<sup>th</sup> related RSH component was relatively high in amplitude, and this is thought to be due to third harmonic components in the airgap flux due to machine design/magnetising effects [103].

One of the big advantages of tracking RSH effects in this quantity is the amount of frequency space available to the RSH components, in which to move, before contacting a lower order PWM harmonic. Table 5.3 shows the speeds at which the RSH components in the two drives will coincide with the lower order PWM harmonics. This is the same if tracking for  $\kappa = -2$  or  $+4$ , as both are able to move  $6f_e$  from the 12<sup>th</sup> and 18<sup>th</sup> PWM harmonics before coinciding with the 6<sup>th</sup> and 12<sup>th</sup> respectively.

	Full-Load Slip	Speed RSH Component Coincides with Next Lowest $6xf_e$ PWM Harmonic
Drive A	1.72Hz	69rpm
Drive B	1.9Hz	75rpm

Table 5.3 Where RSH harmonics coincide with next lowest PWM harmonic

RSH and PWM Components in Current Controller Output  $|V^*|$  for use at Low Speed

Results are shown in figure 5.4, for the same speed and loading conditions as used in the previous two sections, for  $|V^*|$ .  $|V|$  is not used in the vector control process at all.  $V_\alpha$  and  $V_\beta$  are measured for use in the ASO and can be turned into  $|V|$  quite simply. Importantly however,  $|V^*|$  (the voltage magnitude **reference** value passed from the current controllers to the PWM scheme) can be used, conveying the RSH information due to the current controller action.

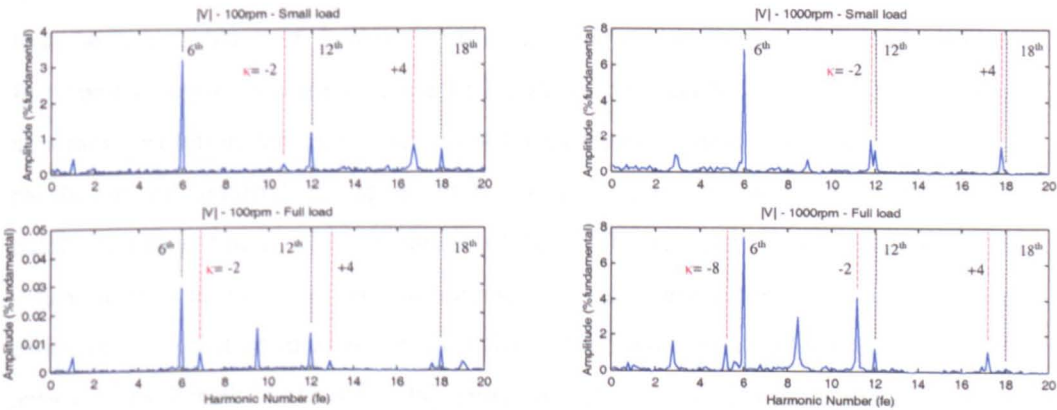


Figure 5.4. FFTs of  $|V^*|$ , captured from rig A at 100rpm and 1000rpm

Note that now, although the PWM components are larger than in  $|I|$  with respect to the dc fundamental, the RSH components are much more discernible. At the low



speed of 100rpm the RSH components can be clearly identified and should be trackable with a suitable signal processing method. The scheme described in the next section therefore makes use of  $|V^*|$  at lower speed.

### **5.2.3 RSH Tracking**

Interest in obtaining speed information from RSH effects dates back as far as the early 1980s [116]. Analogue techniques were utilised to obtain slip frequency information by Ishida et al [116]. Williams modified the technique, using measurement of the dc link voltage and switched capacitor filters [117]. Zinger et al proposed the use of a Phase Locked Loop (PLL) approach, but this required a modified machine [13]. The performance of these methods is limited by their analogue nature and particularly with regard to accuracy and speed range.

Digital signal processing techniques have since been utilised for RSH speed tracking, using measurement of stator current [28, 102-114]. Digital methods offer advantages, as discussed in chapter 2 with regard to Digital Signal Processors (DSP), such as increased accuracy and flexibility. Methods are not subject to analogue tolerances and drift of components, parameters can be varied in real-time and advanced methods can be used.

Primarily this work has been based on use of the Fast Fourier Transform (FFT) [28, 102-109], the batch sampling technique used to obtain the previous spectral figures. The FFT approach provides much improved accuracy and an extended speed range, when compared with the analogue methods. The main restriction in using the FFT is that, because a batch of data is required, its dynamic performance is quite limited. For good dynamic performance the FFT data batch must be short and for increased accuracy/resolution the data batch must be extended. Ideally, where accuracy and resolution are required, the speed of the motor should remain constant during the batch sampling time. The advantage of the FFT approach is in it also returning information relating to other harmonics. To turn the information into a speed estimate an algorithm must select the RSH. Much work was undertaken on the FFT approach by Ferrah [103, 105, 106], Hurst and Habetler [102, 107], and Blasco [28, 49, 104, 109]. The work of Ferrah [103], and Hurst and Habetler [102], includes initialisation procedures used to determine necessary algorithm parameters, such as the number of rotor slots. Blasco used an FFT derived speed estimate to tune  $T_r$  in a sensorless drive [28, 49, 104, 109].

Ferrah [110-114], and Hurst and Habetler [108], extended their respective works, to propose alternative spectral analysis methods to track RSH effects for speed estimation. This was in an attempt to overcome the dynamic limitations of the FFT, which are due to both its batch nature and its computational requirements. In 1996 Ferrah presented a method, based on Fast Recursive Least-Square (FRLS) predictive adaptive filtering [111], quoted to outperform the FFT, in terms of updating the estimated speed, by a factor of approximately 15:1 [112]. The update time for this method was quoted as 4ms at a 5kHz sampling rate, but the accuracy was not as good as using an interpolated FFT method [112].

Later the same year Ferrah et al proposed an RSH identifier based on the Recursive Maximum Likelihood – Adaptive Tracking Filter [112, 113]. The method was found to be highly computationally efficient, offering good accuracy, achieving a quoted speed update of 0.2ms at a 5kHz sampling rate [112, 113]. The high dynamic performance is due to its recursive nature of the method, but, for reasons that will shortly be established, this nature means that any other harmonics in the input must be appreciated before the RSH identifier, rather than afterwards (in the FFT). This project considers the development of the RML-ATF into a full sensorless speed estimator. The use of the input quantities considered previously is incorporated, as is modified input pre-filtering, these are not previously considered in other works. The developed method works with the sensorless model based ASO method to form a hybrid sensorless drive for accurate speed holding.

### **5.3 The Adaptive Tracking Speed Estimator (ATSE)**

The speed estimate based on RSH effects is obtained using a signal-processing system of several stages. The system is based on recursive, adaptive filtering techniques that are eminently suited to digital implementation on a DSP [118]. The RML-ATF algorithm is used to obtain the estimate of RSH frequency, but it is necessary to select and pre-filter the input quantity before the application of this algorithm. Pre-filtering is set-up using knowledge of rotor slot number, motor pole number, fundamental excitation frequency and an initial guess at the motor speed. The RSH estimate then returned by the RML-ATF is turned into a more accurate value of motor speed (than the original guess), also through knowledge of slot number, pole number and fundamental frequency.

The various stages of the estimator algorithm are presented, in the order that they are applied, in the following sections. The complete system is termed the Adaptive Tracking Speed Estimator (ATSE) and can be seen, presented in block diagram format, in section 5.3.6.

### **5.3.1 Input Selection**

For the tuning sensorless drive system, the relevant RSH is tracked in  $|I|$  and  $|V^*|$  quantities. These were shown in section 5.2 to offer advantages over the tracking of RSH effects in a single measured stator current. In these quantities the RSH amplitude, when compared to PWM harmonics, is suitable for tracking and the full load operating speed, before the RSH coincides with a PWM harmonic, is minimised. The former of these advantages will allow good RML-ATF tracking performance. The latter increases the speed range in which the algorithm can be successfully applied. The applicable speed range is thus similar to that offering good performance from the model-based implementation, as shown in the previous chapter.

It was also noted and discussed, in section 5.2, that tracking RSH effects in  $|V^*|$  at lower speeds, where the RSH frequency approaches and is within the bandwidth of the current controllers, may improve the system robustness. Whilst PWM harmonics are more significant in voltage quantities than in current quantities, the current controllers act to attenuate the RSH effects appearing in  $|I|$  in the lower speed region. This attenuation of the RSH effects in  $|I|$  results in an increase in RSH amplitude in  $|V^*|$ . Hence it is appropriate to use  $|V^*|$  at lower speed. The important point here is that the voltage is not measured for use in this system.  $|V^*|$ , the reference value feeding the PWM routines from the current controllers, is used.

The designed system uses both  $|I|$  and  $|V^*|$  as inputs to the ATSE with a changeover mechanism.  $|V^*|$  is used at speeds where the RSH is near and within the designed current control bandwidth and  $|I|$  is used at speeds above this. The ASO speed estimate is used to determine which input to use, although excitation frequency would also be applicable, and hysteresis is included in the changeover mechanism. More precisely, for an increasing speed the input changes from  $|V^*|$  to  $|I|$  at 420 rpm. For a decreasing speed the input changes from  $|I|$  to  $|V^*|$  at 360 rpm. At these speeds the rotor slot harmonic to be tracked will be at a little above 100Hz, this is the designed bandwidth of the current controllers. Similar specifications are applied to both rigs. Changing the input produces an immediate change in amplitude seen by the following

stages of the system. An estimation glitch filters through the ATSE system, but this is momentary and does not affect the tuning system (to be presented in section 5.5). The tuning is not affected, because the drive is in the transitory state (tuning is disabled) and because the glitch disappears at a rate that is much faster than the tuning dynamics. This effect will be seen in the results sections of this chapter.

As well as varying the input quantity, the harmonic tracked within the particular quantity is also varied and so is the ATSE sample frequency. Both these changes are effected under the control of the input changeover mechanism. When tracking in  $|I|$  the  $\alpha=-2$  harmonic is tracked as this is the fundamental RSH effect. In the speed range where  $|V^*|$  is used, the  $\alpha=+4$  harmonic is tracked, because the Signal to Noise Ratio (SNR) is higher in the higher order RSH range. The sample frequency is varied at this point because it is a convenient opportunity to do so. Having a suitable sample frequency is important in recursive signal-processing techniques [118]. Although a minimum sample frequency is required for digital filter operation [118], too high a frequency would also be inappropriate. Similar to the sampling of an encoder, where a high sample rate will give poor speed resolution, too high a sample rate for the filter algorithms used here will produce output resolution and noise problems [118]. In this work a 4kHz sample rate is used at higher speed, where  $|I|$  is the system input, and 2kHz is used where  $|V^*|$  is the system input. It is convenient to use sample frequencies that are related to the DSP interrupt/PWM switching frequencies. For correct operation of the discretised bandpass filter, which forms the next stage of the circuit, four times the maximum input frequency must be used for correct operation. The maximum RSH frequency is 650Hz, for rated synchronous speed, so 4kHz is used at the higher speeds. The algorithm steps the sample frequency down to the next most appropriate level to cover the low speed range, this being 2kHz.

### **5.3.2 Bandpass Pre-Filter**

After appropriate input selection, the next stage of the ATSE involves bandpass filtering the input quantity. The filter is centred around the estimated slot harmonic to be tracked. The centre frequency is obtained by using equation 5.3, with speed estimated by the ASO and excitation frequency obtained through the differentiation of the DRFO flux angle; i.e. both quantities are obtained from the model based sensorless system.



The RSH frequency is identified by the RML-ATF on the assumption that it is the strongest harmonic component in the input quantity. The bandpass filter (BPF) is therefore necessary to minimise the effects of other harmonics, most notably the fundamental and inverter PWM harmonics. These harmonics were shown to be similar in amplitude to the RSH and greater for low load conditions in measured  $I_a$ . Although these effects are reduced by selection of an appropriate input variable, such as those used here. If the PWM harmonics are strong in the input quantity passed to the RML-ATF the algorithm will be confused and possibly track them instead of the RSH. Certainly the speed estimate noise level will increase where PWM harmonics exist and the speed accuracy may be compromised, depending on the operating condition. The implemented BPF is based on the s-domain transfer function shown in equation 5.6

$$TF = \frac{2\zeta\omega_n s}{s^2 + 2\zeta\omega_n s + \omega_n^2} \quad (5.6)$$

where,

$$\omega_n = 2\pi f_{centre} = \text{BPF centre frequency} \quad (5.7)$$

$$\zeta = \omega_{bw}/2\omega_n = \text{BPF damping factor } (\omega_{bw} \text{ is the filter bandwidth}) \quad (5.8)$$

The filter is discretised using the bi-linear transform, as used before to discretise the speed and current control laws shown in chapter 4. This method is presented in texts on control and signal-processing theory [98]. However, due to the effects of the digitisation, the centre frequency of the BPF described by 5.7 will not be entirely accurate. The accuracy is improved by pre-warping [95] the sample period used in the filter coefficient calculations and this is calculated as shown in equation 5.9

$$t_s^{warped} = \tan(\pi f_{centre}/f_{sample})/(\pi f_{centre}) \quad (5.9)$$

This is an adaptive filter algorithm, filter parameters are recalculated on a per-sample basis, as the centre frequency must be varied. The damping factor is held at a constant value and this has the beneficial effect of narrowing the filter bandwidth as the centre frequency decreases. The PWM harmonic spread tightens as the fundamental frequency reduces and narrowing of the filter bandwidth allows it to

more selectively pick out the RSH at lower speed; this will increase the importance of an accurate centre frequency estimate however. In this work  $\zeta$  is set, as suggested in [119], such that the bandwidth is equal to  $f_c$  for a given no-load centre frequency. The bandwidth allows the RSH to be seen in the filter output, given an error in BPF centre, and where the RSH will move during transients.

A filter response is made more ideal by increasing the filter order and this can be achieved by cascading lower order filters. Note that this increases the processing time, but can be achieved by only calculating filter coefficients once. The BPF used in this work is 2<sup>nd</sup> order.

### **5.3.3 Notch Pre-Filtering to Selectively Eliminate PWM Harmonics**

The ATSE algorithm tracking performance is improved if, as well as bandpass filtering, selected inverter harmonics are removed using narrow-band notch filters. This technique was first suggested in a previous paper by the author, where the ATSE technique was applied to speed trim a V/F drive (this is included as Appendix A) [14]. The excitation frequency must be known to centre the BPF and to calculate speed from the RSH estimate. It can therefore be used to centre notch filters to eliminate the 6<sup>th</sup>, 12<sup>th</sup> and 18<sup>th</sup> PWM associated harmonics in the 2 input quantities used. The transfer function of the filter is the same as that utilised in the RML-ATF algorithm and is presented in the next section (equation 5.10).

The elimination of these PWM harmonics is particularly beneficial at low load. In section 5.2 it was shown that RSH existence criteria is the same as that for PWM harmonics. At low load the RSH exists at a frequency very close to an inverter harmonic. If the motor operates at synchronous speed, the RSH and PWM harmonic coincide and would be difficult to distinguish or track with any spectral analysis technique (without using impractically high resolution). Fortunately, at natural no-load (due to windage and friction) for the 2 machines used in this work, the RSH is sufficiently far away from the associated PWM harmonic for reasonable tracking performance and far enough away to allow a narrow notch filter eliminating the PWM harmonic to be applied. The notch filters used were of 1Hz bandwidth. As load is increased the notch filter is still used, but becomes insignificant. The RSH moves away from the PWM harmonic under these conditions.

### 5.3.4 RML-ATF (RSH Estimator)

The RML-ATF algorithm is an adaptive signal processing technique, in this case based around a 2<sup>nd</sup> order digital notch filter. The common use of notch filtering, to eliminate known, fixed frequency, narrow band, unwanted components, has been shown in section 5.3.3. Other examples would include elimination of mains induced noise in biomedical instrumentation and various applications in communications and radar, etc [118]. Here the RML-ATF technique is used to eliminate a component whose frequency is not explicitly known. The output of the notch, with the RSH component hopefully eliminated, is not then used (other than in the recursive elimination process for subsequent samples). Here the RSH elimination allows us to obtain, from the centre frequency of the notch, an estimate of the RSH frequency. The statistical Maximum Likelihood Method [120, 121] is used to update the notch filter parameter directly relating to the centre frequency at each sampling instant.

The general method has been presented in papers appearing in relevant signal processing publications, with a view to general sinusoid parameter (frequency) identification [120, 121]. It was first applied to RSH estimation in motor drives by Ferrah [112, 113] and a subsequent paper was published that tested the method on induction machines with varying design specifications [114]. The conclusion of this work indicated the excellent performance of the algorithm and although, as would be expected from any harmonic identification method, the technique performed best on machines with open and unskewed slots, operation on closed and skewed slot machines was also demonstrated.

This section details the algorithm as applied in this work. The notch filter used has the z-domain transfer function defined by equation 5.10

$$TF = \frac{1 + \theta z^{-1} + z^{-2}}{1 + r \theta z^{-1} + r^2 z^{-2}} \quad (5.10)$$

The difference equation for the filter, simply formed from 5.10 (where z is the delay operator), is shown in equation 5.11

$$o/p(k) = i/p(k) + \theta i/p(k-1) + i/p(k-2) - r \theta o/p(k-1) - r^2 o/p(k-2) \quad (5.11)$$

The centre frequency of the notch filter is related to  $\theta$  as shown in equation 5.12

$$f_{centre} = \frac{1}{2\pi} \cos^{-1}\left(\frac{-\theta}{2}\right) f_{samp} \quad (5.12)$$

The notch filter bandwidth is related to the parameter  $r$  as shown in equation 5.13

$$f_{bw} = \frac{1}{2} (1 - r) f_{samp} \quad (5.13)$$

In the algorithm  $\theta$  is therefore the parameter adjusted such that the notch filter will cancel out the strongest harmonic component seen in the input. Mathematically the RML adjusts  $\theta$  to minimise the cost function shown in equation 5.14

$$J(k) = \sum_{k=1}^N \lambda^{N-k} o/p^2(k) \quad (5.14)$$

It is clear that minimisation of  $J(k)$  will effectively be minimising the output of the notch filter, thus cancelling the strongest input component. Note that two variables have been introduced, in the above equations, that must be set and/or controlled, these being  $r(k)$  and  $\lambda(k)$ . As previously mentioned,  $r(k)$  controls the notch filter bandwidth.  $\lambda(k)$  weights the significance of previous samples used in the minimisation process. Both parameters can vary between 0 and 1 and have the following effects.

- For  $r(k)=1$  the notch bandwidth is infinitely narrow
- For  $r(k)=0$  the notch bandwidth is half the sample frequency
- For  $\lambda(k)=1$  all  $N$  previous values are taken into account in the algorithm
- For  $\lambda(k)=0$  no weight is given to previous values in the algorithm

These parameters will effect the dynamics and accuracy of the RSH tracking. In this work both were set to fixed values of 0.97. Whilst other work has considered the variation of these parameters depending on drive conditions [14, 112-114, 119], this would be difficult to manage and may degrade the algorithm robustness. Those values used are sufficient to tune each drive in the steady state, for encoder like

accuracy and stability, and provide sufficient dynamic performance, to track during speed varying conditions and tune immediately that a steady state operating condition is reached [119]. The tracking dynamics need only to be sufficiently faster than the tuning dynamics.

The algorithm is implemented digitally, according to the above theory, as presented below. At each sample point the RML-ATF algorithm firstly calculates the notch filter output, with a new value of input, at the present estimated notch centre frequency. This is as shown in equation 5.15

$$\overline{o/p(k)} = i/p(k) + \theta(k-1)i/p(k-1) + i/p(k-2) - r(k)\theta(k-1)o/p(k-1) - r^2(k)o/p(k-2) \quad (5.15)$$

Note the use of the current input  $i/p(k)$ , but the previous value of centre frequency  $\theta(k-1)$ . The algorithm then adjusts the notch centre frequency as necessary to minimise the output, using equation 5.16

$$\theta(k) = \theta(k-1) + P(k)\varphi(k)\overline{o/p(k)} \quad (5.16)$$

where

$$\varphi(k) = -i/p(k-1) + r(k)o/p(k-1) - r(k)\theta(k-1)\varphi(k-1) - r^2(k)\varphi(k-2) \quad (5.17)$$

$$P(k) = \frac{P(k-1)}{\lambda(k) + P(k-1)\varphi^2(k)} \quad (5.18)$$

Based on previous values,  $\varphi(k)$  is a signed measure of the difference between filter input and output. It is larger if the input is inside the notch and negative if the input frequency is greater than the notch centre.  $P(k)$  is the covariance of  $\theta(k)$  and note that it is directly affected by  $\lambda(k)$  and  $\varphi(k)$ . High values of  $\lambda(k)$  and  $\varphi(k)$  reduce  $P(k)$  and thus the centre estimate adjustment of equation 5.16 is less significant.

The output is next recalculated using the new value of notch centre frequency, as shown in equation 5.19

$$o/p(k) = i/p(k) + \theta(k)i/p(k-1) + i/p(k-2) - r(k)\theta(k)o/p(k-1) - r^2(k)o/p(k-2) \quad (5.19)$$

Assuming, through having bandpass filtered the input around the crudely estimated RSH prior to applying the RML-ATF algorithm, that the RSH was the strongest harmonic component in the algorithm input,  $\theta$  now directly relates to the RSH frequency. The frequency is obtained by applying the relationship shown in equation 5.12.

### 5.3.5 Calculating the Motor Speed

The motor speed is calculated from the RSH estimate by rearranging equation 5.3. It is effectively the inverse process of that used to centre the BPF pre-filter and is shown below in equation 5.20

$$f_r = \frac{p}{z} (f_{sh} \pm \kappa f_e) \quad (5.20)$$

This is the general equation where  $\pm\kappa$  depends on which input quantity is fed into the ATSE algorithm and hence which slot harmonic effect was tracked.

Note that, assuming a highly accurate slot harmonic frequency has been obtained, the speed calculation is directly affected by error and noise in  $f_e$ . The values of  $z$  and  $p$  are fixed mechanical motor quantities and therefore, for a high quality speed estimate, the  $f_e$  estimate/measure should be as accurate and noise free as possible. For use in V/F and IRFO drives  $f_e$  is applied and therefore explicitly available. For the sensorless DRFO scheme  $f_e$  is obtained by differentiating the rotor flux angle and then filtered to reduce the noise level. It is possible to use a second RML-ATF to identify  $f_e$ , as proposed in [122]. However, whilst the algorithm is not considered computationally intensive, neither is it trivial and it is suggested that the increased system complexity may affect the robustness. This work found  $f_e$  obtained from the differentiated and filtered rotor flux angle to be perfectly adequate for application of the tuning system.

In order to give the ATSE speed estimate the correct sign, as the RSH information contains no directional information, the sign of the ASO estimated speed is applied. The RSH estimate degrades substantially at very low speed, so as not to be applicable for tuning purposes in this region and this will be discussed in following sections.

The ASO speed estimate is suitably accurate in terms of its directional information, because the scheme will not be used for absolute speed estimation about zero speed.

### 5.3.6 The Complete ATSE System

The component parts of the ATSE, described in the previous five sections, are shown in the block diagram representation of figure 5.5.

Not shown is that the input selector also controls the system sample frequency and  $\kappa$  used in the RSH related equations.

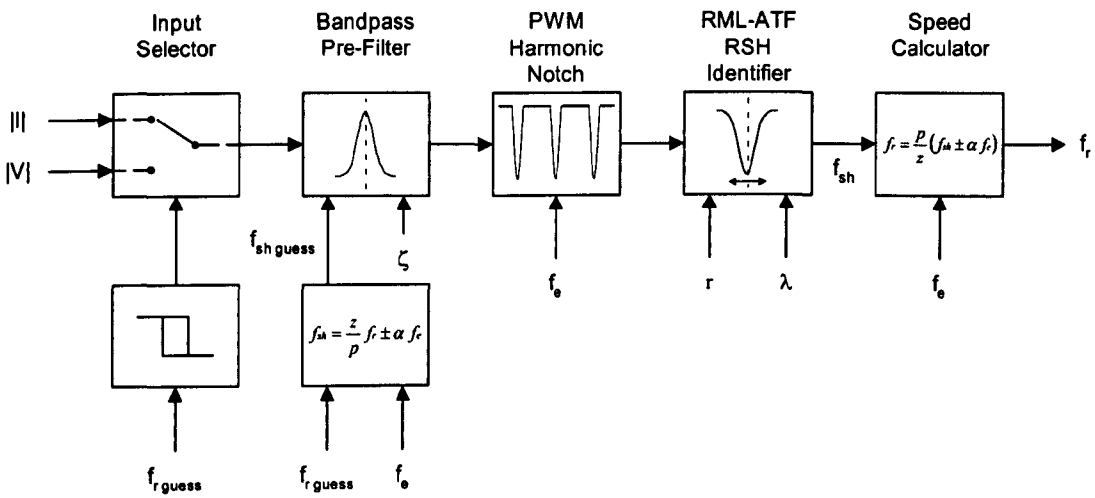


Figure 5.5 Block diagram of the Adaptive Tracking Speed Estimator (ATSE)

The system performance is reviewed in section 5.4, where results from the system will be presented. It must however, be remembered that if comparing the ATSE system to a batch frequency estimation technique, such as an FFT based algorithm, the developed system obtains high dynamic performance from its continuous, recursive nature. The individual filter implementations are based on Infinite Impulse Response (IIR) digital representations of analogue equivalents. However, because the filters are adaptive (the filter parameters vary on a per sample basis) the system is eminently suited to a digital implementation and would be difficult to implement in an analogue fashion. Due to this continuous implementation the algorithm does therefore rely on the described input selection and pre-filtering, applied before the RML-ATF RSH identifier. The pre-filtering is applied such that the input quantity to the RSH identifying section contains an RSH as the largest harmonic component. This being the case, the RML-ATF returns an RSH frequency estimate, the accuracy

and resolution of which is ideally dependent upon the parameters  $r(k)$  and  $\lambda(k)$ . With an FFT implementation, the limiting factors are firstly that a batch of data is required, and secondly that the algorithm is computationally intensive. As such a speed estimate cannot readily be achieved in the dynamic state. To obtain a high accuracy and resolution the batch of data captured must be increased. The advantage with an FFT type approach is, of course, that while what may seem like redundant information is captured, PWM information is inherently available. A search algorithm, knowing where PWM harmonics will exist, can possibly obtain a good RSH estimate where the RSH amplitude is of a similar order to noise harmonics and smaller than nearby PWM effects.

5.4 ATSE Performance Analysis

In this section the performance of the ATSE speed estimator is demonstrated. Prior to using the ATSE estimate to tune the Adaptive Speed Observer (ASO) based sensorless implementation, the results shown here demonstrate the tracking performance of the ATSE applied as an observer of speed in the untuned ASO sensorless implementation. The algorithm is tested for a variety of speed and load conditions. The rotor time constant ( $T_r$ ) and stator resistance ( $R_s$ ) used in the ASO scheme are not optimised, and in some cases purposefully detuned, to show that the ATSE still tracks real speed. At the end of this section the region of reliable ATSE operation is defined.

Where speed measures and estimates are shown in this section (and in section 5.6), unless otherwise stated, the colour coding key shown in table 5.4 is used.

Encoder Measured Speed	_____
ASO Estimated Speed	_____
ATSE Estimated Speed	_____

Table 5.4. Key to speed measures/estimates shown in figures (unless otherwise stated)

5.4.1 ATSE Steady State Tracking Performance

Figure 5.6 demonstrates both rig A (upper trace) and rig B (lower trace) running at a demanded speed of 300rpm in the sensorless mode. In both traces the speed is shown measured by the encoder and estimated by the ASO and ATSE schemes. Note that the speed loop has acted to reduce the average error between the reference and ASO



estimated speed to zero. The true speed however, is in error by around 10rpm. The error is due to an intentional detuning of the  $T_r$  value, by some 25% of that quoted in chapter 3. Each drive is running at  $\frac{1}{2}$  rated  $I_q$ .

Note that encoder measured and ATSE estimated speeds show an excellent match, thus demonstrating the ability of the ATSE to provide a highly accurate speed estimate. It is also necessary to realise that the erroneous ASO measured speed is used in the ATSE algorithm to centre the BPF pre-filter. This being the case, the returned value of speed is still a close match to that of the real machine. The effect of the BPF being centred with some error is evident on the upper trace, by the noise level on the ATSE estimate being somewhat more than the resolution of the encoder measurement, and on the lower trace, by the slight under estimate on the average ATSE speed. In the full tuning system, where the BPF centre estimate will be improved by the tuning, the ATSE estimate noise/resolution will be improved and the average estimate error reduced.

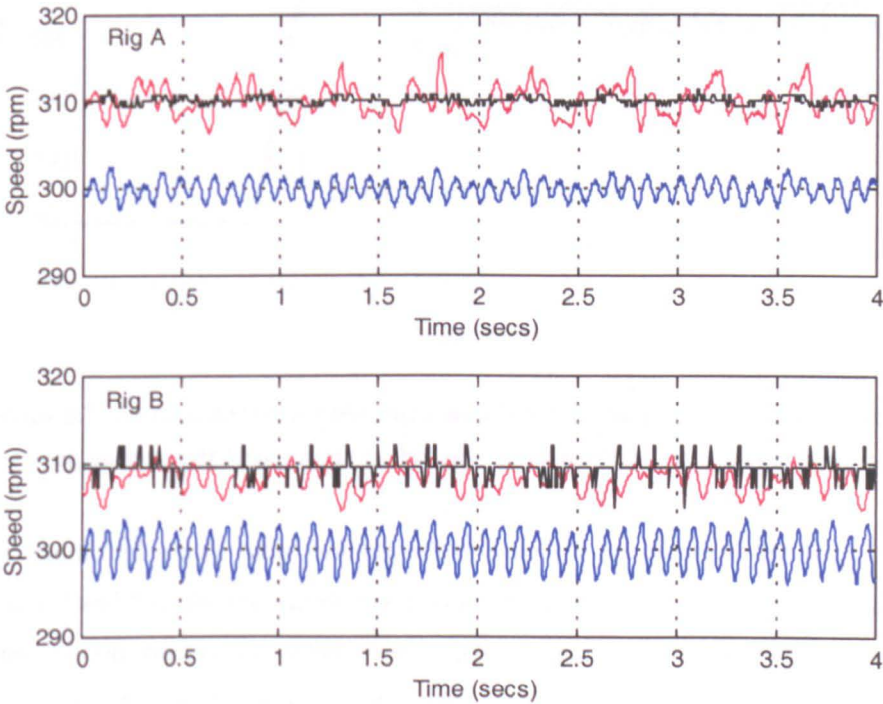


Figure 5.6. Encoder (measured), ASO and ATSE (estimated) speeds from both rigs running at a steady 300rpm under  $\frac{1}{2}$  rated load. Drives are operating under detuned ASO sensorless control

5.4.2 ATSE Speed Transient Tracking Performance

Figures 5.7 and 5.8 show the ASO system performing speed transients from 200rpm to 1000rpm, under  $\frac{1}{4}$  rated load, for rig A and rig B respectively. The value of  $T_r$  is

adjusted at 200rpm for zero average speed error on the sensorless system. This will therefore account for small errors on  $R_s$  and the inductance parameters that have not been tuned.

The estimated ATSE speed is seen to track the real speed with good dynamic performance. This is without any form of RML-ATF parameter management, as mentioned previously. A glitch can be seen in the ATSE estimated speed where the sample frequency and input quantity to the algorithm are both changed.

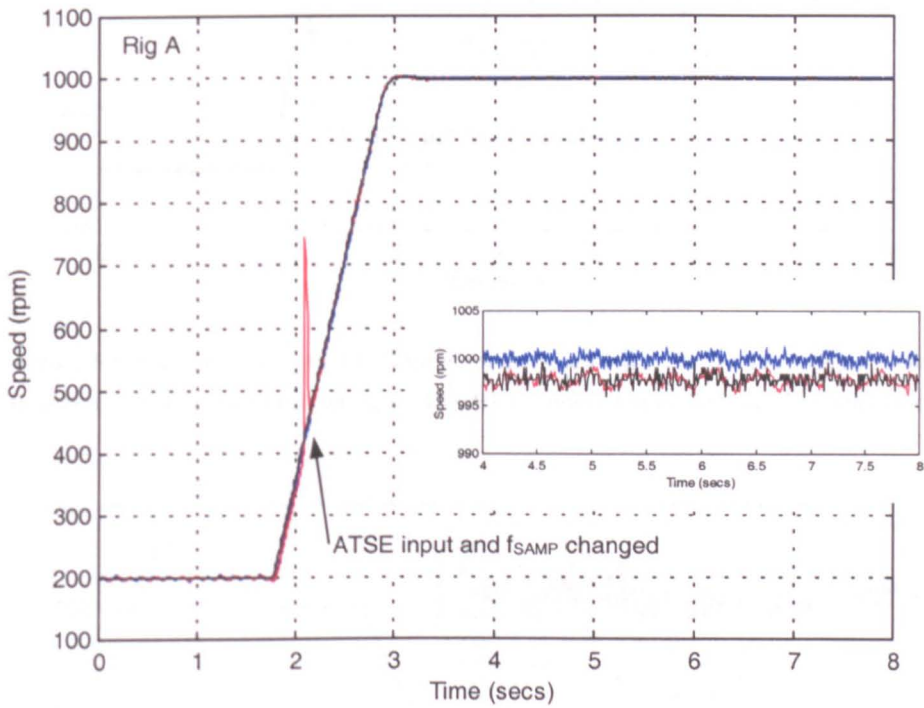


Figure 5.7. Encoder, ASO and ATSE speed measures during a 200rpm to 1000rpm speed transient, under ¼ rated load, on rig A. The drive is operating in the sensorless ASO mode

In the magnified steady state images, which accompany the transient responses of figures 5.7 and 5.8, the measured and estimated speeds can be seen at 1000rpm. In the case of both results, the steady state error, between ASO estimated and encoder measured speed, is in the order of a few rpm. The ATSE estimate can be seen to be highly accurate in both results. The ATSE estimate resolution is within that of the 2500-line encoder used on rig B and comparable with that of the 10000-line device used on rig A.

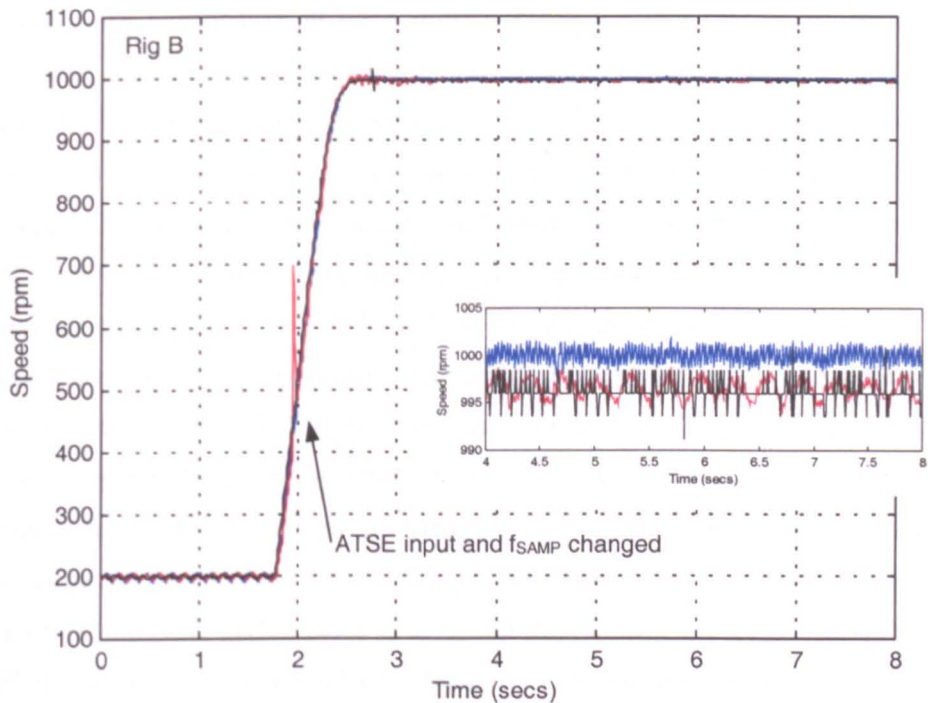


Figure 5.8. Encoder, ASO and ATSE speed measures during a 200rpm to 1000rpm speed transient, under  $\frac{1}{4}$  rated load, on rig B. The drive is operating in the sensorless ASO mode

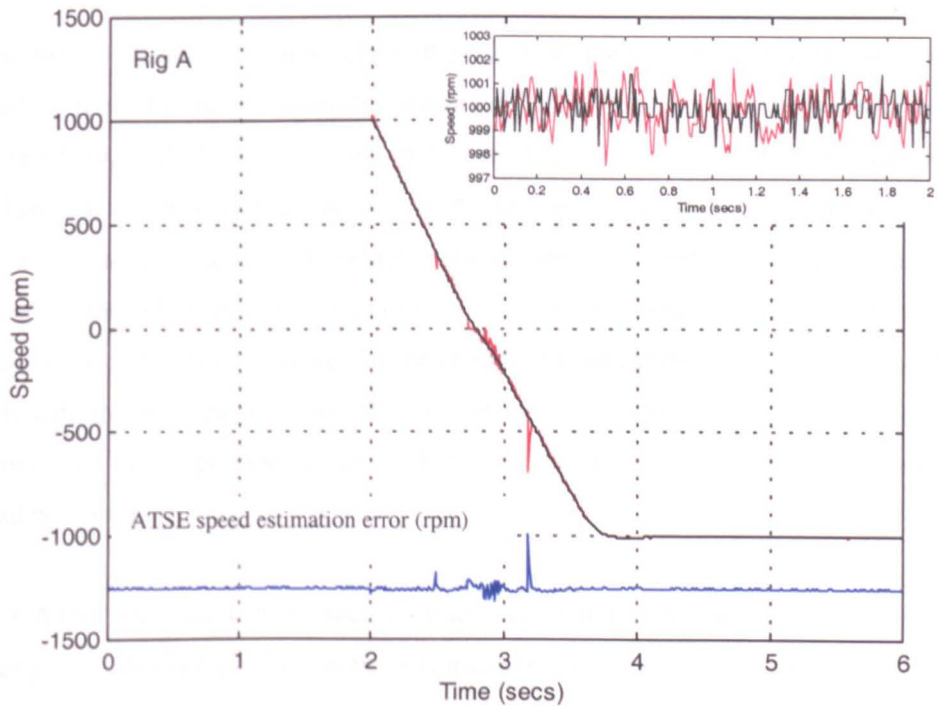


Figure 5.9. Encoder, ASO and ATSE speed measures during a  $\pm 1000$ rpm unloaded speed transient, on rig A. The drive is operating in the sensorless ASO mode

The no load transient tracking performance is shown in figure 5.9, where the sensorless implementation on rig A drive undergoes a 1000rpm speed reversal. In this result, although automatic tuning is not utilised, the speed error at 1000rpm is minimal. The ASO estimated speed is not shown, so that the encoder and ATSE speeds can be clearly seen. Again the two speed measures/estimates are in close agreement and are comparable in terms of both accuracy and resolution. The ATSE tracks the real speed well during the transient. The points at which input and sample frequency change can be seen in both directions and the hysteresis effect can be seen, where the changeover point is varied depending on whether the drive is decelerating or accelerating. The ATSE estimation sign is taken from that of the ASO estimate without any problems. Some error and noise can be seen on the estimate at and around zero speed, but this is as expected and was considered in the previous section. This is the region where the RSH tracking system will become confused with inverter harmonics and ASO performance is degraded (this centres the BPF). Noise persists until the harmonic is again reliably detected. An operating region for the ATSE estimator is defined later, in section 5.4.5.

### **5.4.3 ATSE Load Rejection Tracking Performance**

The results shown in figures 5.10 and 5.11 show the various speed measures when load is applied/removed from the sensorless ASO system. For the plots shown in figure 5.10, each drive is running at 1/5 rated  $I_q$ , when full rated load is applied at  $t=1\text{sec}$ . The left hand trace shows rig A running at 600 rpm, whilst the right hand trace shows rig B running at 900rpm. The difference in reference speed is simply to illustrate the ATSE performance at different speed and load conditions. Again the  $T_r$  value used in the ASO scheme, for the results of both figures 5.10 and 5.11, has been detuned, by between 10% to 30% of the rated hot value. It is evident, as was considered in the previous chapter, that speed error due to detuning will vary with load condition.

The ATSE estimate can be seen to track the speed variation, as the load-state is changed, with very good dynamic performance. The accuracy is again encoder like in each steady state condition. Particularly evident on the rig A trace is that the noise level on the ATSE estimate, if comparing the two steady states, has decreased under full load. Here the RSH effect being tracked has increased in amplitude and the tracking performance is improved.



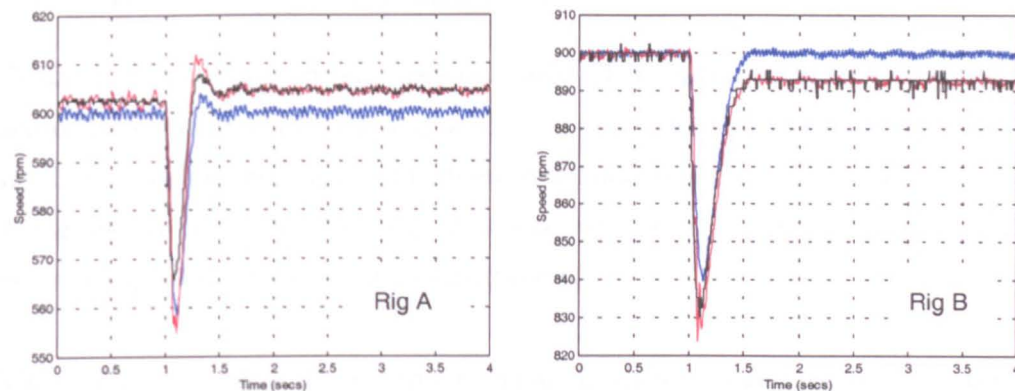


Figure 5.10. Encoder, ASO and ATSE speed measures during a 1/5 to full rated load torque impact at 600rpm (rig A) and 900rpm (rig B). The drive is operating in the sensorless ASO mode

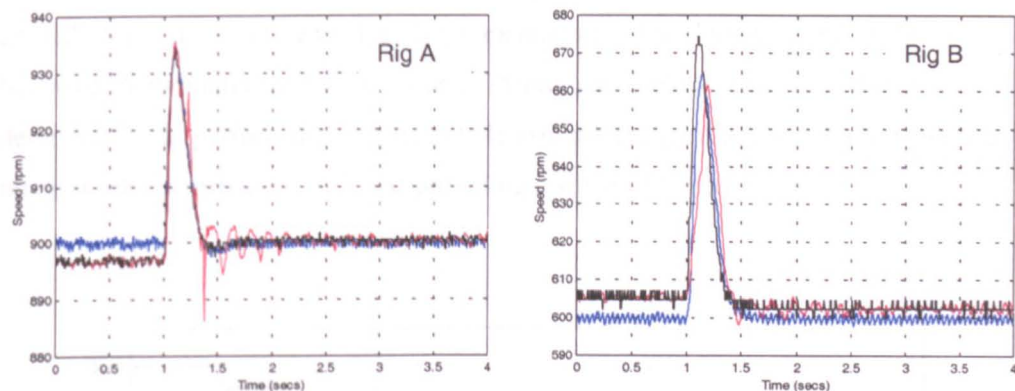


Figure 5.11. Encoder, ASO and ATSE speed measures during a full to 1/5 rated load torque removal at 900rpm (rig A) and 600rpm (rig B). The drive is operating in the sensorless ASO mode

In figure 5.11 each drive is operating in the steady state, at full load, prior to  $t=1\text{sec}$ . At  $t=1\text{sec}$  the load is immediately reduced to 1/5 rated and the ATSE is seen to track the transient. In the left hand trace, for rig A, the drive is operating at 900rpm demand speed. The ATSE tracks the transient with good dynamic performance and with excellent steady state accuracy. It is however noticeable that the ATSE estimate is a little noisy as the speed loop settles. Here the drive is operating at low  $I_q$ , which is reduced to bring the speed error down, and hence the RSH is being disguised by the no load PWM harmonic. The steady state value, after around a second of settling, is providing an excellent speed estimate again however. In the right hand trace, for rig B running at 600rpm, similar effects are noticed, where the ATSE estimate during the transient is slightly off. Again the steady state performance is very good though.

5.4.4 ATSE Low Speed Tracking Performance

Figure 5.12 shows the encoder measured and ATSE estimated speeds from ASO sensorless implementations running on the two rigs. Both are operating under full rated load with the speed demand reduced from 300rpm to 30rpm in steps of 30rpm. These speeds correspond to 10Hz electrical down to 1Hz electrical. The ASO estimated speed is not shown for increased clarity.

The ATSE speed tracks the real speed very well, again with encoder like accuracy, down to below 90rpm (3Hz). Below this speed the algorithm is confused by close proximity, large amplitude PWM harmonics, as predicted in section 5.2. It is considered that this is a similar operating range as that where satisfactory operation is gained from the ASO sensorless implementation. The fact that the ASO system becomes particularly noisy at around 75rpm and below also contributes to the deterioration in performance of the ATSE estimator algorithm, in which it plays an integral role (centring the BPF and providing a value of  $f_e$ , etc).

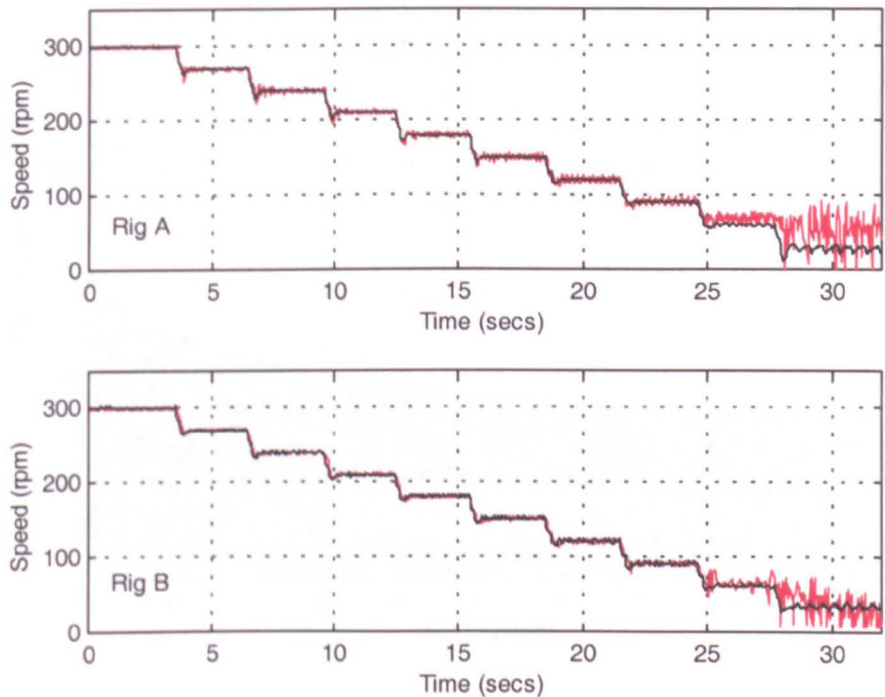


Figure 5.12. Encoder and ATSE speed measures during fully loaded speed deceleration from 300rpm to 30rpm in 30rpm steps. Both drives are operating in the sensorless ASO mode

5.4.5 Defined Region of ATSE Operation

From the results obtained and the tables presented in section 5.2, showing at what speed the tracked RSH will first contact with the next lowest inverter harmonic, a suggested operating region is defined for reliable use of the ATSE. This is shown in figure 5.13 and is highly similar for both drives used in this work.

The RSH, from which the ATSE speed estimate is obtained, is not reliably detected in the region of 75rpm and below throughout the load range. In this region the RSH effect exists with large PWM harmonics in close proximity and the RML-ATF cannot readily discern the RSH effect. The BPF bandwidth must be made small in this region and therefore the centre estimate is crucial. Unfortunately these demands are not met unless a high accuracy speed measure is used to centre the BPF initially and this is self-defeating! Small errors in the BPF centre frequency result in the RSH tracking algorithm tending to track PWM and noise effects. A tuning system should be disabled if operating in this region.

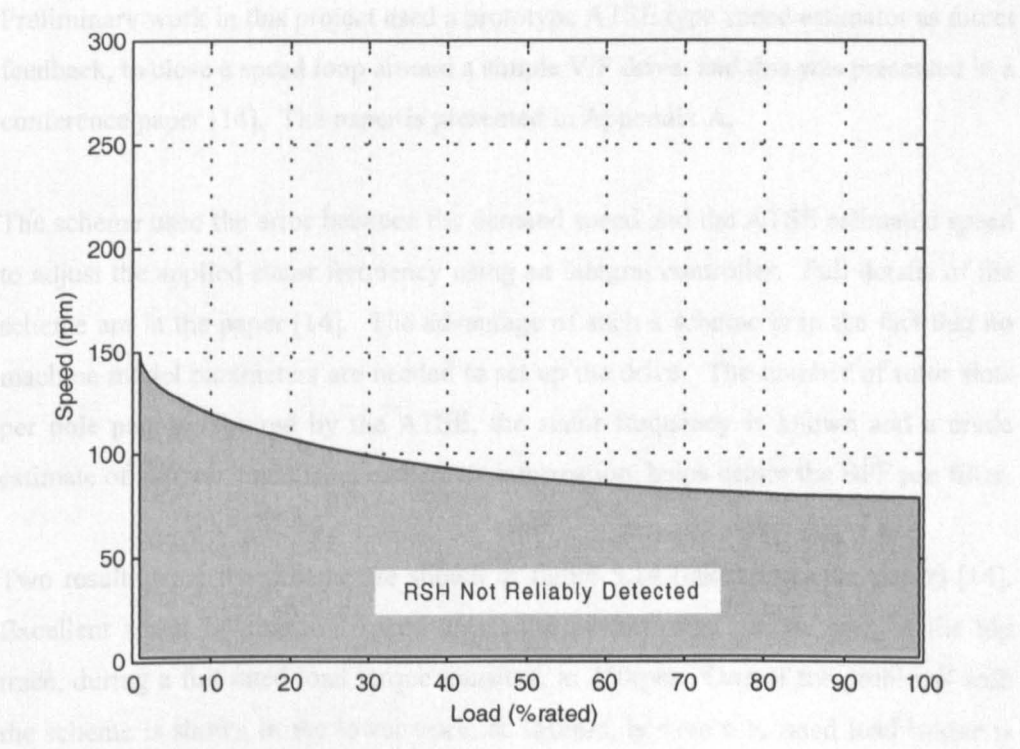


Figure 5.13. ATSE suggested operating region, when applied to speed estimation, in the sensorless ASO implementation on the 2 motor drives

Above the unreliable detection speed range the ATSE estimated speed is reliable, particularly at higher load. At very low loads, up to around 150rpm running speed,

the RSH based speed estimate is certainly less reliable. However, natural no-load is around 1/10 of the rated full load value, for the drive rigs used, due to windage and friction. Good performance is obtained if the drive is tuned when entering the region of 75rpm to 150rpm, but the load must be increased to above ¼ rated before highly reliable tracking is obtained. Above 150rpm and for the rest of the speed range, tracking is excellent down to natural no load.

Not dissimilar speed range constraints were encountered in the work of Blasco, when using FFT derived RSH speed estimator [28]. His work was carried out in Nottingham and used drive rig A (as used in this work), tracking the  $\kappa = -1$  slot harmonic effect.

## **5.5 Sensorless Drive Tuning**

### **5.5.1 Considering Direct RSH Speed Estimate Feedback**

Preliminary work in this project used a prototype ATSE type speed estimator as direct feedback, to close a speed loop around a simple V/F drive, and this was presented in a conference paper [14]. The paper is presented in Appendix A.

The scheme used the error between the demand speed and the ATSE estimated speed to adjust the applied stator frequency using an integral controller. Full details of the scheme are in the paper [14]. The advantage of such a scheme is in the fact that no machine model parameters are needed to set up the drive. The number of rotor slots per pole pair is required by the ATSE, the stator frequency is known and a crude estimate of slip, obtained from nameplate information, helps centre the BPF pre-filter.

Two results from the scheme are shown in figure 5.14 (taken from the paper) [14]. Excellent speed holding and speed correction performance can be seen in the top trace, during a full rated load torque transient, at 750rpm. One of the problems with the scheme is shown in the lower trace, at 150rpm, as here a ½ rated load torque is applied and removed and the very poor torque regulation can be seen. This is due to the V/F scheme and not associated with the speed estimator. There is more pressure on the speed estimator at this speed however, due to the PWM harmonics, etc, and the fact that the poor torque regulation results in a larger than anticipated immediate



speed loss, which must be tracked. Note that a good average speed is still maintained.

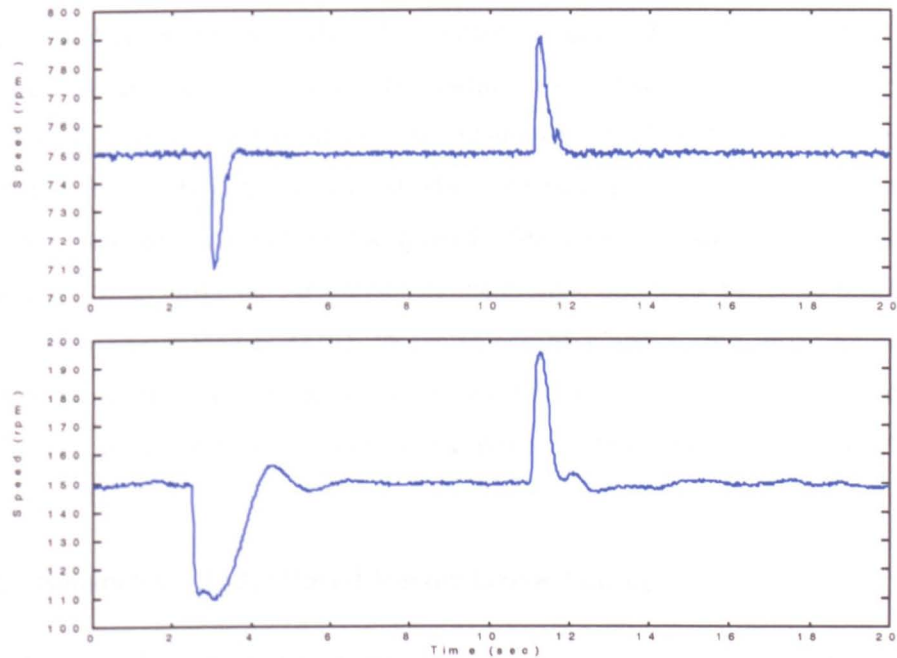


**Figure 5.14** RSH based speed estimate as used to provide direct speed feedback in a basic V/F drive. Top trace - full load applied and removed at 750rpm. Lower trace – half rated load applied and removed at 150rpm

The work of Shuli [119] looks in more detail at the principle of using an RML-ATF derived speed estimate as direct feedback, to facilitate a sensorless IRFO drive for example. Most particularly he looks at the management of  $r$  and  $\lambda$  parameters and considers their adjustment, based on whether the drive is in a steady state or transient condition. Results are presented that show an estimator tracking speed with excellent accuracy and dynamics, in an encoded IRFO drive, but none are shown with the estimate used as feedback.

From preliminary tests in this work [15], it was considered that the limitations of such a method are the requirement for an initial speed estimate, the requirement to robustly indicate drive-state (steady/transient) and the requirement for good appreciation of speed estimator (RML-ATF) dynamics. Where an RML-ATF estimator is tested for use in a sensorless system, as has been shown in this chapter, its ability to accurately track speed must be tested where the initial speed guess, which sets up pre-filtering, is in error. The work of Shuli [119] is utilised here to set good general tracking parameters  $r$  and  $\lambda$ , where the estimate is used for tuning. A scheme requiring the management of ATSE parameters would lead to a scheme that requires advanced set-

up of the estimator, perhaps rather than the set-up of a machine model and this was thus avoided. If the parameters were to be managed for direct feedback, between steady state and transient conditions, then also these conditions must be robustly indicated and the estimator (RML-ATF) dynamics must be fully appreciated. Neither of these considerations are trivial. The estimator dynamics and accuracy will be a function of pre-filtering (speed estimate required), speed, load, etc. Setting the parameters for steady state looks good where the estimator is simply an observer, in direct feedback this may increase the speed feedback delay to an extent that makes a sensorless system unstable. As previously mentioned, this work therefore makes use of Shuli's dynamic studies [119], to set values of  $r$  and  $\lambda$ , but does not further consider the ATSE as a direct feedback speed estimator. For these reasons and due to the poor torque regulation, the project work moved on to the tuning of a model based vector system.

### **5.5.2 Sensorless Model Based Vector Drive Tuning**

The ATSE speed measure, demonstrated in the previous section, is used to tune the ASO (model-based sensorless) implementation for highly accurate steady-state speed holding. Whilst this type of tuning mechanism may often be termed along the lines of 'tuning against rotor time constant variation', this assumes that estimates for all other parameters are highly accurate. This work is concerned with obtaining accurate speed holding, such that the developed sensorless drives can obtain best possible performance in speed synchronised applications. The ATSE speed is therefore used to tune  $T_r$ , because this, as was shown in the preceding chapter, is the parameter that most affects the speed accuracy. Some degradation in transient performance can be tolerated, as long as the speed holding accuracy is obtained, by artificially using  $T_r$  adjustment to account for small discrepancies in other parameters. Of course, large variations in parameters, such as  $R_s$  for example, would cause problematic drive operation ( $R_s$  at low speed).

$T_r$  tuning schemes have been proposed and implemented in previous work. The most notable examples are those presented by Blasco, based on the use of FFTs [28, 49, 109], and by Jiang, where the adaptation mechanism was not explicitly defined [86]. The work presented here is thought to be the first example of the RML-ATF based speed estimator used to tune a model-based system. For reasons discussed in the previous sections, this is thought to be the most practically viable solution yet

presented for sensorless high accuracy speed holding over the majority of the rated speed range and into field weakening.

In the low speed region, that is  $< 75\text{rpm}$ , tuning is disabled. In this region it is considered that signal injection methods would be necessary to extract high-accuracy saliency based speed information and  $R_s$  estimation would be critical for stable operation of the ASO method (and those like it). These areas were not explored in this work, as the processing capacity of the DSP platform was fully utilised to run the developed algorithm on two drives, with a view to testing speed synchronised applications. Other notable research work looks at this area of sensorless control [40, 63].

The tuning algorithm implemented here is shown, as a block diagram, in figure 5.15.

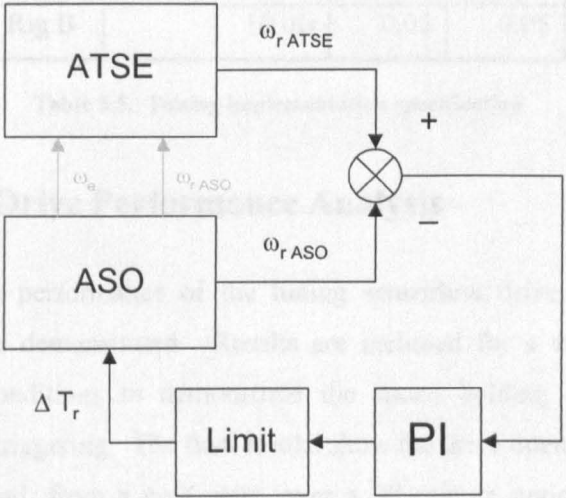


Figure 5.15. Block diagram of the  $T_r$  tuning system

The ATSE speed estimate is compared with that of the ASO. The error is used directly to drive a PI control, whose output is a  $T_r$  adjustment value. The output is limited to realistic  $T_r$  variation due to temperature effects, of around 40% for heating, but 20% in the opposite direction, mainly for load-induced variation. The PI control and limiting of course incorporate anti-windup to switch off the integrating term if a limiting value is reached. The  $T_r$  adjustment feeds into the ASO to correct the speed error. Note that the ASO speed and excitation are used in the ATSE for centring of the BPF pre-filter. The system is hence self-tuning.

Tuning PI gains are set such that the tuning is relatively slow compared to the speed loop. Designs were tested in Simulink, where the error between the actual speed was

compared with an ASO simulation with an erroneous  $T_r$ . The tuning dynamics are considered slow enough to neglect any ATSE estimation delay and the gains are shown in table 5.5.

Tuning is disabled in the transient state and this is triggered using the reference speed input. The input reference is a clean signal and speed transient requests can simply be determined by comparing present and past reference values (effectively  $d_{ref}/dt$ ). Load impacts are detected by comparing reference speed and ASO estimated speed and looking for sudden variation, given a suitable noise margin to allow for noise on the ASO estimate. Even if the real speed is in error, the speed loop acts to produce zero steady state error between the demand and fed-back ASO estimated speed.

	Sample Time	kp	ki
Rig A	10 ms	0.02	0.05
Rig B	10 ms	0.02	0.05

Table 5.5. Tuning implementation specification

5.6 Tuning Drive Performance Analysis

In this section the performance of the tuning sensorless drive, described in the previous section, is demonstrated. Results are included for a variety of different speed and load conditions to demonstrate the speed holding accuracy and the transient detection triggering. The final results show the drive operating at low speed, under full rated load, from a cold start, over a 30 minute period, both with and without tuning. The tuned system holds the demanded speed with encoder like accuracy over the full test period. The untuned system, tuned prior to  $t=0sec$ , accumulates an error of several rpm on both drives.

In all of the results shown, no concerted effort has been made to optimise motor parameters for particular operating conditions.  $R_s$  is measured at initial drive start up, such that it may have varied slightly prior to and over the duration of a test. The  $T_r$  compensation scheme is therefore being primarily used to adjust for speed holding accuracy, as was the stated intention of the tuning system.

5.6.1 Sensorless Tuning Drive Steady State Performance

In figure 5.16 the tuning drive is operated in the steady state at 100rpm, 500rpm and 1000rpm. The figure includes twelve separate results, each captured over a 2 second

period. At each speed the encoder measured speed is shown for natural no load,  $\frac{1}{4}$ ,  $\frac{1}{2}$  and full rated loads. The drive is running fully sensorless, the encoder is used simply to measure the true drive speed.

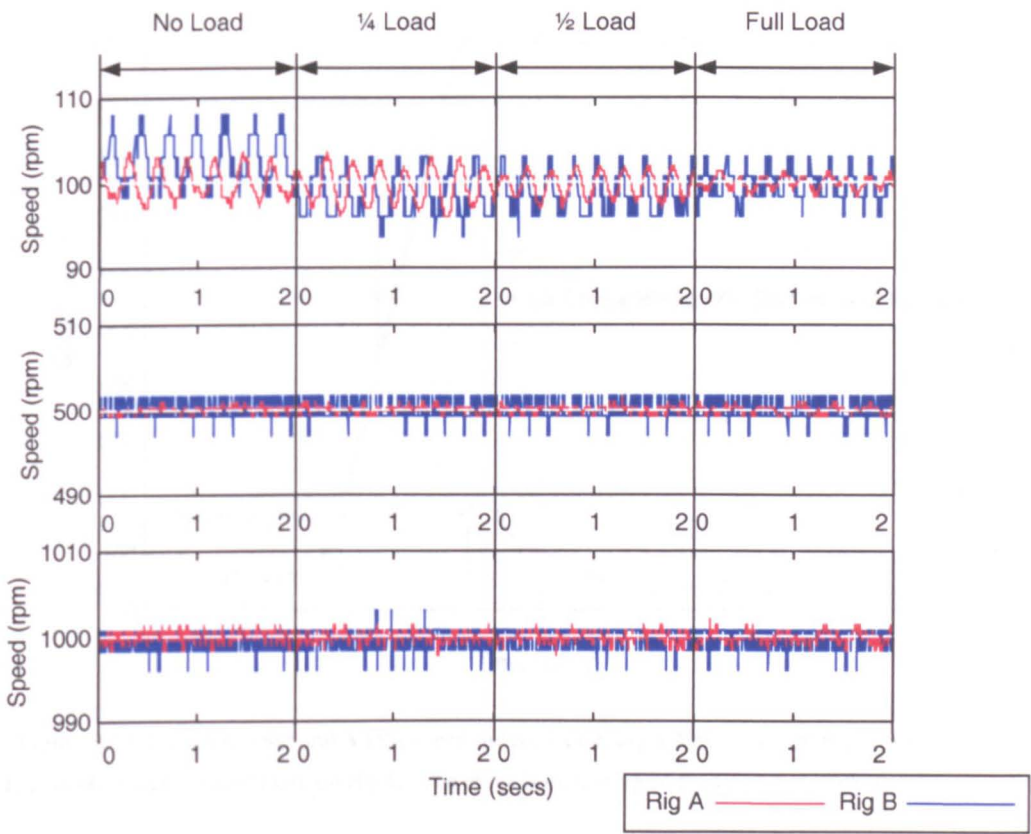


Figure 5.16. Encoder measured speed from both drive rigs, when operating the tuning sensorless control strategy, for a variety of steady state speed and load conditions

Note that, for all bar one result, both drives are shown to hold the desired demand speed with encoder like accuracy under all load conditions. The exception to this is at 100rpm, no-load on rig B, where the real speed is seen to have a small error. Here the ATSE speed estimate is not considered 100% reliable, as was defined in section 5.4.5. Note that erroneous tuning of  $T_r$  at no and low loads is however much less significant than at higher loads. When the load is increased to  $\frac{1}{4}$  rated the actual average speed is significantly more accurate.

It is clear that the sensorless implementation is somewhat noisier at 100rpm than at higher speed, but this was shown in the previous chapter to be a function of the ASO sensorless algorithm responding to inverter distortion.



5.6.2 Sensorless Tuning Drive Transient Performance

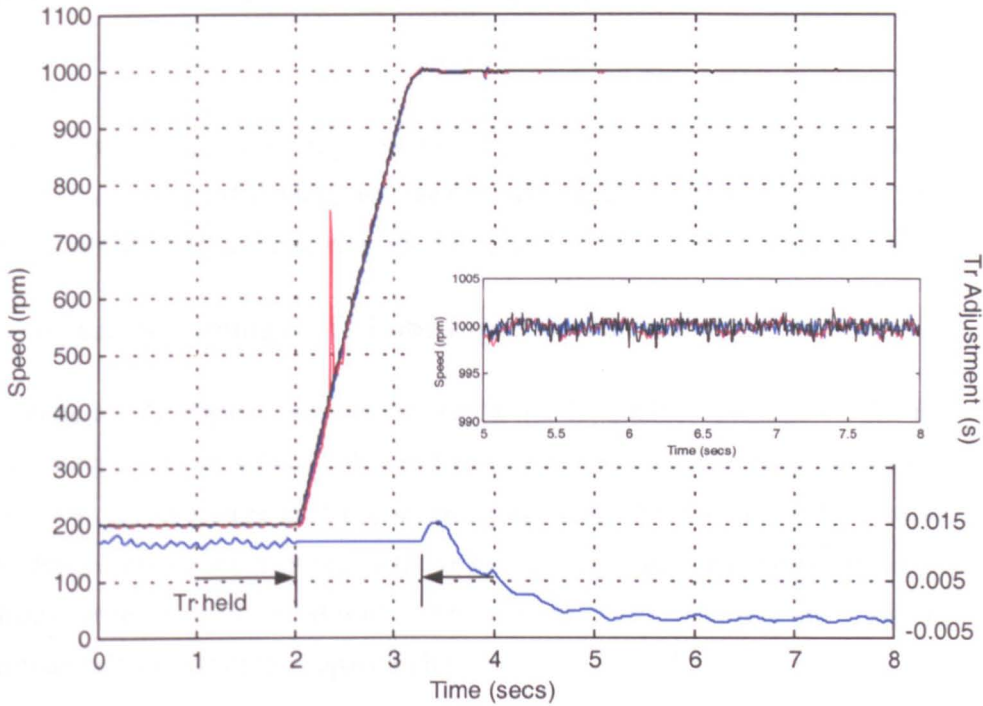


Figure 5.17. Encoder, ASO and ATSE speed measures during a 200rpm to 1000rpm speed transient, under ¼ rated load, on rig A. The drive is operating in the tuning sensorless mode

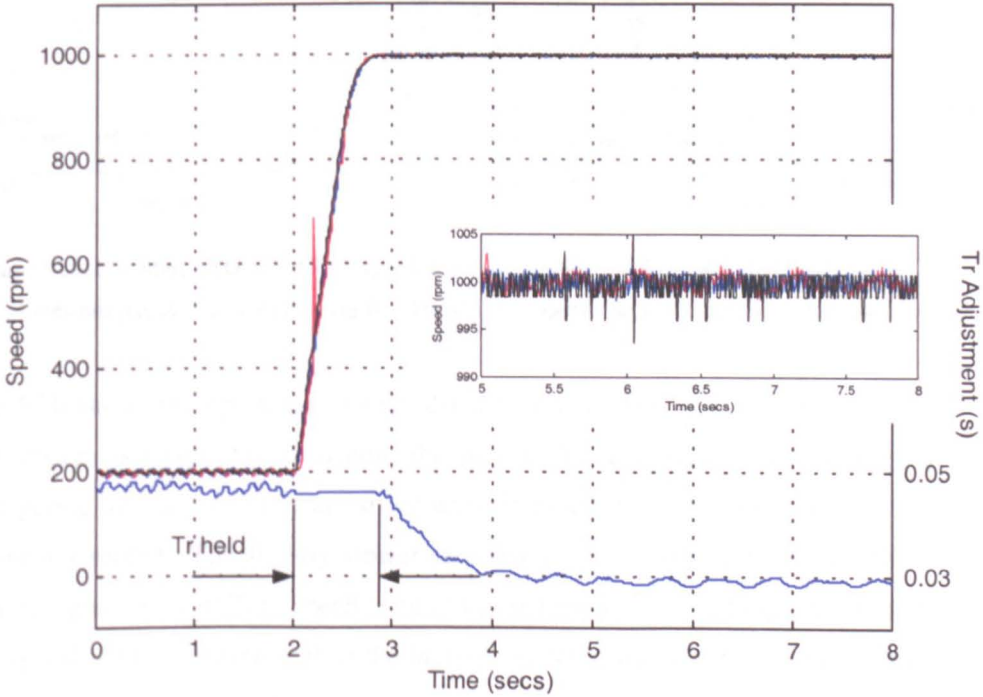


Figure 5.18. Encoder, ASO and ATSE speed measures during a 200rpm to 1000rpm speed transient, under ¼ rated load, on rig B. The drive is operating in the tuning sensorless mode

The transient performance of the tuning drive is shown for rig A in figure 5.17 and for rig B in figure 5.18. This is for an acceleration, from 200rpm to 1000rpm, under ¼ rated load. Similar conditions to those of the tracking results shown in section 5.4 apply.

In both results the steady state speed is shown to be encoder like.  $T_r$  can be seen to vary, such that the speed holding accuracy is maintained in the steady state. The tuning is disabled ( $T_r$  is held constant) for the duration of the transient, as is desired.

5.6.3 Sensorless Tuning Drive Load Rejection Performance

Drive tuning during impact load variation is shown, for similar operating conditions to the tracking results of section 5.4.3, in figures 5.19 and 5.20. In figure 5.19 each drive is subjected to a large load impact being applied. The tuning can be seen to hold as desired during the majority of the impact and the error that would persist in the steady state is then tuned out. Encoder like speed-holding accuracy is demonstrated either side of the impact region.

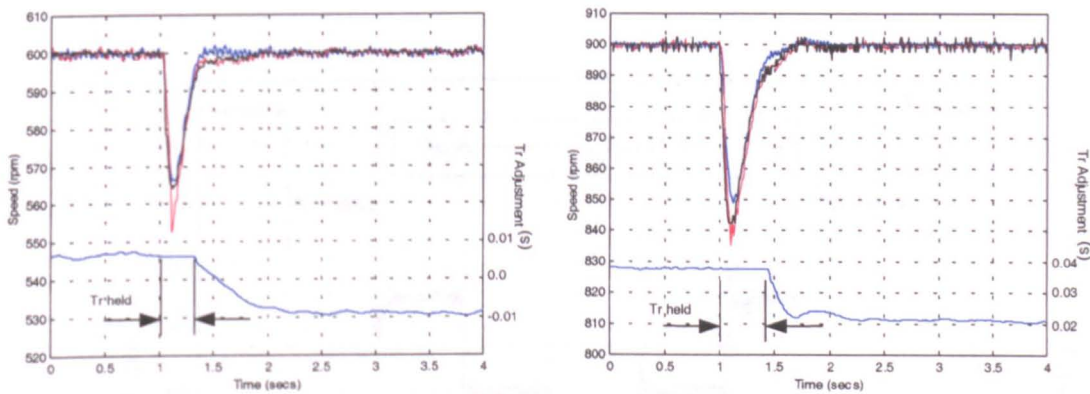


Figure 5.19. Encoder, ASO and ATSE speed measures during a 1/5 to full rated load torque impact at 600rpm (rig A) and 900rpm (rig B). The drive is operating in the tuning sensorless mode

Figure 5.20 shows the operation of each drive where a large load is removed. The tuning system is again shown to hold the present  $T_r$  adjustment value during the impact period and any steady state speed error is tuned out when the load rejection response has settled. The slightly slower response of the tuning system is related to the lower significance of  $T_r$  to speed error at lower load and the settling period of the ATSE speed estimate, which prefers the increase in RSH amplitude where the load is increased, rather than reduced.

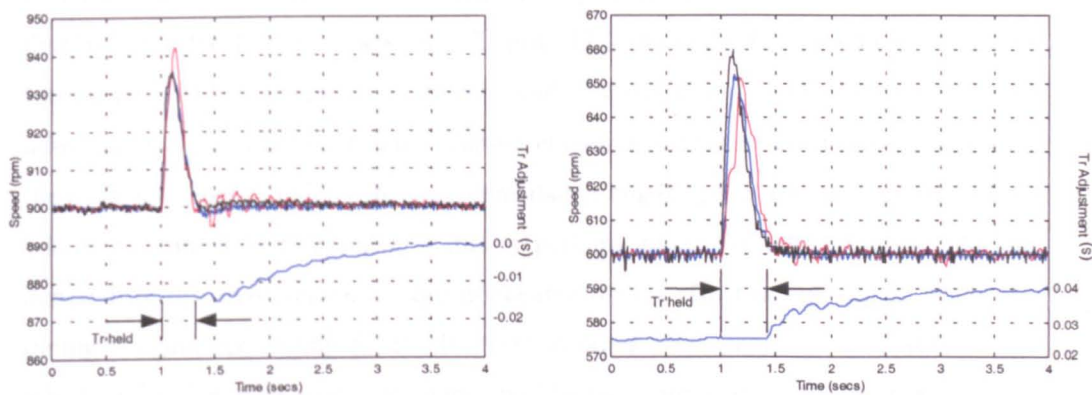


Figure 5.20. Encoder, ASO and ATSE speed measures during a full to 1/5 rated load torque impact at 900rpm (rig A) and 600rpm (rig B). The drive is operating in the tuning sensorless mode

5.6.4 Sensorless Tuning Drive Low Speed Performance

The low speed performance of the tuning drive is shown in figure 5.21. Encoder measured speed is shown with both drives following the same reference demand. Both drives are operating at their full rated loads.

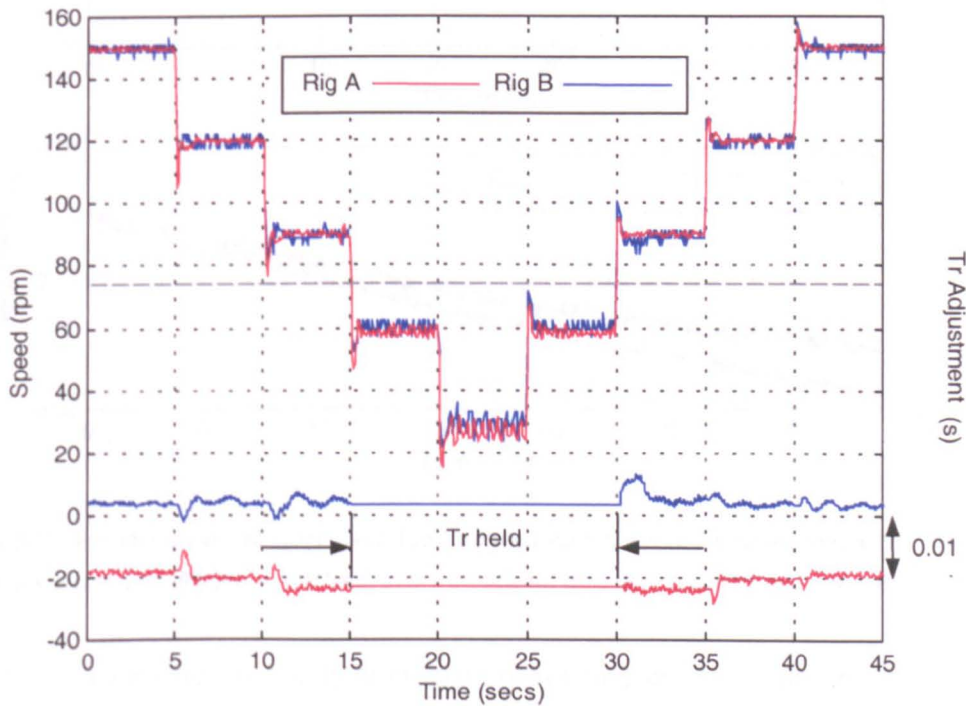


Figure 5.21. Encoder measured speed from both drive rigs, when operating the tuning sensorless control strategy at full load, at low speed. The drives enter and return from the region where tuning is disabled. Speed demand is varied in 30rpm steps, from 150 rpm to 30rpm



Starting at 150rpm (5Hz electrical) and varying in steps of 30rpm, the speed demand is reduced to 30rpm and then increased back up to 150rpm. The drives are shown to display encoder like accuracy at 150rpm, 120rpm and 90rpm, where tuning is functional. When operating at 60rpm and 30rpm tuning is disabled and the  $T_r$  adjustment value is held constant. Tuning is re-enabled when the drives come out of the very low speed region. It is evident that a small speed accuracy error persists where the tuning is disabled and this is perhaps more evident in rig A. As the demand to this drive varies, a more noticeable tuning effect is seen in  $T_r$ , where the tuning is again accounting for small errors in other drive parameters. Errors due to misidentification of the stator resistance will be most prevalent in this region.

5.6.5 Sensorless Tuning Drive Compensating Temperature Variation

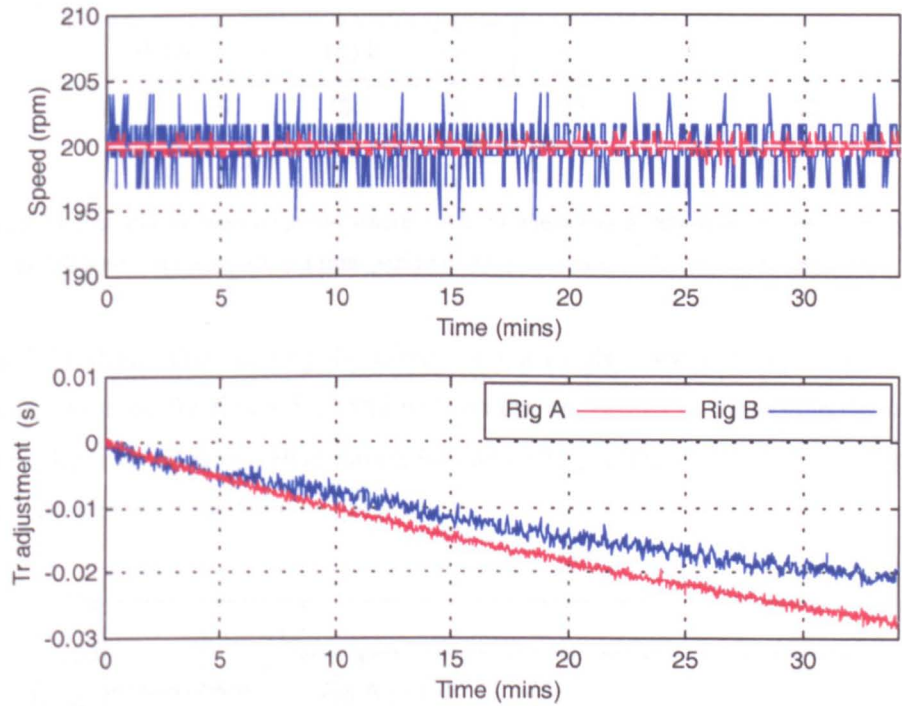


Figure 5.22. Encoder measured speeds, and  $T_r$  adjustment values, where the tuning sensorless system is operating at 200rpm, at full load, over a significant time period and from a cold start

Figure 5.22 demonstrates the ability of the sensorless tuning drive to maintain speed holding accuracy, whilst parameters vary due to motor heating. The dominant effect here is due to resistance variation, but where this introduces small error in orientation, the inductance parameters will vary also, due to varying flux.

For the test, both drives were run at 200rpm under full load conditions. The upper trace displays the encoder measured speeds, although these play no part in the control scheme, and each drive is seen to maintain the 200rpm demanded speed with encoder like accuracy. The difference in resolution between the encoder measurements, as with the previous results, is due to the different number of encoder pulses per revolution (both are sampled at 100Hz) for each rig. The lower trace shows how  $T_r$  values for each drive are adjusted over the experiment time. Note that they vary by approximately 15%-20% of their rated value in this time. The base value of  $T_r$  was adjusted at the experiment start, for zero speed error.

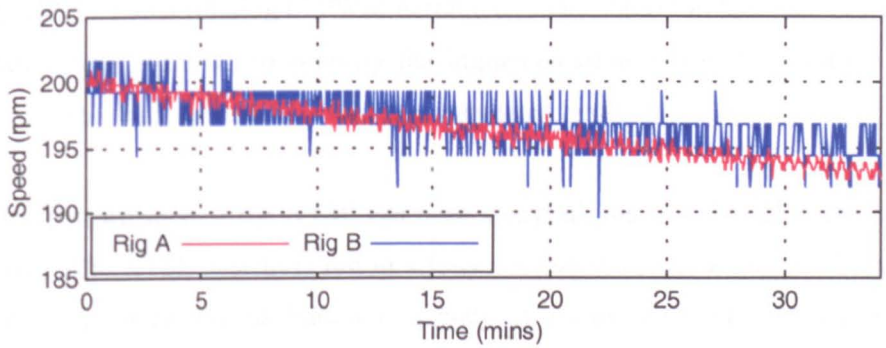


Figure 5.23. Encoder measured speeds, where the ASO sensorless system is operating at 200rpm, at full load, over a significant time period and from a cold start. Tuning is disabled

Figure 5.23 shows that running the drives over a similar time period under similar conditions to those for figure 5.22 and with no tuning, results in the accumulation of around a 5rpm speed error. Here tuning was disabled just prior to  $t=0$ mins. For both tests the motors were run from a cold start.

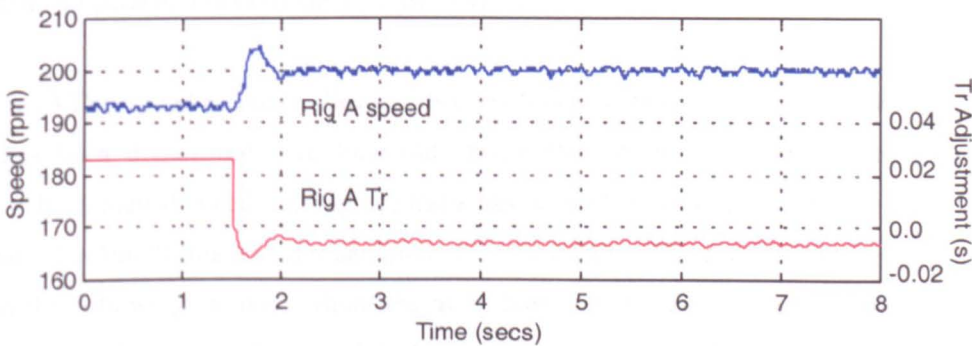


Figure 5.24. Encoder measured speeds and  $T_r$  adjustment value, where tuning is enabled on the ASO sensorless system shortly after the end of results 5.22

Figure 5.24 shows how the drive returns to a correct operating speed when tuning is re-enabled (on rig A) shortly after the test shown in figure 5.23. The tuning removes the accumulated parameter error, through  $T_r$  adjustment, in less than 1 second.

## **5.7 Conclusion**

This chapter has described and demonstrated the ATSE system as an effective estimator of 'true' speed in a sensorless induction motor drive. Various amendments have been made to the structure presented in previous work [14 112-114, 119], to improve the practical performance; including selection of an appropriate input quantity and the notch filtering of PWM harmonics. The algorithm has been run with fixed parameters ( $r$  and  $\lambda$ ) to simplify the implementation and hence improve the robustness. Those used are in-line with that suggested by Shuli [119].

Where the performance of the ATSE has been analysed, the full algorithm has been considered. The ATSE system is run in a fully sensorless mode, where pre-filtering is set-up using speed and excitation frequency measures obtained from the ASO system. If an RML-ATF slot harmonic estimator is implemented/tested with the pre-filtering set-up using a real measure of speed (to eliminate pre-filtering variability), then the system must also be tested with fixed error in this set-up. For example, it is suggested that if the BPF and RML-ATF algorithm were applied to an input signal that was simply white noise, the RML-ATF would return the centre frequency of the BPF as the RSH estimate! It is considered that results presented have used suitable scaling for critical analysis of the steady state accuracy provided by the ATSE. The speed estimate is seen to return the real motor speed, where errors between this and that demanded persist, due to model parameter error.

Use of the ATSE speed estimate, through its comparison with the ASO model-based speed, has been demonstrated to tune out steady state error in the model-based system. The achieved speed holding accuracy has been shown to be well within the resolution of a 10000-line encoder sampled at 0.01seconds. The accuracy is further tested in the following chapter, where the algorithm is considered for use in speed synchronised applications. The complete ATSE speed estimator and tuning algorithm are executed on the DSP architecture utilised with minimal computational requirement. The DSP system runs code for motor control, PWM, data capture, multi-motor synchronisation (next chapter), etc, on two DSPs (with communication

routines) for two motor drives. The code has not been extensively optimised for speed.

With regard to the direction of further work, it would be interesting to test the performance of the developed algorithm on alternative machines, those with design features that perhaps promote the slot harmonic effects seen in stator quantities (open and unskewed slots). Whilst the reasons for minimising these effects are well defined [103], negative effects associated with using an open-slot rotor may well be outweighed by the desire for a high performance sensorless solution in certain applications, and hence tolerated. The author would expect the performance of the algorithm at lower loads to be improved with open and unskewed slot machines and the low speed range somewhat extended. The work could look at operation at synchronous speed and in the regenerative mode. At synchronous speed the RSH will coincide with a PWM harmonic. The use of field weakening could prevent this condition occurring, such that at low motoring or regenerating loads the machine is operated at fixed slip. Field weakening operation, with fixed slip, at low load is a suggested technique to improve sensorless methods at low speed [50].

Use of the ATSE speed estimate as direct feedback has been considered in publications by the author as part of this project. The first, included as part of Appendix A, looks at using the RSH speed estimate to speed trim a V/F scheme [14]. The second, also part of Appendix A, whilst presenting the tuning drive, demonstrates and briefly discusses direct feedback in the DRFO sensorless system [15]. The work has not been presented in this chapter, because it is considered that firstly a machine fully promoting RSH effects over the speed and load range would be required, and secondly, the work of Shuli should be extended, to more fully analyse ATSE estimation dynamics [119].

For improvement of the presented algorithm at very low speed it would be suggested that this work could be combined with signal injection methods [20]. The low speed problems evident in this work are due to both the model-based implementation and the ATSE struggling in this region. The implemented algorithm would be improved with robust compensation/removal of inverter non-linearities, but a low speed limit would still exist. Signal injection methods, that are applicable in this speed region particularly, are considered the most viable option.

These considerations for further work are again addressed in chapter 7. In the conclusion of this chapter a sensorless drive implementation has been engineered that provides highly accurate speed holding capability in the majority of the rated speed range. This is for motoring loads from natural no load to rated full load and the algorithm has been applied to two 4kW motors with differing electrical and mechanical specifications. The dynamic performance is dependent on the model-based sensorless implementation and that implemented here is regarded as a high performance candidate. Operation in the very low speed range, where ATSE tuning is not applicable, is possible: ATSE tuning is disabled and the scheme relies on the sensorless model set-up.  $R_s$  estimation techniques, such as that proposed by Campbell [40, 59], would further strengthen the low speed performance of a model-based implementation. The ATSE algorithm is a practically viable solution for speed estimation in commercial motor drive products, due to a minimal processing overhead compared with methods such as the FFT. Commercial interest has been shown in the algorithm from two UK based drive manufacturers.

---

## CHAPTER 6    The Synchronised Sensorless Drive System

---

### 6.1 Introduction

The purpose of the work presented in the previous chapters has been the development of a fully sensorless motor drive algorithm with high accuracy speed holding capability. Application areas that require such accuracy, as briefly introduced in chapter 1, would include any based on multi-axis control. This chapter assesses the suitability of the engineered sensorless drive for use in such applications. The developed two-drive system is tested in a variety of synchronisation configurations. Sensorless results are compared with those obtained under encoded control.

Electronic multi-axis control is developed, because many mechanisms in manufacturing require that various constituent component parts be synchronised. Traditionally this is achieved by the connection of the various elements, through mechanical linkages and gearing, to a common source of mechanical power (for example an electric motor large enough to provide the total power requirement). More recently mechanisms have been developed where the constituent components are driven independently (by smaller individual electrical drives). Here the synchronisation is achieved electronically and the control is designed for a given system specification - to emulate an existing mechanically coupled example perhaps [123, 124]. A major advantage associated with an electronically coupled system is an increased flexibility: gearing ratios can be adjusted in software and machinery can be quickly set-up to vary product specification with a minimum of downtime. The motivation for moving from mechanically coupled to electronically coupled systems is further considered in section 6.2.

Section 6.3 introduces and describes methods by which electronic axis coupling can be implemented, from simple open loop synchronous command generation, to the advanced Electronic Line-Shaft technique [123, 124]. The envisaged performance of

these techniques will be discussed, particularly considering how they compare with that of a traditional mechanically coupled implementation.

Results will be presented in section 6.4 from a practically implemented encoded solution, running on the developed two-drive system. Here the various control techniques are tested. The fully sensorless system is operated, running the leading candidate synchronisation algorithms, in section 6.5. The results obtained are compared/contrasted with those acquired under encoded conditions.

The work is extended in section 6.6 to test the validity of position correction in the sensorless mode. The parallel-cross-coupling synchronisation method introduced in section 6.3 [125, 126], running on the encoded and sensorless systems, is modified to include correction of position error, incurred due to load disturbances. The real incremental relative position, obtained using the encoder speed measurement, is used to assess the system performance. This is in terms of both position and speed synchronisation.

Section 6.7 discusses application areas, where the sensorless solution may be utilised and considers the appropriate synchronisation schemes for use with  $>2$  drives.

In the conclusion of this chapter the performance of the sensorless system is critically discussed. The purpose of considering multi-motor control, whilst it is used here as a test exercise to assess the developed sensorless drive performance, is that it has not yet been considered as an application area where sensorless techniques could be utilised. Ideas for further work are presented, which would be expected to extend the range of sensorless drive operation.

## 6.2 Electronically Synchronised Control

Many manufacturing processes require the synchronisation of several axes relative to a master command. These processes would include, for example, the manufacture of sheet materials, such as paper and the cold rolling of sheet steel [123, 127, 128], and processes that involve the handling of sheet material, such as printing and packaging manufacture [129-131]. Other applications would include various cutting and grinding functions, such as component manufacture (cutting screw threads for example) [132]; also electric vehicle applications [133, 134], where each wheel is

driven independently, and where electronic control could provide such functions as differentials, traction control and anti-lock braking [135].

Coupling of multiple axes would traditionally be achieved through a mechanical power transmission system, incorporating such devices as line-shafts, gears, chains, belts, clutches, differentials, pulleys, etc. The total process power would be derived from a large common source. Figure 6.1 shows a typical structure of a mechanically synchronised 4-axis system.

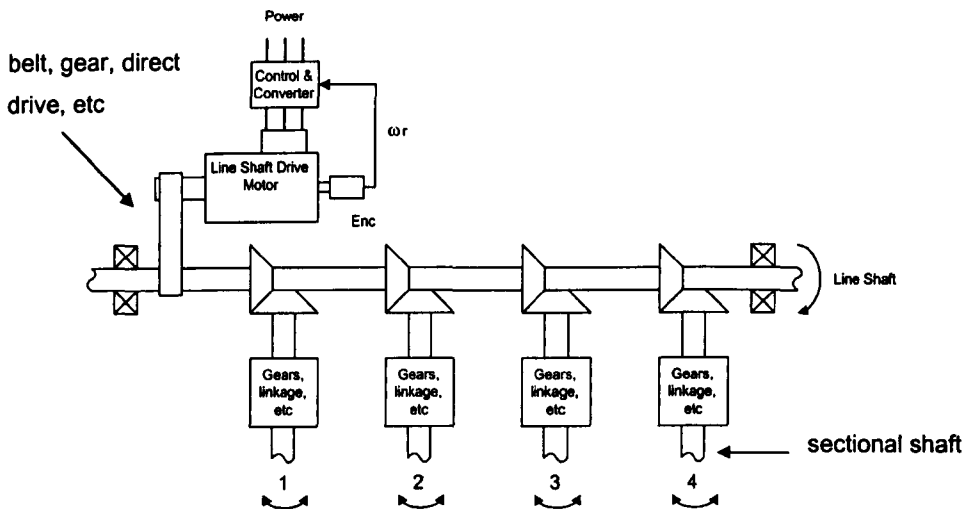


Figure 6.1. Mechanically synchronised multi-axis system.

More recent developments in manufacturing technology have seen mechanical transmissions partly (hybrid) or fully replaced with electrical actuators that drive individual axes. As an example the 'shaftless' printing concept has seen very large growth in the printing industry [130, 131]. These systems are coupled electronically and controlled in such a way as to emulate the system they replace. Many of the advantages associated with this type of solution are outlined in the following paragraphs.

- Increased Flexibility

Flexibility is increased with electronic synchronisation, as the system is not defined by the mechanical structure. Where product features are defined by the relative motion of various axes in the system, changes can be made with simple parameter variation in the control software. The possibility of variation in a mechanical system would greatly increase the system complexity and changes would most likely result in



significant downtime. With electronic coupling the system specification can be adjusted simply (cheaply), and possibly without the process being halted.

- **Increased Speed**

If the maximum process speed attainable from a mechanically synchronised mechanism is in any way limited by the linking transmission system, removal of the system and replacement with electronic coupling provides the opportunity to alleviate this problem. The mechanical system drive must consider the inertia of the complete mechanism (including the transmission) and individual section drives used in an electronic system could offer the possibility of optimisation for increased speed.

- **Known and Controllable Tolerances**

In the mechanical system, maximum and minimum tolerances are an accumulation of the sectional tolerances and will be highly dependent upon the transmission. The transmission will of course suffer wear. With the electronically coupled system, whilst each section may have associated tolerances, the transmission effects are removed and overall tolerances can be more readily predicted and controlled by the control structure.

- **Simple Expandability**

For a process to be expanded or modified, where mechanically synchronised, the line-shaft or drive train must be extended/adjusted and it is suggested that this would not be a simple procedure. In large mechanisms the line-shaft may have to be some length to reach particular sections and this is not ideal. With an electronic synchronisation, sections can be added, adjusted, moved, etc with only cabling considerations. Even where mechanical synchronisation is used for critical applications, hybrid systems can be created, where inconveniently sited sections of a mechanism are synchronised electronically.

- **Increased Reliability/Lower Maintenance Costs**

A mechanical system will have associated maintenance and servicing overheads. If this system is replaced with an electronic system, general maintenance and servicing, particularly due to wear, will be considerably reduced and hence reliability will be increased. Some form of intelligent monitoring system could also be incorporated into the synchronisation communication structure quite simply, because a

communication architecture must exist for control, and is unlikely to be an additional hardware overhead.

- **Smaller Size**

Similarly to reducing maintenance overheads, it is suggested that removal of a mechanical transmission will reduce the size, and hence increase the power density, of the complete mechanism.

- **Sectional Protection**

With electronic coupling, each controlled section can be managed for unexpected conditions, such as sectional overload, individually. For a mechanically synchronised system, say a printing press encountering a paper jam, without appropriate sectional feedback to the main motor drive, damaging torque may be distributed to the jammed section. With the electronic sectional drive, overload protection (torque limiting) can be simply managed in the drive for a particular section. The main control algorithm, given that a suitably advanced strategy is used, should handle the synchronisation.

- **Selective Decoupling**

Where necessary, to adjust start up positioning, or perhaps even to carry out on-line maintenance, sections of a mechanism that are electronically coupled can be selectively decoupled. In a printing application for example, an individual section can be aligned for the print head/plate to be changed. This does not involve decoupling the mechanical system, or aligning the complete process.

- **Noise/Torque Ripple Minimisation**

Removal of the mechanical transmission will remove sources of mechanical noise/vibration and variation, such as torsional elasticity, gearing noise/chatter, belt slip, etc.

The schematic of a typical 4-axis electronically synchronised system is shown in figure 6.2. Note that the mechanical systems and large motor and power converter shown in figure 6.1 have been replaced with four motors and power converters that will each have lower power ratings. Common connection is made electrically: power must be distributed to each unit and communication must be available between each unit for control.

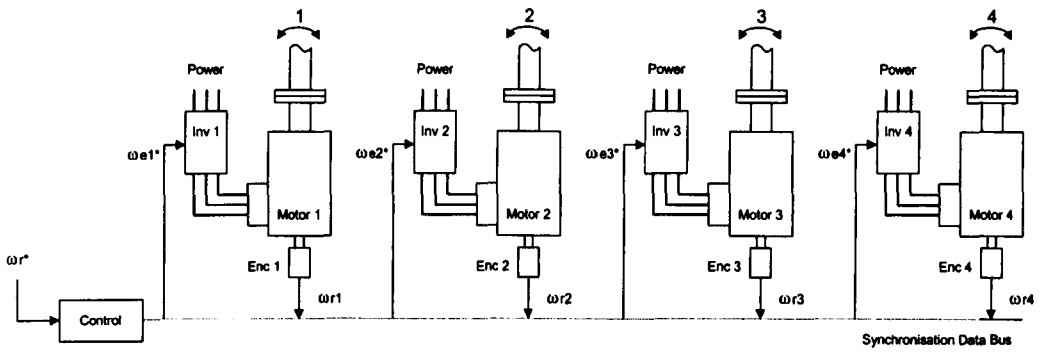


Figure 6.2. Electronically synchronised multi-axis system.

Much research interest has been directed at developing and improving the control techniques used in this form of multi-motor drive [123-126]. The disadvantages associated with many techniques being that they do not show the inter-shaft stiffness/rigidity that may be inherent in mechanically coupled drives through all operating conditions [129]. With mechanical systems the inter-shaft coupling is dependent on the torque obtainable through the transmission and thus the maximum torque that may otherwise be applied, to a sheet material for example, will be suitably limited. An electronic synchronising algorithm must deal with such conditions as sectional overload, where the section speed may not be controllable [123, 124].

In truth, and similarly to sensorless drive solutions, an electronic synchronisation technique must be married to an application. In hybrid systems, important sections can remain mechanically coupled, yet the flexibility of an electronically coupled section could be exploited at the far reaches of the mechanism. Four methods for electronic synchronisation are discussed in the following section.

### 6.3 Methods for Synchronised Control

Various control techniques have been proposed for synchronised motion, varying from a simple open loop synchronised command technique, through master slave schemes [127, 136], to cross-coupled [125, 126], and line-shaft emulation schemes [123, 124]. The methods are outlined in more detail in the following subsections. Where block diagrams are presented, they are shown for synchronisation of speed and can be adjusted and/or extended to include position synchronisation terms.

For synchronisation, where similar speed encoders are fitted to axis drives, it may be appropriate to provide coupling control terms based on digital phase-locking [132] of

the incremental position signals. A similar technique was initially considered for this work, where perhaps the rotor slot harmonic signals (as the output from pre-filtering stages) from the two motors could be phase locked in the sensorless mode. It was thought that this may be particularly appropriate for speed matching, because the two motors have a similar number of slots per pole pair. However, it must be remembered that the slot harmonic signals are in fact a modulation of the slot/pole frequency and the excitation frequency. Hence the rotor slot ripple frequency is not directly related to speed. Locking the waveforms together would only guarantee speed matching under matched slip conditions. Some form of demodulation would be required to extract a direct speed signal and the resolution of a digital method (rotor slot pulse counting) would be limited by the low resolution provided by a low number of slots. This work considers schemes that provide speed matching using measured/estimated speeds.

### 6.3.1 Synchronous Command Generation

The simplest form of system, which may be appropriate for many synchronised applications, is here termed synchronous command generation. In this method the various axis drives are simply given related command information, as shown in figure 6.3. The *sync* blocks define the relative kinematics of the system, relating how each axis responds to the reference command. As an example, it may be required that axis 1 rotates at a multiple of the axis 2 speed. Hence the sync blocks will contain simple gain factors. The scheme can simply be extended for use with  $n$  drives.

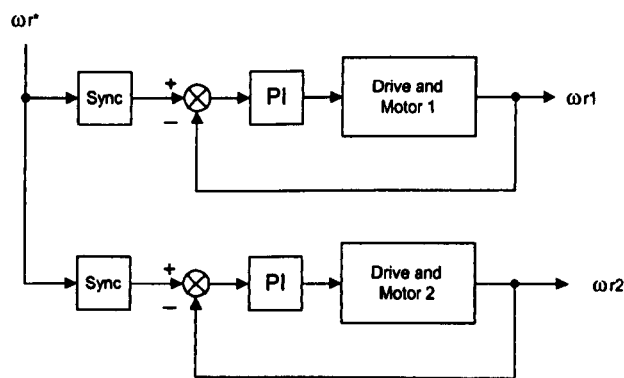


Figure 6.3. Synchronous command generation block diagram

The performance when responding to variations in speed demand will be acceptable for all conditions, given that the reference rate-of-change is limited to be suitably slower than the slowest accelerating axis drive, as shown in equation 6.1.

$$\frac{d\omega}{dt}_{MAX} = \frac{T_e - T_L}{J}_{AXIS MIN} \quad (6.1)$$

To guarantee reasonable synchronisation, for speed matching, such an open loop scheme would require the speed demand to be rate limited, depending on the maximum dynamic torque (maximum electromagnetic torque  $T_e$  – motor rated full load torque  $T_L$ ) and the inertia of the higher inertia drive  $J$  (rig A). For example, in this work the motor rated torque of both drives is 27Nm, whilst the maximum electromagnetic torque is  $k_T$  multiplied by the current limit, say  $7.55 \times 6 = 45.3\text{Nm}$ , and thus the maximum dynamic torque is 18.3Nm.  $18.3/0.3$  (rig A inertia) gives a slower rate of change limit than  $18.3/0.12$  (rig B inertia), so the maximum is limited to the former. If the reference is not limited, the synchronisation will depend on the relative axis closed-loop characteristics and the relative axis loading. Only if the axis characteristics are well matched and loading is guaranteed to be balanced, or could be neglected, would the scheme display good synchronisation.

Where loading will not be distributed evenly between axes and each individual axis may see large and sudden load variation, then the scheme offers no interactive synchronisation during drive recovery. In these instances the individual drives may still remain within process tolerance, but if a single axis drive were to go into torque limit then the axis speed will not be controlled. In the basic set-up this information is not seen by the reference command and not responded to by other axes.

Although this is a very common form of speed synchronisation, the drives used in this work have markedly different mechanical characteristics and would not display good synchronisation in an unlimited dynamic state (large-scale step changes in speed demand) or for sudden and large variation of load. Results obtained using this scheme are presented to provide a benchmark for the testing of more advanced schemes, where there is some interaction between drives. The alternative schemes considered are presented in the following three sections.

### 6.3.2 Master/Slave

The simple master slave scheme is presented in figure 6.4 for a two-axis system. Here the measured (or estimated) speed of the master drive is fed to the slave drive as the reference command. The master drive responds to reference changes in a standard fashion with the slave attempting to follow the speed of the master.

Considering speed matching of the two drives used in this work (where the sync function is a gain of 1.0), the most viable approach is that the lower inertia induction machine acts as the slave drive. As the acceleration rate is dependent on inertia, the lower inertia machine will more readily be able to track the master speed over a maximised operating range. Again however, conditions may exist, due to high loading of rig B (low inertia), where the slave may not be able to track the master.

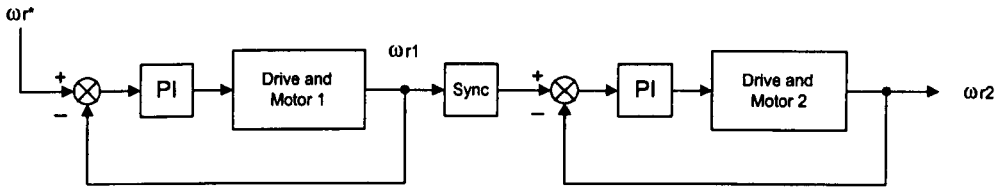


Figure 6.4. Master/Slave synchronisation scheme block diagram

Under normal operating conditions in this scheme the slave drive will be able to respond to variations in the master speed due to sudden load variation. The major disadvantage of the basic scheme is due to the non-symmetrical nature of the response. The master will not respond to sudden slave load variation, and the slave drive will not track the master well if it alone is operating at a large load torque. Indeed, if the slave drive is in torque limit then it has no capability to track the master speed, its speed is uncontrolled and the master ignores this condition.

The master/slave approach is further complicated for operation with more than two axes. A series structure, where each drive down the line has as its reference the measured speed from the previous drive, has disadvantages as already described: a drive will respond to loading changes and overload conditions seen at its reference, but its tracking performance will be related to its particular loading condition, and it will not see variations further down the chain. The chain will also be subject to inappropriate delays as the speed reference is effectively passed between drives. Reference changes will be delayed by the closed loop dynamics of all the previous drives in the chain.

A solution where a single master drive is chosen and several slave drives respond to the master speed may be appropriate for some applications, but here the slave drives are operating in what amounts to a synchronous command generation scheme. An application example where this would perhaps be suited is where a large drive is turning a relatively high inertia work piece and low inertia cutting/milling drives are

operating on this material. Again the drawbacks are that there is no slave drive feedback. As before, this would be considerably problematic if a single slave went into torque limit.

For a system where the overall number of drives is small, a scheme that adaptively controls which drive is master and which are slaves may be appropriate, but this could be subject to instability, particularly for a large number of drives. Only the simple master/slave technique is tested in the following result sections.

### 6.3.3 Cross Coupled Control

The synchronised performance of the master/slave scheme can be improved with drive cross coupling. The scheme shown in figure 6.4 can be simply modified if the measured slave drive speed is fed back to become a term in the master drive error equation. The scheme is shown, for speed matching, in figure 6.5.

Synchronisation based on an example of this technique was considered by Lorenz [136]. For a two-axis system it offers better performance than the simple master/slave. The expandability problems are similar to those described in the previous section however, being associated with the connection of the drives in a chain. Also, the modification of the error equation should be considered in the speed loop design. Gains can be included to weight the importance of relative drive speed error, compared to the error between master drive and reference speed.

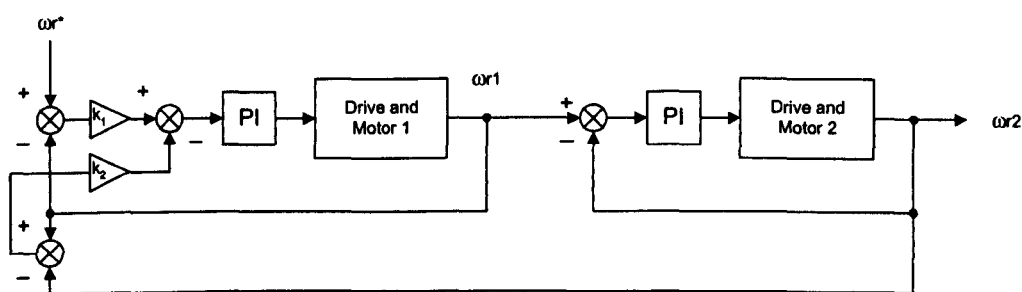


Figure 6.5. Cross-coupling of the master/slave technique

The scheme is far from ideal, because the relative error term is attempting to control a two-stage process (in this case) and may give stability problems. High gains in this part of the structure may provide good speed matching and look good in simulation, but offsets robust control of the overall process speed, which is provided by the closed loop control of drive 1. For examples such as that used in this work, where the

low inertia drive can be termed the slave, it may provide an improvement over the simple master slave structure, because for the main part of the operating range this drive will track the master with sufficiently high dynamic performance.

A parallel cross-coupling technique is shown in figure 6.6 for a two-axis system. In this scheme the speed control of each drive acts on both absolute and relative errors. In both the coupled schemes depicted, the values of gain  $k$  can be set to weight the importance of relative speed control, in contrast to absolute speed control. Alternatively a separate coupling controller could be designed and torque ( $I_q$ ) references accumulated. These gains will be further considered in the following results sections.

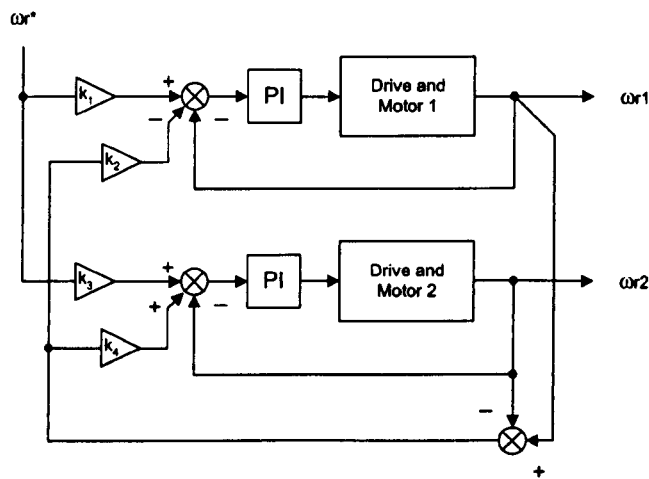


Figure 6.6. Parallel cross-coupled system block diagram

Whilst this parallel nature of design would negate the delays associated with a series chain and offer the possibility of expansion to  $n$  drives, as considered by Perez-Pinal [137], controller design is now effectively multivariable and somewhat complex. The simple structure shown is demonstrated for practical encoder and sensorless implementations in the following section, but controller design has not been optimised.

For high levels of synchronisation it will be important to set high values for the relative error importance. Although this may again look very good in simulation, it may have the effect in practice of altering the individual speed responses considerably and producing unrealistic/damaging torque variations. Again the problem is one of multi-variable control and is considered further in the encoded results section.



### 6.3.4 Virtual Line-Shafting

The fourth control scheme considered was proposed by Valenzuela and Lorenz with a view to its use in paper mill applications [123]. The scheme seeks to emulate the mechanical drive shaft connected to sectional drives in typical mill machinery, providing the slow down/speed up of the whole system in response to a load change on any of the sectional drives. The simplified scheme is illustrated in figure 6.7 and is also considered for use in filament winding [124].

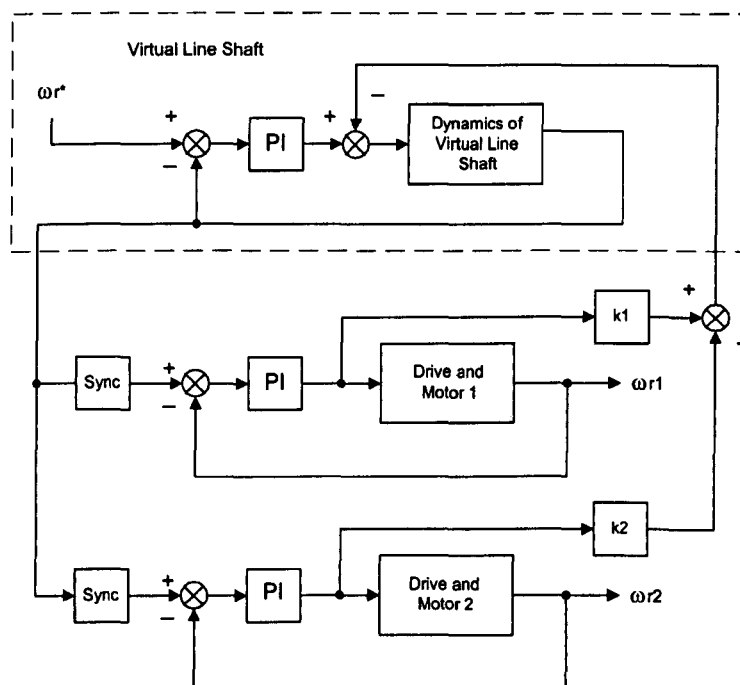


Figure 6.7. Block diagram of the virtual line-shaft system

Control is achieved by using a discretised real-time simulation of a model line-shaft, which exists in software, with associated inertia, etc. The virtual-drive responds to the overall demand speed as if it were a real system, with the output speed (and position) fed as a reference to each of the real sectional drives. Load torque ( $I_q$ ) measured on each of the sectional drives is fed back electronically to the virtual line-shaft, causing slow-down/speed-up of this shaft. This, in turn, is then translated as a variation to the reference speed to each of the sectional drives.

The algorithm can maintain a good degree of synchronism in response to variation in reference demand. The response will (and should) be dominated by the inertia of the virtual-shaft: the reference demand is rate limited by the virtual-shaft closed loop response, before being passed as a reference to the individual drives. Load variation

will also be seen in the virtual-shaft, as sectional torques are accumulated and fed back. The individual load torques thus affect the closed loop response of the virtual-shaft.

The 'sync' and 'k' function blocks shown in the scheme can be used to define the system relative kinematics. The value of k gains in the scheme can also be used in an attempt to match sectional inertias, as the effects of measured torque values on speed will of course be affected by inertial differences between the sectional drives. An effective cross coupling of the axes is inherent in the individual torque feedback to the virtual-shaft, but the effects are filtered (delayed) by the shaft. Sectional overload conditions can be readily handled in this system however, by a ramping of the reflected back load torque when under such conditions, such that the virtual-shaft speed is suitably limited [123, 124].

The virtual line-shaft system is eminently suited to sectional expansion and allows system definition, such that the resulting electronic system can be compared with a mechanically coupled counterpart (defined gearing/differential effects, etc).

### 6.4 Encoded Bi-Axial Synchronisation Results

In this section the two-drive system is tested, running the previously described methods, for speed matching, where both drives are operating under encoded IRFO control. The results presented can thus be used to analyse the performance of the various synchronisation schemes and serve as a comparative set when sensorless operation is considered in section 6.5.

Three sets of tests are performed for each scheme, which allows the synchronisation to be judged where the speed is in the transient state. The tests are as follows:

- The drives response to step changes of reference speed (an acceleration and a deceleration test) of between 200rpm and 1200rpm, with both drives operating under  $\frac{1}{4}$  rated load.
- Drive A suffers a large load torque variation, both applied and removed, of between  $\frac{1}{4}$  rated and full rated load.
- Drive B suffers a large load torque variation, both applied and removed, of between  $\frac{1}{4}$  rated and full rated load.

The two sets of load disturbance tests are performed at 400rpm. Thus the drive is operating within the defined speed range of the sensorless tuning system.

In all the presented results (encoded and sensorless) the key shown in table 6.1 is used, which defines speed and position quantities. Speed error, in all the traces, is offset and this is indicated on the right-hand side of the plots. Scaling is the same as that used and indicated for the actual speed plots.





Rig A Speed	
Rig B Speed	
Relative Speed Error	
Relative Position Error	

Table 6.1 Colour key to the speed and position measures shown in the following results

6.4.1 Synchronous Command Generation

The following results present the encoded two-drive system, running the above described tests, in synchronous command generation mode. Each drive is responding independently to similar command information. The degree of synchronisation naturally achieved in the mode will serve as a bench mark, with which to compare the results from the other schemes. The more advanced schemes will perform the same tests, under the same operating conditions.

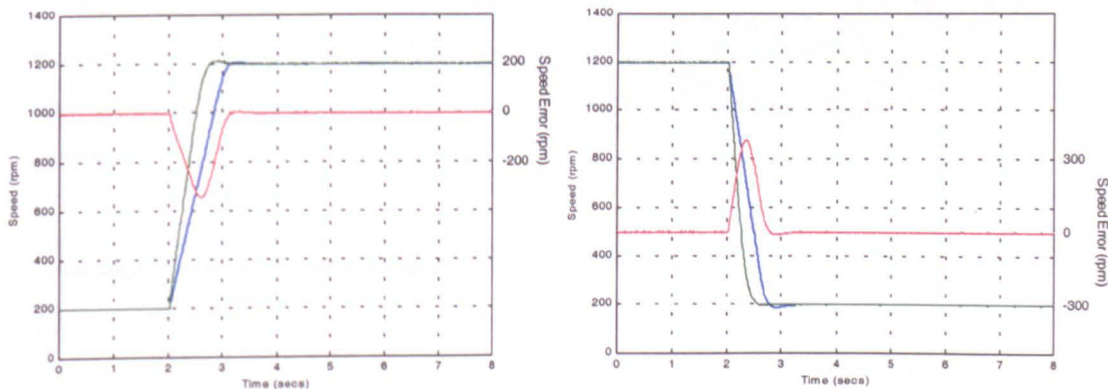


Figure 6.8. Response of the encoded synchronous command generation scheme to step changes in reference command

Figure 6.8 illustrates the degree of synchronisation naturally obtained during the reference command step tests. Each drive, although having similar loading conditions, responds to the reference change with a differing dynamic characteristic. The differing characteristic is of course due to the different inertia of each rig and is as expected. The relative speed error is shown as the red trace on each plot and this

can be seen to have a maximum value of >350rpm. The speed error will vary, for a similar command variation, where the load on each drive is different from that used here.

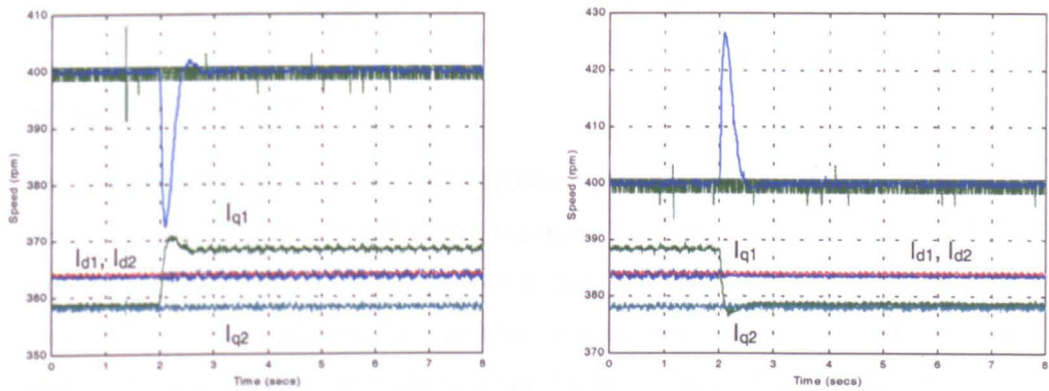


Figure 6.9. Response of the encoded synchronous command generation scheme to large and sudden variation in load torque – Rig A

In figure 6.9 drive A is seen to experience a sudden and large variation in load torque (as previously defined). The left-hand trace shows the load being applied, the right hand trace shows the load being removed. Measured  $I_d$  and  $I_q$  are shown to indicate load applied/removed and, where this test is applied in the performance testing of the other three schemes, this is not again shown. As would be expected, the drive responds individually to the load impact to correct its speed. The speed error is not explicitly shown on these traces, because the operating speed of drive B is unaffected and the error is obvious. In this case the error approaches a maximum of some 30rpm.

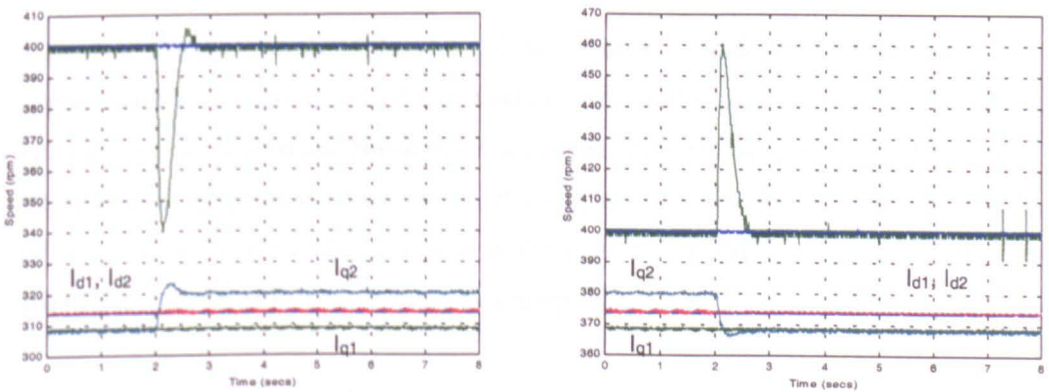


Figure 6.10. Response of the encoded synchronous command generation scheme to large and sudden variation in load torque – Rig B



A similar test is performed on rig B, as shown in figure 6.10. Here the maximum speed deviation is some 60rpm. The reason that load impacts are considered on each drive is to examine how symmetrical the following synchronisation schemes may be under load variation conditions. In this case the synchronisation is symmetrical – there is none in either direction!

6.4.2 Master/Slave

The performance of the simple master/slave scheme improves the synchronisation performance greatly, over much of the operating load range. As previously outlined, the low inertia rig (rig B) is defined as the slave and has as its demanded speed the measured master speed (rig A). Similar tests to those presented in the previous section are illustrated in the following two figures. Figure 6.11 shows the scheme responding to the step variation in reference demand.

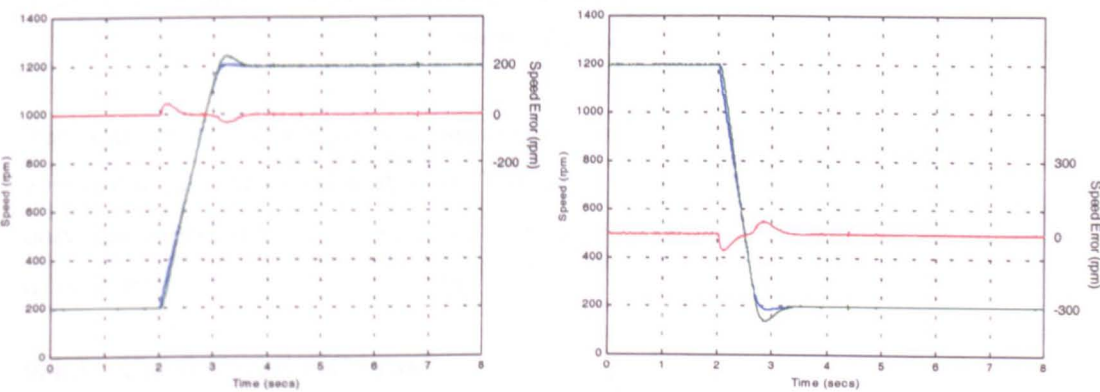


Figure 6.11. Response of the encoded master/slave scheme to step changes in reference command

It is clear that the speeds of the two drives are now a much-improved match. The speeds during the major part of the transient have minimal error and only a small error is seen at the start and finish of the transient, due to drive B settling. This could be alleviated by perhaps adjusting the characteristics of the speed controller in this drive. It must be remembered that now drive A is responding to a step change in speed demand, drive B is responding to a ramp.

Similar synchronisation performance under speed demand variation will be obtained, given that the low inertia slave is not operating under load conditions that limit its response. Should this be the case, some form of reference limiting would be required.

The speed tracking performance of the scheme is shown in figure 6.12 for the rig A load impact test. The  $I_d$  and  $I_q$  traces have been replaced with a plot of speed error, as the speed error is now more difficult to directly distinguish. The slave speed is seen to successfully track the master speed and the speed error is greatly minimised when compared with figure 6.9.

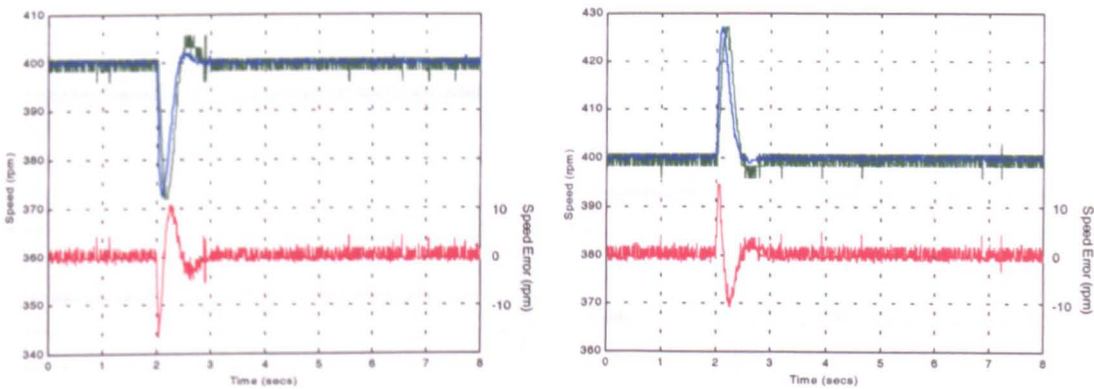


Figure 6.12. Response of the encoded master/slave scheme to large and sudden variation in load torque – Rig A

The response of the scheme to a load impact on rig B is not shown, as it would be identical to that shown in figure 6.10. The speed coupling between drives is one-way only and variations seen on rig B will not be observable by rig A. The following three schemes look at how this can be improved.

6.4.3 Cross Coupled Control

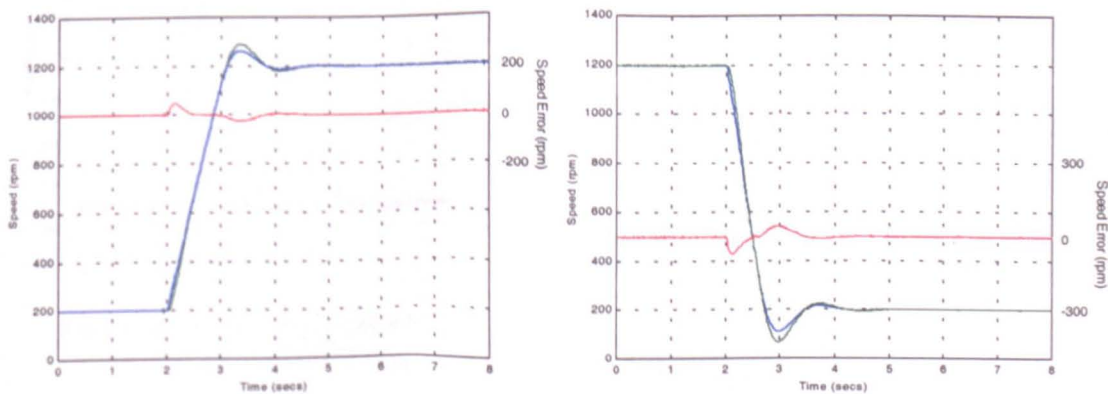


Figure 6.13. Response of the encoded cross-coupled master/slave scheme to step changes in reference command

Figures 6.13 and 6.14 show the response of the revised master/slave scheme, for the speed demand variation and rig A load impact tests respectively, where the measured

rig B speed has been fed back as a term in the rig A speed controller error equation. Referring back to figure 6.5, the gains  $k_1$  and  $k_2$  are set at 0.333 and 0.667 respectively, such that relative error is given twice the importance of absolute error, although the overall error multiplication factor is 1.0. This is in an attempt not to drastically affect the speed control response/design.

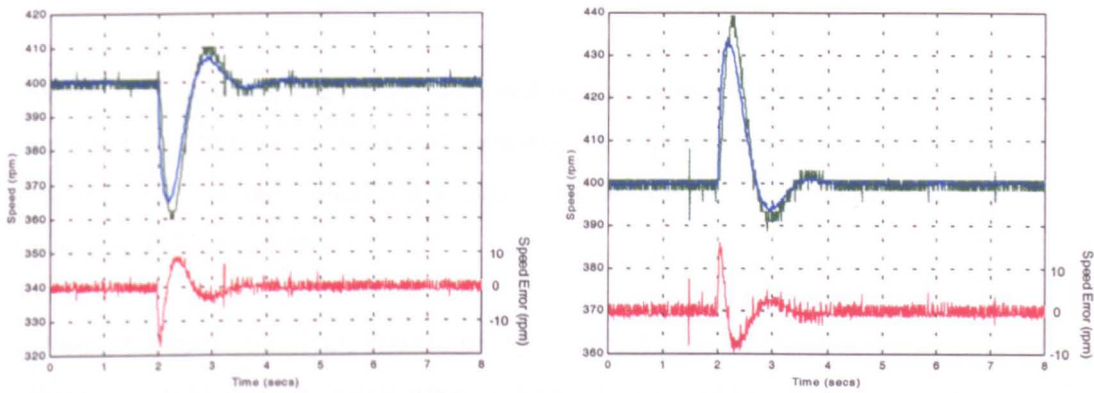


Figure 6.14. Response of the encoded cross-coupled master/slave scheme to large and sudden variation in load torque – Rig A

If these results are compared with those of figures 6.8 and 6.9, it is clear that, whilst the drive cross-coupling has affected the rig A speed response slightly, the results are similar. The error band during the load transient is still in the region of  $\pm 10$ rpm.

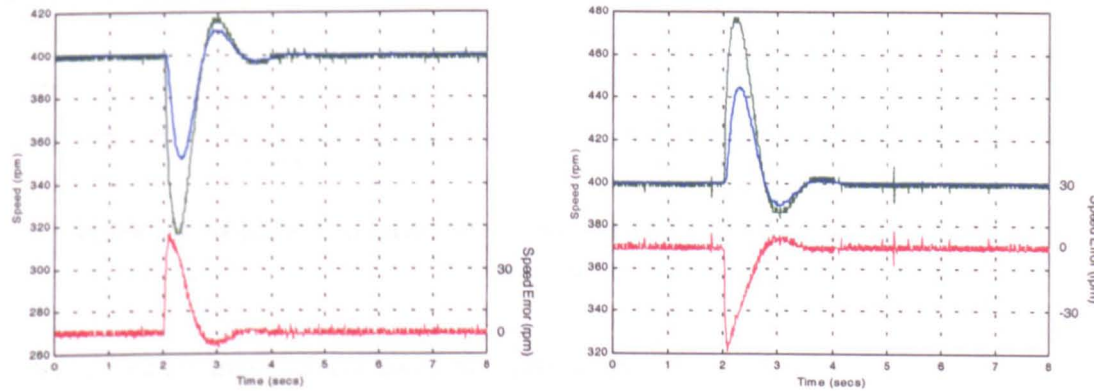


Figure 6.15. Response of the encoded cross-coupled master/slave scheme to large and sudden variation in load torque – Rig B

Figure 6.15 shows the response of the coupled system to a drive B torque impact. It can be seen that rig A responds to the speed variation seen on rig B. Whilst this is the case, the correcting response of rig B is affected by the cross-coupling. As opposed to a 60rpm variation in speed, due to the sudden load torque applied/removed, seen in the rig B response of figure 6.10, the rig B speed is now seen to vary by 80rpm. The



maximum relative speed error however, is reduced by some 12rpm. In this scheme, with the two drives effectively in series, the cross-coupling term is trying to control a two-stage process (synchronisation) of much increased inertia. Although not considered here, it is suggested that such a scheme may benefit from a more involved coupling control design/simulation. A large disadvantage is still the series nature of the scheme and this makes the solution eminently unsuitable for extension to  $n$  drives.

Where the cross-coupling control is carried out in a parallel structure, as illustrated in section 6.3.3 (figure 6.6), the speed variation test response is shown in figure 6.16.  $k$  gains are set similarly, such that  $k_1$  and  $k_3$  in the scheme block-diagram are 0.333, whilst  $k_2$  and  $k_4$  are 0.667.

During the speed transients shown, the speed matching is seen not to be as good as that demonstrated by the master/slave scheme. It is a definite improvement over that of synchronous command generation however. The bowing seen between the drive speeds is due to the speed control responding to both absolute and relative errors.

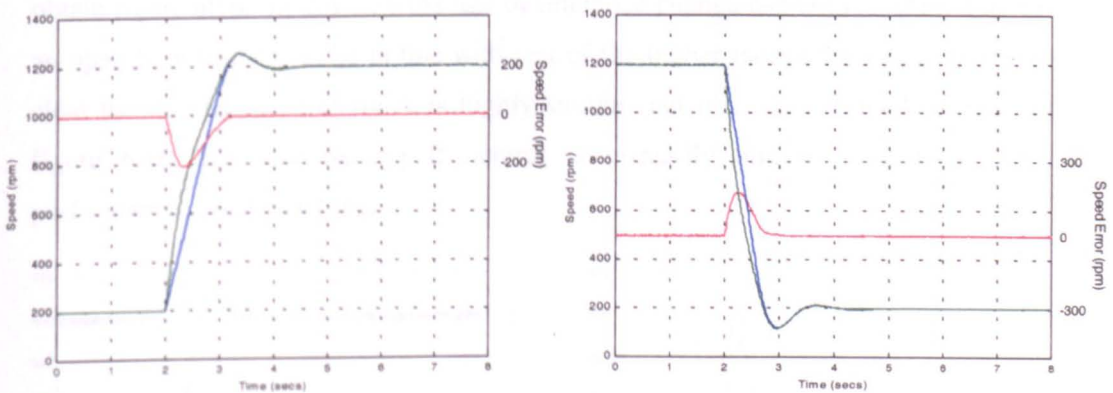


**Figure 6.16. Response of the encoded cross-coupled scheme to step changes in reference command**

An immediate improvement could be made to the scheme if the rate-of-change of reference demand is sensibly limited. With synchronous command generation reference limiting in an open-loop fashion would have to be severe to obtain any form of synchronisation. In this cross-coupled scheme it would simply be necessary to limit the maximum error seen by each speed controller due to large variations in demand speed. In figure 6.16 the response is at first dominated by a reaction to the sudden and large reference variation. As the speed controllers act to reduce this error, the relative speed error becomes significant and this then dominates the response.



Note that the relative error observed is some 40% to 50% less than that seen during the synchronous command tests.

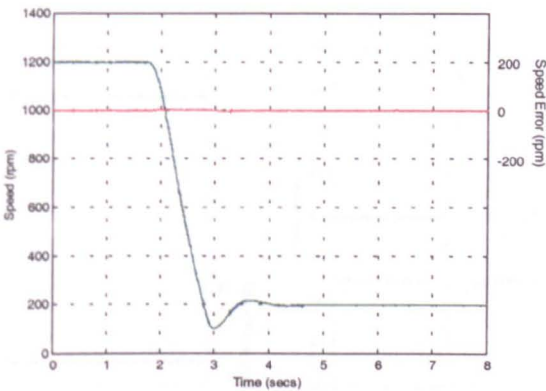


Figure 6.17. Response of the encoded cross-coupled scheme to an effective step change in the reference command (deceleration), but with reference rate of change limited

Figure 6.17 demonstrates the parallel cross-coupled scheme remaining synchronised during the deceleration test, under the same operating conditions as those used to obtain figure 6.16. In this case the rate of reference change has been limited, only in an open loop fashion, to be in line with that of the higher inertia drive (rig A). It is clear that the response of rig A is highly similar (not obviously limited) to that in figure 6.16, but now the rig B control is primarily utilised to provide high performance speed matching.

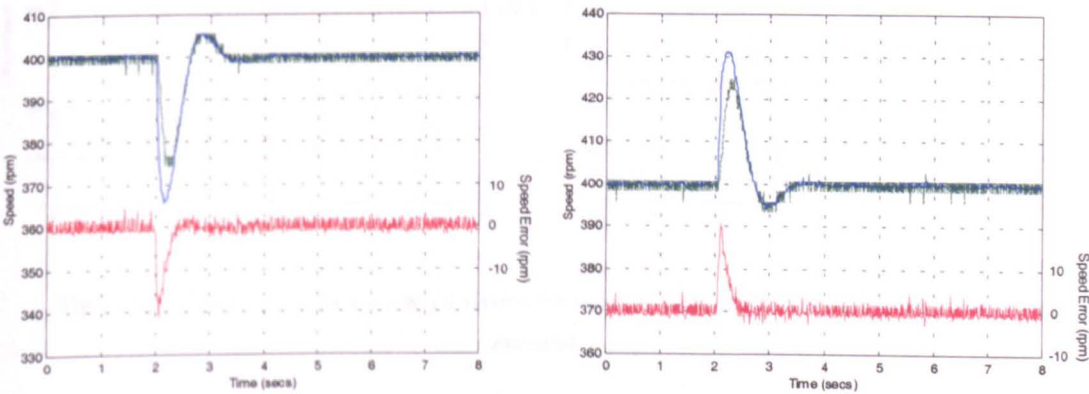


Figure 6.18. Response of the encoded cross-coupled scheme to large and sudden variation in load torque – Rig A

The parallel cross-coupling scheme during load impacts can be seen to remove much of the error seen in the original synchronous command results. Figure 6.18 shows the speed response during the rig A impact, whilst figure 6.19 shows that during an impact on rig B. In figure 6.18 the maximum speed difference is seen to be around

20rpm. In figure 6.19 the speed difference is less than 40rpm. Again the process of cross-coupling is seen to slightly alter the absolute speed response of the drives considered individually.

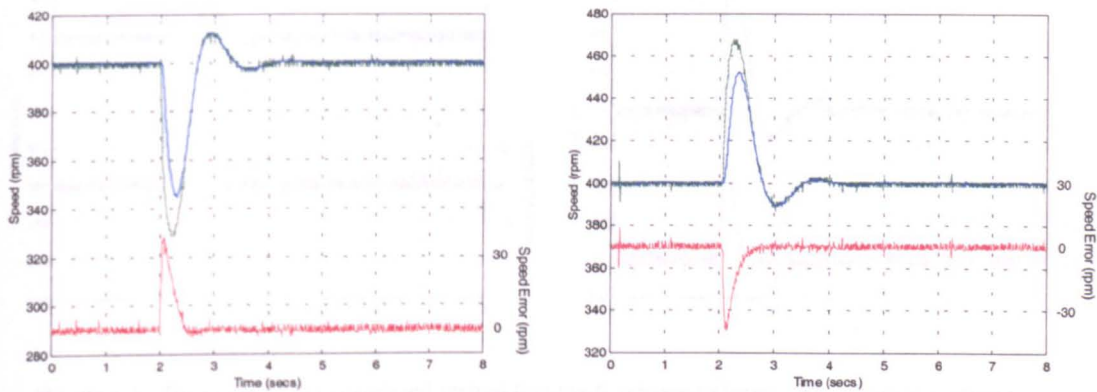


Figure 6.19. Response of the encoded cross-coupled scheme to large and sudden variation in load torque – Rig B

6.4.4 Virtual Line-Shafting

The acceleration and deceleration responses of the encoded virtual line-shaft system are shown in figure 6.20.

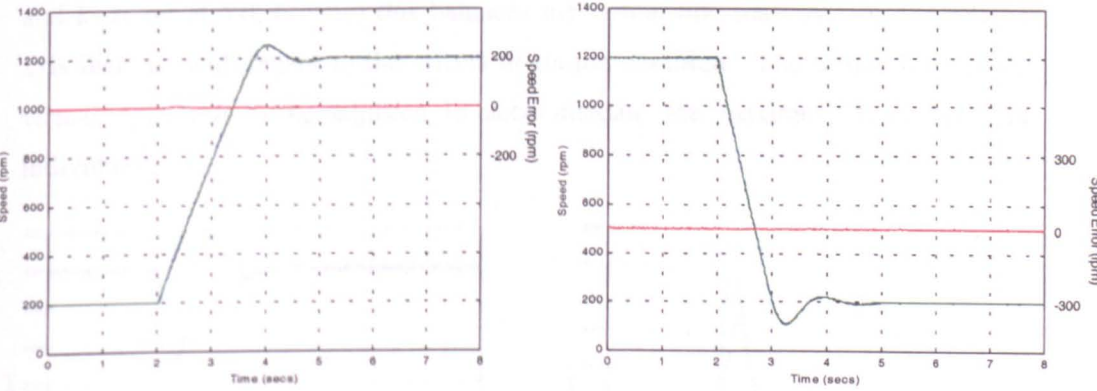


Figure 6.20. Response of the encoded virtual line-shaft system to step changes in reference command

The line-shaft scheme is seen to display excellent synchronisation performance during speed transients. Note however, that the acceleration and deceleration rates have slowed due to the large inertia of the virtual-shaft (here set to twice that of rig A  $\therefore 0.6\text{kgm}^2$ ). As the estimated individual drive torques are reflected back, the acceleration rate is varied such that it can be achieved by both drives. The inertia of the virtual-shaft was chosen as  $0.6\text{kgm}^2$  simply as a ballpark figure, where this is the

combination of the two drive inertias ( $0.3\text{kgm}^2$  and  $0.12\text{kgm}^2$ ), with some allowance for the inertia of a *replaced* mechanical speed coupling system.

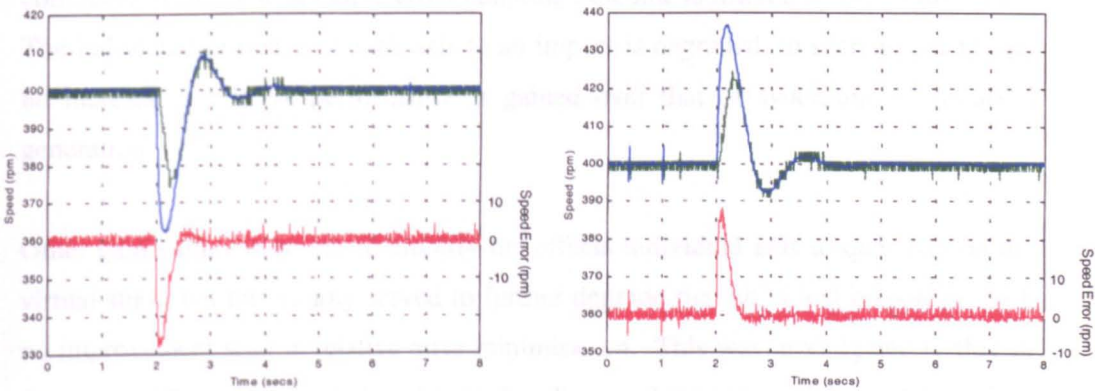


Figure 6.21. Response of the encoded virtual line-shaft scheme to large and sudden variation in load torque – Rig A

The virtual line-shaft performance under load impacts is shown in figures 6.21 and 6.22. Referring to the schematic of figure 6.7, in the case of these tests the sync functions are gains of 1.0, for speed matching. The  $k$  gains are set in an attempt to match the speed variation seen on the virtual-shaft, to that seen as loads on the individual drives. Drive 1 in the figure is rig A in this work, and thus  $k_1$  is set at 2.0 and  $k_2$  is set at 5.0, because this balances the virtual line-shaft system and relative axis inertias, with regard to the effects of torque variation. The torque limit in the virtual system must be adjusted to accommodate the maximum from both the individual drives.

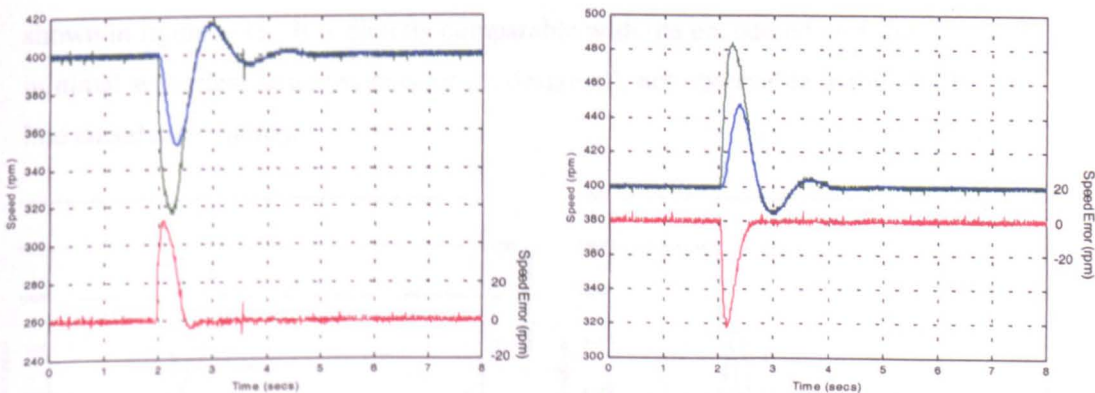


Figure 6.22. Response of the encoded virtual line-shaft scheme to large and sudden variation in load torque – Rig B

The two figures show responses that are not dissimilar in shape from those of the parallel cross-coupled scheme. Speed variation seen on each axis is reflected, through the virtual-shaft, such that a response is obtained from the alternative axis. If



however, the relative speed error is analysed and compared with figures 6.9 and 6.10, it is evident that the scheme does not greatly reduce the error seen in synchronous command mode. The effective cross-coupling outcome is filtered by the virtual-shaft. The individual response of each axis to an impact is degraded, to such an extent that no increase in relative performance is gained over that of synchronous command generation.

Other gain values were set, to amplify the effects individual axis torques had on the virtual-shaft, but this simply served to further degrade the individual responses, with no improvement seen in relative error minimisation. This was investigated further in the work of Perez-Pinal [137], and is further discussed in sections 6.7.2 and 6.8.

6.5 Sensorless Bi-axial Synchronisation Results

In this section the tests are repeated, with both drive rigs running under sensorless control, and with the drive tuning algorithm operational. Only sensorless speeds are used throughout the various control schemes, although encoder measured speed is that used to produce the presented results. These results can be directly compared with those obtained using the encoded system, as in all of the more involved synchronisation structures the same gain values are used.

6.5.1 Sensorless Synchronous Command Generation

The sensorless synchronous command acceleration/deceleration performance is shown in figure 6.23. It is directly comparable with the encoded performance, with minimal sensorless steady state error (as designed), not observable within the 10,000-line encoder resolution.

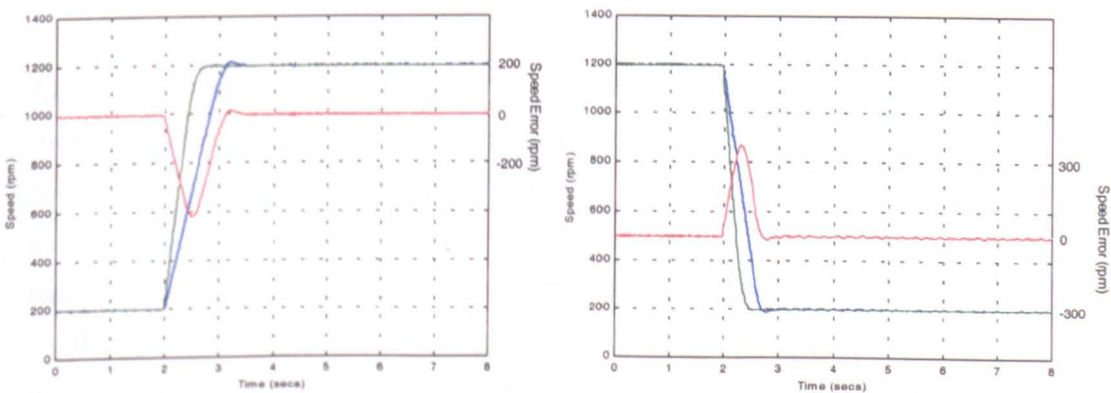


Figure 6.23. Response of the sensorless synchronous command generation system to step changes in reference command

The load impact performance of the sensorless scheme is tested and shown in figures 6.24 and 6.25. Again the load torque is stepped on/off at 2 seconds in each trace, with the same values used as in all of the encoded drive tests. Figure 6.24 shows load applied (left-hand trace) and removed (right-hand trace) from motor drive A, whilst figure 6.25 is for motor drive B.

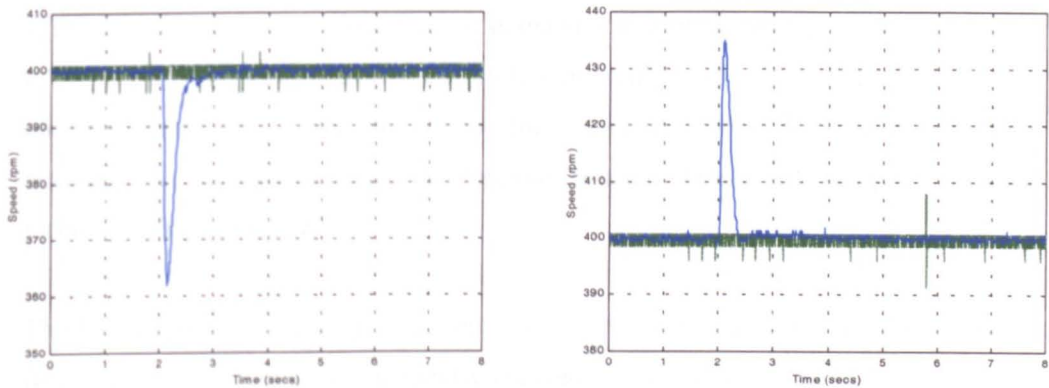


Figure 6.24. Response of the sensorless synchronous command generation scheme to large and sudden variation in load torque – Rig A

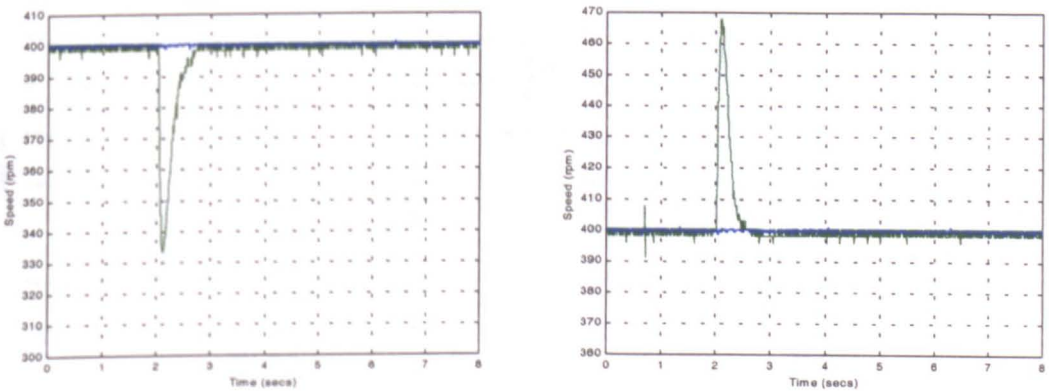


Figure 6.25. Response of the sensorless synchronous command generation scheme to large and sudden variation in load torque – Rig B

Again the performance of the sensorless scheme is suitably comparable with that shown in the encoded results, running this particular control method (figures 6.9 and 6.10). Speed variation at impact on drive A is around 35rpm, compared to just under 30 rpm in the encoded response, with the small variation due to the model-based speed estimate (dynamics and accuracy due to variation of parameters). In the rig B response of figure 6.25 the maximum speed deviation from the reference has risen a little, from 60rpm to around 68rpm. These values can be compared with the sensorless performance shown in the following sections, where the remaining three synchronisation techniques are considered.

6.5.2 Sensorless Master/Slave

During the development of this work the performance of the developed tuning algorithm operating in a speed synchronised master slave scheme was presented at conference [16].

The sensorless scheme responding to demand variation is here presented in figure 6.26. Again the performance is certainly comparable with that obtained using the encoded solution. In the steady state the sensorless system displays encoder like accuracy. In the transient state the coupling scheme ensures that the relative speed error is greatly minimised.

The load impact performance is shown, where the load to rig A is suddenly varied, in figure 6.27. The speed error is greatly reduced from that shown in figure 6.24. The equivalent response for a rig B impact is not shown, because there is no coupling in this direction. The response obtained would be identical to that shown in figure 6.25.

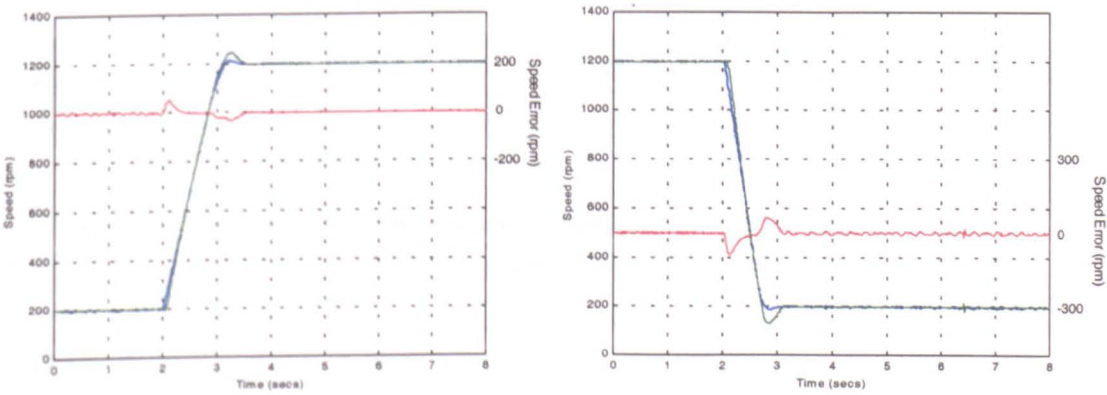


Figure 6.26. Response of the sensorless master/slave system to step changes in reference command

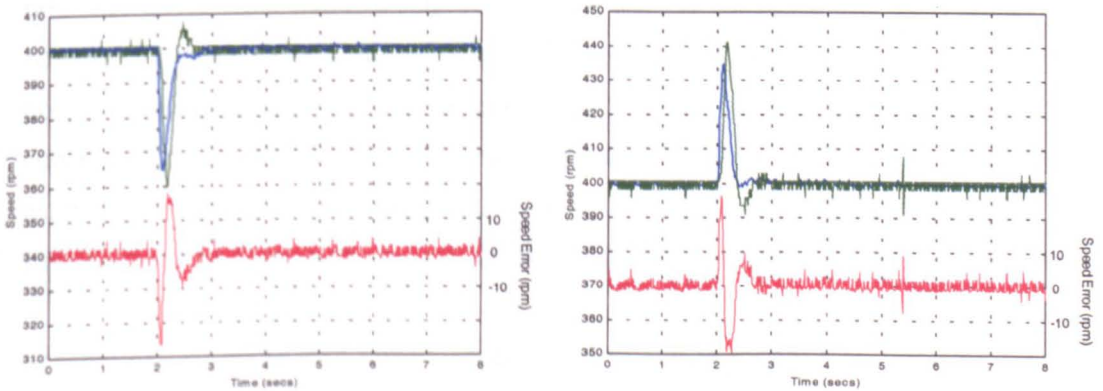


Figure 6.27. Response of the sensorless master/slave scheme to large and sudden variation in load torque – Rig A



6.5.3 Sensorless Cross-Coupled Control

The previous section showed that cross-coupled control based on the series configuration, although offering some advantages over the simple master/slave scheme, was perhaps not as an attractive proposition as the parallel cross-coupled approach. The sensorless results are therefore not presented here, but are included in Appendix K.

For the parallel cross-coupling configuration the relevant three sets of test results are presented as the following three figures. Figure 6.28 shows the acceleration and deceleration performance.

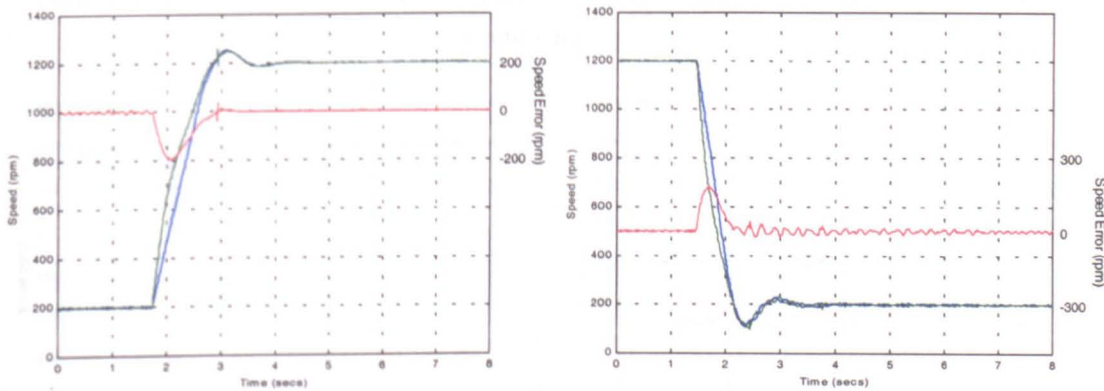


Figure 6.28. Response of the sensorless cross-coupled scheme to step changes in reference command

The performance shown is again very similar to that of the encoded mode, with excellent (encoder-like) synchronisation/accuracy in the steady state. The error accrued during the transient is similar also, and due to the scheme acting on a large reference error. This could be improved, as already mentioned/shown, by reference command rate-of-change limiting. In both traces the scheme is seen to be slightly noisier at the lower speed, due to the model-based scheme and inverter/measurement considerations, as discussed in previous chapters, causing a slightly noisier speed estimate. The speed estimate now has a noise-band that is an accumulation of that from both drives, because the two estimates are compared to produce a relative error.

Synchronisation under load impact conditions is shown in figures 6.29 and 6.30, for impacts on rig A and rig B respectively. When comparing with the encoded conditions, the immediate speed variation on impact is larger in the sensorless

scheme, but this is due to the model-based method and as seen in the synchronous command results. Good synchronisation performance is achieved.

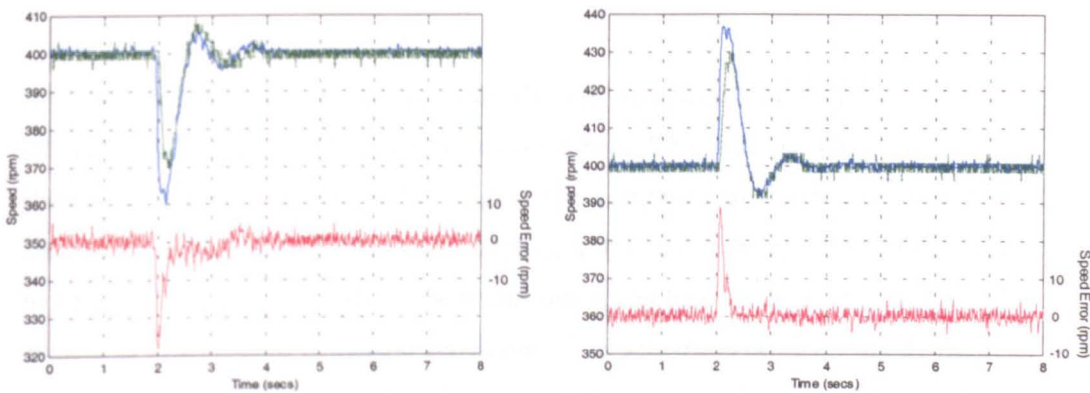


Figure 6.29. Response of the sensorless cross-coupled scheme to large and sudden variation in load torque – Rig A

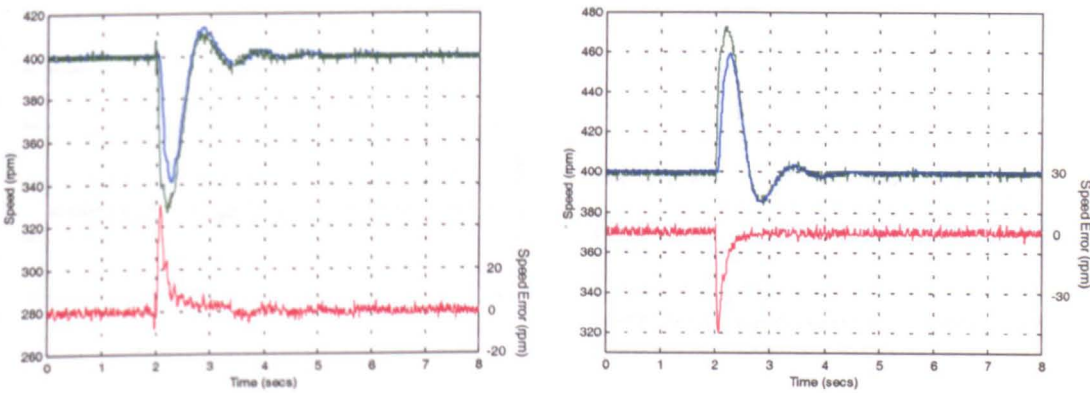


Figure 6.30. Response of the sensorless cross-coupled scheme to large and sudden variation in load torque – Rig B

6.5.4 Sensorless Virtual Line-Shafting

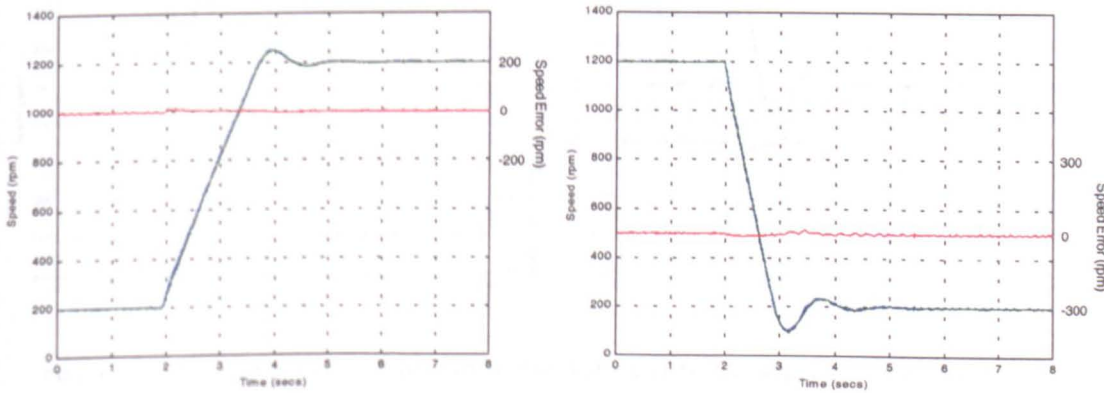


Figure 6.31. Response of the sensorless virtual line-shafting system to step changes in reference command



Figures 6.31 to 6.33 demonstrate the sensorless tuning drive performance when operating the virtual line-shaft synchronisation scheme, and all compare well with the encoded results.

In figure 6.31 the drive speeds are evidently well matched in the transient, due to the inherent limiting provided by the virtual reference. The load impact performance is shown in figures 6.32 and 6.33. Again the responses are comparable with the encoded results. Due to the drive coupling in this mode being effectively filtered, by the inertia of the virtual-shaft, the immediate speed loss on impact is similar to that evident in synchronous command generation. The scheme is however highly flexible, being easily extended to multiple drives, having categorised gains, differentials, etc that can be used to model a given system specification.

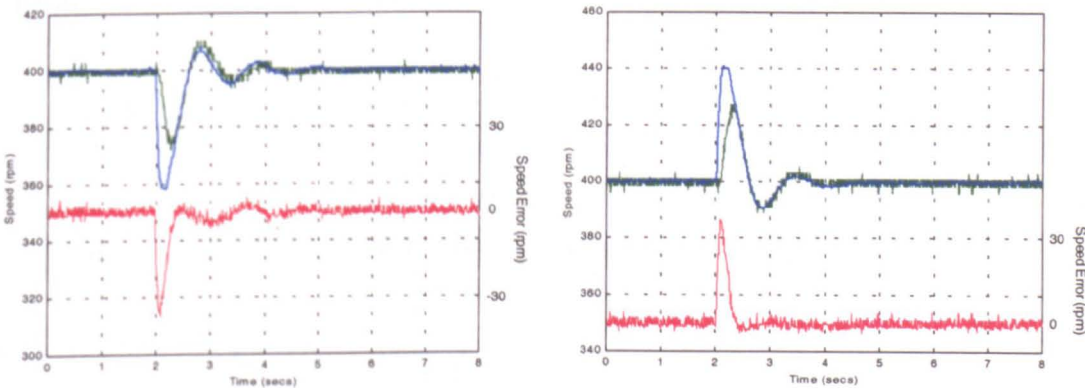


Figure 6.32. Response of the sensorless virtual line-shafting system to large and sudden variation in load torque – Rig A

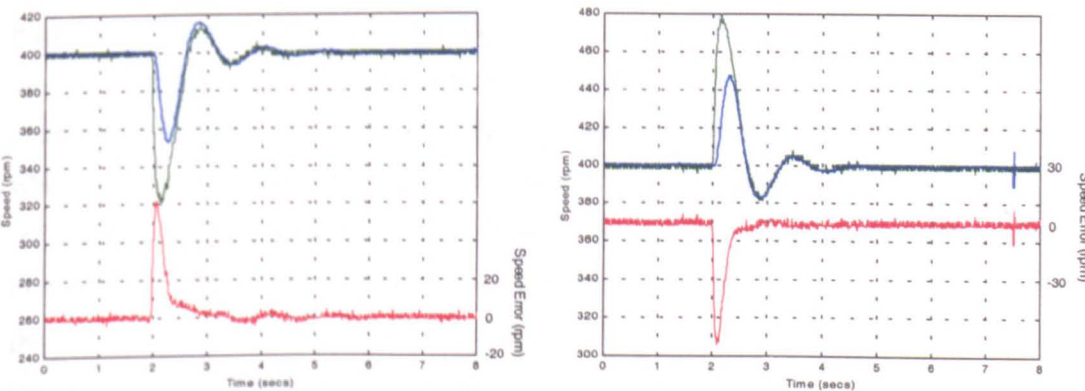


Figure 6.33. Response of the sensorless virtual line-shafting system to large and sudden variation in load torque – Rig B

## 6.6 Position Synchronisation

Although the sensorless solution running on the two drive rigs was engineered for steady state speed holding capability, and the performance of the scheme for such has been demonstrated in the previous section, it was considered worthwhile to test the capability of the scheme to correct incremental position error.

In the previous chapter it was shown that the ASO (model-based) speed estimate is not guaranteed to track the true speed without error **during** load transients, but if some form of incremental position correction were available this may be beneficial in particular applications. The speed control system used in the two drives was modified to include positional correction terms. The technique was applied in the parallel cross-coupled control method, shown to offer good speed synchronised performance in the previous sections.

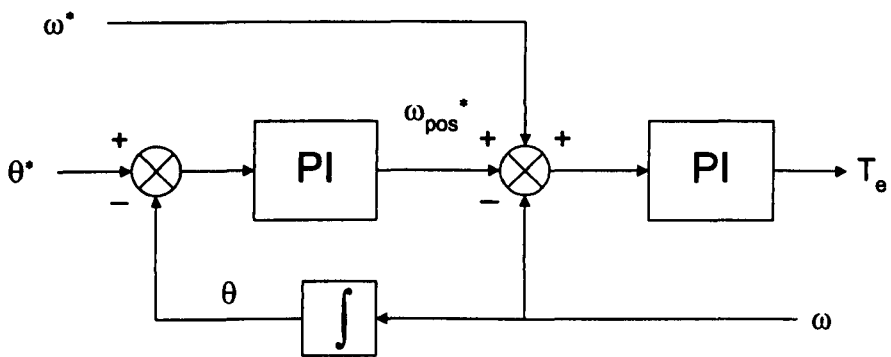


Figure 6.34. Structure of the speed/position controller

Figure 6.34 shows the position controlling type structure. A speed quantity is turned into an incremental position value through integration. The incremental position is compared with a reference value and the error used to drive a PI control mechanism whose output is speed. The motor synchronisation schemes can be modified to include position following using this structure. In the cross-coupled scheme, shown in figure 6.35, the relative speed error is integrated to give an incremental relative position error. A slow PI control mechanism was developed in simulation to tune out the position error between the two drives, with the correctional term fed into the speed control summing junction of rig A. A more involved design would be required for systems with more than two drives, but here the method is used simply to test the viability of the scheme.

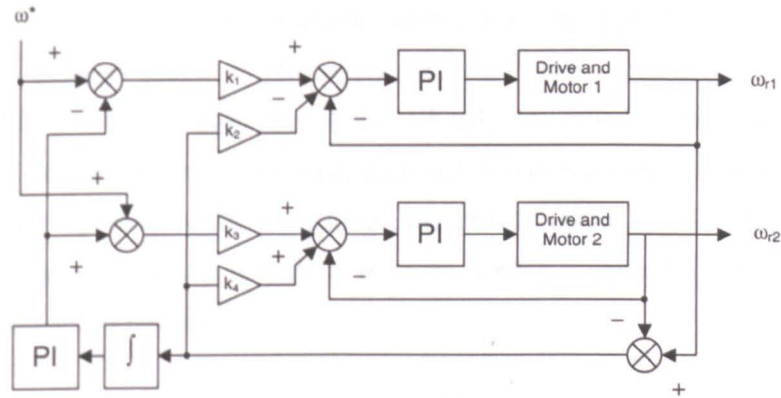


Figure 6.35. Modified structure of the parallel cross-coupled scheme, to include relative position correction

Figure 6.36 again shows the rig A impact performance of the encoded parallel cross-coupled scheme, as previously shown in figure 6.18. In the new figure however, the incremental mechanical position error between the two axes, incurred as a result of the sudden load torque transient, is plotted in black. The error magnitude is approximately 20 degrees as the scale for position is 40 degrees/division. At  $t = 0$ s, the position error trace is zeroed and is thus offset in each of the plots.

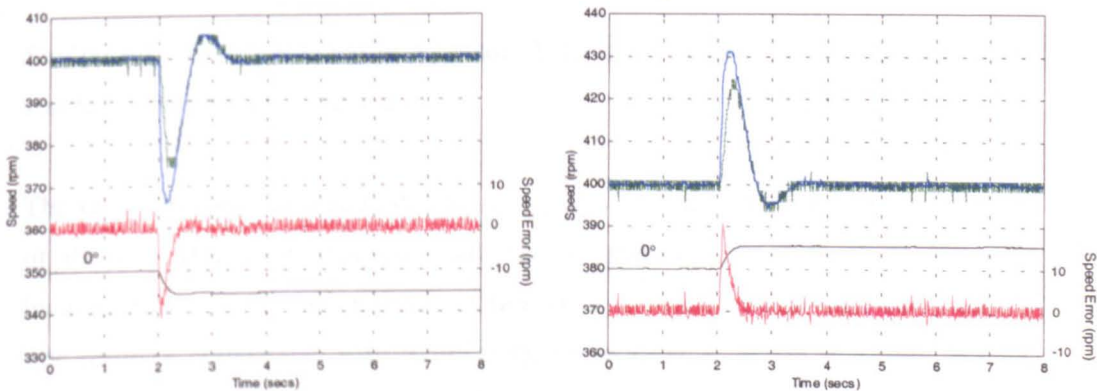


Figure 6.36. Response of the encoded cross-coupling scheme to large and sudden variation in rig A load torque. Relative position error is shown in black and positional correction is not included

Figure 6.37 shows the impact performance of the rig A drive with encoder feedback and with the positional correction terms included in the control structure. Note that the error accumulated at the moment of impact is removed with little alteration of the drive speed response. Some small amount of deviation and creep can be seen on the slope of the position plot and this is due to noise pick-up on the incremental encoder signal (the reset pulse is not used) and sampling effects. In other words, the position



signal is obtained by integrating the speed measured by the encoder, itself obtained by differentiating an incremental position signal! With the type of encoder used, the incremental position output is effectively corrected each revolution using a reset channel, but this causes problems if not robustly identified. For this work the incremental pulse trains only were used, such that erroneous count values accumulate, but this is not a problem if differentiating the signal to obtain speed. Integrating an encoder-measured speed was thought to be more directly comparable with integrating the sensorless speed estimate.

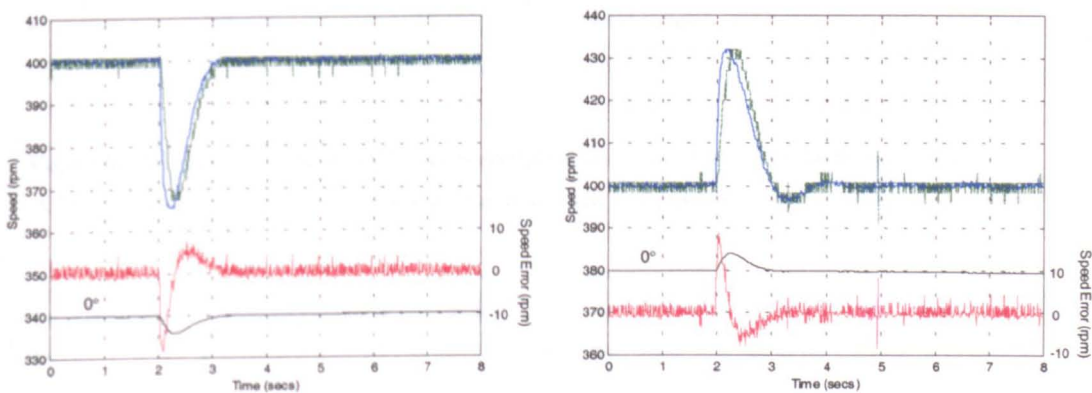


Figure 6.37. Response of the encoded cross-coupling scheme to large and sudden variation in rig A load torque. Relative position error is shown in black and positional correction is included

Similar results are presented in Appendix L for the tests carried out on rig B and a similar performance is obtained.

The sensorless performance is shown in figures 6.38 and 6.39. Figure 6.38 is a copy of the sensorless cross-coupled result shown originally in figure 6.29, but now includes traces of the incremental position error accumulated through the transient. The result is comparable with figure 6.36, but noticeable in the sensorless results, particularly as load is stepped on (left-hand trace), is an increased positional error due to the greater speed error and the tuning effect. Note that the steady state position signal in both traces is particularly flat and this signifies excellent speed matching in this region. Figures 6.38 and 6.39 are repeated for rig B and presented in Appendix M.

Figure 6.39 shows the sensorless synchronised response where position correction terms are included in the control, based on an estimation of position obtained from the integrated sensorless ASO speed. In both traces the position correction is shown to not correct the absolute error accumulated, although it comes pretty close where

the load is stepped off, but to facilitate a degree of correction and certainly constrain the errors seen in figure 6.38.

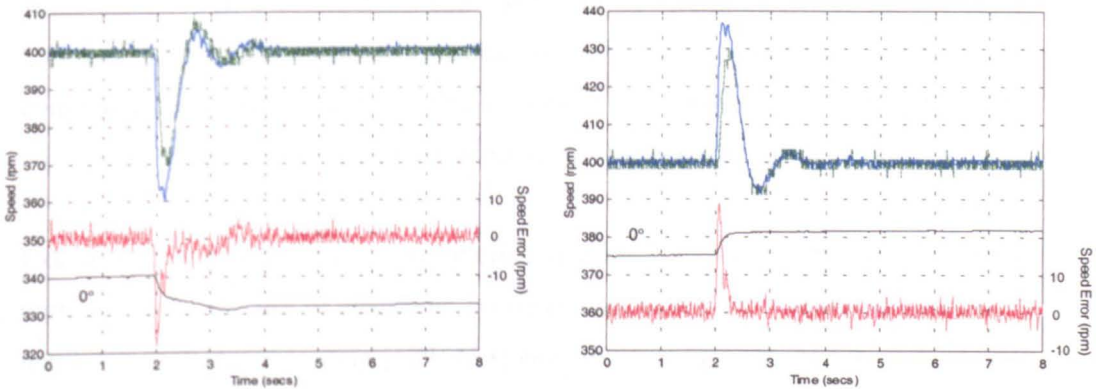


Figure 6.38. Response of the sensorless cross-coupling scheme to large and sudden variation in rig A load torque. Relative position error is shown in black and positional correction is not included

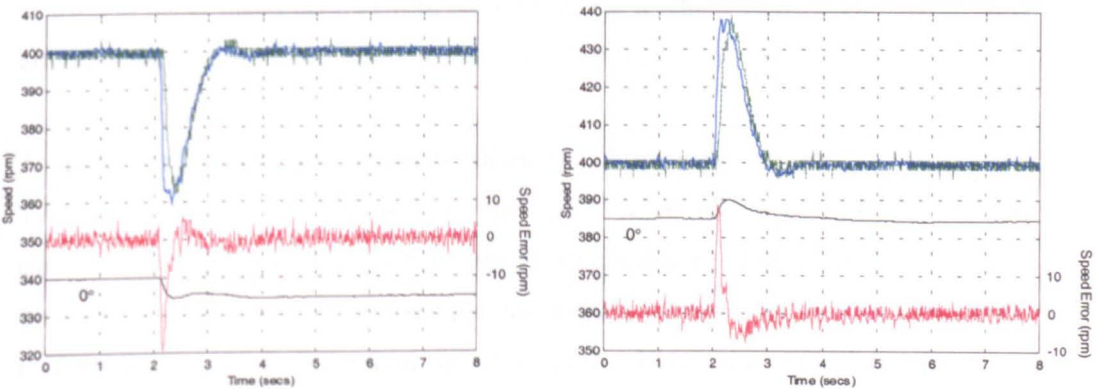


Figure 6.39. Response of the sensorless cross-coupling scheme to large and sudden variation in rig A load torque. Relative position error is shown in black and positional correction is included

## 6.7 Considering Applications and Improving/Extending the Synchronisation Schemes to n Drives

It is considered appropriate that this chapter contains a short section on the development of the synchronisation schemes, for use with larger systems, and some more detail regarding applications exploiting multi-motor control. Although the aim of the project was the development of a speed holding sensorless method, and the demonstration of that method for speed synchronisation, it is important to relate the outcome of the work to intended application.

6.7.1 Applications

Much information regarding application of multi-motor control is available on drive manufacturer web sites, such as those belonging to Control Techniques, ABB, and Siemens. Mainly this constitutes information pertaining to motor drives systems and communication architectures. Other web sites consider the motion control advantages of using multi-motor techniques, but few describe application detail.

Examples of applications in manufacturing that have been presented in more depth, with a view to the use of electronic synchronisation, include packaging [127, 129], textiles manufacture/handling [129, 138] and electronic gearboxes for gear grinding [128]. Applications most often discussed however, with regard to multi-motor control, are sheet steel production and processing [127, 128], but particularly those applications involving paper. Several references note the use of multi-motor control as used in paper manufacture (from pulp) [123, 127], whilst other works (particularly articles) discuss ‘shaftless’ printing-press systems [127, 130, 131].

A quite useful text that generally discusses motor applications is the Control Techniques - Drives and Servos Yearbook [127]. Many of the examples it considers can be envisaged to make use of speed synchronised stages, some offering a description of such. A simple example, taken from the yearbook, is shown in figure 6.40, making use of differential speed control. Here two conveyors are run at different, but related, speeds to vary the delivery rate of a product to different parts of a process. Such an application, albeit somewhat simple, would be highly suited to the sensorless system developed. It is envisaged that such a process, forming part of a larger system, would operate at fixed speed and under a reasonably constant load.

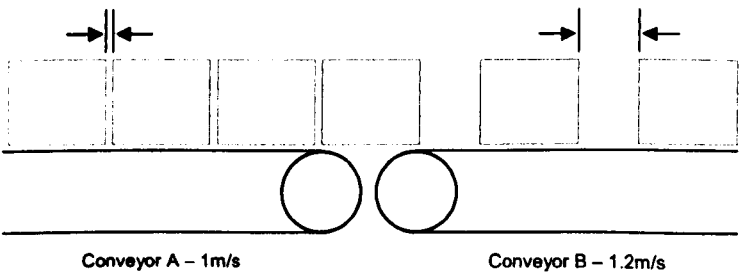


Figure 6.40. Differential speeds to achieve product delivery rate variation

As another example, paper manufacture will be considered in more detail. It is in this area that Valenzuela and Lorenz direct their work on the electronic line-shafting system [123].

### **Paper Manufacture**

Paper is manufactured from wood pulped with water. Originally the pulp material would have been drained, pressed and dried by evaporation, effectively making paper on a sheet by sheet basis [127]. Now paper making machines generally manufacture paper rolls, at speeds in the region of 1000 to 2000 m/s, with web widths of up to 5m [127].

A typical process consists of three main functions [127]. Firstly there is a 'wire-section', where pulp is fed in and the consistency controlled through draining/drying. The wire-section feeds the very raw paper into 'press and drying sections', which may be of several stages. It is in these sections that speed differential controls are exploited to control the paper quality and specification. The final paper product is finally collected on a reel (at the 'reel-section'). Supplementary to this system may be various 'winding and cutting stages', where paper is processed to suit further applications, such as printing [127, 130, 131].

Without exploring too deeply, there are various processes here that have different requirements in terms of motor drive selection. There is a definite advantage in the use of robust sealed AC machines in the wire, press and drying sections for example, the environment of which may not be suited to DC motor use. For similar reasons, the developed sensorless scheme could be exploited, as conditions are far from ideal for encoder fitting. These stages may operate under constant average speed and load conditions, with the initial stages correcting speed, due to load torque impacts. In many cases the motors may drive sections through reduction gearboxes [127], which would suit the developed algorithm: the drive induction motor operating out of the low speed region. Starting considerations are such that material is fed into a system running at speed. Thus there is no co-ordinating force required at start-up (low-speed). The reel section must be run with a varying speed, because the material surface speed must be maintained, but it is suggested that the dynamic of speed variation in this stage may not be excessive, such that the tuning system (in the developed sensorless method) may be constantly enabled. The supplementary winding stages will have similar operating conditions.

It is considered that many of the manufacturing examples, stated at the start of this section, may make use of the developed sensorless system. Multi-motor control must be used in these examples, because a large production/processing system is required to be co-ordinated.

### **Electric Vehicles**

Another notable application area, where multi-motor control is exploited, is the design/operation of electric vehicles (EVs). The traditional mechanical transmission, associated with internal combustion engine vehicles, can be removed in EVs, with motors driving each driven wheel independently [133]. Apart from the removal of large and heavy mechanical components, one of the advantages of electric motor use is in the fact that, unlike the standard internal combustion engine, the electric motor can be operated to provide rated torque throughout their rated speed range. Thus this very often fulfils the required torque/speed operational characteristics of vehicle operation, without the need for variable gearing. The advantages of AC motor use, over that of its DC counterpart, are again related to its greater reliability, robustness and low maintenance requirements. EVs are also a hostile environment for the use of a shaft-mounted encoder, which would suffer significant vibration and be highly liable to damage [134]. It is also considered that they may be difficult to fit.

In internal combustion engine vehicles, mechanical devices provide functions, such as differentials, traction control and anti-lock braking. In EVs these functions could be performed using electronic balancing/synchronisation methods [135]. Some of the functions may be provided through management of torque sharing in the motor drives, others may require the measure/estimate of speed.

In the sensorless method developed in this project, the operation is without tuning in the low speed region. This is however, a realistic operating region for the EV. Remember that standard model-based performance is available, from the developed system in this region however, and this may be sufficient. It would be interesting to further explore this application, with a view to drive requirements.



**6.7.2 Extending the Synchronisation Schemes**

A particularly important consideration with regard to the presented synchronisation methods, particularly in the manufacturing process examples, is in how easily they can be extended for use with multiple ( $n$ ) drives. The requirement for such expansion has been somewhat considered as the chapter has progressed.

Using the paper-manufacturing example, the wire-section may often set the speed reference for the overall process [127]. Given that the following sections are controlled with sufficient dynamics/stiffness, then the entire process is controlled within tolerance. Thus the method effectively uses a master/slave approach, with multiple open loop slaves following the wire-section master [127]. Such a method is preferred to operating a series structure, due to the problems already discussed, with regard to delaying reference signals. Processes such as machining applications reportedly make use of the simple synchronous command type structure [129, 130], where servo performance tool-piece drives are used, such that loading effecting individual drives does not cause the component to go out of tolerance.

In this work the higher performance synchronisation schemes have been demonstrated to be that of the cross-coupled technique and that of the virtual line-shaft. The virtual line-shaft being similar to an intelligent master with parallel slave system, where the master is imaginary and some form of interaction is available between it and the slaves. The approach is eminently suited to implementation with a number of drives, although the exact balancing of reflected back torques, etc, and the designing of virtual inertia, and virtual speed control, may be somewhat involved, and is not tackled in-depth in the presented papers [123, 124]. It is feasible that torque-limiting situations are readily handled in such a system, as reported in [123, 124], and which may be appropriate in the paper handling processes the paper considers. In the pulp to paper manufacturing process, described as an example in this chapter, torque-limiting conditions, in a section other than the wire-section, would result in a loss of synchronisation. Virtual line-shafting could thus provide optimised performance, in terms of process operating speed and handling of overload conditions, in this example. In this work however, it did not demonstrate high inter-shaft stiffness during load transients, due to coupling effects being filtered by the virtual-shaft. An attempt to amplify fed-back torque commands did not alleviate this, as a larger available correction limit must then be made available for the virtual-shaft control. Hence schemes based on this method, and that of synchronous command generation,

would tend to rely on high-performance servo axis drives [129], and/or feed-forward control techniques [123, 124, 139, 140].

The best performance during load transient effects was observed in the operation of the parallel cross-coupled structure. The scheme does not however, offer the same simple expansion, for use with multiple drives, as that of the virtual line-shaft. The work of Perez-Pinal considers the relative merits of the cross-coupled and virtual line-shaft schemes and considers expanding cross-coupling, by the production of a type of overall velocity error, through the combination of errors that exist between pairs of drives [137]. Another approach is similar to the virtual line-shaft technique without the virtual-shaft, where output torques from individual drives are used to affect the other drives [137]. These approaches have not been investigated further (practically) however, because only a two axis system is available.

Like the concept of mechanical/electronic hybrid multi-motor systems forming an optimal system, it is suggested that a pure electronic system (or purely electronic parts) may make use of different/hybrid strategies. In other words, there is nothing to stop a combined press-drying stage, in the paper-manufacturing example, making use of cross-coupling, taking as its reference the speed of the wire-section. Effectively combining master/slave and cross-coupled schemes. Again it would be interesting to further examine/investigate practical applications.

## **6.8 Conclusions**

Multi-motor systems, with a particular view to operating with sensorless induction motor drives, have been considered in this chapter.

The principle of replacing mechanical transmission systems, with electronic systems, has been introduced (section 6.2) and the many anticipated benefits examined. The main drawback is related to the maximum achievable system stiffness, available with the electronically synchronised system, when large-scale speed and load transients are experienced.

In section 6.3 algorithms have been presented that achieve speed synchronisation, from the simple open loop scheme (synchronous command generation), where individual drives respond to similar reference information, through to the advanced virtual line-shaft technique, which models a mechanical line-shaft system [123, 124].

Each of the techniques considered varies in performance and each has been tested on the dual motor drive system developed for this work. Results were presented in section 6.4, where both drives operate in the encoded mode. This was for defined speed and load transient tests.

The tuning sensorless drive system developed in the previous chapters has been tested, with a view to its use in the speed-synchronised system. The results from the bi-axial system, when running the same test conditions as in the encoded experiments, are presented in section 6.5. Encoded and sensorless results are seen to be highly comparable. The speed sensorless drive is seen to maintain encoder like speed holding accuracy and, for the better performing synchronisation schemes, it is seen that the relative speed error is constrained - to a similar degree as in the encoded implementation. In other words, where the speed error is not suitably constrained this is a function of the synchronisation scheme, and not to do with the sensorless system.

The sensorless speed holding technique has not been engineered to provide a highly accurate estimate of speed under transient conditions and does not provide tuning in this mode. The sensorless estimate is thus not guaranteed under transient conditions. Its integrity, when used to provide positional information, must therefore be questioned during such transient conditions, but, in section 6.6, it has been demonstrated to somewhat counteract relative positional error accrued during load transients. Relative position error correction is integrated into a cross-coupled synchronisation scheme. The position error used to drive the correction control is derived from only sensorless speed estimates. The positional results truly confirm the speed holding accuracy of the engineered algorithm: the position measure is very flat during the data capture period. This is effectively the integral of the speed error, with results captured over some 8 seconds.

The performance of the various synchronisation strategies is reconsidered in section 6.7. The virtual line-shaft technique holds perhaps the most potential for a multi-motor system and is particularly suited to expansion. However, the torque measures, reflected back to the imaginary overall system, serve as cross-coupling terms, which are effectively filtered by the closed loop dynamics of the virtual-shaft. Thus performance under load impact conditions, for the simple system tested here, is inferior to that obtained from the parallel cross-coupling technique. Expansion of the cross-coupled scheme was therefore considered in the MSc work of Francisco Perez-

Pinal [137], as a spin-off from the work of this project. Methods were presented for expansion and simulation-tested [137]. The work is not considered practically here, due to time constraints and the related fact that only a dual-drive system was engineered. It is considered however, that some of the presented/tested synchronisation schemes could immediately further enhance existing multi-motor applications/implementations, which reportedly tend to exploit the low performing algorithms.

Section 6.7 also considers applications in a little more detail, particularly paper manufacture and electric vehicles. It is considered that the developed sensorless drive could find a place in parts of such applications, although to fully test such a claim is beyond the scope of this work. It is felt that the sensorless synchronisation results presented certainly indicate that a system based on such a method may be exploited in industrial/manufacturing applications, like those outlined. There are of course particular applications, such as robotics, that call for exceptionally high performance. Such an application may make use of small (low inertia and hence high bandwidth) machines to give a very fast response to transient conditions and would severely test high performance encoded solutions. The algorithm would not be applicable in such circumstances. Also, there may be applications where the low speed/starting performance/synchronisation is critical. The developed system does not tune around standstill, offering the basic model-based performance. It is believed however, that in many applications such operation will be sufficient, to start a process for example, where the normal process speed and load operating range is well within the operating range of the developed sensorless system. As an example, drives in the paper manufacturing and printing industries may be run up to speed before material is handled, other processes may produce small amounts of wasted output where the system is run-up to the nominal operating conditions.

Relating to the purposes of this project, introduced in chapter 1, there is a strong motivation to use high performance AC drives in multi-motor applications [127]. Use of DC drives, in a system where the motor count may be large, will incur costs associated with reliability/maintenance factors for example. Low performance AC techniques (V/F for example) will not provide adequate performance. Where use can be made of sensorless techniques, the vulnerability of encoder use is removed and this is particularly useful in parts of steel and paper processes. In the examined paper-production process, operating conditions would not favour use of DC machines or electrical shaft-encoders, due to damp/wet conditions.

Similarly to marrying a particular sensorless algorithm to a particular (individual) drive application, it is considered that multi-motor systems may benefit through the good engineering of individual sections of a process. Some sections may require mechanical linkage, providing stiff control. Other sections may utilise electronic control, but this may be achieved using a most appropriate coupling strategy and, where possible, sensorless methods. As mentioned early in this chapter, where parts of a process are perhaps situated some way away from the main sections, electronic synchronisation can certainly be exploited, rather than unrealistically extend mechanical line-shaft, etc.

In the conclusion of this chapter it is considered that the possibility exists, and that this possibility has been demonstrated, that sensorless control methods may be utilised in multi-motor systems. It would be most rewarding to further engineer such solutions, given practical application scenarios.

---

## CHAPTER 7 Conclusions and Further Work

---

### 7.1 Introduction

As outlined in chapter 1, from the outset this project had the following main aim:

*To develop and demonstrate a fully sensorless induction motor drive that has sufficient speed holding capability to make it suitable for industrial processes where multi-motor control is required.*

It is felt, in the conclusion of the project, that this aim has been achieved. Primarily, this was accomplished by fulfilling the following particular aims/objectives:

1. Investigate the alternatives, but select and test a most suitable model-based sensorless vector scheme – to facilitate a sensorless drive with high dynamic performance capability
2. Investigate methods for tuning the developed model-based system, most particularly to maintain encoder like steady state speed holding accuracy. Also, such a scheme should ideally be operational over a maximised operating range and have practical validity
3. Test and demonstrate the self-tuning, accurate speed-holding sensorless drive
4. Investigate suitable multi-motor control schemes for use in industrial manufacturing processes. Realistically this is in a suggested power range of 2kW to 100kW, and not applicable to the extreme demands of robotics for example
5. Compare and contrast encoded and sensorless implementations of the multi-motor synchronisation schemes. Thus, this also tests feasibility of

practical application of the sensorless system, through its application to a second motor drive

The main aim of the work was, of course, the engineering of a practical drive system suitable to perform the above tasks. Supplementary aims/issues explored most significantly included an investigation into the possibility of using the RSH based accurate sensorless speed identifier as direct feedback in a sensorless drive. Also the possibility of using the sensorless multi-motor system to correct/compensate for position error accumulated during speed transient conditions, bearing in mind that the system was developed for performance in the steady state.

This chapter now goes on to give a more thorough review of the work, with particular consideration to the model-based system development, the RSH based speed estimator and tuning, and the multi-motor control. Ideas for further work are discussed in section 7.6 and project outcomes are detailed in section 7.7.

### 7.2 Thesis Review

The motivational criteria for operation of induction motors under vector (or field orientated) control, for high dynamic performance, and without shaft-mounted speed sensors, for reasons of practicality, reliability and cost, were outlined in chapter 1. The chapter also highlighted that, whilst having succeeded in providing field orientated dynamic performance, the speed holding accuracy associated with sensorless techniques (that have mainly had commercial impact) results in them not being suitable for speed critical applications. The problems associated with the techniques are related to them being based on the motor electric dynamic model and thus relying on knowledge of parameters that vary heavily with operating condition. Applications that have therefore not generally utilised sensorless methods were considered to be any based on multi-motor synchronised control.

Further project background was given in chapters 2 and 3. Chapter 2 provided the mathematical background pertaining to the decoupling of flux and torque producing components of induction motor stator current, for field orientation or vector control. The various means of achieving field orientation were discussed, along with relative advantages/disadvantages. The operation of the voltage source inverter (VSI) type power converters was considered and discussed, as this provides the variable magnitude, variable phase, stator voltage required for vector control of an induction

motor. Associated discussion centred on the non-ideal nature of the voltage waveform produced, as this is of particular relevance when considering the tracking of rotor slot harmonics, used later in the work. Finally the chapter further presented the motivation for sensorless induction motor operation, a review of sensorless induction motor control and a more detailed look at the leading algorithms that attain such control using the induction motor model, knowledge of electrical parameters and measurement of stator terminal quantities.

Worthy of a particular mention is that chapter 2 also considered sensorless induction motor control based on signal injection methods. The author notes that such techniques have been shown to provide excellent low speed performance, both in terms of orientation and closed loop position control, particularly in [20]. The reasons for not using, exploring and extending such techniques in this work were based on the motivational criteria of this project. The desired aim was based on the algorithm having immediate commercial relevance, perhaps as an extension to existing drive products, operating over the majority of the speed and load range and not requiring in-depth machine and/or inverter knowledge. It is acknowledged that signal injection techniques are the viable solutions in providing low speed performance, but it is considered that there is much engineering required in terms of bringing such algorithms towards a general commercial implementation. There are also other various drawbacks to the techniques and these were highlighted in chapter 2.

Chapter 3 detailed the experimental system, developed as part of this work, consisting of two 4kW-induction machines, each with a 7.5kW inverter. Although these items have similar ratings, they are each from different manufacturers. Each induction machine could be loaded by an associated dc machine, providing variable torque loads. The different dc machines resulted in each rig having quite markedly different inertias, which was to be a worthwhile test of the speed synchronisation techniques. Both rigs were fitted with encoders to provide speed measures in the implementation of encoded induction motor vector control, to act as a benchmark for sensorless performance, and to measure the performance of sensorless operation. The chapter also presented the control and data capture processing platforms and the developed interface system, which coupled the processing platform and motor drives, built as part of the project. The motor control code for the complete dual drive system was run on a dual floating-point DSP processor system. Chapter 3 described this system,



how processing tasks were divided between the 2 processors and how overall drive rig control and data capture was developed on the host PC.

### **7.3 The Sensorless Model-based Implementation**

The foundation of the developed speed holding sensorless drive method is the Kubota adaptive speed observer (ASO) [83]. Both the method and the detail of the particular implementation were fully presented in chapter 4. The reasons for choosing the ASO technique were highlighted as it requiring neither direct integration of sensed motor terminal quantities, nor knowledge of mechanical drive parameters. Whilst similar attributes are associated with the Ohtani method [81], the Kubota scheme was more readily implemented on the development system, where an encoded mode of operation was available. The Kubota scheme facilitates DRFO, for flux and torque current decoupling, and is a popular model-based sensorless vector technique used in many further works. Like all the model-based techniques however, its performance is related to how accurately motor parameters are known and tracked. Whilst forming the basis of the developed technique, the Kubota algorithm could be replaced with alternative methods, where the developed speed tuning algorithm would still be applicable.

Speed and current control design specifications were presented in chapter 4, along with the specifications of the ASO. The chapter went on to test the performance of the ASO scheme, as an observer of speed in an encoded IRFO implementation, and in the fully sensorless DRFO mode. The encoded results acted as a benchmark for those obtained from the sensorless scheme, which were seen to be highly comparable. Of concern with model-based methods is the low speed performance and, as was evident in one of the presented results, orientation and speed estimation can be compromised in this region; the result showed a loss of orientation on motor drive rig A when decelerating to standstill under full load. A second result, obtained with adjusted parameters, demonstrates that the technique gives excellent performance with tuned parameters, but together the results demonstrate that performance is compromised if these parameters are not precisely known in the low speed region.

Based on the work of others, chapter 4 goes on to consider the causes and effects of parameter variation. The review highlights that the primary parameter variations, effecting sensorless performance within the rated speed region (fully fluxed), are related to the resistance parameters. The resistances are greatly affected by

temperature variation, both ambient and (primarily) motor heating.  $R_s$  greatly affects the stability of a sensorless drive and is particularly influential at low speed. Its significance lessens with increasing speed. With regard to speed estimation accuracy  $T_r$  is the significant parameter. The effect of error on this parameter, with regard to speed accuracy, is constant throughout the speed range and it is impossible to simultaneously estimate speed and  $T_r$  under normal model-based operating conditions [28]. Being the most significant,  $T_r$  is the parameter most suitably adjusted to obtain accurate speed holding and can be used to artificially accommodate the lesser significance of inductance parameter error on speed estimation accuracy (below base speed). This is given that the sensorless drive  $T_r$  is tuned by obtaining a second and accurate measure of drive speed.

### 7.4 The Adaptive Tracking Speed Estimator (ATSE)

Having engineered a suitable sensorless strategy, in the Kubota scheme, the bulk of the research work in this project was presented in chapter 5, as the Adaptive Tracking Speed Estimator (ATSE). Using the developed ATSE system, a secondary (high-accuracy) speed estimate was obtained, based on rotor slotting information contained in stator quantities, for tuning of  $T_r$  in the sensorless ASO scheme. Compared with tuning against individual parameter variation, this ensured accurate speed holding.

The chapter firstly reviewed the mechanisms that lead to the production of RSH effects seen in stator quantities. It went on to consider the effects of PWM harmonics, which exist with the RSH effects, that create tracking difficulties. In particular this work looked at rotor slotting and inverter harmonics in three available quantities, these being:

- A single sampled stator current
- The transformed overall current vector magnitude
- The PWM reference voltage vector magnitude

Previous work, regarding the tracking of RSH effects using digital methods, had been carried out using sampled stator currents [28, 102-109]. Blasco improved the robustness of his algorithm by exploiting two RSH effects in a single stator current [28], but none had made use of the alternative variables. The use of voltage and current vectors gave an immediate tracking range improvement, by extending the operating range in which the RSH effect could move, due to load, before contacting

the next lowest PWM component. Use of the voltage vector magnitude improved the algorithm performance at lower frequencies/speeds, where the RSHs are attenuated in current quantities, due to the current controller action. The current controllers act to attenuate the RSH effects, so their output must contain RSH information. The reference value of voltage, fed to the PWM scheme from the dq current controllers is thus used as an input to the ATSE, not a measured stator voltage. This fits with the fact that in many commercial drives voltages will not be measured (voltage transducers will not be fitted).

The ATSE system, obtaining a speed estimate from the RSH effects, is fully described in the chapter. The input to the system is selected, based on the ASO estimated speed, as either  $||$  or  $|V|$ . The system sample frequency is conveniently changed at the input changeover, to improve the signal to noise ratio at lower speeds and hysteresis is included in the changeover mechanism. Pre-filtering, before the RSH identifier, has made use of notch filters to remove inverter effects and improve the no/light load performance. In effect the pre-filtering 'promotes' a particular RSH component. The RSH component frequency is identified using the RML-ATF method [113], where the centre frequency of a notch filter is recursively adjusted to minimise the output. Thus the RSH, as the strongest component in the input, is eliminated and the frequency identified. It is noted that a similar effect would be realised by maximising the output if using a bandpass (BPF) tracking filter. The notch code is slightly more efficient however. Minimal algorithm parameter management is required, the notch bandwidth and averaging parameters of the RML-ATF routine are fixed, in line with that proposed by Shuli [119], to provide good accuracy and allow dynamic tracking for tuning. Speed is calculated using knowledge of  $f_c$  from the differentiated rotor flux angle.

ATSE results are presented that demonstrate the steady state and dynamic tracking performance of the algorithm under similar operating conditions to those used to test the ASO. A defined region of operation is shown, being highly similar to the model-based ASO algorithm and similar to that described by Blasco for his FFT work [28]. The advantage with the developed system, over that of the FFT, is that the computational requirement of the ATSE system is minimal. The complete control algorithm (speed and current control, sensorless ASO, RSH based speed estimator,  $T_r$  tuning, PWM, etc) can be implemented on a single DSP unit for an individual drive. Blasco made use of a dedicated RSH identifying processor [28]. An FFT, at first thought, should give superior performance, in terms of accuracy and PWM harmonic

rejection, because all spectral information (in a window) is captured. PWM and RSH harmonics can be identified and a search routine can determine the RSH effects. The RML-ATF, due to its recursive nature, should offer improved dynamic performance with lesser computational requirement, but is likely to offer an increased likelihood of becoming confused with inverter harmonics and lesser accuracy. It is noteworthy that, through input selection and pre-filtering, the ATSE system presented here is comparable with the FFT of Blasco [28], in terms of operating range (related to PWM harmonic rejection) and accuracy. This is especially significant, because the author and Blasco made use of the same drive rig.

The tuning system, also presented in chapter 5, simply compares the RSH based speed measure and the sensorless ASO measure. The error is used to drive a PI controller whose output is a  $T_r$  adjustment term. As such the BPF centre estimate is self-correcting. The dynamics were set-up in simulation, with the ATSE speed estimate regarded as real speed, to tune out large errors in less than a second, not significantly effecting the speed control dynamics. The results presented show the developed scheme to maintain encoder-like speed holding under a variety of speed and load conditions. The mechanism is seen to maintain the encoder-like speed accuracy of both drives when operating at 200rpm under fully loaded conditions for 30+ minutes. The relevance of this test being in that the drives were operated from a cold start and the heating effects, causing resistance parameters to vary, were thus significant. From a similar cold start, a further result under similar test conditions and with no tuning, shows the two drives to each accumulate an error of some 5rpm to 7rpm over the same period. The low speed performance is also demonstrated, where tuning is disabled below 75rpm, as in this region the ATSE estimate is unreliable. There is a similar constraint placed upon the model-based ASO method, due to the unoptimised/unimproved action of the VSI power converters, measurement methods, etc, at low speed. The ASO algorithm shows suitable performance for starting and unsustained operation at low speed, with tuning re-enabled when returning from this region. Other work looks more specifically at improving low speed operation, using  $R_s$  estimation in model-based methods [40], and signal injection techniques [20]. It was not the primary consideration of this work, but is highlighted for further work. Many applications may not require high performance operation in this region/mode.

## **7.5 Speed Synchronisation/Multi-Motor Control**

Having engineered the desired sensorless drive, with a tuning mechanism for highly accurate speed holding, the algorithm was tested. Firstly the applicability of the algorithm was considered, by applying it to a similar induction motor drive rig with minimal modification required (speed and current controller redesign, as would be expected). Secondly the two tuning drives were tested in various speed-synchronised configurations.

Speed synchronisation, as far as the author is aware, is something not yet tested with sensorless algorithms, primarily due to the fact that their speed holding capability would generally render them unsuitable for such an operating scenario. The possibility exists for signal injection based schemes to offer such performance, as they have been demonstrated to offer closed loop position control, but, as established, much engineering is required to bring these methods to market. There are significant drawbacks, not least with regard to operating range, and synchronisation of these methods has not been tested in literature. In fact, where a position-based system is engineered using such techniques, a speed control operation may not be highly practicable. The position signal must be differentiated to provide a speed signal, which may be noisy, and continuous high-speed operation may not be achievable, as it would constitute highly dynamic position control.

Chapter 6 investigates the background of speed synchronised control. The many advantages of removing a traditional mechanical coupling and instead using electronically coupled individual motor drives are discussed. The drawback is in how well electronic coupling can resemble (if required) the overall inertia, and rigid coupling of individual axes, in a mechanical system.

Methods for electronic coupling are reviewed in the chapter, ranging from a simple open loop synchronous command method, where the individual drives simply follow the same command information, to a virtual line-shaft technique, intended to emulate a mechanical system. The performance of the various schemes is tested under step speed reference transients and load impact conditions, using the encoded drive rigs. Loading of each machine is considered, bearing in mind the differing inertias.

Undergoing the same tests, the tuning sensorless drive rigs are shown to operate in a speed-synchronised mode. The results obtained are highly comparable with the

encoded versions. The sensorless tuning system provides excellent steady state synchronisation, with the relevant coupling schemes minimising (or not) the transient error. In terms of position error during the transient, where tuning is disabled, the sensorless scheme will not offer the synchronisation performance of the encoded version, but, in terms of steady state speed locking and transient speed error minimisation, sensorless and encoded results are highly comparable.

Of the tested methods, the two leading techniques are the parallel cross-coupled method and the virtual line-shaft. The master/slave technique can give excellent 1-way coupling, particularly for drives of strongly differing inertias (as used in this work), but the master will not respond to disturbances that affect the slave. The cross-coupled method gives excellent synchronisation during torque impact conditions, but would require some form of command rate limiting to offer good synchronisation during speed transients. Command rate limiting is inherent in the line-shaft method and it varies depending on drive loadings. The coupling in this mode is not excellent during torque impact conditions however, where it seems to act like a form of filtered (by the inertia of the software virtual shaft) cross-coupling. Various works look at more involved (rigid) controller design [124, 139, 140], and it is suggested that the scheme would respond differently to drives with reduced and well matched inertias. The virtual shaft offers a possibility to readily manage sectional overload, as reported in [123, 124], but this work was not extended to test this.

The cross-coupled technique was extended to test the possibility of minimising relative position error (between the 2 drives), accumulated during a load impact condition, by turning the ATSE sensorless speed estimates into a relative incremental position error signal. The tuning drive was not designed to operate in this mode, with the estimate not guaranteed during transient periods, but it was demonstrated that the correctional term did serve to minimise the positional error accumulated. Both encoded and sensorless results, with and without positional correction, were presented for comparison.

Finally chapter 6 considered, in a little more detail, applications where the sensorless algorithm may be applied and considered the expansion of multi-motor schemes, for use with more than two drives. It is thought that electronically synchronised motor drives could further impact into applications still relying on mechanical synchronisation, by using the more advanced electronic synchronisation methods. In

many applications the more basic ones are currently used. Performance enhancement could perhaps be gained by the choice of the most suitable synchronisation scheme to operate a particular section of an application, as discussed in the chapter. Making use of the sensorless method presented, or any extended from this work, in synchronised control brings the benefits described in chapter 1, relating to the use of induction motors and the removal of the speed sensor.

### 7.6 Further Work

With a view to using the ATSE system, as simply a speed measure or for tuning, in a commercial system, it would be beneficial for manufacturers to further examine the logistics of perhaps implementing an estimator on an expansion DSP system. The algorithm is suitable for implementation on a floating point DSP, not as sophisticated as those used in this work, and would require minimal parameter set-up. It would be useful to examine which few parameters must be passed to the DSP system in order for a most reliable speed estimate to be returned. This could be offered as a performance enhancement/expansion item.

Regarding developing the presented tuning drive algorithm, the author would be most interested in the performance gained by considering the use of machines with promoted RSH effects. In many applications the requirement for a robust sensorless induction motor drive may be such that, perhaps trading somewhat against motor losses, the RSH effects could be enhanced, making the motor itself a better sensor. This would include having motors with a high number of open and unskewed slots. Under such circumstances the performance of the ATSE and tuning algorithms presented in this work should certainly be greatly improved. The low-speed operating limit would be extended, primarily by the slot number increase, and the low load limit would be extended, by the opening and unskewing of the slots increasing RSH amplitude. With promoted effects it may be possible to reconsider the use of an ATSE derived speed estimate as direct speed feedback. In this case it would be necessary to further investigate the operation of the algorithm under light regenerating loads, as this could lead to the motor running at synchronous speed. Under such conditions RSH effects would coincide with inverter harmonics. It may be possible to operate such a mode with some form of field weakening however, to make sure RSH and inverter harmonics never coincide. For direct feedback it would be necessary to more explicitly examine ATSE dynamics.

The direction of research and commercial activity in the field of motor drives seems to suggest a move toward integrated products, where machines and power converters are combined [35]. The matrix converter concept (replacing the VSI) allows the removal of the large dc link capacitors associated with standard inverters and, although requiring more power electronic switches (silicon technology – price reducing?), offers the possibility of a reduction in volume of this component [34, 35]. The current point of investigation remains the more involved cooling aspect, with regard to combining of converter and motor [35]. With the possibility of such integrated drive products however, it would seem a particular waste to still fit a shaft mounted encoder, such that the most realistic means of sensorless operation must surely be to promote the RSH producing effects in the rotor. The use of matrix converter may also alleviate some of the low speed problems that are due to deadtime, as the commutation process is somewhat different in this type of converter [34].

In terms of improving the algorithm in the low speed region, bearing in mind that the above suggestions may offer much improved performance anyway, it would be interesting to combine the solution developed here with a signal injection method. Signal injection is considered the only technique, so far suggested in research, that allows a true high performance operation at low and zero speed, where rotor information is made available on the stator side by persistent high frequency excitation [20]. Although the drawbacks with such methods include increased losses, torque ripple, acoustic noise, etc, it may be possible to minimise the impact of these considerations, by only operating this mode in the minimal part of the operating range. Engineering would be required to combine the method presented in this work with a signal injection method. A reliable switch over between operating modes, with good dynamic performance, must be assured. The solution would offer the possibility of very high performance throughout the operating region below base speed.

It would also be useful to investigate the performance of the ATSE based method well into the field-weakening region. Here the speed estimate may perhaps be reconsidered for direct feedback, because inverter/RSH harmonic confusion is less evident and RSH effects can be robustly tracked in current quantities (less noisy than voltage). In this mode it may be wise to exploit stator flux orientation for improved flux control [27, 85], but field weakening operation would still require extended parameter knowledge [50, 51]. The immediate considerations that would need to be



addressed include the possibility of variation in PWM harmonics that would limit tracking. Also the fact that the execution time of the ATSE system would become more significant as speed increases, with an increase in sample frequency required to track the higher frequency RSH effects. All modes of operation, including some signal injection methods, would still benefit from the promotion of RSH effects, as considered earlier.

Although not the primary objective of this work, it having been used as a demonstration of the developed sensorless system, it would perhaps be interesting to consider further work in the area of multi-motor control. Various schemes have been presented, all with their relative merits, but each seems to hold restrictions with regard to their not being able to resemble the inherent shaft stiffness of a mechanical line-shaft. Cross-coupled techniques offer perhaps the best performance with regard to maintaining synchronisation under impact load conditions, but the virtual line shafting technique offers the best performance under speed transient conditions and will manage an axis torque limit situation most effectively [123, 124]. Some further work has been undertaken as a spin off from this project, by Perez-Pinal, in extending cross-coupled techniques [137], but it would be interesting to explore the true performance of a real mechanical system in a particular application. Much of the research work presented in this area does not include plentiful amounts of comparative results, nor results from mechanical systems.

In short, it is considered that for both sensorless and multi-motor synchronisation methods to greatly extend into new/all application areas, a method must be married to an application. In terms of sensorless drives, advantage can be gained by suitable choice of machine, bearing in mind self-sensor performance, but the power converter control may require simply flexibility in terms of its software control component. A wide range of methods are available that should offer suitable performance in a given application. The advantages of a flexible software based system can be exploited such that a solution is engineered for a given problem, with a fixed power converter requirement.

### **7.7 Project Outcomes**

This project has resulted in five conference papers [14-18], included as Appendix A. It is hoped that the ATSE work will shortly be presented as a journal publication.

Interest in the ATSE speed estimation technique, and sensorless model-based drive tuning, has been shown by 2 UK drive manufacturers.

---

## References

---

- [1]. De Almeida A.T and Fonseca P, "Characterisation of EU Motor Use", (in Energy Efficiency Improvements in Electric Motors and Drives), *Springer-Verlag*, Germany, pp.143-167, 2000
- [2]. Boyle G, "Renewable Energy: Power for a Sustainable Future", *Oxford University Press*, 1996
- [3]. Westbrook M.H, "The Electric Car", *The Institution of Electrical Engineers*, 2001
- [4]. Ruch C.A, "George Westinghouse – Engineer and Doer", *IEEE Transactions on Industry Applications*, Vol.20, No.6, pp.1395-1402, 1984
- [5]. Williamson S, "The Induction Motor – A State of the Ark Technology", *IEE Power Engineering Journal*, Vol.10, pp.247-254, 1996
- [6]. Mohan N, Undeland T.M and Robbins W.P, "Power Electronics – Converters, Applications and Design", *John Wiley and Sons*, 1989
- [7]. Hughes A, "Electric Motors and Drives", *Newnes*, 1990
- [8]. Bose B.K, "Power Electronics and Variable Frequency Drives", *IEEE Press*, 1997
- [9]. Blaschke F, "The principle of field orientation as applied to the new transvector closed loop control of rotating machines", *Seimens Review*, Vol.39, No.5, pp.217-220, 1972
- [10]. Hasse K, Zur Dynamik drehzahl geregelter Antriebe mit stromrichter gespeisten Asynchron-Kurzschlußlaufermaschinen (on dynamic of the speed controlled static ac drive with squirrel-cage induction machine), *PhD Thesis, Technical University Darmstadt*, Germany, 1969
- [11]. Vas P, "Vector Control of AC Machines", *Clarendon Press*, 1990
- [12]. Leonhard W, "Control of Electrical Drives", *Springer-Verlag*, 1986

- [13]. Zinger D, Profumo F, Lipo T.A and Novotny D.W, "A Direct Field Oriented Controller for Induction Motor Drives Using Tapped Stator Windings", *IEEE PESC Conference*, pp.855-861, 1988
- [14]. Turl G, Sumner M and Asher G.M, "Use of Adaptive Notch Filtering for Accurate Speed Holding in a Sensorless Induction Motor Drive", *IEE PEVD Conference*, pp.268-273, 2000
- [15]. Turl G, Sumner M and Asher G.M, "A Hybrid Sensorless Induction Motor Control Strategy for High Performance Drive Applications", *IEEE PESC Conference*, pp.20-25, 2001
- [16]. Turl G, Sumner M and Asher G.M, "A High Performance Sensorless Induction Motor Drive for use in Multi-Motor Speed Synchronised Applications", *EPE Conference*, pp.(on CD-ROM), 2001
- [17]. Turl G, Sumner M and Asher G.M, "A Multi-Induction-Motor Drive Strategy Operating in the Sensorless Mode", *IEEE IAS Annual Meeting*, pp.1232-1239, 2001
- [18]. Turl G, Sumner M and Asher G.M, "A Synchronised Multi-Motor Control System using Sensorless Induction Motor Drives", *IEE PEMD Conference*, pp.38-43, 2002
- [19]. Hindmarsh J, "Electrical Machines and their Applications", *Butterworth Heinemann*, 1977
- [20]. Teske N, "Sensorless Position Control of Induction Machines Using High Frequency Signal Injection", *PhD Thesis, The University of Nottingham, England*, 2001
- [21]. Jansen P.I, Lorenz R.D and Novotny D.W, "Observer-Based Direct Field Orientation: Analysis and Comparison of Alternative Methods", *IEEE Transactions on Industry Applications*, Vol.30, No.4, pp.945-953, 1994
- [22]. Verghese G.C and Sanders S.R, "Observers for Flux Estimation in Induction Machines", *IEEE Transactions on Industrial Electronics*, Vol.35, No.1, pp.85-94, 1988
- [23]. Atkinson D.J, Acarnley P.P and Finch J.W, "Observers for Induction Motor State and Parameter Estimation", *IEEE Transactions on Industry Applications*, Vol.27, No.6, pp.1119-1127, 1991

- [24]. Garces L.J, "Parameter Adaption for the Speed-Controlled Static AC Drive with a Squirrel-Cage Induction Motor", *IEEE Transactions on Industry Applications*, Vol.IA-15, No.2, pp.173-178, 1980
- [25]. Koyama M, Yano M, Kamiyama I and Yano S, "Microprocessor-Based Vector Control-System for Induction-Motor Drives with Rotor Time Constant Identification Function", *IEEE Transactions on Industry Applications*, Vol.22, No.3, pp.453-459, 1986
- [26]. De Doncker R.W and Novotny D.W, "The Universal Field Oriented Controller", *IEEE Transactions on Industry Applications*, Vol.30, No.1, pp.92-100, 1994
- [27]. Xu X, De Donker R and Novotny D.W, "A Stator Flux Oriented Machine Drive", *IEEE PESC Conference*, pp.870-876, 1988.
- [28]. Blasco-Gimenez R, "High Performance Sensorless Vector Control of Induction Motor Drives", *PhD Thesis, The University of Nottingham*, England, 1996
- [29]. Depenbrock M, "Direct Self-Control (DSC) of Inverter-Fed Induction Machine", *IEEE Transactions in Power Electronics*, Vol.3, No.4, pp.420-429, 1988
- [30]. Habetler T.G, Profumo F, Pastorelli M and Tolbert L.M, "Direct Torque Control of Induction Machines Using Space Vector Modulation", *IEEE Transactions on Industry Applications*, Vol.28, No.5, pp.1045-1053, 1992
- [31]. Asher G.M, Sumner M, Cupertino F and Lattanzi A, "Direct Flux Control of Induction Motor Drives", *EPE Conference*, pp.(on CD-ROM), 2001
- [32]. Sokola M and Levi E, "A Novel Induction Machine Model and its Application in the Development of an Advanced Vector Control Scheme", *International Journal of Electrical Engineering Education*, Vol.37, No.3, pp.233-247, 2000
- [33]. Levi E and Vukosavic S.N, "Identification of the Magnetising Curve During Commissioning of a Rotor Flux Oriented Induction Machine", *IEE Proceedings - Electric Power Applications*, Vol.146, No.6, pp.685-693, 1999
- [34]. Empringham L, "Matrix Converter Current Commutation", *PhD Thesis, The University of Nottingham*, England, 2000

- [35]. Wheeler P.W, Rodriguez J, Clare J.C and Empringham L, Weinstein A, "Matrix Converters: A Technology Review", *IEEE Transactions on Industrial Electronics*, Vol.49, No.2, pp.276-288, 2002
- [36]. Van Der Broeck H.W, Skudelny H-C and Stanke G.V, "Analysis and Realization of a Pulsewidth Modulator Based on Voltage Space Vectors", *IEEE Transactions on Industry Applications*, Vol.24, No.1, pp.142-149, 1988
- [37]. Evans P.D and Close P.R, "Harmonic Distortion in PWM Inverter Output Waveforms", *IEE Proceedings – Electric Power Applications*, Vol.134, No.4, pp.224-232, 1997
- [38]. Abbondanti A and Brennen M.B, "Variable Speed Induction Motor Drives Use Electronic Slip Calculator Based on Motor Voltages and Currents", *IEEE Transactions on Industry Applications*, Vol.IA-11, No.5, pp.483-488, 1975
- [39]. Rajashekara K, Kawamura A and Matsuse K, "Sensorless Control of AC Motor Drives – Speed and Position Sensorless Operation", *IEEE Press*, 1996
- [40]. Campbell J.A.C, "A Sensorless Induction Motor Drive Employing an Artificial Neural Network for On-Line Parameter Adaptation", *PhD Thesis, The University of Nottingham*, England, 2002.
- [41]. Holtz J, "Methods for Speed Sensorless Control of AC Drives", *IEEE PCC-Yokohama Conference*, pp.415-420, 1993
- [42]. Ilas C, Bettini A, Ferraris L, Griva G and Profumo F, "Comparison of Different Schemes without Shaft Sensores for Field Oriented Control Drives", *IEEE IECON Conference*, pp.1579-1588, 1994
- [43]. Ohyama K, Asher G.M and Sumner M, "Comparative Experimental Assessment for High-Performance Sensorless Induction Motor Drives", *IEEE ISIE Symposium*, pp.386-391, 1999
- [44]. Ohyama K, Asher G.M and Sumner M, "Comparison of the Practical Performance and Operating Limits of Sensorless Induction Motor Drive using a Closed Loop Flux Observer and a Full Order Flux Observer", *EPE Conference*, pp.(on CD-ROM), 1999
- [45]. Sumner M and Asher G.M, "Autocommissioning for Voltage-Referenced Voltage-Fed Vector Controlled Induction Motor Drives", *IEE Proceedings – Electric Power Applications*, Vol.140, No.3, pp.187-200, 1993

- [46]. Kerkman R.J, Thunes J.D, Rowan T.M and Schlegal, "A Frequency Based Determination of the Transient Inductance and Rotor Resistance for Field Commissioning Purposes", *IEEE Transactions on Industrial Applications*, Vol.32, No.3, pp.577-584, 1996
- [47]. Schierling H, "Self-Commissioning – A Novel Feature of Modern Inverter-Fed Induction Motor Drives", *IEE PEVD Conference*, pp.287-290, 1988
- [48]. Blasco-Gimenez R, Asher G.M, Sumner M and Bradley K.J, "Dynamic performance limitations for MRAS based sensorless induction motor drives. Part 1: Stability analysis for the closed loop drive", *IEE Proceedings - Electric Power Applications*, Vol.143, No.2, pp.113-122, 1996
- [49]. Blasco-Gimenez R, Asher G.M, Sumner M and Bradley K.J, "Dynamic performance limitations for MRAS based sensorless induction motor drives. Part 2: Online parameter tuning and dynamic performance studies", *IEE Proceedings - Electric Power Applications*, Vol.143, No.2, pp.123-134, 1996
- [50]. Blasco-Gimenez R, Asher G.M, Sumner M, Cilia J and Bradley K.J, "Field Weakening at High and Low Speed for Sensorless Vector Controlled Induction Motor Drives", *IEE PEVD Conference*, pp.258-261, 1996
- [51]. Levi E and Wang M, "Main Flux Saturation in Sensorless Vector Controlled Induction Machines for Operation in the Field Weakening Region", *EPE Conference*, pp.(on CD-ROM), 1999
- [52]. Bose B.K and Patel N.R, "A Sensorless Stator Flux Oriented Vector Controlled Induction Motor Drive with Neuro-Fuzzy Based Performance Enhancement", *IEEE IAS Annual Meeting*, pp.393-400, 1997
- [53]. Cabrera L.A, Elbuluk M.E and Husain I, "Tuning the Stator Resistance of Induction Motors using Artificial Neural Network", *IEEE Transaction on Power Electronics*, Vol.12, No.5, pp.779-787, 1997
- [54]. Vas P, Stronach A.F and Neuroth M, "Application of Conventional and AI based Techniques in Sensorless High-Performance Torque-Controlled Induction Motor Drives", *IEE Colloquium – Vector Control Revisited*, pp.8/1-8/7, 1999
- [55]. Paice D, "Motor Thermal Protection by Continuous Monitoring of Winding Resistance", *IEEE Transactions on Industrial Electronics*, Vol.IECI-27, No.3, pp.137-141, 1980

- [56]. Akatsu K and Kawamura A, "Sensorless Speed Estimation of Induction Motor based on the Secondary and Primary Resistance On-Line Identification without any Additional Signal Injection", *IEEE IAS Annual Meeting*, pp.1575-1580, 1998
- [57]. Ha I.J and Lee S.H, "An Online Identification Method for Both Stator and Rotor Resistances of Induction Motors without Rotational Transducers", *IEEE Transactions on Industrial Electronics*, Vol.47, No.4, pp.842-853, 2000
- [58]. Habetler T.G, Profumo F, Griva G, Pastorelli M and Betteni A, "Stator Resistance Tuning in a Stator-Flux Field Oriented Drive using an Instantaneous Hybrid Flux Estimator", *IEEE Transactions on Power Electronics*, Vol.13, No.1, pp.125-133, 1998
- [59]. Campbell J.A.C and Sumner M, "An Artificial Neural Network for Stator Resistance Estimation in a Sensorless Vector Controlled Induction Motor Drive", *EPE Conference*, pp.(on CD-ROM), 2001
- [60]. Kubota H and Matsuse K, "Speed Sensorless Field-Oriented Control of Induction Motor with Rotor Resistance Adaptation", *IEEE Transactions on Industry Applications*, Vol.30, No.5, pp.1219-1224, 1994
- [61]. Choi J-W and Sul S-K, "A New Compensation Strategy Reducing Voltage/Current Distortion in PWM VSI Systems Operating with Low Output Voltages", *IEEE Transactions on Industry Applications*, Vol.31, No.5, pp.1001-1008, 1995
- [62]. Silva C, Asher G.M and Sumner M, "Influence of Dead-Time Compensation on Rotor Position Estimation in Surface Mounted PM Machines using HF Voltage Injection", *IEEE PCC Conference*, pp.1279-1284, 2002
- [63]. Holtz J and Quan J, "Sensorless Vector Control of Induction Motors at Very Low Speed using a Nonlinear Inverter Model and Parameter Identification", *IEEE IAS Annual Meeting*, pp.2614-2621, 2001
- [64]. Blaschke F, Van der Burgt J and Vandenput A, "Sensorless Direct Field Orientation at Zero Flux Frequency", *IEEE IAS Annual Meeting*, pp.189-196, 1996
- [65]. Schroedl M, "Sensorless Control of AC Machines at Low Speed and Standstill Based on the INFORM Method", *IEEE IAS Annual Meeting*, pp.270-277, 1996



- [66]. Schroedl M, Hennerbichler D and Wolbank T.M, "Induction Motor Drive For Electric Vehicles without Speed and Position Sensors", *EPE Conference*, pp.271-275, 1993
- [67]. Sul S-K and Ha J-I, "Sensorless Field Orientation Control of an Induction Machine by High Frequency Signal Injection", *IEEE IAS Annual Meeting*, pp.426-432, 1997
- [68]. Cilia J, Asher G.M, Bradley K.J and Sumner M, "Sensorless Position Detection for Vector-Controlled Induction Motor Drives using an Assymmetric Outer-Section Cage", *IEEE Transactions on Industry Applications*, Vol.33, No.5, pp.1162-1169, 1997
- [69]. Degner M.W and Lorenz R.D, "Position Estimation in Induction Machines Utilising Rotor Bar Slot Harmonics and Carrier-Frequency Signal Injection", *IEEE Transactions on Industry Applications*, Vol.36, No.3, pp.736-742, 2000
- [70]. Holtz J, Jiang J and Pan H, "Identification of Rotor Position and Speed of Standard Induction Motors at Low Speed including Zero Stator Frequency", *IEEE IECON Conference*, pp.971-976, 1997
- [71]. Holtz J, "Sensorless Position Control of Induction Motors – An Emerging Technology", *IEEE Transactions on Industrial Electronics*, Vol.45, No.6, pp.840-852, 1998
- [72]. Jansen P.L and Lorenz R.D, "Transducerless Position and Velocity Estimation in Induction and Salient AC Machines", *IEEE Transactions on Industry Applications*, Vol.31, No.2, pp.240-247, 1995
- [73]. Spiteri Staines C, Asher G.M, Sumner M and Bradley K.J, "A Periodic Burst Injection Method for Deriving Rotor Position in Saturated Cage-Salient Induction Motors without a Shaft Encoder", *IEEE Transactions on Industry Applications*, Vol.35, No.4, pp.851-858, 1999
- [74]. Teske N, Asher G.M, Sumner M and Bradley K.J, "Encoderless Position Estimation for Symmetric Cage Induction Machines Under Loaded Conditions", *IEEE Transactions on Industry Applications*, Vol.37, No.6, pp.1793-1800, 2001
- [75]. Lorenz R.D, "Self Sensing Motion Control for Electrical and Hybrid Electrical Vehicles", *IEE Power Conversion and Applications Lecture*, Birmingham, UK, May 2001

- [76]. Schauder C, "Adaptive Speed Identification for Vector Control of Induction Motors without Rotational Transducers", *IEEE Transactions on Industry Applications*, Vol.28, No.5, pp.1054-1061, 1992
- [77]. Tamai S, Sugimoto H and Yano M, "Speed Sensor-less Vector Control of Induction Motor with Model Reference Adaptive System", *IEEE IAS Annual Meeting*, pp.189-195, 1987
- [78]. Jansen P.L and Lorenz R.D, "Accuracy Limitations of Velocity and Flux Estimation in Direct Field Oriented Induction Machines", *EPE Conference*, pp.312-318, 1993
- [79]. Peng F and Fukao T, "Robust Speed Identification for Speed Sensorless Vector Control of Induction Motors", *IEEE IAS Annual Meeting*, pp.419-426, 1993
- [80]. Cilia J, "Sensorless Speed and Position Control of Induction Motor Drives", *PhD Thesis, The University of Nottingham, England*, 1997
- [81]. Ohtani T, Takada N and Tanaka K, "Vector Control of Induction Motor without Shaft Encoder", *IEEE Transactions on Industry Applications*, Vol.28, No.1, 1992
- [82]. Ohyama K, Shinohara K and Nagano T, "Stability Analysis of Direct Field Oriented Control System of Induction Motor without Speed Sensor Using Adaptive Rotor Flux Observer", *ICEM Conference*, pp.1006-1011, 1998
- [83]. Kubota H, Matsuse K and Nakano T, "DSP-Based Speed Adaptive Flux Observer of Induction Motor", *IEEE Transactions on Industry Applications*, Vol.29, No.2, pp.344-348, 1993
- [84]. Yang G and Chin T-H, "Adaptive-Speed Identification Scheme for a Vector-Controlled Speed Sensorless Inverter-Induction Motor Drive", *IEEE Transactions on Industry Applications*, Vol.29, No.4, pp.820-825, 1993
- [85]. Xu X and Novotny D.W, "Implementation of Direct Stator Flux Orientation Control on a Versatile DSP Based System", *IEEE Transactions on Industry Applications*, Vol.27, No.4, pp.694-700, 1991
- [86]. Jiang J and Holtz J, "High Dynamic Speed Sensorless AC Drive with On-Line Parameter Tuning and Steady State Accuracy", *IEEE Transactions on Industrial Electronics*, Vol.44, No.2, pp.240-246, 1997

- [87]. Kim Y.R, Sul S.K and Park M.H, "Speed Sensorless Vector Control of Induction Motor Using an Extended Kalman Filter", *IEEE Transactions on Industry Applications*, Vol.30, No.5, pp.1225-1233, 1994
- [88]. Al-Tayie J.K and Acarnley P.P, "Estimation of Speed, Stator Temperature and Rotor Temperature in Cage Induction Motor Drive Using the Extended Kalman Filter", *IEE Proceedings - Electric Power Applications*, Vol.144, No.5, pp.301-309, 1997
- [89]. Terörde G and Belmans R, "Improved Control of Induction Motor Drives Without a Shaft Sensor", *EPE Conference*, pp.(on CD-ROM), 2001
- [90]. Brahim L.B and Kurosawa R, "Identification of Induction Motor Speed Using Neural Networks", *IEEE PCC Conference*, pp.689-694, 1993
- [91]. Sumner M. "Vector Controlled Induction Motor Drive Using Transputer Parallel Processors", *PhD Thesis, The University of Nottingham, England*, 1990.
- [92]. Cupertino F, "An Investigation into Direct Flux Control", *Internal Report, The University of Nottingham*, 2000
- [93]. "TMS320C4x – User's Guide", *Texas Instruments*, 1996
- [94]. "DSPLINK – System Expansion Interface", *Loughborough Sound Images (now Bluewave)*, 1991
- [95]. Balmer L, "Signals and Systems – an Introduction", *Prentice Hall*, 1991
- [96]. Levi E and Wang M, "Impact of Parameter Variations on Speed Estimation in Sensorless Rotor Flux Oriented Induction Machines", *IEE PEVD Conference*, pp.305-310, 1998
- [97]. Kubota H, Matsuse K and Nakano T, "New Adaptive Flux Observer of Induction Motor for Wide Speed Range Motor Drives", *IEEE IECON Conference*, pp.921-926, 1990
- [98]. Franklin G.F, Powell J.D and Emami-Naeini A, "Feedback Control of Dynamic Systems", *Addison-Wesley Publishing Company*, 1994
- [99]. Kubota H and Matsuse K, "The Improvement of Performance at Low Speed by Offset Compensation of Stator Voltage in Sensorless Vector Controlled Induction Machines", *IEEE IAS Annual Meeting*, pp.257-261, 1996

- [100]. Kubota H, Sato I, Tamura Y, Matsuse K, Ohta H and Hori Y, "Stable Operation of Adaptive Observer Based Sensorless Induction Motor Drives in Regenerating Mode at Low Speeds", *IEEE IAS Annual Meeting*, pp.469-474, 2001
- [101]. Sugimoto H, "One Improving Measures of Stability in Regeneration Operation of Speed Sensorless Vector Control Induction Motor System Using Adaptive Observer of Secondary Magnetic Flux" (sic), *IPEC Conference*, pp.1069-1074, 2000
- [102]. Hurst K.D and Habetler T.G, "Sensorless Speed Measurement Using Current Harmonic Spectral Estimation in Induction Machine Drives", *IEEE PESC Conference*, pp.10-15, 1994
- [103]. Ferrah A, "A Novel Approach to Sensorless Speed Detection Using Rotor Slot Harmonics", *PhD Thesis, The University of Nottingham, England*, 1993
- [104]. Blasco-Gimenez R, Asher G.M, Sumner M and Bradley K.J, "Performance of FFT-rotor slot harmonic speed detector for sensorless induction motor drives", *IEE Proceedings - Electric Power Applications*, Vol.143, No.3, pp.258-268, 1996
- [105]. Ferrah A, Bradley K.J and Asher G.M, "An FFT-Based Novel Approach to Non-invasive Speed Measurement in Induction Motor Drives", *IEEE Transactions on Instrumentation and Measurement*, Vol.41, No.6, pp.797-802, 1992
- [106]. Ferrah A, Bradley K.J and Asher G.M, "Sensorless Speed Detection of Inverter Fed Induction Motors Using Rotor Slot Harmonics and Fast Fourier Transform", *IEEE PESC Conference*, pp.279-286, 1992
- [107]. Hurst K.D, Habetler T.G, Griva G and Profumo F, "Speed Sensorless Field-Oriented Control of Induction Machines Using Current Harmonic Spectral Estimation", *IEEE IAS Annual Meeting*, pp.601-607, 1994
- [108]. Hurst K.D and Habetler T.G, "A Comparison of Spectrum Estimation Techniques for Sensorless Speed Detection in Induction Machines", *IEEE Transactions on Industry Applications*, Vol.33, No.4, pp.898-905, 1997
- [109]. Blasco-Gimenez R, Asher G.M and Sumner M, "Rotor Time Constant Identification in Sensorless Vector Control Drives Using Rotor Slot Harmonics", *EPE Conference*, pp.1.083-1.088, 1995

- [110]. Ferrah A, Bradley K.J, Asher G.M and Woolfson M.S, "An Investigation into Speed Measurement of Induction Motor Drives Using Rotor Slot Harmonics and Spectral Estimation Techniques", *IEE Electrical Machines and Drives Conference*, pp.185-189, 1993
- [111]. Ferrah A, Bradley K.J, Woolfson M.S and Asher G.M, "A New Sensorless Dynamic Speed-Estimator for Induction Motor Drives Using Predictive Adaptive Filtering", *IEEE Instrumentation and Measurement Technology Conference*, pp.458-463, 1996
- [112]. Ferrah A, Bradley K.J, Hogben P.J, Woolfson M.S and Asher G.M, "A Transputer-Based Speed Identifier for Induction Motor Drives Using Real-Time Adaptive Filtering", *IEEE IAS Annual Meeting*, pp.394-400, 1996
- [113]. Ferrah A, Bradley K.J, Hogben-Laing P.J, Woolfson M.S, Asher G.M, Sumner M, Cilia J and Shuli J, "A Speed Identifier for Induction Motor Drives Using Real-Time Adaptive Digital Filtering", *IEEE Transactions on Industry Applications*, Vol.34, No.1, pp.156-162, 1998
- [114]. Ferrah A, Hogben-Laing P.J, Bradley K.J, Asher G.M and Woolfson M.S, "The Effect of Rotor Design on Sensorless Speed Estimation Using Rotor Slot Harmonics Identified by Adaptive Digital Filtering Using the Maximum Likelihood Approach", *IEEE IAS Annual Meeting*, pp.128-135, 1997
- [115]. De Jong H.C.J, "AC Motor Design", *Clarendon Press*, 1976
- [116]. Ishida M and Iwata K, "A New Slip Frequency Detector of an Induction Motor Utilizing Rotor Slot Harmonics", *IEEE Transactions on Industry Applications*, Vol. IA-20, No.3, pp.575-582, 1984
- [117]. Williams B.W, Goodfellow J.K and Green T.C, "Sensorless Speed Measurement of Inverter Driven Squirrel Cage Induction Motors without Rotational Transducers", *IEE PEVD Conference*, pp.297-300, 1990
- [118]. McClellan J.H, Shafer R.W and Yoder M.A, "DSP First – A Multimedia Approach", *Prentice Hall*, 1999
- [119]. J. Shuli, "Dynamic Performance of the Recursive Maximum Likelihood Adaptive Filter for Fast Tracking of Induction Motor Speed", *Internal Report, The University of Nottingham, England*, 1998

- [120]. Pei S-C and Tseng C-C, "Real Time Cascade Adaptive Notch Filter Scheme for Sinusoidal Parameter Estimation", *Signal Processing* 39, pp.117-130, 1994
- [121]. Nehoral A, "A Minimal Parameter Adaptive Notch Filter With Constrained Poles and Zeros", *IEEE Transactions on Acoustics, Speech and Signal Processing*, Vol.33, No.4, 1985
- [122]. Cilia J, Asher G.M, Shuli J, Sumner M, Bradley K.J and Ferrah A, "The Estimation of the Fundamental Frequency in Sensorless Vector Controlled Induction Motor Drives using a Real-Time Adaptive Filter", *PEMC Conference*, pp.1017-1021, 1998
- [123]. Valenzuela M.A and Lorenz R.D, "Electronic Line-Shafting Control for Paper Machine Drives", *IEEE Transactions on Industry Electronics*, Vol.37, No.1, pp.158-164, 2001
- [124]. Anderson R.G, Meyer A.J, Valenzuela M.A and Lorenz R.D, "Web Machine Coordinated Motion Control via Electronic Line-Shafting", *IEEE Transactions on Industry Electronics*, Vol.37, No.1, pp.247-254, 2001
- [125]. Tomizuka M, Hu J-S, Chiu T-C and Kamano T, "Synchronization of Two Motion Control Axes Under Adaptive Feedforward Control", *ASME Transactions – Journal of Dynamic Systems, Measurement and Control*, Vol.114, pp.196-203, 1992
- [126]. Koren Y, "Cross-Coupled Biaxial Computer Control for Manufacturing Systems", *ASME Transactions – Journal of Dynamic Systems, Measurement and Control*, Vol.102, pp.265-272, 1980
- [127]. "Drives and Servos Yearbook 1990-1", *Control Techniques Drives PLC*, 1990
- [128]. Jones R, Wymeersch W and Lataire P, "Vector Controlled Drives in a Steel Processing Application", *EPE Conference*, pp.508-512, 1993
- [129]. Hartley M, "Servo Drives Spread their Wings", *Drives and Controls Magazine*, p.40, Nov/Dec 2000
- [130]. "Gears Help to Keep the *Daily Mail* Presses in Synch", *Drives and Controls Magazine*, p.45, Oct 2000
- [131]. Brandenburg G, Geißenberger S, Kink C, Schall N-H and Schramm M, "Multimotor Electronic Line Shafts for Rotary Offset Printing Presses: A

- Revolution in Printing Machine Techniques”, *IEEE/ASME Transactions on Mechatronics*, Vol.4, No.1, pp.25-31, 1999
- [132]. Dinsdale J and Jones P.F, “The Electronic Gearbox – Computer Software Replaces Mechanical Couplings, *Annals of the CIRP*, Vol.31, No.1, pp.247-249, 1982
- [133]. SakaiS-I, Sado H and Hori Y, “Motion Control in an Electric Vehicle with Four Independently Driven In-Wheel Motors”, *IEEE/ASME Transactions on Mechatronics*, Vol.4, No.1, pp.9-16, 1999
- [134]. Peng F-Z, “Speed and Flux Sensorless Field Oriented Control of Induction Motors for Electric Vehicles”, *IEEE APEC Conference*, pp.133-139, 2000
- [135]. Chan C.C and Chau K.T, “Modern Electric Vehicle Technology”, *Oxford University Press*, 2001
- [136]. Lorenz R.D and Schmidt P.B, “Synchronized Motion Control for Process Automation”, *IEEE IAS Annual Meeting*, pp.1693-1698, 1989
- [137]. Perez-Pinal F.J, “Multi-Motor Induction Motor Drives”, *MSc Dissertation, The University of Nottingham*, England, 2001.
- [138]. Budig P-K, “Multi-Motor Drives for Textile Machines”, *EPE Conference*, pp.1.421-1.426, 1995
- [139]. Ho S, Jones A and Cox C.S, “Torque Disturbances and their Effect on Process Control”, *IEE PEVD Conference*, pp.602-607, 1994
- [140]. Beaven R.W, Wilkes L.D, Wright M.T, Garvey S.D and Friswell M, “The Application of Setpoint Gain Scheduling to Improve the Performance of High Speed Independent Drives”, *IEE Colloquium on Precision Motion Control in Robotics and Machine Drives*, pp.7/1-7/5, 1994

## APPENDIX A Project Resulting Conference Papers

### A.1 IEE PEVD 2000 – London

#### USE OF ADAPTIVE NOTCH FILTERING FOR ACCURATE SPEED HOLDING IN A SENSORLESS INDUCTION MOTOR DRIVE

G Turl, M Sumner, G.M. Asher

The University of Nottingham, UK

##### ABSTRACT

This paper presents a high accuracy, sensorless, induction motor speed control scheme. It is based on a typical V/F drive and uses an Adaptive Notch Filter to provide real-time speed measurement and feedback. This facilitates precise steady state speed control of an induction machine over a wide speed range. The implementation requires only knowledge of the number of rotor slots and does not require resistance or inductance parameters.

##### INTRODUCTION

High performance operation can be obtained from an induction motor drive where accurate instantaneous speed can be derived. This speed information is generally obtained from a shaft-mounted transducer. This reduces the reliability and increases the cost of the overall drive. In some cases the use of such a transducer is not a practical consideration.

Sensorless speed control aims to provide this high performance, without the use of sensors/transducers. Many existing sensorless techniques use machine model parameters and voltage/current measurement to obtain a speed estimate [1, 2]. It is inherently necessary to have accurate parameter estimation to obtain accurate speed information and these parameters may vary with operating conditions. Other techniques require specially modified motors and signal injection [3]. This may also impose practical constraints and increase power losses. The technique described in this paper is suitable for a majority of unmodified induction machines and relies on only a few, well known machine parameters.

Conductor slotting on the rotor of an induction motor causes harmonics to be present in the stator current. The frequencies of the harmonics relate to the number of rotor slots and the rotor speed. Real time tracking of the harmonics allows real time tracking of the rotor speed. Previous work in this area has seen various signal-processing techniques, such as the Recursive Maximum Likelihood – Adaptive Tracking Filter (RML-ATF), used to tune parameter based sensorless schemes [4-7]. The motor parameter that these schemes rely on is knowledge of the number of rotor slots.

These frequency-tracking schemes can become confused by the presence of nearby inverter harmonics and this is particularly problematic at low load, when the slot harmonic magnitude will be small and at low speed, when inverter, motor and slot harmonics will be in close proximity. At zero speed, harmonics relating to speed will obviously not exist and harmonics that exist above zero hold no directional information.

The work presented here describes the use of an RML-ATF algorithm to obtain precise steady state speed control of a practical drive system. Factors that influence the performance of the RML-ATF are explored and discussed, as is the management of algorithm parameters.

A control strategy is presented which fulfils the desired aim of the work. True closed-loop speed control is demonstrated using the RML-ATF as real-time feedback. Minimum knowledge of motor parameters is required to produce the speed holding performance demonstrated. The scheme relies only on nameplate data and knowledge of the number of rotor slots. The latter could be determined from simple standstill tests.

The work is not concerned with dynamic performance to a variation of speed demand, but does consider load impact response in steady state operation. Results are presented which demonstrate the improved steady state speed holding performance of the drive.

##### RML-ATF

The largest slot harmonic will exist at a frequency obtained from the following, equation(i):

$$f_{sh} = \frac{z}{p} (f_0 - f_{slip}) \pm f_0 \quad (i)$$

This is where the machine has  $p$  pole pairs and  $z$  rotor slots,  $f_0$  is the fundamental excitation frequency and  $f_{slip}$  is the slip frequency. If  $(z/p + 1)$  or  $(z/p - 1)$  is even or a multiple of 3, the corresponding harmonic will not exist. In many machines only one harmonic will exist, if both exist the one with larger amplitude can be used.



The RML-ATF technique has been used in other applications that require the tracking of single sinusoids and the precise nature of the algorithm has been presented before [7-10]. The configuration used in this work consists of a digital notch filter whose centre frequency is recursively tuned to minimise the signal around an estimated slot harmonic. When the signal is at a minimum, the centre frequency is that of the slot harmonic and rotor speed can be calculated. Unlike FFTs, the RML-ATF can be implemented as a recursive real time measurement of speed, at realistic sample rates.

Information about the induction motor, such as the number of rotor slots, is known and this allows for direct implementation of RML-ATF algorithms.

The inverter has been modified to allow direct access to the gate control of the switching devices. This allows flexible software based implementation of a suitable PWM strategy. Both voltage and current transducers are fitted to allow measurement of these quantities. The latter is necessary for implementation of the RML-ATF.

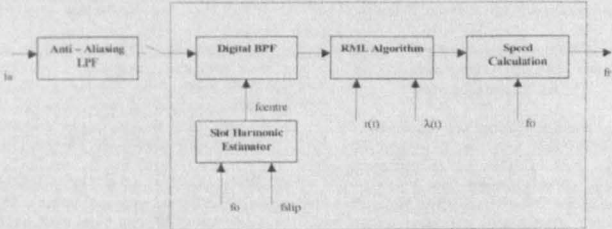


Figure 1: Structure of the RML-ATF Speed Estimator

Parameters used in the RML-ATF algorithm define the size of the notch stop band and the amount of past samples used in an averaging process. These parameters must be managed to obtain suitable speed accuracy in steady state and suitable speed tracking in dynamic situations.

A Band Pass Filter (BPF) is necessary to pre-filter the line current prior to the RML-ATF. This minimises the effects of the fundamental and other harmonics. The performance of this filter and its management can drastically affect the performance of the RML-ATF.

Improved performance can be obtained if the initial guess for the slot harmonic frequency is accurate. If this is the case, then the bandwidths of both the RML-ATF and the BPF can be minimised for improved accuracy. As is evident in equation(i), this requires an estimate of slip and this can be obtained from a measurement of current amplitude and knowledge of simple motor ratings, obtained from nameplate data. This still results in a simple sensorless scheme, requiring little advanced knowledge of motor parameters.

A typical RML-ATF structure is as shown in figure 1.

EXPERIMENTAL RIG

The motor rig used for experimental testing consists of a 4-pole, 4kW, closed-slot, squirrel cage induction motor, fed by a 10kW IGBT inverter.

The induction motor is coupled to a load DC machine. This is controlled by a 4-quadrant DC converter and provides a constant torque load throughout the speed range. The total inertia of the rig is several times bigger than that of the induction motor alone, due to the use of the DC machine. This is a consideration for design of the control scheme.

The rig is fitted with a 10000 pulse per revolution incremental encoder. This gives a robust measurement of speed, to which results from the RML-ATF routine can be compared.

The RML-ATF algorithm and all drive control and data capture is implemented on a DSP board housed in a PC. The DSP used is a Texas TMS320C44 floating point unit and the main board has room for additional processors, should this expansion be required. Use of a processor such as this, allows for fast and accurate calculation of the RML-ATF and associated filter functions in real time. Where necessary, accurate mathematical functions can be used, trigonometric for example. As opposed to look-up tables, this facilitates very accurate positioning of filter functions and calculation of their associated parameters.

EXPERIMENTAL IMPLEMENTATION

Pre-filtering Prior to the RML-ATF Algorithm

The immediately evident problems associated with tracking a speed harmonic are:

- a) Rotor slot harmonics exist with other inverter harmonics and the fundamental stator current frequency.
- b) At low load the stator current amplitude will be small, hence the slot harmonic will have a poor signal to noise ratio.
- c) At low speed the switching harmonics will be in close proximity. The slot harmonic may pass through several switching harmonics through the rated load range

The induction machine used in the experimental rig has 28 rotor slots and 2 pole pairs. Referring back to equation(i) and the criteria for existence of slot harmonics, it is clear that only one harmonic will exist for the test machine and at no load, when slip will be small, this will be close to the 13th inverter harmonic.

It must be noted that this is a very testing condition for the RML-ATF. Other machines of a similar power rating will often have more rotor slots per pole pair, which places the rotor slot harmonic, at and around no load, at a higher frequency. When this is the case, the inverter harmonics will possibly be of a smaller magnitude.

To overcome the no load problem and the significance of lower order harmonics, narrow bandwidth notch filters were included. These filters eliminate troublesome inverter harmonics. The 13th harmonic filter remains permanently on, whilst the others are switched out when the stator current rises above a set level. This is the only modification made to the general RML-ATF structure shown in figure 1. The filters are included prior to the BPF.

The performance of the BPF algorithm affects the performance of the RML-ATF. If a filter with a small pass band can be placed accurately at the slot harmonic frequency, the quality of current fed to the RML-ATF is good and the speed estimate highly accurate. This defeats the object, to be able to place the filter with high accuracy requires that the speed be known.

Here the scheme uses the knowledge of simple nameplate parameters to provide an initial guess. In the implemented experimental scheme, rated machine slip was divided by rated torque current ( $I_q$ ). Measurement of  $I_q$  then translates to an estimated slip and through knowledge of the excitation frequency, a crude estimate of speed is available. This is used to centre the BPF. It must be remembered that the control scheme is based around simple V/F control. The excitation frequency is known, although as vector orientation is not, the transform angle used to obtain  $I_q$  is approximate.

The bandwidth of the BPF must be sufficiently large to allow for the error in this initial speed estimate and to allow the RML-ATF to track a speed change without loss of signal. This scheme uses a filter with constant

damping factor. In this case the bandwidth will change with centre frequency. This is useful as the inverter harmonic spread tightens at lower speeds.

#### Speed Measurement Using the RML-ATF

RML-ATF parameters need to be managed for a given sample frequency. The key parameters are:

- a) the bandwidth of the notch filter [  $r(t)$  ]
- b) the number of past samples used in the averaging process [  $\lambda(t)$  ]

It was found that the BPF algorithm required a sample frequency of at least four times the maximum frequency to be tracked. An increase in sample frequency will improve the dynamic performance of the RML-ATF speed track, but reduce the accuracy. The  $r(t)$  and  $\lambda(t)$  parameters relate to this choice of sample frequency, the quality of the initial speed guess, the desired speed accuracy and the desired dynamic response.

In this implementation two RML-ATF schemes are used at differing sample frequencies. A 4kHz scheme will track speeds to 1500rpm, this is rated speed. A second scheme uses an 800Hz sample rate for improved accuracy at lower speeds to around 400rpm. The speed estimate is taken from the most appropriate source referenced to a pre-set level of demand speed.

In the steady state,  $r$  and  $\lambda$  parameters are set such that the bandwidth of the notch filter is small and the number of past samples used in the averaging process is high. Thus the accuracy of the RML-ATF speed estimate is maximised. There is a trade-off against the dynamic performance and parameters should be set to allow for appropriate speed tracking if demand speed changes, or for slow variations in load.

For load impacts  $r$  and  $\lambda$  parameters must be relaxed, effectively widening the notch bandwidth and reducing the past sample average. In this scheme this occurs instantaneously when the time derivative of stator current goes above a set threshold level. After this trigger the parameters climb back to steady state values.

The limits, between which the parameters vary, differ according to the sign of the current derivative. The performance of the RML-ATF is degraded at no load when compared to full load, due to the lower slot harmonic amplitude. Hence the different parameter management for a load stepped on than for a load stepped off.

All parameters used throughout the complete scheme relate to the number of rotor slots on the machine and

the desired speed tracking bandwidth. The algorithm therefore remains generic and applicable to alternative machines.

The Control Strategy

The control strategy is based around a V/F drive whose voltage demands are set in the rotating dq frame. This is not a vector drive, so this transformation is approximate. In the steady state however, if measured current is transformed in the same way, the dq currents give an approximation of machine flux and torque. The torque producing current ( $i_q$ ) is used to obtain the initial estimate of speed for the BPF, as outlined earlier.

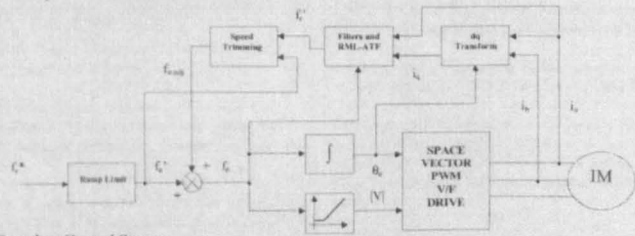


Figure 2: The Complete Control Structure

The scheme demonstrates the performance improvements that can be made to simple V/F control by accurately measuring the motor speed. This tests the accuracy and robustness of the RML-ATF, by using its speed information as direct feedback. Such a scheme is less sensitive to any error or noise, that may appear on the speed estimate, than a field oriented vector scheme. Also, the excitation frequency is known in V/F control and this information is required by the RML-ATF.

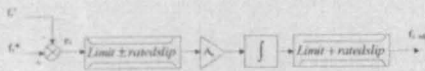


Figure 3: Structure of the Speed Trimmer

Whilst not trying to achieve the performance of vector control, by recursively adjusting the excitation frequency, the control scheme is able to account for changes in speed due to load.

The overall control strategy can be seen illustrated in figure 2.

The speed signal obtained from the RML-ATF is used as a real-time measure of speed and directly fed back to enable accurate speed trimming for variations in load

condition. The speed-trimming scheme is shown in more detail in figure 3.

The error between the desired speed and that measured by the RML-ATF, is related and limited to rated machine slip. The excitation frequency is then recursively adjusted to minimise the error.

The adjustment of the excitation frequency is ramp limited. This will limit the instantaneous current in a similar way to the ramp limit in the standard V/F drive. As the scheme is an add on to a V/F scheme, where vector orientation is not assured, the ramp limit must be set within the current handing and regeneration capabilities of the V/F drive.

In this experimental rig a brake unit has been fitted, thus the limitations of the control scheme can be fully explored. Computer simulation of the drive was used to set suitable gain parameters.

RESULTS

The first result demonstrates the performance of the RML-ATF as a speed observer. The algorithm set-up is as described in the experimental implementation. The control strategy is not enabled and the RML-ATF is used to observe the speed of a standard V/F scheme during a load impact. This result is shown in figure 4.

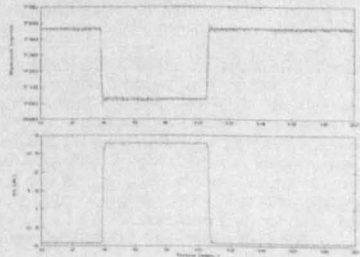


Figure 4: Encoder and RML-ATF Speed during a Load Impact in V/F Mode.



The speed demand is 750 rpm, half rated. The graph shows a typical V/F characteristic. At no load the speed is close to the demand and when the load is applied, the speed simply drops. It is difficult to distinguish between the RML-ATF estimate and the speed measured by the encoder. The no load performance shows no sign of noise and the parameter management scheme ensures that the RML-ATF tracks the fast variation in speed when the load is switched in and out.



Figure 5: Steady State, Encoder and RML-ATF Measurement of Speed in V/F Mode

The graph shown in figure 5 demonstrates that the accuracy of the RML-ATF, here measuring a 300rpm demand at half load, is within the accuracy of the encoder.

Figure 6 shows a result obtained from the speed-trimming scheme. This is the upper most graph. The demand speed, time scale and load impact is as shown in figure 4. This illustrates the steady state accuracy and dynamic performance of the speed trimming control. An encoded vector control response, obtained from the same rig, is shown in the lower graph for comparison.

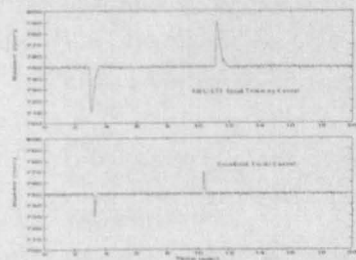


Figure 6: Speed Response of Speed Trimming and Encoded Vector Scheme during a Full Load Impact.

It can be seen that, in the speed trimming scheme, the no load speed is at that of the demand. Upon application and removal of the load, the control scheme corrects for the error and produces a steady state speed equal to that of the demand.

The scheme has been tested over the full range of rated motor speed. Figure 7 shows the speed responses of the speed trimming scheme at 300 rpm and 1500rpm. In all cases the encoder has been used as the observer

of speed and plays no part in the control structure. All responses shown are for full load impacts.

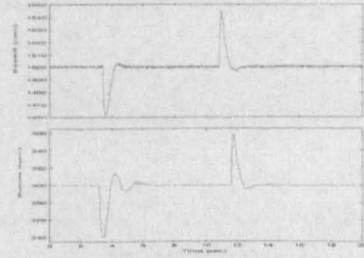


Figure 7: Speed Response of Speed Trimming Scheme during Full Load Impacts, at 1500rpm and 300rpm.

It is clear that the response at 300rpm, 5Hz mechanical, is degraded from that at both 1500rpm and 750rpm.

Although field orientation is not known in V/F mode, the inclusion of an Id current controller gave better regulation. Figure 8 shows the drive running at 150rpm during a half load impact, with Id current control.

Due to the poor regulation at the lower speeds, the trimmer dynamic performance varies with speed for a fixed load impact. In these conditions the load impact has a more significant effect on speed and the speed-trimming scheme can saturate.

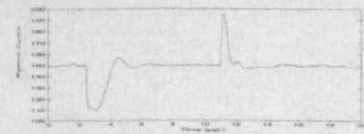


Figure 8: Speed Response of Speed Trimming Scheme during a Half Load Impact, at 150rpm.

CONCLUSIONS AND DISCUSSION

It is clear that the RML-ATF and the implemented control scheme facilitate highly accurate steady-state speed holding to below 300rpm. Its use as a direct feedback speed measurement demonstrates its robustness. Figure 6 shows that although the dynamic performance of the speed trimming scheme is not as fast as the vectored scheme, the steady state performance is as good. At the wide range of speeds, the control scheme maintains a steady state motor speed within only a 1-2 bit encoder resolution.

The control scheme shown and the RML-ATF method of speed measurement are viable for use in a

## A.2 IEEE PESC 2001 - Vancouver

commercial drive. The RML-ATF could easily be run on a DSP system separate from the drive and the modifications required to a standard V/F scheme, to include the speed trimmer, are minimal. In this implementation the complete control algorithm and the RML-ATF are implemented on a single processor.

The implications of the speed measurement accuracy, shown in the results presented here, would facilitate tuning of a simple sensorless scheme, to provide performance on a par with that of encoded vector control. A scheme such as this could help to overcome the poor torque control performance at low speeds.

In this implementation, the speed measure obtained from the RML-ATF is shown to greatly improve the performance of the V/F drive. True closed loop speed control is demonstrated, without the use of an encoder and with no use of motor model parameters. This scheme could be used for applications where accurate speed holding is required, but fast speed demand variation is not. This would include some rolling road or winding applications.

## REFERENCES

- [1]. Schauder C, 1992, "Adaptive Speed Identification for Vector Control of Induction Motors without Rotational Transducers", *IEEE Trans Indust Apps*, 28, pp 1054-1061.
- [2]. Holtz J, 1996, "Sensorless Control of AC Motor Drives", *IEEE Press Book*, pp 21-29
- [3]. Holtz J, 1998, "Sensorless Position Control of Induction Motors - An Emerging Technology", *IEEE Trans Indust Electronics*, 45, pp 840-852
- [4]. Hurst K D, Habetler T G, Griva G and Profumo F, 1994, "Speed Sensorless Field-Oriented Control of Induction Machines using Current Harmonic Spectral Estimation", *Proc IEEE IAS*, pp 601-607
- [5]. Blasco-Gimenez R, 1995, "High Performance Sensorless Vector Control of Induction Motor Drives", *PhD Thesis, University of Nottingham, England*
- [6]. Jiang J and Holtz J, 1997, "High Dynamic Speed Sensorless AC Drive with On-Line Parameter Tuning and Steady State Accuracy", *IEEE Trans Indust Electronics*, 44, pp 240-246
- [7]. Cilia J, Asher G M, Shuli J, Sumner M, Bradley K J and Ferrah A, 1998, "The Recursive Maximum Likelihood Algorithm for Tuning the Rotor Time Constant in High-Performance Sensorless Induction Motor Drives", *Proc ICEM*, 2, pp 926-930
- [8]. Ferrah A, Bradley K J, Hogben-Laing P J, Woolfson M S, Asher G M, Sumner M, Cilia J and Shuli J, 1998, "A Speed Identifier for Induction Motor Drives using Real-Time Adaptive Digital Filtering", *IEEE Trans Indust Apps*, 34, pp 156-162
- [9]. Shuli J, Asher G M, Sumner M, Bradley K J, Cilia J and Ferrah A, 1998, "Dynamic Tracking of Induction Motor Speed using Rotor Slot Harmonics and the Recursive Maximum Likelihood Algorithm", *Proc EPE*, pp 179-183
- [10]. Soo-Chang P and Chien-Cheng T, 1994, "Real Time Cascade Adaptive Notch Filter Scheme for Sinusoidal Parameter Estimation", *Signal Processing* 39, pp 117-130

## A.2 IEEE PESC 2001 - Vancouver

## A Hybrid Sensorless Induction Motor Control Strategy for High Performance Drive Applications

G. Turl, M. Sumner and G.M. Asher  
 School of Electrical and Electronic Engineering  
 The University of Nottingham  
 Nottingham, NG7 2RD, UK

**Abstract**-This paper presents a sensorless induction motor drive scheme comprising a model-based speed estimator for dynamic performance and a rotor slot harmonic estimator for speed accuracy. The slot harmonic speed estimate is used to tune the machine model, providing speed-holding accuracy comparable to a sensorless drive fitted with a 10,000 line encoder sampled every 0.01 sec.

System performance is evaluated over the full speed and load range, with a view to its use in multi-motor, speed-synchronized drives, an application typically requiring the performance of an encoded system.

## I. INTRODUCTION

Encoderless control of induction motor drives is a commercially established means of providing high dynamic performance from an induction motor, bringing both economic and practical benefits. Many sensorless techniques use machine electrical parameters and voltage/current measurement (quantities that would typically be measured or known) to obtain a speed estimate through application of the machine dynamic equations. These techniques are typified by those due to Schauder [1], Ohtani [2] and Kubota [3]. In these model-based techniques parameters will vary with operating condition and this will affect the drive performance.

More recently sensorless position control has been demonstrated [9-12], but these techniques may require specially modified motors and/or signal injection and this may impose practical limitations and increase power losses. It is believed that the range of these techniques is limited to the very low speed region, because of the large voltages required for signal injection at higher speeds.

An alternative approach is to combine model-based estimators with an independent estimation of speed, for example that obtained from harmonics in voltage and current due to rotor slotting. With this technique accurate steady state speed holding accuracy has been demonstrated [4-6]. The majority of work in this area has used spectral estimation techniques based on batch processing methods, such as the Fast Fourier Transform (FFT). Whilst this provides high accuracy, the delay associated with its operation varies with operating speed and can be significant at low speed.

Excellent dynamic tracking performance has been combined with steady state accuracy through use of continuous adaptive signal processing methods. This is very well demonstrated in work based on the Recursive Maximum Likelihood algorithm [7-8]. This technique has been shown to be suitable for a majority of unmodified induction machines, but the performance can be compromised at very low speeds and low loads.

The work presented here employs a model-based speed estimator for speed feedback to the speed controller (to retain high dynamic performance) and tuning that uses speed measurement derived from the rotor slot harmonics (RSH). The slot harmonic estimate is compared with the model estimate and the error used to tune the rotor time constant ( $T_r$ ) in the model-based estimator. The tuning maintains a steady state speed accuracy that will be resilient to small errors in the other model parameters. The paper briefly outlines the full sensorless algorithm, its primary intention being to test the solution over the full speed and load range. Some of these tests follow the challenging criteria set out in a paper by Ohyama [13]. The paper also presents the use of the RSH signal directly for speed feedback, and suggests suitable operating regions for each mode of operation.

## II. MODEL-BASED SENSORLESS SCHEME

The technique selected for this work is that presented by Kubota in a range of papers, the original reference being [3], and is therefore not explained in great detail here. A conventional observer structure observes rotor flux and stator currents. The rotor speed is not observed directly in this structure; an estimate of stator current error is used indirectly to adjust for speed in the observer model via a PI controller.

Fig. 1 shows the general Direct Rotor Field Orientated (DRFO) sensorless vector structure where the Kubota scheme appears as a component block. Inputs are measured voltage and current and outputs are speed and rotor flux estimates. The use of an RSH speed measurement to tune a model-based system should be applicable for the majority of algorithms of this type. The Kubota algorithm is used here as it was considered to be one of the better performing algorithms in comparative tests made between three of the more popular methods [13].



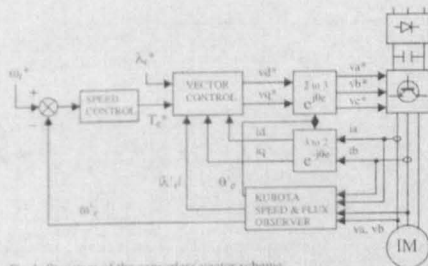


Fig.1 Structure of the sensorless vector scheme

III. TUNING USING ROTOR SLOT HARMONICS

A. Rotor Slot Harmonics

The first order RSH frequencies are defined by the following equation

$$f_{sh} = \frac{z}{p} (f_e - f_{slip}) \pm f_e \quad (1)$$

where  $p$  is the number of pole pairs,  $z$  is the number of rotor slots,  $f_e$  is the excitation frequency and  $f_{slip}$  is the slip frequency. In many machines only one harmonic will be present. In practice RSH due to higher order MMF harmonics will exist and may be of use in a robust tracking algorithm. Equation (1) is modified to

$$f_{sh} = \frac{z}{p} (f_e - f_{slip}) \pm \alpha f_e \quad (2)$$

where  $\alpha$  is a positive integer.

Slot harmonics obey similar existence criteria to PWM switching harmonics in an inverter drive. In addition, it is clear from the previous equations that at no load, where  $f_{slip}$  will be very small, a single RSH will be close to an inverter harmonic. This can be seen in fig. 2, which displays FFTs of a single stator current. The upper trace is taken at low load and the lower trace at full rated load. It is clear that with increasing load the slot harmonic moves away from the associated inverter harmonic and increases in amplitude. The machine used in this research has 14 slots per pole pair. The clearly visible RSH are those corresponding to  $\alpha=1$  and  $\alpha=3$ . Whilst others are evident, they are small in amplitude and not detectable at all speeds and loads. These results, and those in the following figure, were obtained at half rated speed (750rpm).

At lower speeds the RSH will cross inverter harmonics. Whilst the switching harmonic spread tightens with decreasing speed, the RSH will move a fixed distance from no load to full load. In this machine a greater range is obtained before this crossing occurs if the  $\alpha=3$  harmonic is tracked, due to the absence of a  $15^{th}$  inverter harmonic.

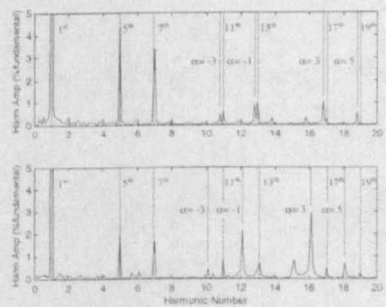


Fig.2 Stator current spectra at low and full rated load, showing the inverter harmonics and the rotor slot harmonics for  $\alpha = -3$ , etc

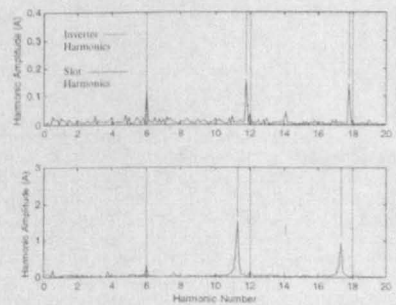


Fig.3 Stator current magnitude spectra at low and half rated load, showing the inverter harmonics and the rotor slot harmonics for  $\alpha = -3$ , etc

It was found that the range, before RSH contact with inverter harmonics, could be extended still further. When currents are measured and converted to the rotating frame, as necessary for vector control, a value for the stator current magnitude ( $I$ ) can be obtained. Fig. 3 shows how the RSH and inverter harmonics appear in this quantity. Note that the inverter harmonics appear as multiples of 6k, where  $k=(0,1,2,...)$ . The RSH are also transformed and, for our test machine, appear larger than those due to the PWM. This is a very useful consideration for the slot harmonic tracking algorithm. Another consideration is that of current control bandwidth. It was found that the RSH seen in the stator current reduced with speed, particularly in and around the current control bandwidth. When this occurs, an increase is seen in RSH amplitude in measured voltage and therefore in the voltage demand ( $V$ ) that exists in software.

The slot harmonic is tracked with an Adaptive Tracking Filter (ATF) using the Recursive Maximum Likelihood (RML) algorithm. The precise nature of the algorithm has been presented before [7-8]. The configuration utilized here

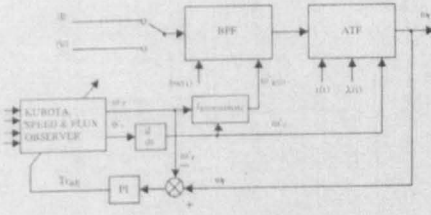


Fig.4 The RSH speed estimator and tuning scheme, with speed, flux, fundamental and slot harmonic frequency estimates obtained from observer

consists of a digital notch filter, the centre frequency of which is recursively tuned to minimize the signal around an estimated slot harmonic. When the signal is at a minimum, the centre frequency of the notch is that of the slot harmonic and the rotor speed can be calculated.

Unlike FFTs, the ATF can be implemented as a recursive real time measurement of speed at realistic sample rates. Parameters used in the ATF algorithm define the size of the notch stop band and the amount of past samples used in an averaging process [7]. For tuning of a model-based system, in the steady state, parameters are maintained at constant values and reasonable dynamic tracking is retained. A complex parameter management strategy, where modes of operation must be triggered, is not necessary.

A Band Pass Filter (BPF) is required to pre-filter the line current prior to the ATF. This minimizes the influence of the fundamental and other inverter harmonics. Here it is necessary to have some estimate of speed and fundamental frequency. These estimates are obtained from the model-based system, where speed is available directly and the fundamental frequency is available via differentiation of the flux angle.

B. Tuning the Model-Based System

A block diagram of the ATF and tuning system is shown in Fig 4. The tracking BPF pre-filter is centred with speed and fundamental frequency estimates obtained from the Kubota observer. The bandwidth of this filter is proportional to the centre frequency. It therefore decreases with speed and hence as the inverter harmonic frequencies tighten.

The output from the BPF is passed to the ATF function and an estimate of speed is produced, given knowledge of the fundamental from the observer. The notch filter bandwidth and averaging control parameters,  $r(t)$  and  $\lambda(t)$ , are held constant in this set-up.

ATF and observer speed are compared and the error used to drive a  $T_r$  adjustment value via a PI controller. This control was set-up experimentally to have a bandwidth of approximately 1Hz.

Note that two inputs to the algorithm are shown.  $\lambda$  is used as input for speeds where the RSH is outside of the current

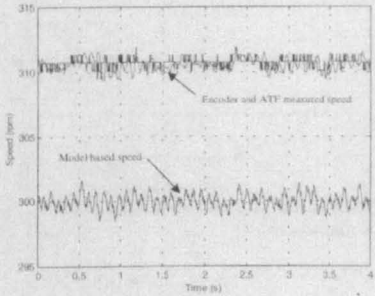


Fig.5 Encoder, ATF and model based speed estimates at 300rpm under sensorless control

control bandwidth and  $|\lambda|$  is used inside. Hysteresis is included in the changeover mechanism.

IV. EXPERIMENTAL RESULTS

The motor rig used for experimental testing consists of a 4-pole, 4kW, closed-slot, squirrel cage induction motor, fed by a 7.5kW IGBT inverter. Information about the motor, such as model parameters and number of rotor slots, is known. A 4-quadrant DC machine acts as load and the drive is fitted with a 10,000 line encoder for speed comparison. The complete sensorless algorithm, including PWM generation, is implemented on a Texas TMS320C44 DSP processing platform. Such is the nature of the ATF algorithm that supplementary dedicated processors are not required for the slot harmonic tracking.

A. Performance of the ATF Speed Estimator

Fig. 5 and Fig. 6 are included to demonstrate the performance of the ATF speed estimate. Fig. 5 displays the sensorless (model-based) speed used as feedback, the actual speed, as measured by the encoder, and the speed measured by the ATF. The drive is operating at approximately half load with a speed reference of 300rpm. The rotor time constant is purposefully de-tuned and tuning is disabled. Note that, although the model-based speed centres the BPF for the ATF algorithm, the ATF speed returns a speed signal that is almost identical to the encoder speed, both in terms of absolute accuracy and resolution. This shows that the ATF is robust to parameter inaccuracies within the model.

The upper trace in Fig. 6 shows the ATF tracking during a large speed transient. This is with ATF algorithm parameters set for steady state operation. With a more complex parameter management strategy the dynamic performance would be improved, as shown in the lower trace. These particular results were obtained with a low load and are



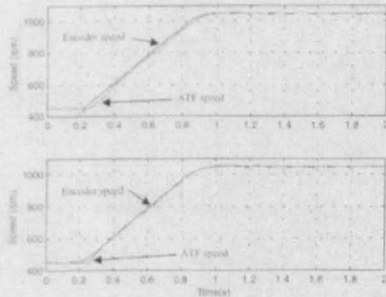


Fig.6 Encoder and ATF speed estimates during a speed transient under sensorless vector control

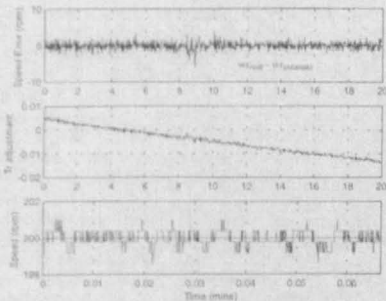


Fig.7 Speed error,  $T_r$  tuning and a speed sample from the sensorless drive at full load with tuning enabled

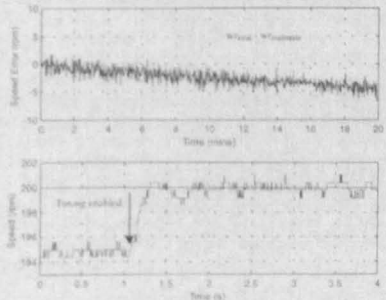


Fig.8 Speed error at full load with no tuning and measured speed with tuning enabled at 1 sec

therefore fast speed transients; the dynamic response of the ATF is being truly tested.

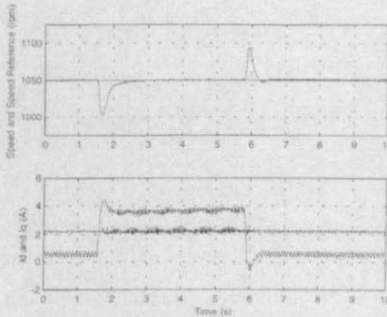


Fig.9 Load rejection performance of the tuned sensorless drive at 1050rpm

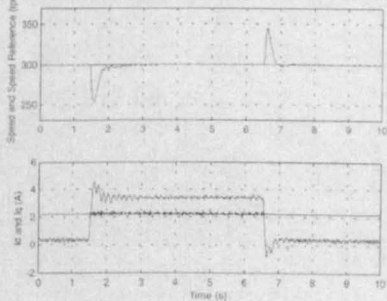


Fig.10 Load rejection performance of the tuned sensorless drive at 300rpm

*B. The Model-Based Scheme with  $T_r$  Tuning*

Fig. 7 is a result obtained with the tuned drive. The upper trace shows that the tuning scheme maintains an average error of 0rpm. The drive is operating at 200rpm with full load over a 20-minute period. The middle trace shows how  $T_r$  is tuned over that time. It can be seen, from the lower trace, that the sensorless drive displays encoder like accuracy: here the real speed is measured with the encoder, but this plays no part in the control strategy, it is used simply for illustration.

In Fig. 8 it is clear how the speed drifts under similar operating conditions with no tuning. The drive was tuned prior to  $t=0$ mins, then  $T_r$  is held constant. The lower trace displays data captured a little after  $t=20$ mins where tuning is re-enabled at approximately 1 second.

The load rejection performance is demonstrated at different speeds in Fig. 9 and Fig. 10. In both cases the drive is running at no load when close to full load is applied for several seconds before then being removed. Note that in both cases a small speed error persists for a short time just after the

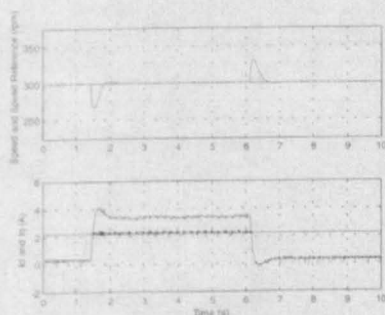


Fig.11 Load rejection performance of the encoded drive at 300rpm

load is switched in. This is due to small errors in the other motor parameters used in the sensorless scheme and would include variation in inductance parameters, due to loading, and error in  $R_s$ . Note that the  $T_r$  tuning responds to this and the speed error converges to zero in less than a second. This was one of the design criteria for the work; that the drive would maintain steady state speed holding, tolerating small error in model parameters. The steady state speed is maintained at the expense of some dynamic performance. This is an important consideration in multi-motor applications.

The response of an encoded Indirect Rotor Field Orientated (IRFO) scheme, running on the same rig, is shown in Fig. 11 for comparison.

An important aspect of sensorless drive performance evaluation is the region of low speed operation, see Fig. 12 and Fig. 13. These results show the drive running, with tuning, from 150rpm to 0rpm under both no and full load conditions. The staircase speed transients are considered a challenging test for a sensorless drive [13]. It is known that both the model-based sensorless scheme and the ATF algorithm will fail at low speed. Note that tuning is therefore disabled for speeds less than 75rpm.

The results show that excellent speed holding performance is maintained above the tuning threshold. The degradation in sensorless performance below the threshold is clear. Here the sensorless speed and flux estimator is affected by problems with voltage measurement and the influence of inverter deadtime on the quality of the voltage waveforms. Under loaded conditions, without a very good estimate of  $R_s$ , the drive will not hold at zero speed. In this case the  $R_s$  value was tuned by hand.

### C. The ATF Speed used as Direct Feedback

The continuous nature of the ATF speed measurement algorithm does allow for very high dynamic performance given use of suitable parameters. This high dynamic performance is at the expense of an increase in noise margin.

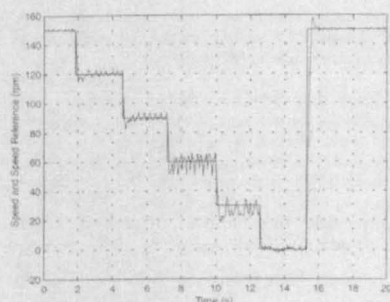


Fig.12 Low speed staircase speed transient of the tuned drive under no load

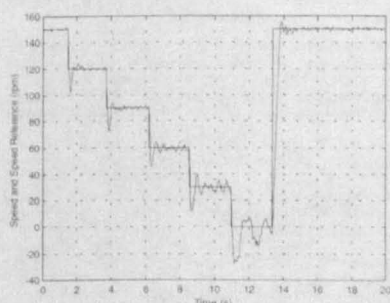


Fig.13 Low speed staircase speed transient of the tuned drive under full load

The following two figures illustrate the use of an ATF speed measure, set-up for high dynamic performance, as direct feedback. This signal is passed through a 5Hz bandwidth low-pass filter before being used as the feedback signal. The speed loop bandwidth is the same as the previous sensorless scheme. Fig. 14 shows encoder-measured speed during the transient for four different loads. Some noise and ripple is noticeable in the no load result, but otherwise performance is akin to sensed operation. The realistic operating range for this mode is  $>300$ rpm. Below this speed noise harmonics will affect the tracking ability of the ATF and the RSH decreases in amplitude, due to the action of the current controller.

In Fig. 15 the direct feedback drive is running at 900rpm; a large load is applied and removed. Note that the steady state speed holding is excellent. The response to the load impact is encoder like. When the load is removed however, the ATF speed holds a small error for a short period of time. This can be seen in the plot of  $I_q$ . This is the more difficult tracking situation for the ATF. Here the slot harmonic has reduced from being very strong and is now both much smaller and closer to the no load inverter associated harmonic. Note that

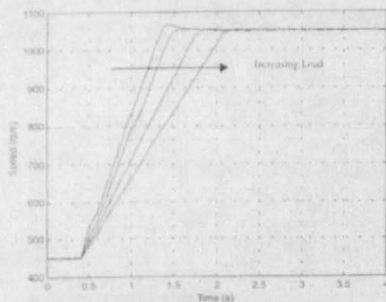


Fig. 14 Speed transients with direct ATF feedback under various loads (zero to full load)

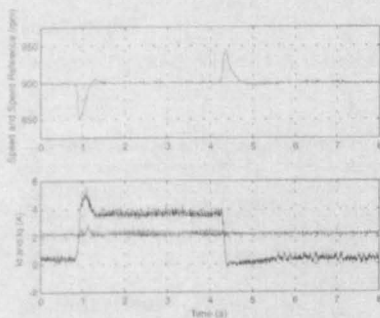


Fig. 15 Load rejection performance of the direct ATF feedback drive at 900rpm

the drive returns to a good steady state speed, but the dynamics are slower.

This particular mode of operation is suited to field weakening operation. Here the slip is larger at no load, therefore the slot harmonic is further from the associated inverter harmonic. Also, the rotor currents are greater for a given load, thus increasing the RSH amplitude.

#### V. CONCLUSIONS AND FURTHER WORK

This paper demonstrates the significant performance enhancements that can be made to model-based sensorless techniques using a high performance RSH tracking algorithm – in this case the RML-ATF. The drive combines excellent steady state accuracy with the high dynamic performance available from the model-based vector scheme. The performance has been tested and demonstrated over a range of speed and load conditions and results have been presented using scaling suitable for critical analysis.

The results indicate that the control structure as it stands is suitable for synchronised drive applications that do not

operate at speeds below 3 Hz for significant periods. This operating range demands an accurate knowledge of  $R_s$ .  $R_s$  estimators can be incorporated into the drive to improve low speed performance [14].

Direct speed feedback from the RML-ATF signal can be used for speeds above 10 Hz, and can certainly help with field weakening operation. The RML-ATF signal is more accurate than the model based speed estimate, and is therefore more suitable for providing the speed reference for a second drive. A second motor rig is currently under construction to test the suitability of the algorithm for multi-motor drive applications. This is the ultimate goal for the project.

#### ACKNOWLEDGEMENTS

The authors would like to acknowledge the financial support of EPSRC and FKI Industrial Drives

#### REFERENCES

- [1] Schauder C., "Adaptive speed identification for vector control of induction motors without rotational transducers", *IEEE Transactions on Industry Applications*, 1992, Vol. 28, No. 5, pp. 1051-1061
- [2] Ohtani T., Takada N. and Tanaka K., "Vector control of induction motor without shaft encoder", *IEEE Transactions on Industry Applications*, 1992, Vol. 28, No. 1, pp. 157-164
- [3] Kubota H., Matsuse K. and Nakano T., "New adaptive flux observer of induction motor for wide speed range motor drives", *IEEE IECON Conference*, 1990, pp. 921-926
- [4] Blasco-Gimenez R., Asher G.M. and Sumner M., "Rotor time constant identification in sensorless vector control drives using rotor slot harmonics", *EPE Conference*, 1995, Vol. 1, pp. 1.083-1.088
- [5] Hurst K.D., Habetler T.G., Griva G. and Profumo F., "Speed sensorless field-oriented control of induction machines using current harmonic spectral estimation", *IEEE IAS Annual Meeting*, 1994, pp. 601-607
- [6] Jiang J. and Holtz J., "High dynamic speed sensorless AC drive with on-line parameter tuning and steady state accuracy", *IEEE Transactions on Industrial Electronics*, 1997, Vol. 44, No. 2, pp. 240-246
- [7] Ferrah A., Bradley K.J., Hogben-Laing P.J., Woolson M.S., Asher G.M., Cilia J. and Shuli J., "A speed identifier for induction motor drives using real-time adaptive digital filtering", *IEEE Transactions on Industry Applications*, 1998, Vol. 34, No. 1, pp. 156-162
- [8] Ferrah A. et al., "The effect of rotor design on sensorless speed estimation using rotor slot harmonics identified by adaptive digital filtering using the maximum likelihood approach", *IEEE IAS Annual Meeting*, 1997, pp. 128-135
- [9] Jansen P.L. and Lorenz R.D., "Transducerless position and velocity estimation in induction and salient AC machines", *IEEE Transactions on Industry Applications*, 1995, Vol. 31, No. 2, pp. 240-247
- [10] Ha J.-I. and Sul S.-K., "Sensorless field orientation control of an induction machine by high frequency signal injection", *IEEE IAS Annual Meeting*, 1997, pp. 426-432
- [11] Teske N., Asher G.M., Sumner M. and Bradley K.J., "Suppression of saturation saliency effects for the sensorless position control of induction motor drives under loaded conditions", *IEEE Transactions on Industry Applications*, 2000, Vol. 47, No. 5, pp. 1142-1150
- [12] Schroedl M., "Sensorless control of AC machines at low speed and standstill based on the 'INFORM' method", *IEEE IAS Annual Meeting*, 1996, pp. 270-277
- [13] Ohyama K., Asher G.M. and Sumner M., "Comparison of the practical performance and operating limits of sensorless induction motor drive using a closed loop flux observer and a full order flux observer", *EPE Conference*, 1999, pp. (on CD-ROM)
- [14] Campbell J.A., Sumner M. and Curtis M., "An improved sensorless vector controlled induction motor drive employing artificial neural networks for stator resistance estimation", *IEEE PEVD Conference*, 2000, pp. 274-279

## A.3 EPE 2001 – Graz

A High Performance Sensorless Induction Motor Drive for use in Multi-Motor Speed Synchronised Applications

G. Turl

### A High Performance Sensorless Induction Motor Drive for use in Multi-Motor Speed Synchronised Applications

G. Turl, M. Sumner and G. M. Asher  
 School of Electrical and Electronic Engineering  
 The University of Nottingham, University Park  
 Nottingham NG7 2RD, UK  
 Tel: +44 (0) 115 9515549  
 Fax: +44 (0) 115 9515616  
 Email: [gt@eee.nottingham.ac.uk](mailto:gt@eee.nottingham.ac.uk)  
 URL: <http://www.eee.nottingham.ac.uk/power/>

#### Acknowledgements

The authors would like to acknowledge the financial support of EPSRC and FKI Industrial Drives.

#### Keywords

Harmonics, Induction Motors, Sensorless Drives, Vector Control

#### Abstract

This paper presents a high performance sensorless induction motor drive that is based on the machine electrical model and tuned by a robust speed estimate. This estimate is obtained from an adaptive algorithm tracking rotor slot harmonics that appear in voltage and current quantities. The resultant system is tested for use in multi-motor, speed synchronised drives, an application typically requiring encoded performance. Excellent system performance is demonstrated on a dual 4kW experimental rig.

#### Introduction

Sensorless control of induction motor drives is a large research area that aims to extract high dynamic performance from an induction machine without the need for a mechanical speed transducer. Removal of this transducer is beneficial for both economic and practical reasons. A majority of established techniques, and those that have impacted on industry, make use of voltage/current measurement and knowledge of electrical machine parameters. Speed and flux estimates (parameters required for high bandwidth 'vector' control) are obtained through application of the machine dynamic equations. The performance of these techniques will vary, as parameters vary, with operating condition. Although parameter variation is a consideration in encoded systems with regard to field orientation (affecting torque loop bandwidth), speed holding capability is not compromised; for this reason sensorless techniques have not impacted into areas where precise speed holding is a necessity.

Application areas that require high accuracy speed holding are any based on multi-axis control. Many mechanisms in manufacturing require that various component parts are synchronised and this is generally achieved by connection of the various elements, through mechanical linkages and gearing, to a common source of mechanical power. More recently mechanisms have been produced where constituent components are driven independently. Here the synchronisation is achieved electronically and control is designed to emulate the prior system specifications. The advantage of this electronically coupled control is an increase in flexibility; gearing ratios can be adjusted in software and machinery can be quickly set-up to vary product specification with a minimum of downtime.

This paper describes a practically implemented sensorless scheme that has similar speed holding accuracy to an encoded drive. A model-based sensorless technique, based on that due to Kubota



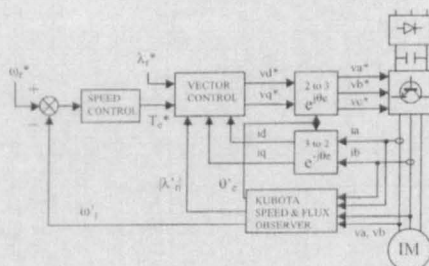


Fig. 1: Structure of the sensorless vector scheme

[1], is augmented with an estimation of true speed derived from rotor slot harmonics (RSH). This estimate is extracted from voltage and current quantities using the Recursive Maximum Likelihood algorithm [2]; this technique gives a high bandwidth speed estimate and has been shown to be suitable for a majority of unmodified induction machines [3]. The slot harmonic estimate is compared with the model estimate and the error used to tune the rotor time constant ( $T_r$ ) in the model-based observer. The paper outlines the full sensorless method and goes on to demonstrate two sensorless drives, both using this algorithm, running in speed synchronism using a master-slave approach.

### Model-Based Sensorless Control

Sensorless control techniques based on knowledge of machine electrical parameters are typified by those due to Schauder [4], Ohtani [5] and Kubota [1]. The work presented here is based on the latter method, considered to be one of the better performing algorithms in comparative tests made between the three [6].

Fig. 1 shows the Kubota method as a speed and flux observer in a Direct Rotor Field Oriented (DRFO) sensorless vector structure. Inputs to the observer are measured voltages and currents. The precise nature of the observer algorithm is detailed in several papers by Kubota, the original reference being [1], and has been used in other sensorless work; it is therefore not presented in detail here. A conventional observer structure observes rotor flux and stator currents. The rotor speed is not observed directly: an estimate of stator current error, together with estimated flux, is used to adjust for speed in the observer model via a PI controller.

More recently sensorless position control has been demonstrated [7-10], but these techniques may require specially modified motors and/or signal injection and this may impose practical limitations and increase power losses. It is believed that the range of these techniques is limited to the low speed region because of the voltage capacity required for signal injection at high speed.

### Tuning Using Rotor Slot Harmonics

The use of an RSH speed measurement to tune a model-based system should be applicable for a majority of algorithms of the type previously described.

#### Rotor Slot Harmonics

The first order RSH frequencies are defined by the following equation

$$f_{sh} = \frac{z}{p} (f_r - f_{slip}) \pm f_e \quad (1)$$

where  $p$  is the number of pole pairs,  $z$  is the number of rotor slots,  $f_r$  is the excitation frequency and  $f_{slip}$  is the slip frequency. In many machines only one harmonic will be present. In practice RSH due

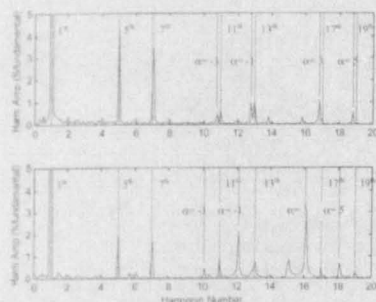


Fig.2: Stator line current spectra at low and full rated load, showing inverter and rotor slot harmonics for  $\alpha=-3$ , etc ( $n_s=750$ rpm)

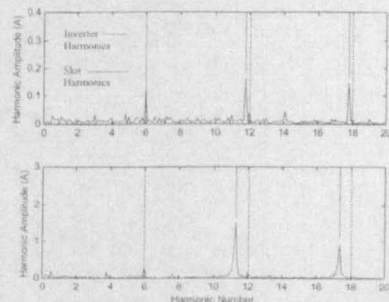


Fig.3: Stator current magnitude spectra at low and half rated load, showing inverter and rotor slot harmonics for  $\alpha=-3$ , etc ( $n_s=750$ rpm)

to higher order MMF harmonics will exist and may be of use in a robust tracking algorithm. Equation (1) is modified to

$$f_{sh} = \frac{z}{p} (f_e - f_{slip}) \pm \alpha f_e \quad (2)$$

where  $\alpha$  is a positive integer.

In an inverter drive slot harmonics exist with PWM switching harmonics. Note, from equation 1, that when  $f_{slip}$  is small a single RSH will be close to an inverter harmonic. This can be seen in fig. 2, which displays FFTs of a stator line current. The upper trace is taken at low load and the lower trace at full rated load. As load increases the slot harmonic moves away from the associated inverter harmonic and increases in amplitude. The machine used in this research has 14 slots per pole pair. The clearly visible RSH are those corresponding to  $\alpha=-1$  and  $\alpha=+3$ . Whilst others are evident, they are small in amplitude and not detectable at all speeds and loads. These results, and those in the following figure, were obtained at half rated speed (750rpm).

At lower speeds the RSH will cross inverter harmonics as the load is increased. Whilst the switching harmonic spread tightens with decreasing speed, the RSH will move a fixed distance from no load to full load. In this machine a greater range is obtained before this crossing occurs if the  $\alpha=+3$  harmonic is tracked, due to the absence of a  $15^{th}$  inverter harmonic.

It was found that the range, before RSH contact with inverter harmonics, could be extended still further. When currents are measured and converted to the rotating frame, as necessary for vector control, a value for the stator current magnitude ( $|I|$ ) can be obtained. Fig. 3 shows how the RSH and inverter harmonics appear in this quantity. Note that the inverter harmonics appear as multiples of  $6k$ , where  $k=(0,1,2,...)$ . The RSH are also transformed and, for our test machine, appear larger than those due to the PWM. This is a very useful consideration for the slot harmonic tracking algorithm. Another consideration is that of current control. It was found that the RSH seen in the stator current reduced with speed, particularly within and around the current control bandwidth. When this occurs, an increase is seen in RSH amplitude in measured voltage and therefore in the voltage demand ( $|V|$ ) that exists in software.

The slot harmonic is tracked with an Adaptive Tracking Filter (ATF) using the Recursive Maximum Likelihood (RML) algorithm. The precise nature of the algorithm has been presented before [2]. The configuration utilised here consists of a digital notch filter, the centre frequency of which is

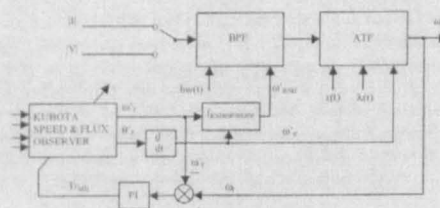


Fig. 4: The RSH speed estimator and tuning scheme with speed, flux, fundamental and slot harmonic frequency estimates obtained from the observer

recursively tuned to minimise the signal around an estimated slot harmonic. When the signal is at a minimum, the centre frequency of the notch is that of the slot harmonic and the rotor speed can be calculated.

Unlike FFTs, the ATF can be implemented as a recursive real time measurement of speed at realistic sample rates. Parameters used in the ATF algorithm define the size of the notch stop band and the amount of past samples used in an averaging process [2]. For tuning of a model-based system, in the steady state, parameters are maintained at constant values and reasonable dynamic tracking is retained. A complex parameter management strategy, where modes of operation must be triggered, is not necessary.

A Band Pass Filter (BPF) is required to pre-filter the line current prior to the ATF. This minimises the influence of the fundamental and other inverter harmonics. Here it is necessary to have some estimate of speed and fundamental frequency. These estimates are obtained from the model-based system, where speed is available directly and the fundamental frequency is available via differentiation of the flux angle.

#### Tuning the Model-Based System

A block diagram of the ATF and tuning system is shown in Fig 4. The tracking BPF pre-filter is centred with speed and fundamental frequency estimates obtained from the Kubota observer. The bandwidth of this filter is proportional to the centre frequency. It therefore decreases with speed and hence as the inverter harmonic frequencies tighten.

The output from the BPF is passed to the ATF function and an estimate of speed is produced, given knowledge of the fundamental from the observer. The notch filter bandwidth and averaging control parameters,  $\tau(t)$  and  $\lambda(t)$ , are held constant in this set-up.

ATF and observer speeds are compared and the error used to drive a  $T_r$  adjustment value via a PI controller. This control was set-up experimentally to have a bandwidth of approximately 1Hz. Note that two inputs to the algorithm are shown.  $|I|$  is used as input for speeds where the RSH is outside of the current control bandwidth and  $|V|$  is used inside. Hysteresis is included in the changeover mechanism.

#### Multi-Axis Control

Many manufacturing processes require the synchronisation of several axes relative to a master command. This is certainly the case in the manufacture of sheet material, such as paper and steel, and various cutting and grinding applications. Such coupling was generally achieved through the use of gears, linkages and belts with the process power derived from a common source.



Newer developments in manufacturing technology have seen mechanical transmissions replaced with electrical actuators that drive individual axes [11]. These systems are coupled electronically and controlled in such a way to emulate the systems they replace. The advantages associated with this solution are increases in flexibility and reliability and a reduction in overall size of the machinery: product specifications can now be adjusted quickly and simply, possibly without a process being halted; smaller size is due to the reduction in the amount of moving parts in a machine, hence there is less associated maintenance; and the tolerances and accuracy of manufacture are now no longer related to the tolerances, accuracy and wear of the mechanical linkages.

Various control techniques have been proposed for synchronised motion, a common two being synchronous command generation and the master-slave method. The work presented here concentrates on the latter. In this case a high inertia drive is speed controlled and the speed of this drive is fed as a reference to a second, low inertia machine. With this technique load impacts and reference changes seen on the high inertia drive will be responded to by the low inertia rig. This is not the case for impacts to the low inertia drive.

Much research interest has been aimed at improving the control techniques used in these multi-motor drives. The disadvantage of the aforementioned techniques being that they do not display the inter-shaft stiffness that it is possible to obtain from mechanically coupled drives through all operating conditions: with mechanical systems the inter-shaft coupling is dependent on the torque obtainable through the mechanical transmission. With multi-motor examples there is also the consideration of drive rating. In the master-slave approach for example there will be problems if the slave drive is operating in saturation for any period. In this case it can not possibly track the master. More advanced control methods are outlined in [11-13]. This paper concentrates on the simple master-slave algorithm to demonstrate the performance of the described sensorless method.

### Experimental Results

The first motor rig used for experimental testing consists of a delta connected, 4-pole, 4kW, closed-slot, squirrel cage induction motor, fed by a 7.5kW IGBT inverter. The motor is fitted with a 10,000 line encoder for speed comparison. The second rig utilises a similarly rated machine and power converter (both from different manufacturers) and is fitted with a 2,500 line encoder.

Information such as number of rotor slots is known for both rigs and electrical parameters have been obtained from no load and locked rotor tests. DC machines that act as load are coupled to each induction machine. The inertia of the DC drive used on rig 1 is several times larger than that used on rig 2.

The complete control structure for both drives is implemented on a Texas TMS320C44 processing platform housed in a host PC. The system comprises 2 C44 DSP processors, one is in communication with the host PC, power converters and measurement circuitry, whilst the other is used for data processing only.

#### Performance of the ATF Speed Estimator

Fig. 5 is included to demonstrate the accuracy attainable from the ATF speed estimate. It displays the sensorless speed (used as feedback), the encoder measured speed (10,000 line encoder sampled every 0.01 seconds) and speed estimated by the ATF. The drive is running with a demand speed of 300rpm at approximately  $\frac{1}{2}$  rated load. The rotor time constant is purposefully de-tuned and the tuning mechanism is disabled. Note that, although the model-based speed centres the BPF for the ATF algorithm, the ATF returns a speed signal that is almost identical to the encoder speed, in terms of both absolute accuracy and resolution. This shows that the ATF is robust to parameter inaccuracies within the model.



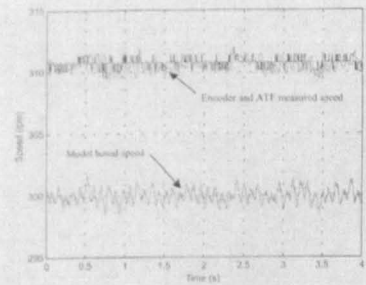


Fig. 5: Encoder, ATF and model-based speed estimates at 300rpm under sensorless control (de-tuned)

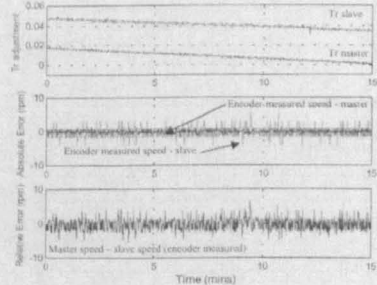


Fig. 6: Absolute and relative speed error and  $T_r$  tuning from dual sensorless drive operating at 200rpm under full load

The Model-Based Scheme with  $T_r$  Tuning

Fig. 6 is a result obtained with the tuned master-slave configuration in the steady state. Both drives are running at their respective full rated loads, with a master command speed of 200rpm, over a 15 minute period. The upper trace shows how  $T_r$  varies as the motor temperature rises. The centre trace displays the error between each drive and the reference speed; this is as measured by the encoders, although they play no part in the control strategy. The difference in resolution between the two traces is due to the different number of lines on each encoder: they are sampled at the same rate. The lower trace shows the relative error between the two drives. Both of these lower traces indicate that the drive displays encoder like accuracy.

If the drive is run under similar conditions with no tuning, the absolute speed error approaches 5 rpm over the same running time. The errors are dependent upon the relative loading and thus the relative heating effect in each machine.

Variation of the Reference Demand

The results below show the sensorless master-slave configuration responding to changes in master reference. In fig. 7 the reference is varied in 100rpm steps from 100 to 900rpm. The upper trace

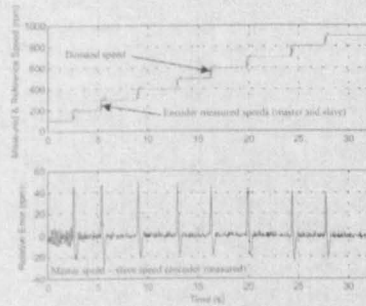


Fig. 7: Sensorless self-tuning drive responding to 100rpm step changes in master reference. Lower trace shows relative speed error

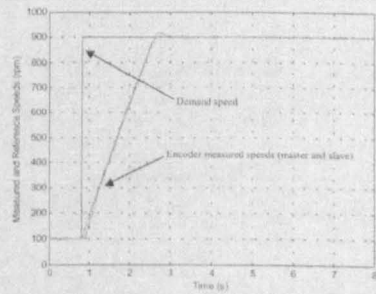


Fig.8: Sensorless self-tuning drive responding to a large (800rpm) step change in master reference. Speed is measured by the encoder

# A High Performance Sensorless Induction Motor Drive for use in Multi-Motor Speed Synchronised Applications

G. Turl

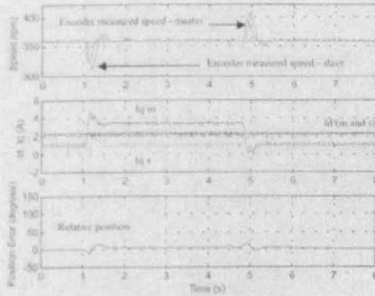


Fig. 9: Response of the tuned sensorless drive to a large load impact seen on the master drive at 360rpm

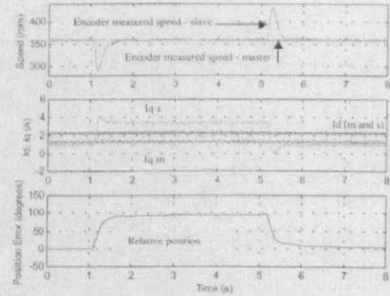


Fig. 10: Response of the tuned sensorless drive to a large load impact seen on the slave drive at 360rpm

shows the demand speed together with the encoder-measured speed from both drives. In the lower trace the relative error is shown. Note that, when in the steady state, both drives are operating within the encoder resolution accuracy. For this result both drives were operating with a small load (approximately  $\frac{1}{4}$  rated).

In fig. 8 we see the master-slave scheme accelerating over a longer period of time. In this case the master is operating at around  $\frac{1}{4}$  rated load, whilst the slave operates at about  $\frac{1}{4}$  rated. Note that there is a small relative error at both the beginning and end of the transient, but generally the slave tracks the master very well. Due to the difference in load inertia, if the two drives were reacting independently to the same demand, the acceleration rates would be markedly different.

## Load Rejection Performance

As previously discussed, the nature of the master-slave control technique is suitable for circumstances where the master drive only will be subject to disturbance loads. Figures 9 to 13 show the performance of the tuned sensorless drive under various load impact conditions.

In fig. 9 can be seen the effect of a large load disturbance applied to the master drive. The slave drive is operating with a load of around  $\frac{1}{4}$  rated. The slave responds to the disturbance with dynamics defined by the speed controller and doesn't saturate. In the lower trace it is clear that some error is transferred to the relative position of the 2 drives, but this is minimal and in the order of a few degrees.

The fig. 9 result can be contrasted with those shown in figs. 10 and 11. Fig. 10 illustrates the response of the drive system with a load impact applied to the slave drive. The change in load, and resultant response of the speed control, generates a large positional error. This would be the case with a fully sensed system operating this control method and for systems that attempt synchronisation using only locked and limited reference commands. Fig. 11 shows the speed and current responses of the sensed system and these are comparable with the sensorless result.

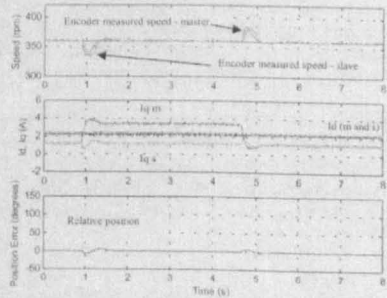


Fig. 11: Response of the sensed drive to a large load impact seen on the master drive at 360rpm

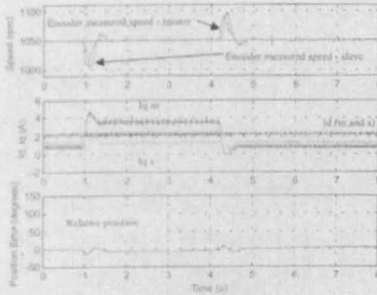


Fig. 12: Response of the tuned sensorless drive to a large load impact seen on the master drive at 1050rpm

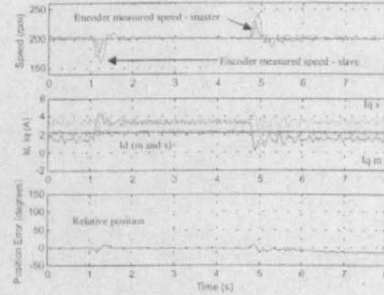


Fig. 13: Response of the tuned sensorless drive to a large load impact seen on the master drive at 200rpm

Figures 12 and 13 are included to demonstrate the level of performance achieved at other operating speeds. In fig. 13, at 200rpm, the response is a little noisy at lower operating loads on the master drive; this is clear as the load is removed. As the speed reduces below around 100rpm the tuning for both drives is disabled. In this region the model-based control method suffers degradation in performance, due to problems with measurement and inverter deadtime, and tuning becomes difficult because the ATF algorithm responds to inverter harmonics that are now in very close proximity to the RSH.

### Conclusions and Further Work

This paper has demonstrated the significant performance enhancements that can be made to model-based sensorless techniques using a high performance RSH tracking algorithm – in this case the RML-ATF. The drive combines excellent steady state accuracy with the high dynamic performance available from the model-based vector scheme. The tuning accounts for errors in model parameters that will compromise accurate speed holding performance as operating conditions vary. This includes variation in resistance values with operating temperature and variation in inductance parameters, due to saturation, with load.

The results indicate that the control structure as it stands is suitable for synchronised drive applications that do not operate at speeds below 100rpm. Operation below this speed demands an accurate knowledge of  $R_s$  for good observer operation and may require some form of signal injection for robust speed tracking.  $R_s$  estimators can be incorporated into the drive to improve low speed performance [14]. Signal injection methods are aimed at the low speed region [7-10].

This work has concentrated on the development of a sensorless drive with encoder like speed holding capability and the proposed scheme has achieved this for speeds above 100rpm. The master-slave multi-motor control scheme has demonstrated excellent speed locking performance from a fully speed sensorless induction motor drive. Further work will be aimed at extending the range of operation to lower speeds and incorporating the more advanced control techniques for multi-motor operation.

### References

- [1] Kubota H., Matsuse K. and Nakano T., "New adaptive flux observer of induction motor for wide speed range motor drives", *IEEE IECON Conference*, 1990, pp.921-926



## A High Performance Sensorless Induction Motor Drive for use in Multi-Motor Speed Synchronised Applications

G. Turi

- [2]. Ferrah A., Bradley K.J., Hogben-Laing P.J., Woolfson M.S., Asher G.M., Cilia J. and Shuli J., "A speed identifier for induction motor drives using real-time adaptive digital filtering", *IEEE Transactions on Industry Applications*, 1998, Vol.34, No.1, pp.156-162
- [3]. Ferrah A. et al "The effect of rotor design on sensorless speed estimation using rotor slot harmonics identified by adaptive digital filtering using the maximum likelihood approach", *IEEE IAS Annual Meeting*, 1997, pp.128-135
- [4]. Schauder C., "Adaptive speed identification for vector control of induction motors without rotational transducers", *IEEE Transactions on Industry Applications*, 1992, Vol.28, No.5, pp.1051-1061
- [5]. Ohtani T., Takada N. and Tanaka K., "Vector control of induction motor without shaft encoder", *IEEE Transactions on Industry Applications*, 1992, Vol.28, No.1, pp.157-164
- [6]. Ohyama K., Asher G.M. and Sumner M., "Comparison of the practical performance and operating limits of sensorless induction motor drive using a closed loop flux observer and a full order flux observer", *EPE Conference*, 1999, pp.(on CD-ROM)
- [7]. Jansen P.L. and Lorenz R.D., "Transducerless position and velocity estimation in induction and salient AC machines", *IEEE Transactions on Industry Applications*, 1995, Vol.31, No.2, pp.240-247
- [8]. Ha J-I. and Sul S-K., "Sensorless field orientation control of an induction machine by high frequency signal injection", *IEEE IAS Annual Meeting*, 1997, pp.426-432
- [9]. Teske N., Asher G.M., Sumner M. and Bradley K.J., "Suppression of saturation saliency effects for the sensorless position control of induction motor drives under loaded conditions", *IEEE Transactions on Industry Applications*, 2000, Vol.47, No.5, pp.1142-1150
- [10]. Schroedl M., "Sensorless control of AC machines at low speed and standstill based on the "INFORM" method", *IEEE IAS Annual Meeting*, 1996, pp.270-277
- [11]. Valenzuela M.A. and Lorenz R.D., "Electronic Line-Shafting Control for Paper Machine Drives", *IEEE Transactions on Industry Applications*, 2001, Vol.37, No.1, pp.158-164
- [12]. Lorenz R.D. and Schmidt P.B., "Synchronized motion control for process automation", *IEEE IAS Annual Meeting*, 1989, pp.1693-1698
- [13]. Danbury R. and Jenkinson M., "Synchronised servomechanisms – the scalar-field approach", *IEE Proceedings on Control Theory Applications*, 1994, Vol.141, No.4, pp.261-273
- [14]. Campbell J.A., Sumner M. and Curtis M., "An improved sensorless vector controlled induction motor drive employing artificial neural networks for stator resistance estimation", *IEE PEVD Conference*, 2000, pp.274-279

## A.4 IEEE IAS Annual Meeting 2001 – Chicago

## A Multi-Induction-Motor Drive Strategy Operating in the Sensorless Mode

G Turi, M Sumner and G M Asher  
 School of Electrical and Electronic Engineering  
 University of Nottingham  
 University Park  
 Nottingham, NG7 2RD, UK

**Abstract**—This paper describes the development of a sensorless induction motor drive scheme that can be used for high-performance process control applications where multi-motor speed synchronisation is required. The scheme employs a Model Reference Adaptive System (MRAS) to provide a direct field orientated drive with speed estimation. Tuning of the MRAS is achieved using a measurement of speed derived from the rotor slot harmonic content of the stator current. The performance of the system matches that achieved using an encoder and excellent speed synchronisation of two drives is demonstrated experimentally.

## 1. INTRODUCTION

Induction motor drives are now being seriously considered for demanding industrial applications. High torque bandwidth and accurate steady state speed holding are readily available from encoded vector control drives and parameter sensitivity can be minimised using on-line parameter estimation. Therefore, the cage induction motor can now be found in applications where previously only the DC machine was considered, such as mill drives, machine tools, dynamometers and rolling roads.

Sensorless induction motor drives are now commonly available from major inverter manufacturers. Typical industrial sensorless controllers employ a model-based speed (and usually rotor flux) estimator in conjunction with a Direct Rotor Field Orientated (DRFO) vector control scheme. This provides a drive system with a significant improvement in torque response and speed holding when compared to the traditional and modified open loop V/F schemes [1]. However, the stability and accuracy of such control schemes are directly related to the accuracy to which the electrical parameters of the machine are known. These schemes are particularly sensitive at low speeds, where the problem associated with estimating a small back EMF, within a voltage signal measured from a PWM inverter, is particularly troublesome. It would be difficult to summarise the different approaches used by researchers to identify the machine parameters, evaluate their influence on drive performance and indeed modify model-based sensorless schemes to be more robust to electrical parameter variations. As yet there does not appear to be a definitive model-based sensorless control scheme which is both robust to machine parameter variations and able to work in the very low speed/low torque region. For this reason, they are still not considered suitable for high performance drive applications.

Several researchers have investigated the use of machine saliency for extracting motor position information. In effect, this approach considers the rotor as a position encoder: saliencies can be introduced into the rotor in the form of distributed slot leakage [2] or distributed rotor resistance [3] and this saliency is then picked up using a high frequency excitation and subsequent signal processing of the measured stator currents. Excellent position control and low speed performance has been demonstrated [4], but the obvious drawback is the requirement for a specially modified motor, although it should be noted that Holtz has demonstrated the feasibility of a similar technique using a standard cage machine [5]. The more significant drawbacks when considering process control are the introduction of extra losses due to the excitation signal and a significant increase in vibration and audible noise. These may not be acceptable, for example on paper or steel mill applications.

As an alternative approach, the rotor saliency due to rotor slotting can be employed for speed sensing, without the need for signal injection. Rotor slot harmonics (RSH) 'naturally' exist within the stator current and can be tracked through most of the torque and speed range. Unfortunately, as with model-based techniques, the speed information disappears at low speeds and loads as the slot harmonic either reduces in magnitude (with reducing load), or becomes swamped in inverter/machine related harmonics. It does however offer a true speed measurement over a significant part of the operating range and can therefore be employed within a sensorless speed control system.

This paper proposes the application of sensorless induction motor drives to high performance industrial applications where multi-drive synchronisation is required. Applications to be considered are the simple electronic gearbox or differential, for electric vehicle systems, and the co-ordination of several sectional drives within a processing mill. Sensorless drives would be of considerable benefit in, for example, a paper mill, where wet or humid conditions can seriously degrade the operation of an electronic encoder. Section II describes the model-based estimator and slot harmonic methods used to create the high performance sensorless control structure. Section III provides an overview of the experimental facility. Section IV outlines the multi-motor control structures investigated for the applications listed. Sections V and VI present the experimental results and the conclusions from this work.

## II. HIGH PERFORMANCE SENSORLESS VECTOR CONTROL

The design rules used to develop the encoderless drives in this work were (a) that the speed measurement technique should not disturb normal drive operation and (b) that it should be as accurate as possible over the largest possible torque and speed range. To this end the system used comprised three elements:

- 1) Model Reference Adaptive System (MRAS)
- 2) Rotor Slot Harmonic Measurement using a Recursive Maximum Likelihood - Adaptive Tracking Filter (RML-ATF)
- 3) Intelligent Parameter Prediction (IPP)

Before describing the full system, the constituent parts will be briefly reviewed.

#### A. Model Reference Adaptive System (MRAS)

The particular model-based scheme chosen was developed by Kubota [6]. A conventional observer structure is used to estimate the rotor flux and the stator currents. The error between the stator current estimate and its measured value is then used indirectly to adjust the speed parameter in the observer using a PI controller, as shown in Fig. 1. The flux estimate is used for DRFO. The Kubota algorithm is used here as it was considered to be the best algorithm in comparative tests made between three of the more popular methods [1]. It is fairly easy to commission, requiring only the electrical parameters of the motor. However, although the scheme works well at all speeds and loads when the parameters are correctly tuned, its performance seriously deteriorates when the motor temperature varies (with loading for example).

### B. RML-ATF

The slot harmonic estimator has been well described in

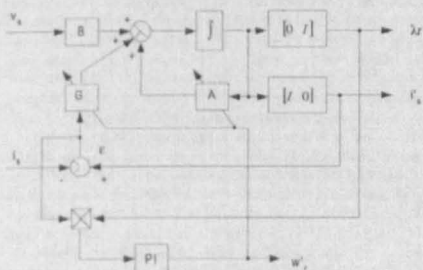


Fig. 1. Overview of the Kubota speed/flux observer

[7]. The rotor slot harmonic will exist in the motor current at a frequency ( $f_{sk}$ ) defined by equation (1) for the motors employed in this project.

$$f_{sh} = \frac{z}{p} (f_e - f_{slip}) \pm \alpha f_e \quad (1)$$

In (1),  $p$  is the number of motor pole pairs,  $z$  is the number of rotor slots,  $f_e$  is the excitation frequency and  $f_{slip}$  is the slip frequency. Higher order MMF harmonics will exist due to the PWM modulation of voltage and machine effects; this is accounted for by the inclusion of  $\alpha$ , which is a positive integer.

In essence, the RML-ATF acts as an adaptive bandstop filter. The centre frequency of the filter is adjusted until the output is minimised: at which point the centre frequency is equal to the strongest component in the input signal. The stator current measurement therefore has to be pre-filtered to remove the fundamental and other inverter harmonics. A second order bandpass filter is used, with centre frequency and bandwidth set using the outputs of the MRAS. Even if the MRAS is seriously detuned, the centre frequency estimate will be close enough to ensure that the RML-ATF locks onto the real slot harmonic, providing an accurate speed measurement as illustrated in Fig. 2.

The configuration utilised in this work, tracks the RSH effects seen in both the current and voltage magnitude. These quantities are easily obtained in a vector control system. An advantage of using these variables is that the inverter harmonics appear at multiples of six times the fundamental frequency, as opposed to odd multiples of  $f_e$  and hence the frequency space is less crowded. For both test machines the relative amplitude of the RSH was also amplified with respect to the inverter harmonics, when compared to the harmonics present in a single line quantity only. A change

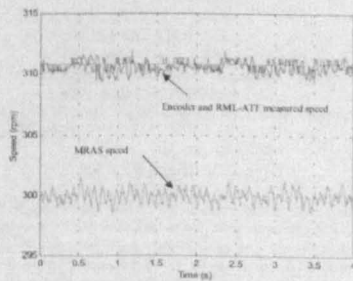


Fig. 2. Encoder, ATF and model-based speed estimates at 300rpm under sensorless control. The MRAS is purposefully detuned



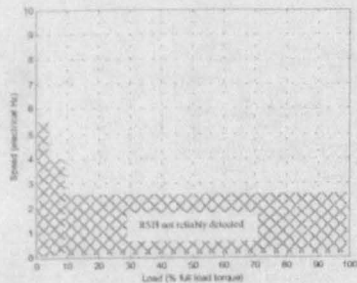


Fig. 3. Operating region of the RML-ATF

over mechanism is employed, incorporating hysteresis, to change between current and voltage quantities at given speeds. When speed is at a low value (<12-14 Hz), the RSH is within the frequency range of the current controller; the controller acts to reduce these harmonics and in doing so creates rotor slot harmonics in the voltage waveform. Therefore voltage can be used to identify the RSH frequency. Indeed the voltage demand rather than the measured value can be employed. Above a set speed the tracking is switched back to measured current.

Two problems exist with the implementation of the RML-ATF. Firstly, the dynamic response of the filter is dependent on the RSH frequency and effectively the speed. At low speeds the delay associated with the ATF prohibits its use for direct speed feedback. It can however be used to tune the MRAS system. The tuning scheme is shown in Fig. 4, where estimates of speed and excitation frequency from the Kubota observer centre the bandpass filter. The filter output is passed to the RML-ATF algorithm that provides a measure of slot harmonic frequency; this is converted to a speed measure using the knowledge of excitation frequency from the observer. Comparing ATF estimated speed with that from the observer produces an error suitable to trim the rotor time constant value used in the model via a PI controller. This was set-up experimentally to have a bandwidth of approximately 1Hz. As the speed increases above 900 rpm, direct feedback and Indirect Field Orientation (IRFO) can be used, given that the MRAS system is reasonably tuned.

The second problem arises at very low speeds, due to the size of the slot harmonic, particularly at low loads, being small compared to the fundamental and inverter harmonics. At low speeds, the harmonics are relatively bunched together, and the inverter harmonics increase due to the effects of inverter switch deadtime. The RML-ATF struggles to distinguish the RSH from other harmonics and the speed accuracy deteriorates rapidly. The slot harmonic cannot be used below approximately 75 rpm.

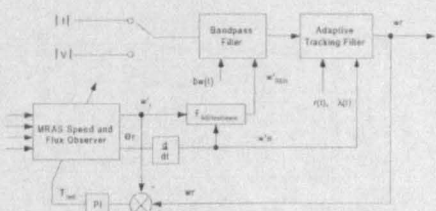


Fig. 4. The model-tuning strategy

C. IPP

As mentioned earlier, the performance of the MRAS will deteriorate as the resistive parameters used by the model become detuned. The particular problem for the scheme used here, is that at very low speeds the RML-ATF cannot be relied upon to give an accurate speed measurement and therefore cannot be used to tune the MRAS. The control system described by this work would ideally be limited to prolonged operation only above 900 rpm and 10% to 15% full load torque (see Fig. 3). The MRAS can work correctly within the 'limited operation' regions as long as it is for short-term duration only, i.e. during acceleration or deceleration, and the system developed for this project has this restriction. Should more prolonged operation be required, an update of the resistive parameters will be necessary as the machine heats up and this can be achieved using intelligent prediction, e.g. an Artificial Neural Network as proposed by Campbell [8]. Note that this predictor does not need to be particularly accurate, as the whole speed estimator/vector control system will be properly tuned when it re-enters the normal operating region.

The overall speed measurement/control strategy has four modes of operation:

- 1) MRAS with IPP
- 2) MRAS with RML-ATF tuning
  - i) RSH derived from voltage demand (<12-14Hz)
  - ii) RSH derived from measured stator current magnitude (>12-14Hz)
- 4) RML-ATF used directly for speed feedback and IRFO

III. EXPERIMENTAL FACILITY

The test rigs have been constructed specifically to evaluate the synchronisation of two sensorless induction motor drives. For these tests both motors are rated at 4 kW. A full motor parameter list is given in the Appendix. The induction motors are mounted on separate bedplates, each with its own independent loading system. In both cases the

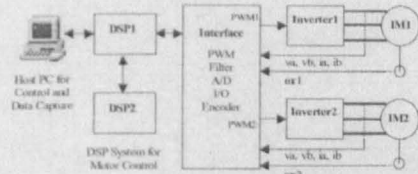


Fig. 5. Overall layout of the experimental structure. Load machines not shown

load comprises a DC machine fed from a four quadrant fully controlled rectifier. Differing load machine specification results in one rig having an overall inertia that is several times larger than the other. Each bedplate includes a high-resolution incremental encoder for speed evaluation only.

The induction motors are supplied from IGBT inverters. The sensorless control algorithms are performed on two TMS320C44 Digital Signal Processors (DSP) mounted on a motherboard within a PC. Measurements of motor currents and voltages are passed to the control processors via 16 bit A/D converters with associated signal conditioning circuitry. A simple digital interface allows the DSPs to measure the encoder signals from each drive. PWM signals for the two inverters are generated on external timer circuits using values downloaded from the DSPs. A sample frequency of 8KHz is used for the vector control of each drive, with a PWM switching frequency of 4 kHz.

For the sensorless vector scheme, current controller bandwidth is designed to be 100Hz. Speed control bandwidth is 1.6Hz, with the MRAS observer bandwidth set-up experimentally to be suitably faster than this. Rotor time constant tuning was also set-up experimentally, to tune out large (yet realistic) errors in around 1 second. The RML-ATF algorithm runs at a sample frequency of 4kHz when  $||$  is used as the input (the RSH frequency is higher than 100Hz) and at 2kHz when  $V$  is used. Algorithm parameters, as defined in [7], are set for steady state conditions and are not changed during operation.

In the steady state, and in the RML-ATF operating region previously defined, the tuning mechanism will maintain correct speed holding, comparable to a 10,000-line encoder sampled every 10ms. After a sudden variation in load torque a MRAS speed error will exist due to parameter error. The tuning mechanism will tune out the error although the tuning time constant will vary very slightly according to the new load state: the RML-ATF dynamics are mildly affected by the amplitude variation in slot harmonic signal. An increase in load torque will hence be responded to slightly more quickly than a reduction.

A block diagram of the experimental rig is shown in Fig. 5. The performance of the sensorless tuning drives is

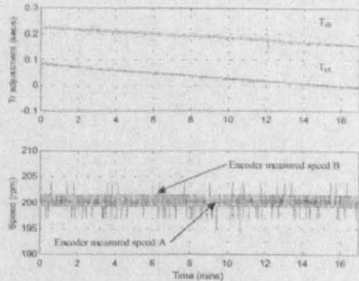


Fig. 6. Steady state performance of the sensorless tuning drive

illustrated in Fig. 6 and Fig. 7. In Fig. 6 both sensorless drives are running at 200 rpm under full rated load. The upper trace displays how each value of  $T_r$  is adjusted over this time. The lower trace shows that both drives run with encoder like accuracy. Drive A is fitted with a 10,000-line encoder, whilst drive B uses a 2,500-line device, both are sampled every 10mS. The encoders play no part in the control scheme. Under similar conditions without tuning, the speed would vary by a few rpm.

Fig. 7 shows the response of drive A to a large load impact whilst running at 900rpm. Again the speed accuracy in the steady state is encoder like.

IV. MULTI-MOTOR CONTROL STRUCTURE

The previous section described the high performance sensorless system obtained. In order to synchronise the speed of these drives, an overall 'process-control' monitor is required to adjust the individual speeds of each drive to maintain some form of process co-ordination. The experimental system described above has been used to evaluate the application of sensorless drives to multi-motor

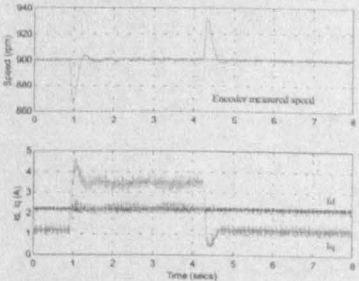


Fig. 7. Load rejection performance of the sensorless tuning scheme



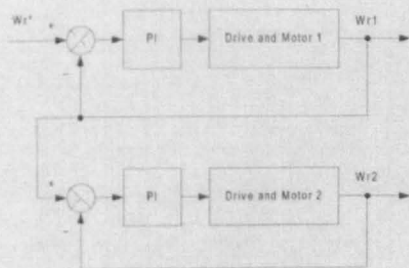


Fig. 8. Structure of the master-slave control scheme

control, using three different process control strategies. These strategies will be described, with illustrative performance obtained from a fully sensed multi-motor system for comparison.

In certain applications it is sufficient to have drives that each respond to a common command and are well matched in terms of closed-loop response. In this case, to maintain satisfactory synchronism, it must be ensured that none of the individual drives see large disturbance torques, or load torques, that will greatly affect the predicted closed-loop response. This, effectively open-loop, coupling scheme has not been considered here.

In all of the proposed schemes the process control works to match drive speeds. In some applications it would be necessary to include a position control term. All the load rejection tests are performed at 500rpm.

A. Master-Slave

In this simple control scheme the user assigns one of the drives to be a master, with subsequent drives being defined as

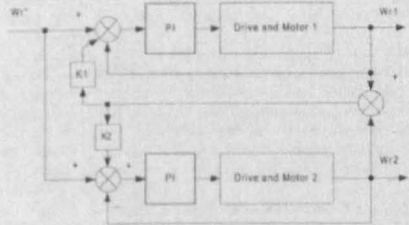


Fig. 10. Structure of the cross-coupled control scheme

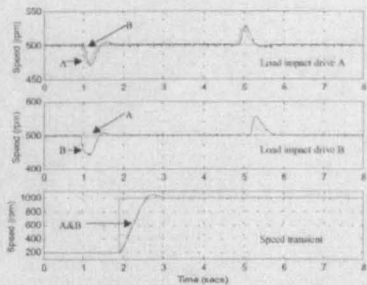


Fig. 9. Response of the encoded master-slave scheme to load impact and demand speed variation (Master – A, green Slave – B, red)

slaves. The actual speed of the master serves as the speed reference for the slaves; any load disturbance or speed reference change applied to the master, will be followed by the slaves, but disturbances seen by any individual slave will not be reflected to the master, nor any other slave drive. This scheme is illustrated in Fig. 8.

Fig. 9 shows encoded results, where the higher inertia drive has been assigned the master. The upper trace shows how both drives respond to a large load disturbance applied to the master. The second trace shows the lack of backward coupling, where a load disturbance applied to the slave is not seen by the master drive. The lower trace shows both drives keeping well synchronised during a step change in reference speed. Given the described limitations, the scheme works well, but one way coupling would also cause a problem where the slave drive performance was affected by its operation close to or in torque limit. Under these conditions it could not be guaranteed to follow the master.

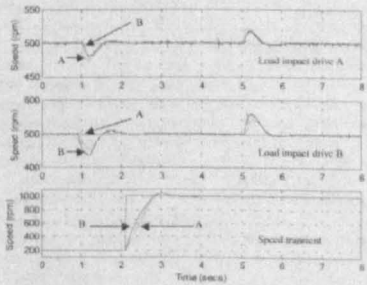


Fig. 11. Response of the encoded cross-coupled scheme to load impacts and demand speed variation

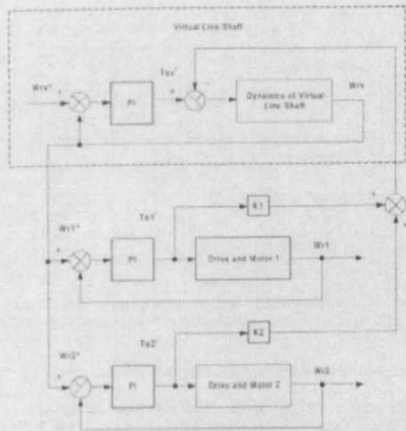


Fig. 12. Structure of the virtual-line-shaft control scheme

B. Cross-Coupling

A significant improvement can be introduced through cross-coupling [9]: i.e. letting each of the drives act on both absolute and relative errors, as illustrated in Fig. 10. The feedback of relative drive error to each of the controllers allows a form of load torque reflection from one drive to the other. Gains  $k_1$  and  $k_2$  can be set to define the importance of relative coupling, but their affect on speed controller design must be considered. This allows both drives to react to load torques imposed on the other, preventing the large relative position error seen when using the master-slave approach.

A similar coupling strategy was proposed by Lorenz in [10]. A master-slave structure is used and the slave speed fed back to the master for coupling. In both of these schemes simple gains can be used, to weight relative and absolute speed control response, or a separate coupling controller could be designed.

Results for the scheme are shown in Fig. 11. Note, from the top two traces, that a response is obtained from each drive to impacts on the individual drives. In the lower trace a response to a step reference speed variation is shown. There is a noticeable difference between the two speeds here. At the beginning of the transient both drives are responding to the large absolute error. This would be improved with reference rate limiting.

The major drawback with this approach is that it would be difficult to extend the scheme for operation with more than two drives.

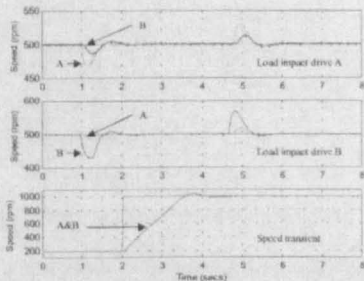


Fig. 13. Response of the encoded virtual-line-shaft scheme to load impacts and demand speed variation

C. Electronic (Virtual) Line-Shaft

The third control scheme evaluated was proposed by Valenzuela and Lorenz and considered for use in paper mill applications [11]. This scheme seeks to emulate the mechanical drive shaft connected to sectional drives in typical mill machinery, providing the slow down/speed up of the whole system in response to a load change on any of the sectional drives. It achieves this by using a real time simulation of a line-shaft, with associated inertia, etc. The drive responds to the actual demand speed, as if it were a mechanical system, with the output speed (and position) fed as a reference to each of the sectional drives. Load torque imposed on any of the sectional drives is fed back electronically to the line-shaft and causes slow down or speed up of the virtual-shaft which is then translated to a slow down or speed up of the reference speed to each of the sectional drives. A good degree of synchronism is maintained. The (simplified) overall control scheme is illustrated in Fig 12 with performance shown in Fig. 13. Here the response of the system is dominated by the inertia of the virtual system (in this case set to  $0.6\text{kgm}^2$ ). This limits the reference seen by each drive and hence the slow response to the step change in speed demand in the lower trace shows excellent speed synchronisation. The upper two traces show less effective cross-coupling during load impacts. The inertia of the virtual shaft again limits this response, but this can be improved by balancing inertias through the  $k$  gains (here set to 1.0).

It should be noted that none of these multi-motor schemes has yet been optimised for best performance. Research here is on going. The results presented here demonstrate encoded control, for comparison with a sensorless system, i.e. merely to demonstrate the viability of using sensorless drives for these applications.

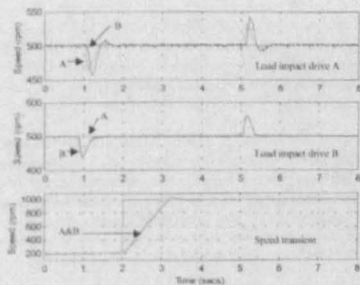


Fig. 14. Response of the sensorless master-slave scheme to load impacts and demand speed variation (Master - A, green Slave - B, red)

V. EXPERIMENTAL RESULTS FOR THE SENSORLESS SYSTEM

Sensorless experimental results are shown in Figs. 14 to 17. These were obtained under similar speed and load conditions to those used in the encoded experiments of the previous section. Fig. 14 shows sensorless master-slave results, Fig.15 sensorless cross-coupled performance and Fig. 16 shows the response of the sensorless virtual-line-shaft system. In the case of the master-slave and virtual-line-shaft results, the performance is practically indistinguishable from the equivalent results of the encoded system. Both drives show similar torque performance and encoder like steady state accuracy.

In the cross-coupled result of Fig. 15, the torque response and steady-state speed holding is similar to the encoded result, but there is a degree of noise and oscillation noticeable on both drives when recovering from torque impacts. Indeed this scheme was found to be very noisy and oscillatory at lower speed (below around 400rpm). It is considered that the

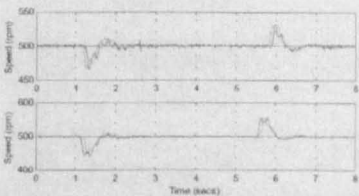


Fig. 15. Response of the sensorless cross-coupled scheme to load impacts

extra cross-coupling terms effectively increase the feedback gain to each drive controller when the drive speeds are not matched. This can cause a short-term change in the closed loop response of each drive. The additional noise on the MRAS signal compared to the encoded signal (see Fig. 2) will also be amplified by the cross coupling gains and will probably cause the problems at lower speed. This will be investigated further.

Fig. 17 again shows the encoder like performance of the developed sensorless scheme. Here the relative positions of the 2 drives are shown during the load impact tests on the master-slave schemes. Notice the large relative position error during impacts on the slave machine. The master-slave coupling minimises this affect when impacts hit the master drive. Note that the encoded and sensorless results are directly comparable. The relative position is derived from encoder measurements, but the encoder is NOT used within the control. When the speeds are synchronised there is no slope in the position error (it remains constant) – the speeds remain locked tight even in sensorless control mode!

VI. CONCLUSIONS

This paper has described a new sensorless induction motor drive that can be used where speed synchronisation is

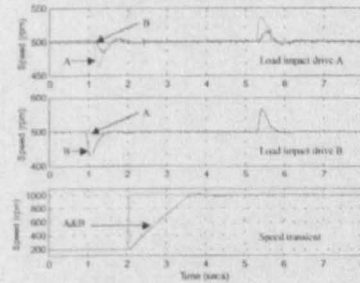


Fig. 16. Response of the sensorless virtual-line-shaft scheme to load impacts and demand speed variation

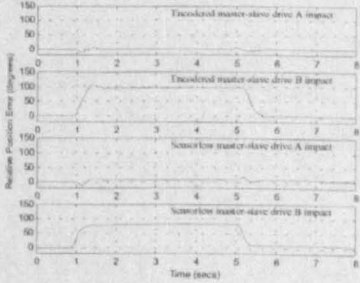


Fig. 17. Relative position, drive A to drive B, during load impacts in the master-slave mode for both encoded and sensorless operation

required. The steady state accuracy and resolution of the scheme matches that of a 10,000-line encoder and the torque response is comparable to that achieved with a sensed vector controlled drive. The drive will operate at very low speeds and loads, although extra parameter adjustment will be necessary if sustained operation under these conditions is required.

Sensorless synchronised drives have been demonstrated experimentally. The relative drive positions remain locked under steady state conditions. Relative position errors during transient operation are similar to those present in the sensed drive and are a result of the synchronisation process, not the sensorless scheme. Further work is now required to improve transient response, and eliminate the low speed oscillations.

#### APPENDIX

Induction machine specifications and RSH tracking parameters are as follows:

##### A. Machine A parameters

$P_{rated} = 4\text{ kW}$ , 4-pole,  $\Delta$ -connected,  $V_{rated} = 415\text{ V}$ ,  $I_{rated} = 8\text{ A}$ ,  
 $\eta_{rated} = 1420\text{ rpm}$ ,  $J = 0.3\text{ kgm}^2$   
 $R_s = 5.32\Omega$ ,  $T_r = 0.168\text{ s}$ ,  $L_s = 0.64\text{ H}$ ,  $L_r = 0.633\text{ H}$ ,  $M = 0.6\text{ H}$

##### B. Machine B parameters

$P_{rated} = 4\text{ kW}$ , 4-pole,  $\Delta$ -connected,  $V_{rated} = 415\text{ V}$ ,  $I_{rated} = 8.42\text{ A}$ ,  
 $\eta_{rated} = 1420\text{ rpm}$ ,  $J = 0.1\text{ kgm}^2$   
 $R_s = 5.6\Omega$ ,  $T_r = 0.11\text{ s}$ ,  $L_s = 0.56\text{ H}$ ,  $L_r = 0.56\text{ H}$ ,  $M = 0.53\text{ H}$

##### C. RML-ATF and BPF parameters

RML parameters:  $r = 0.99$ ,  $\lambda = 0.99$   
 BPF parameter:  $\zeta = 0.027$

#### ACKNOWLEDGMENT

The authors would like to acknowledge the financial support of EPSRC and FKI Industrial Drives

#### REFERENCES

- [1] Ohyama K., Asher G.M. and Sumner M., "Comparison of the practical performance and operating limits of sensorless induction motor drive using a closed loop flux observer and a full order flux observer", *EPE Conference*, 1999, pp.(on CD-ROM)
- [2] Jansen P.L. and Lorenz R.D., "Transducerless position and velocity estimation in induction and salient AC machines", *IEEE Transactions on Industry Applications*, 1995, Vol.31, No.2, pp.240-247
- [3] Cilia J., Asher G.M. and Bradley K.J., "Sensorless position control for induction motor drives using an asymmetric rotor and high frequency injection", *EPE Conference*, 1997, pp.486-491
- [4] Teske N., Asher G.M., Sumner M. and Bradley K.J., "Suppression of saturation saliency effects for the sensorless position control of induction motor drives under loaded conditions", *IEEE Transactions on Industrial Electronics*, 2000, Vol.47, No.5, pp.1142-1150
- [5] Holtz J., "Sensorless position control of induction motors - An emerging technology", *IEEE Transactions on Industrial Electronics*, 1998, Vol.45, No.6, pp.840-852
- [6] Kubota H., Matsuse K. and Nakano T., "New adaptive flux observer of induction motor for wide speed range motor drives", *IEEE IECON Conference*, 1990, pp.921-926
- [7] Ferrah A., Bradley K.J., Hogben-Laing P.J., Woolfson M.S., Asher G.M., Cilia J. and Shull J., "A speed identifier for induction motor drives using real-time adaptive digital filtering", *IEEE Transactions on Industry Applications*, 1998, Vol.34, No.1, pp.156-162
- [8] Campbell J.A., Sumner M. and Curtis M., "An improved sensorless vector controlled induction motor drive employing artificial neural networks for stator resistance estimation", *IEEE PESC Conference*, 2000, pp.274-279
- [9] Koren Y., "Cross-coupled biaxial computer control for manufacturing systems", *ASME Journal of Dynamic Systems, Measurement and Control*, 1980, Vol.102, pp.265-272
- [10] Lorenz R.D. and Schmidt P.B., "Synchronized motion control for process automation", *IEEE IAS Annual Meeting*, 1989, pp.1693-1698
- [11] Valenzuela M.A. and Lorenz R.D., "Electronic line-shafting control for paper machine drives", *IEEE Transactions on Industry Applications*, 2001, Vol.37, No.1, pp.158-164



## A.5 IEE PEMD 2002 – Bath

## A SYNCHRONISED MULTI-MOTOR CONTROL SYSTEM USING SENSORLESS INDUCTION MOTOR DRIVES

G. Turt, M. Sumner and G.M. Asher

The University of Nottingham, UK

## ABSTRACT

This paper outlines a high-performance induction motor sensorless control strategy engineered for high speed holding accuracy. The strategy utilises a model-based method, tuned by a speed estimate derived from rotor slot harmonic effects seen in stator quantities. Two 4kW machines, both running the developed scheme, are speed synchronised using a bi-axial cross-coupled control method. Results are shown to be comparable to those obtained from the same synchronisation scheme, and on the same rig, using encoded indirect rotor flux oriented (IRFO) control.

## INTRODUCTION

Sensorless vector control of induction motor drives continues to be a challenging research area. Work continues to improve the low speed and zero-speed holding of such systems by employing more and more complicated signal injection techniques and in some cases using modified motors [3, 4]. Other research looks to improve the reliability and robustness of model based speed estimators, such as those reviewed in [1], or employ expert systems for parameter modelling and control.

It is now obvious that the selection of a particular sensorless control strategy will depend, to a large extent, on the target application. In many cases V/F control will be suitable, where a simple load needs to be controlled at a fairly approximate speed. Fans, pumps, compressors have been traditional applications for such techniques.

Crude model based systems are now available in commercial drives and provide (slightly) better starting torque and better speed holding, and perhaps allow a more efficient drive operation. Simple conveyors can use such systems. The sensorless position control schemes outlined in [3, 4] are perhaps more suited to the high performance applications of machine tools, or traction, although there is still plenty of engineering required to embed these techniques into commercial drives.

This paper describes a sensorless induction motor control system designed specifically for a limited range of applications, namely those where multi-motor drive synchronisation is required. The system does not guarantee accurate speed control below 5 Hz or at no-load, but it does guarantee encoder like accuracy in its speed control in the range 5 – 50Hz, and at loads above 10 % rated. As such it is eminently suitable for applications such as paper or steel mills, where multi-drive synchronisation is demanded, at speed, in the presence of severe torque transients. These applications in particular present difficult environments for speed encoders to work reliably.

The control method employs a model based sensorless speed control algorithm. This model is continually tuned on-line by a speed measurement derived from the rotor slot harmonic (RSH) signals present in the stator current and voltage. The full system is described in [6] and only briefly outlined here. The operating limits of the drive are determined by the RSH estimator, and for this work have been set to the worst case.

## THE SENSORLESS TUNING DRIVE

### The Model-Based Algorithm

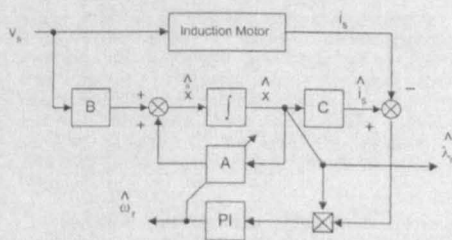


Figure 1: Sensorless Model-Based System

A comparative assessment, undertaken by Ohyama et al, reviewed the practical performance of three of the leading candidates for sensorless DRFO vector control [7]. Due to the conclusions of the paper, the scheme proposed by Kubota et al

was chosen to form the basis of the work presented here. The algorithm is based on a full-order adaptive observer, used to estimate stator current ( $i_s$ ) and rotor flux ( $\lambda_r$ ) in an encoded system. The scheme is presented in [5] and extended to estimate both rotor speed and rotor flux for use in a sensorless DRFO system. A block diagram of the scheme is shown in figure 1.

The scheme is described by the system of equations, defined in the stationary stator frame of reference, shown below.

$$\begin{aligned} x &= [i_s \quad \lambda_r]^T \\ i_s &= [i_{as} \quad i_{\beta s}]^T \quad \lambda_r = [\lambda_{ar} \quad \lambda_{\beta r}]^T \quad v_r = [v_{ar} \quad v_{\beta r}]^T \\ A &= \begin{bmatrix} A_{11} & A_{12} \\ A_{21} & A_{22} \end{bmatrix} \quad B = \begin{bmatrix} B_1 \\ 0 \end{bmatrix} \quad C = \begin{bmatrix} I & 0 \end{bmatrix} \\ A_{11} &= -(R_s/(\sigma L_s)) + (1-\sigma)/\sigma T_r \\ A_{12} &= M/(\sigma L_s L_r) ((1/T_r)I - \omega_r J) \\ A_{21} &= (M/T_r)I \\ A_{22} &= -(1/T_r)I + \omega_r J \\ B_1 &= (1/\sigma L_s)I \\ I &= \begin{bmatrix} 1 & 0 \\ 0 & 1 \end{bmatrix} \quad J = \begin{bmatrix} 0 & -1 \\ 1 & 0 \end{bmatrix} \end{aligned} \quad (i)$$

It can be seen that the adaptation mechanism for speed estimation consists of a PI controller acting on the instantaneous torque error in the model; this is shown in equation (ii).

$$\omega_r = K_p (e_{\text{torque}} - e_{\text{torque}}) + K_i \int (e_{\text{torque}} - e_{\text{torque}}) dt \quad (ii)$$

#### The RSH Speed Estimator

Due to the necessary permeance variation between conducting aluminium bars and laminated iron at or near the surface of an induction motor rotor, speed related harmonics exist in the air-gap MMF wave. These effects are seen in stator terminal quantities.

The process is effectively the amplitude modulation of the applied stator frequency with the slot harmonic passing frequency (speed related). Slot harmonic effects have been well studied in

previous works [8]. The slot harmonic frequencies are defined by equation (iii).

$$f_{sh} = v \frac{z}{p} f_r \pm \kappa f_r \quad (iii)$$

where  $v=1,2,3,\dots$   
 $\kappa=1,2,3,\dots$   
 $z$  is the number of rotor slots  
 $p$  is the number of motor pole pairs

Note that it is frequency only that robustly conveys speed information. The only amplitude consideration is whether or not an RSH effect can be tracked in noise and amongst other harmonics that will exist in stator quantities.

In particular, the slot harmonic components will exist with PWM harmonics. Most notably, at low load (with  $f_r$  and  $f_s$  approximately equal), a slot harmonic will exist in close proximity to an inverter harmonic and may cause tracking problems. The PWM harmonics, as well as machine design related harmonics in the air-gap flux, also give rise to other slot harmonic effects. Hence the  $\kappa$  term in equation (iii). The  $v$  term signifies that RSH components exist due to higher order slotting effects, but these are not exploited.

Having extracted a speed signal, by tracking RSH effects using FFTs, the work of Blasco Gimenez demonstrated the principle of tuning a model based Rotor Flux - Model Reference Adaptive System (RF-MRAS) [9].

In this work the speed signal is obtained by using a recursive adaptive digital signal-processing system that offers higher dynamic tracking performance than the FFT and with less computational cost. The Adaptive Tracking Speed Estimator (ATSE) system is presented in figure 2. An estimation of  $f_s$  and  $f_r$ , each provided by the model based speed estimator, are combined to provide an estimate of RSH frequency. This value sets-up pre-filtering, to negate the effects of noise harmonics around the estimated RSH, prior to the RSH identifier. The identifier is based on the Recursive Maximum Likelihood - Adaptive Tracking Filter (RML-ATF) [10].

The RML-ATF identifies the strongest harmonic signal in the input quantity, hence the need for pre-filtering. The algorithm consists of the digital realisation of an adjustable centre frequency notch filter. The centre frequency is adjusted to minimise the output and hence the strongest frequency component is identified. This technique was first suggested for induction motor speed identification by Ferrah et al [10], and is explained in more depth in previous publications by the authors [6].

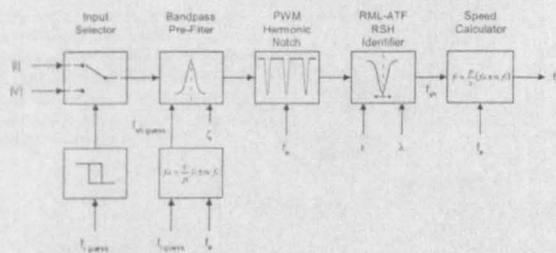


Figure 2: The RSH Speed Estimator

The RSH estimate obtained is turned into a speed estimate using the relationship shown in equation (iii), with  $f_e$  obtained by the differentiation of the flux angle (obtained from the motor model).

The previous work also demonstrated the advantages of tracking RSH effects in the quantities  $|I|$ , obtained from vector  $I_d$  and  $I_q$  currents, and  $|V|$ , the reference output of the PWM scheme [6]. A change-over is made between these input variables, where  $|V|$  is better tracked at low speed due to current controller effects. The previous papers also describe algorithm parameters [6, 10].

The Tuning System

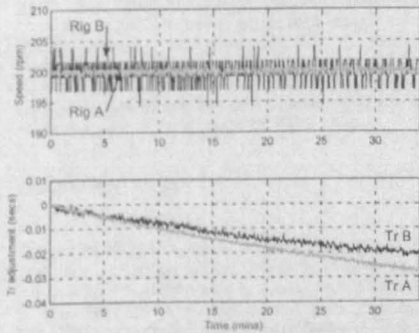


Figure 3: The Sensorless Tuning Drive Speed Holding Performance

The rotor time constant has been shown in previous work to be the motor model parameter most significantly affecting speed estimate accuracy [9]. It is the parameter adjusted by Blasco Gimenez in his FFT tuning work [9]. Here the error between the model speed estimate and

that obtained from the ATSE is directly used to produce a  $T_r$  correction term through a PI control mechanism.

Figure 3 shows the 2-drive experimental rig (to be described shortly) running at a 200rpm demanded speed, over a 20 minute period. Both motors are running the sensorless tuning algorithm. There is no synchronisation used, other than that both drives are given the same reference command. The test is conducted under full-rated load for both machines and from a cold start. Over this time the  $T_r$  adjustment (lower trace) is seen to vary significantly to correct primarily for resistance changes in the motor due to the heating effects. Without tuning each drive would accumulate an error of some 6rpm to 7rpm over a similar period.

BI-AXIAL SPEED SYNCHRONISATION

Many manufacturing processes require that constituent parts of a mechanism be synchronised. These processes would include any based on the manufacture or handling of sheet materials such as paper or rolled steel. Traditionally processes would be synchronised through a mechanical transmission system consisting of a line-shaft, gearing, pulleys, etc.

More recently there has been a large interest in electronic synchronisation, because it offers certain advantages in terms of flexibility and reliability. For example, where product specifications vary with the relative motion of constituent sections, this can be changed in software with a minimum of down time and possibly even online. The increased reliability has much to do with the removal of the mechanical transmission.

Various algorithms have been proposed for axis synchronisation, from simple synchronous command generation, through master/slave algorithms [2], and cross-coupled techniques [11], to the virtual-line shaft method [12]. This work considers the coupling of a 2-machine system, both running the previously described sensorless tuning algorithm, using a parallel cross-coupling



technique. A previous paper looked at drive speed matching using the master/slave method, where the measured/estimated speed of one drive serves as the reference to the second [2]. The major disadvantage with this scheme is that the coupling is only one way: the master drive cannot respond to speed variation seen by the slave.

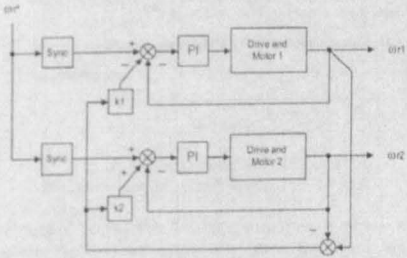


Figure 4: Synchronisation Block Diagram

The synchronisation here is achieved using the technique shown in figure 4. The speed controller of each drive acts on both absolute (reference – drive speed) and relative (drive speed 1 – drive speed 2) errors. The  $k$  gains can be used to weight the relative importance of the two error components.

Such synchronised control is not generally considered possible using sensorless techniques, due to the speed error associated with the model based methods. This work therefore compares the performance attainable with the engineered sensorless tuning solution with that from the same set-up running under encoded IRFO control.

EXPERIMENTAL SET-UP

The experimental system is shown in figure 5. Two 4kW induction motor drives are controlled using a DSP board housed in a host PC. The PC is used for high level control and data capture. The DSP board contains two Texas C44-processor modules and these are used for all motor control functions. Only one processor can communicate with the outside world and this is connected to an interface platform. The platform includes PWM timing and data acquisition circuitry. The PWM boards are interfaced to two modified commercial IGBT inverters. Suitable voltage and current transducers are interfaced to A/D boards, via anti-aliasing filters.

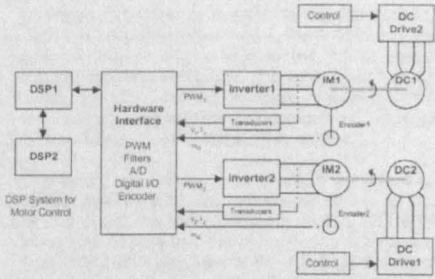


Figure 5: The Experimental Set-up

Processing tasks are performed on both processors. The second processor performs the model based observer, RSH speed estimation and tuning routines. The first processor performs data transfer tasks, speed and current control loop routines, speed synchronisation and PWM timing calculations. Of course there is also a processing overhead associated with inter-processor communication.

Each induction motor drive is connected to a dc machine that acts as a variable torque-loading device. Both rigs are fitted with incremental encoders, the first is a 10,000-line device, the second a 2,500-line device. The encoders are fitted to verify the performance of the sensorless method and for use in the encoded scheme; they play no part in the sensorless algorithm!

Induction motor specifications are given in the appendix, along with the estimated inertia of each drive rig.

RESULTS

Synchronisation is tested for large step changes in individual drive load torque. The two drives have different mechanical characteristics and, although the electrical characteristics (power ratings, etc) are not dissimilar, the response to the tests will certainly vary between drives.

Speed Synchronisation

Figure 6 shows the encoded IRFO synchronised system during a drive A load impact condition. It is evident that drive B responds to the impact, due to the synchronisation, and the maximum speed error is 20rpm. Without synchronisation, the maximum speed error is around 35rpm (the drive A drop in speed without a response from drive B).

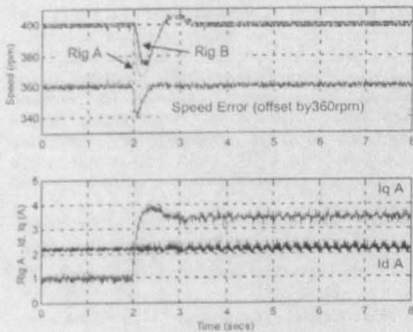


Figure 6: Encoded IRFO Speed Synchronisation. Load Applied to Drive A

Figure 7 shows the encoded response where a large load is removed from drive B. Here the speed error is limited to 40rpm, whereas in an uncoupled system the maximum error is 60rpm+.

$I_d$  and  $I_q$  plots are shown in the lower traces of both results, for the drive suffering the impact condition. These are not shown in the following results as the same test conditions are applied.

The synchronisation is set-up such that the relative speed error is given twice the weighting of the absolute error.

The sensorless performance, for the same operating conditions, is illustrated in figures 8 and 9.

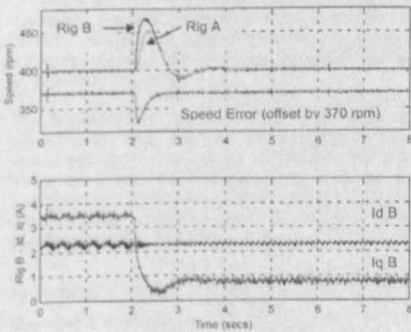


Figure 7: Encoded IRFO Speed Synchronisation. Load Removed from Drive B

In figure 8 drive A again experiences a large step change in load torque (applied). In this case the

maximum speed error is seen to have increased, from the encoded result of figure 6, to nearly 30 rpm. However, this is due to the model based implementation rather than the tuning scheme or synchronisation method: the fall in speed under unsynchronised control is increased, from 35rpm to around 40rpm, for the sensorless control.

The tuning can be seen to maintain encoder-like speed holding with the sensorless drive in the steady state condition. Without tuning, and with the model parameters not set with any attempt for great accuracy (they are not set with high accuracy for these tests), a speed difference of at least some 3rpm to 4rpm would be seen between the steady state conditions.

Figure 9 is comparable to figure 7. Here drive B is operating at a large load torque and this is removed at  $t = 2$ seconds. In this case the maximum speed error is limited to 50rpm, thanks to the synchronisation, from 70rpm when the drive is operated in the unsynchronised sensorless state. Again the drives are seen to hold steady state speed with encoder like accuracy.

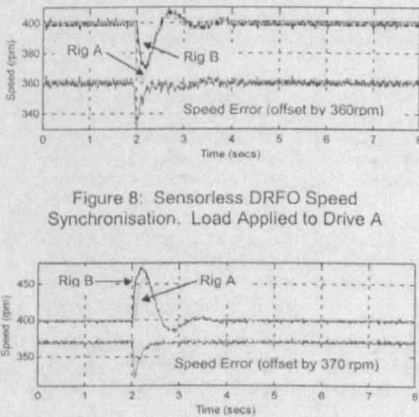


Figure 8: Sensorless DRFO Speed Synchronisation. Load Applied to Drive A

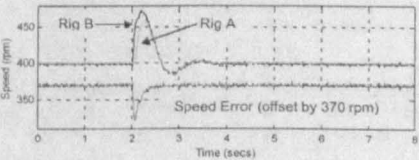


Figure 9: Sensorless DRFO Speed Synchronisation. Load Removed from Drive B

Position Synchronisation

The validity of sensorless position synchronisation is tested in figure 10. The control scheme was modified to include a relative position correction term and the test performed in figure 9 was repeated.

The speed estimate provided by the sensorless scheme is not guaranteed during the transient. The tuning scheme is designed for steady state speed operation. The position correction does, however, go some way toward correcting the relative position error accumulated during the transient. The flatness of the positional error during the steady state reinforces the speed holding capability of the engineered tuning drive.

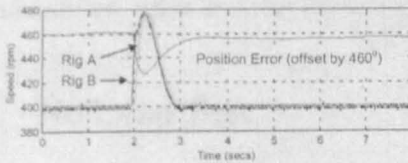


Figure 10: Sensorless DRFO Position Synchronisation. Load Removed from Drive B

#### CONCLUSIONS

In this paper the technique, developed previously by the authors [6], for tuning a sensorless model-based vector drive has been demonstrated for use in a speed-synchronised system. The parallel cross-coupling of two sensorless drives has been shown to constrain the speed error that would normally be seen if the drives were simply to obey similar command information; this was demonstrated under load transient conditions and the two drives used have markedly different inertia.

The technique was extended to show the possibility of using the sensorless scheme to provide position error compensation. This mode of operation will not provide encoder-like relative position holding capability, because the speed-tuning scheme is designed for operation in the steady state.

The steady state speed holding is seen to be encoder-like and this is comparable to the encoded drive having a 10,000-line encoder sampled every 0.01 seconds. Any speed synchronised application where speed holding is required, fixed speed applications perhaps, could consider the use of this algorithm.

#### APPENDIX

##### Machine A Parameters

$R_s=5.32\Omega$ ,  $T_r=0.168s$ ,  $L_s=0.64H$ ,  $L_r=0.633H$ ,  $M=0.6H$ ,  $J=0.3kgm^2$

##### Machine B Parameters

$R_s=5.6\Omega$ ,  $T_r=0.14s$ ,  $L_s=0.56H$ ,  $L_r=0.56H$ ,  $M=0.53H$ ,  $J=0.14kgm^2$

#### REFERENCES

1. Holtz J, 1995, "Methods for speed sensorless control of ac drives", *IEEE Press book - Sensorless control of AC motor drives*, 21-29
2. Turl G, Sumner M, Asher G.M, 2001, "A high performance sensorless induction motor drive for use in multi-motor speed synchronised applications", *EPE Conf*, on CD-ROM
3. Holtz J, 1998, "Sensorless position control of induction motors - an emerging technology", *IEEE Trans Indus Elec*, 840-852
4. Jansen P, Lorenz R.D, 1995, "Transducerless position and velocity estimation in induction and salient AC machines", *IEEE Trans Indus App*, 31, 2, 240-247
5. Kubota H, Matsuse K, Nakano T, 1993, "DSP-based speed adaptive flux observer of induction motor" *IEEE Trans Indus App*, 29, 2, 344-348
6. Turl G, Sumner M, Asher G.M, 2001, "A hybrid induction motor control strategy for high performance drive applications", *IEEE PES Conf*, 20-25
7. Ohya K, Asher G.M, Sumner M, 1999, "Comparison of the practical performance and operating limits of sensorless induction motor drive using a closed loop flux observer and a full-order flux observer", *EPE Conf*, on CD-ROM
8. Ferrah A, 1993, "A novel approach to sensorless speed detection using rotor slot harmonics in induction motor drives", *Phd Thesis, Univ of Nottingham, UK*
9. Blasco-Gimenez R, 1996, "High performance sensorless vector control of induction motor drives", *Phd Thesis, Univ of Nottingham, UK*
10. Ferrah A et al, 1998, "A speed identifier for induction motor drives using real-time adaptive digital filtering", *IEEE Trans Indus App*, 34, 1, 156-162
11. Koren Y, 1980, "Cross-coupled biaxial computer control for manufacturing systems", *ASME Dyn Sys, Meas and Con*, 102, 265-272
12. Valenzuela M.A, Lorenz R.D, 2001, "Electronic line-shafting control for paper machine drives", *IEEE Trans Indus App*, 37, 1, 158-164

---

## APPENDIX B Motor Parameter Determination Rig B

---

The motor parameters for rig B were determined using voltage, current and power measurement, whilst running no load and locked rotor tests. The following two sections show base parameter calculations, although various parameters were later tuned/modified, upon analysis of the rig B model based method.

### B.1 No Load Test

Applied/measured motor quantity	
Applied excitation frequency	50Hz
Measured running frequency (electrical speed)	49.76Hz
Applied RMS line voltage	415V
Measured RMS phase current	2.32A
Measured per-phase motor power	171.6W
Measured per-phase motor apparent power	965VA
Measured per-phase motor reactive power	948VAR

Table B.1. Applied/measured motor quantities during no-load test

The measured (using a dc ohmmeter) motor stator resistance,  $R_s = 5.9\Omega$

Reactive power mainly due to  $L_s$  at no load

$$V_{Ls} = \frac{VAR}{I} = \frac{948}{2.32} = 408.62V$$

$$X_{Ls} = \frac{V_{Ls}}{I} = \frac{408.62}{2.32} = 176.11\Omega$$

$$L_s = \frac{X_{Ls}}{\omega} = \frac{176.11}{2 \times \pi \times 50} = 0.561H$$

(B.1)

## B.2 Locked Rotor Test

Applied/measured motor quantity	
Applied excitation frequency	50Hz
Measured running frequency (electrical speed)	0Hz
Applied RMS line voltage	128.2V
Measured RMS phase current	4.834A
Measured per-phase motor power	240W
Measured per-phase motor apparent power	623VA
Measured per-phase motor reactive power	560VAR

Table B.2. Applied/measured motor quantities during locked rotor test

The measured (using a dc ohmmeter) motor stator resistance,  $R_s = 5.9\Omega$

$$\therefore P_{Rs} = I^2 R_s = 4.838^2 \times 5.9 = 138W$$

(B.2)

Using the measured real power  $R_r$  is calculated, knowing that  $slip = s = 1.0$

$$P_{Rr} = P - P_{Rs} = 240W - 138W = 102W$$

$$\therefore R_r = \frac{P_{Rr}}{I^2} = \frac{102}{4.838^2} = 4.36\Omega$$

(B.3)

Reactive power mainly due to  $l_s + l_r$  for the locked rotor condition

$$V_{l_s + l_r} = \frac{VAR}{I} = \frac{560}{4.838} = 115.75V$$

$$X_{l_s + l_r} = \frac{V_{l_s + l_r}}{I} = \frac{115.75}{4.838} = 23.92\Omega$$

$$l_s + l_r = \frac{X_{l_s + l_r}}{\omega} = \frac{23.92}{2 \times \pi \times 50} = 0.076H$$

(B.4)

For the type of motor used  $l_s$  and  $l_r$  are assumed equal

$$l_s = l_r = \frac{0.076}{2} = 0.038H$$

(B.5)

All of the motor parameters are now defined

$$R_s = 5.9\Omega$$

$$R_r = 4.36$$

$$L_s = 0.56H$$

$$M = L_s - l_s = 0.56 - 0.038 = 0.522H$$

$$L_r = M + l_r = 0.56H$$

$$T_r = \frac{L_r}{R_r} = \frac{0.56}{4.36} = 0.13s$$

$$\sigma = \frac{L_s L_r - M^2}{L_s L_r} = 0.13$$

(B.6)

For completeness, the motor parameters are presented for both induction machines used in table B.3 below.

Motor Parameter	Rig A	Rig B
$R_s$	5.32 $\Omega$	5.9 $\Omega$
$R_r$	3.77 $\Omega$	4.36 $\Omega$
$L_s$	0.64H	0.56H
$L_r$	0.633H	0.56H
M	0.6H	0.522H
$T_r$	0.168s	0.13s
$\sigma$	0.11	0.13

**Table B.3. Motor parameters for both rig A and rig B**

## APPENDIX C Code Listings

[illegible]



## APPENDIX C Code Listings

[illegible]

[illegible]

```

    for(j=0; j<=989; j++)
    {
        sqroot[j] = sqrt((float)((j+10.0)/10.0));
    }
    /* square root array values */

    *LED = outLED;          /* clear LED pack */

    PWM_oneshot();          /* setup 8254 'one shot' mode */
    PWMA_oneshot();

    timer1_int();           /* setup/enable timers and intrpts */
    setup_timers((int)freq);
    INT_ENABLE();

    for(;;)
    {
        if(*DPRAM == 1.0)
        {
            _fm1 = _fm2 = *(DPRAM+1);
            /* update fm */
        }
        else _fm1 = _fm2 = 0.0;

        var1 = (int)*(DPvar1ptr);
        var2 = (int)*(DPvar2ptr);
        var3 = (int)*(DPvar3ptr);
        var4 = (int)*(DPvar4ptr);
        var5 = (int)*(DPvar5ptr);
        var6 = (int)*(DPvar6ptr);
        var7 = (int)*(DPvar7ptr);
        var8 = (int)*(DPvar8ptr);
        /* update data capture variables */
        tr_flag = *(DPRAM+14);
    }
}

void c_int1(void)
{
    INT_ENABLE();
    /*timest = *timlcntr;*/
    /* interrupt timing counter */
    outLED = outLED + 0x00800000;
    /* pin set for interrupt timing */
    *LED = outLED;

    if(start == 0) start++;
    else
    {
        /* trigger previous timeouts */
        PWM_gatepulse(flag);
        PWMA_gatepulse(flag);
    }

    TriggerADC1();          /* trigger A/D boards */
    TriggerADC2();
    TriggerADC3();
    temp = *timlcntr + 150;
    /* delay time for A/D settle */
    /*timest = *timlcntr;*/

    flag = flag * -1;       /* PWM polarity toggle */
}

```

[illegible]

256

```

        errold1mod = err1mod;
        if(Iq1 > 5.0) Iq1 = 5.0;
        if(Iq1 < -5.0) Iq1 = -5.0;
        Iqold1 = data[24] = Iq1;

        wslip1 = Iq1 / (Tr1*Id1);
                                /* current to slip scaling */
        we1 = wr1 + wslip1;
                                /* excitation frequency calc */
                                /* only used in IRFO */

        if(we1 < -377.0) we1 = -377.0;
                                /* we limit */
        else if(we1 > 377.0) we1 = 377.0;
        data[16] = wslip1;
        data[17] = we1;

        fm1 = we1/PIx2;
                                /* convert to elec frequency */
        *(DPRAM+5) = fm1;
        /* ----- */

        count = 0;
    }
    if(count == 2) /* start of encoder speed control */
    {
        /* Speed Measure ----- */
        /*wrref2 = data[18] = PIx2*_fm2;*/
                                /* convert i/p speed to rad/s */
        /*wrref2 = data[18] = _wr1;*/
                                /* reference is rig 1 speed */
        wrref2 = data[18] = wrVelec;

        speed2a2 = GetSpeedCount2();
        speeda2 = GetSpeedValue2(speed1a2, speed2a2,
            time1);
        speed1a2 = speed2a2;
                                /* measure encoder speed */
        wr2 = data[19] = 4.0*speeda2*PI;

        if(wr2 > wr2old+12.0) wr2 = wr2old;
        if(wr2 < wr2old-12.0) wr2 = wr2old;
        else wr2old = wr2;

        if(*(DPRAM+15)<0.0)
        {
            wr2 = wr2;
            *(DPRAM+18) = 2.0*speeda2;
                                /* get encoder speed */

            if((wr_filtB<(wr2+12.0)) &
                (wr_filtB>(wr2-12.0))) _wr2 = wr_filtB;
            else
            {
                _wr2 = wr2;
                wrerrr_count2++;
            }
                                /* error checking for sensorless */
        }
    }
    else

```

```

    {
        wr2 = 0.0;
        *(DPRAM+18) = wr2;

        _wr2 = wr_filtB;
    }

    /* Speed Control ----- */
    err2 = (wrref2 - _wr2);
    /* speed control and current limit */
    err_coup = (_wr1 - _wr2);
    /*err2mod = 0.5*(err2 + err_coup);*/
    err2mod = err2;

    /*Iq2 = Iqold2 + (0.224*err2) - (0.196*errold2);*/

    /* inc damping - inc gain, leave gap unchanged */
    g1 = 1.0*0.16; /* 2.0 */
    g2 = g1 - 0.009;

    /* inc inertia - inc gain of both terms */
    g1 = 1.0*g1; /* 1.2 */
    g2 = 1.0*g2;

    Iq2 = Iqold2 + (g1*err2mod) - (g2*errold2mod);
    /* 3Hz and 10rad/sec */

    errold2mod = err2mod;
    if(Iq2 > 5.0) Iq2 = 5.0;
    if(Iq2 < -5.0) Iq2 = -5.0;
    Iqold2 = data[27] = Iq2;

    wslip2 = Iq2 / (Tr2*Id2);
    /* current to slip scaling */
    we2 = wr2 + wslip2;
    /* excitation frequency calc */
    /* only used in IRFO */

    if(we2 < -377.0) we2 = -377.0;
    /* we limit */
    else if(we2 > 377.0) we2 = 377.0;
    data[20] = wslip2;
    data[21] = we2;

    fm2 = we2/PIx2;
    /* convert to elec frequency */
    *(DPRAM+19) = fm2;
    /* ----- */
}
count++;

if(flag== -1) /* DRFO (observer) angle calc */
{
    lr_ang1 = databuffer[5];
    lr_ang2 = databuffer[15];
}
else
{
    lr_ang1 = lr_ang1 + databuffer[20]/2.0;
    lr_ang2 = lr_ang2 + databuffer[21]/2.0;
}

```



259

\_\_\_\_\_

260



[illegible]



[illegible]





```

if(flag== -1)
{
    /* redefine times for use in PWM scheme */
    _tx1 = t1_1 + t2_1 + t0_1/2;
    _ty1 = _tx1 - t1_1;
    _tz1 = _ty1 - t2_1;
}

if(flag==1)
{
    /* inversion every other int cycle */
    _tz1 = t1_1 + t2_1 + t0_1/2;
    _ty1 = _tz1 - t2_1;
    _tx1 = _ty1 - t1_1;
}

switch(sector1)
{
    /* depend on sector, send times to PWM */
    case 0:
        ta1 = _tx1;
        tb1 = _ty1;
        tc1 = _tz1;
        break;
    case 1:
        ta1 = _ty1;
        tb1 = _tx1;
        tc1 = _tz1;
        break;
    case 2:
        ta1 = _tz1;
        tb1 = _tx1;
        tc1 = _ty1;
        break;
    case 3:
        ta1 = _tz1;
        tb1 = _ty1;
        tc1 = _tx1;
        break;
    case 4:
        ta1 = _ty1;
        tb1 = _tz1;
        tc1 = _tx1;
        break;
    case 5:
        ta1 = _tx1;
        tb1 = _tz1;
        tc1 = _ty1;
        break;
    default:
        INT_DISABLE();
        break;
}

if(ta1 < mintime) ta1 = mintime;
if(tb1 < mintime) tb1 = mintime;
if(tc1 < mintime) tc1 = mintime;
if(ta1 > maxtime) ta1 = maxtime;
if(tb1 > maxtime) tb1 = maxtime;
if(tc1 > maxtime) tc1 = maxtime;
/* limit pulsewidths */

PWM_timesetupSV( ta1, tb1, tc1);
/* PWM output */

```

```

/* >>>>>>>>>>>>>>>>>>>>>>>>>>>>>>>>>>>>>>>>>>>>>>>>>>>>>>>>>>>>>>>>>>>>>> */
if(flag==1) receive_msg(2, databuffer, 1);
/*comm2 = chk_dma(2);*/

/*<< Space Vector 2 >>>>>>>>>>>>>>>>>>>>>>>>>>>>>>>>>>>>>>>>>>>>>>>>>>>>>>>>>>>>>>>>>>>>>> */
_sector2 = theta2/PIby3;
/* express in terms of 6 sectors */
if(_sector2 >= 6.0) _sector2 = _sector2 - 6.0;
sector2 = (int)_sector2;
/* get sector number */
phi2_2 = theta2 - (sector2*PIby3);
/* angle from sector start */
phi1_2 = (PIby3) - phi2_2;
/* angle from sector end */

angle2 = (int)( 999*phi1_2/PIx2 );
t1_2 = time*m2*sine[angle2]; /* calculate t1 */

angle2 = (int)( 999*phi2_2/PIx2 );
t2_2 = time*m2*sine[angle2]; /* calculate t2 */

t0_2 = time - t1_2 - t2_2; /* calculate t0 */

if((sector2==1) | (sector2==3) | (sector2==5))
{
    /* swap timings t1 and t2 for section.. */
    ttemp2 = t1_2;
    /* ....1, 3 and 5. This is equivalent. */
    t1_2 = t2_2;
    /* ....to using the alternate equations */
    t2_2 = ttemp2;
}

if(flag==-1)
{
    /* redefine times for use in PWM scheme */
    _tx2 = t1_2 + t2_2 + t0_2/2;
    _ty2 = _tx2 - t1_2;
    _tz2 = _ty2 - t2_2;
}

if(flag==1)
{
    /* inversion every other int cycle */
    _tz2 = t1_2 + t2_2 + t0_2/2;
    _ty2 = _tz2 - t2_2;
    _tx2 = _y2 - t1_2;
}

switch(sector2)
{
    /* depend on sector, send times to PWM */
    case 0:
        ta2 = _tx2;
        tb2 = _ty2;
        tc2 = _tz2;
        break;
    case 1:
        ta2 = _ty2;
        tb2 = _tx2;
        tc2 = _tz2;
        break;
    case 2:
        ta2 = _tz2;
        tb2 = _tx2;

```

[illegible]

[illegible]



[illegible]

272



[illegible]

1. *Journal of the American Medical Association*, 1997; 277: 1039-1043.

```
/*load_errA = databuffer[35] -
```

[illegible]

```

{
    /*etrB = databuffer[31] -
        PIx2*(databuffer[29]);*/
    etrB = databuffer[31] - databuffer[35];

    /* 37 changed for 35 */
    if(databuffer[38] < 0.0) etrB = -etrB;

    if(databuffer[35] != wrrefB)
        directB = databuffer[35] - wrrefB;
    if((directB>0) &
        ((databuffer[29]*PIx2)>databuffer[35]))
        directB = 100;
    if((directB<0) &
        ((databuffer[29]*PIx2)<databuffer[35]))
        directB = -100;
    if((directB==100) &
        ((databuffer[29]*PIx2)<databuffer[35]))
        directB = 0;
    if((directB==-100) &
        ((databuffer[29]*PIx2)>databuffer[35]))
        directB = 0;
    if(directB != 0) etrB=0.0;

    load_errB = databuffer[35] -
        (databuffer[29]*PIx2);
    load_errB = load_errB*load_errB;
    /* if(load_errB > 0.796) etrB=0.0; */
    if(load_errB > 1.0) etrB=0.0;

    if((databuffer[35]*databuffer[35]) < 246.7)
    {
        kB=0.8;
        etrB=0.0;
    }
    else kB=1.0;

    wrrefB = databuffer[35];

    if(tr_flag > -0.1)
    {
        if(tr_flag == 0.0) Tr_adjB = 0.0;
        etrB = etroB = integral_etrB =
            integral_etroB = 0.0;
        LPF2(0.0, 100.0, 0.5);
    }
    else
    {
        kpB = 0.02;
        kiB = 0.05;
        Tr_adjB = kpA*etrB + kiB*integral_etrB;
        etroB = etrB;

        if((Tr_adjB<0.18) & (Tr_adjB>-0.05))
        {
            integral_etrB = integral_etroB +
                0.01*etroB;
        }
        integral_etroB = integral_etrB;

        if(Tr_adjB > 0.18) Tr_adjB = 0.18;
        else if(Tr_adjB < -0.05)

```

}

### C.3 Filter and RSH Tracking Functions

```
/* ***** */
/* this is development code for the Band Stop Filter fn */
/* */
/* it is not a final program and thus the functionality is */
/* not guaranteed - it has been edited for presentation in */
/* MS Word and this may have introduced errors */
/* */
/* it is included here only to give some indication of */
/* programming detail */
/* ***** */

float BSF1(float input, float fn, float FS, float BW)
{
    float r, theta;
    static float input1=0.0, input2=0.0;
    static float output1=0.0, output2=0.0;
    float output;
    /* int angle; */

    r = 1 - (2*BW/FS);

    /*angle = (int)(999*((2*PI*fn)/(FS*PIx2)));
    theta = -2 * cosine[angle]; */
    theta = -2 * cos(2*PI*fn/FS);

    output = input + input2 - r*r*output2 - theta*(r*output1
        - input1);

    output2 = output1;
    output1 = output;

    input2 = input1;
    input1 = input;

    return(output);
}
```



## APPENDIX C Code Listings

```
/* ***** */
/* this is development code for the Band Pass Filter fn */
/* */
/* it is not a final program and thus the functionality is */
/* not guaranteed - it has been edited for presentation in */
/* MS Word and this may have introduced errors */
/* */
/* it is included here only to give some indication of */
/* programming detail */
/* ***** */

float BPF1(float input, float fn, float FS, float _Z)
{
    double ts, alpha, beta, gamma, aa0, bb1, bb2;
    static double v1=0, v2=0;
    double v0, y0;
    static double vv1=0, vv2=0;
    double vv0, yy0;
    static double vvv1=0, vvv2=0;
    double vvv0, yyy0;

    int tempBPF;

    /*ts = (PI*fn)/FS;
    tempBPF = (int)(999.0*ts/PIx2);
    ts = sine[tempBPF]/(PI*fn*cosine[tempBPF]);*/

    ts = tan(PI*fn/(FS))/(PI*fn);
                                /* pre-warp calculation */

    alpha = 2*PI*fn*ts;          /* prelim coefficient calcs */
    beta = alpha*alpha;
    gamma = beta + 4*_Z*alpha + 4;

    aa0 = 4*_Z*alpha/gamma;      /* calc coefficients */
    bb1 = (2*beta - 8)/gamma;
    bb2 = (beta - 4*_Z*alpha +4)/gamma;

    v0 = input - bb1*v1 - bb2*v2;
                                /* filter equations no.1 */
    y0 = aa0 * (v0 - v2);

    v2 = v1;                    /* update internal variables no.1 */
    v1 = v0;

    vv0 = y0 - bb1*vv1 - bb2*vv2;
                                /* filter equations no.2 */
    yy0 = aa0 * (vv0 - vv2);

    vv2 = vv1;                  /* update internal variables no.2 */
    vv1 = vv0;

    return(yy0);
}
```

```

/* ***** */
/* this is development code for the RSH Identifier (RML) fn */
/* */
/* it is not a final program and thus the functionality is */
/* not guaranteed - it has been edited for presentation in */
/* MS Word and this may have introduced errors */
/* */
/* it is included here to only give some indication of */
/* programming detail */
/* ***** */

float RML1(float y2, float FS, float _R, float _L)
{
    static float e1=0.0, e0=0.0, y1=0.0, y0=0.0, a2=0.0,
                psi1=0.0, psi0=0.0, P2=100.0;
    static float r, L;
                float ebar2, phi2, f;

    int    tempRML;

    r = _R;
    L = _L;

    phi2 = r*e1 - y1;

    psi1 = phi2 - a2*r*psi1 - r*r*psi0;
                                /* which way to move filter */
    if(psi1 > 100.0)  psi1 = 100.0;
    else if(psi1 < -100.0)  psi1 = -100.0;

    ebar2 = y2 + y0 - r*r*e0 - a2*phi2;
                                /* notch filter output (predictor) */

    P2 = P2 / (L + P2*psi1*psi1);
                                /* co-variance of centre f parameter */
    if(P2 > 1000.0)  P2 = 1000.0;
                                /* (this is the degree of certainty.... */
    else if(P2 < -1000.0)  P2 = -1000.0;
                                /* ...that centre f estimate is correct */

    a2 = a2 + P2*psi1*ebar2;
                                /* adjust centre frequency */
    if(a2 > 2.0)  a2 = 2.0;
    else if(a2 < -2.0)  a2 = -2.0;

    e1 = y2 + y0 - r*r*e0 - a2*phi2;
                                /* notch filter output (corrector) */
    if(e1 > 100.0)  e1 = 100.0;
    else if(e1 < -100.0)  e1 = -100.0;

    /* r = R0*r + (1 - R0)*R_INF; */

    y0 = y1;
    y1 = y2;
    psi0 = psi1;
    e0 = e1;

    f = 0.5*INVSPI*FS*acos(-0.5*a2);

    /*tempRML = (int)(-0.5*a2*999.0);
    if(tempRML < 0)  f = 0.5*INVSPI*FS*(PIby2 +
                                invsine[tempRML]);

```

```

        else f = 0.5*INVSPi*FS*(PIby2 - invsine[tempRML]);*/

    return(f);
}

/* ***** */
/* this is development code for the Low Pass Filter fn */
/* */
/* it is not a final program and thus the functionality is */
/* not guaranteed - it has been edited for presentation in */
/* MS Word and this may have introduced errors */
/* */
/* it is included here only to give some indication of */
/* programming detail */
/* ***** */

float LPF1(float input, float FS, float BW)
{
    static float input1=0.0, output=0.0;
        float k;

    k = (2.0*PI*BW)/FS;
    output = k*input1 + (1-k)*output;

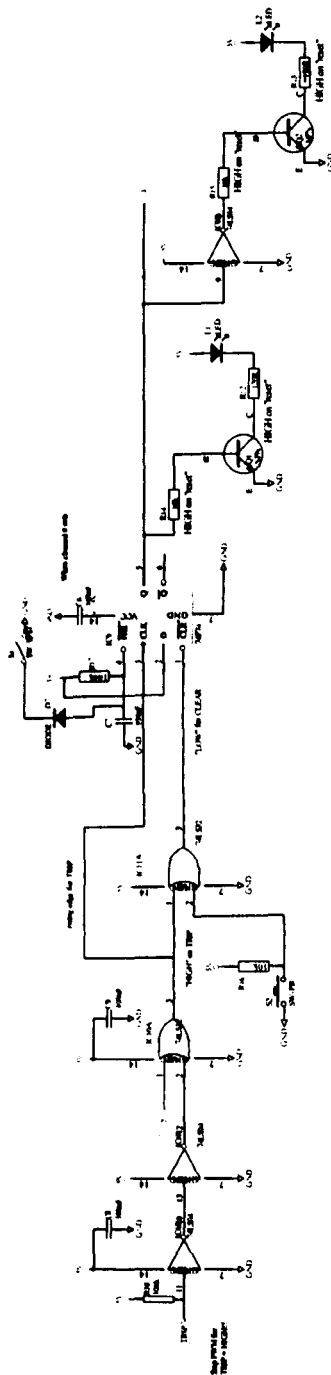
    input1 = input;

    return(output);
}

```



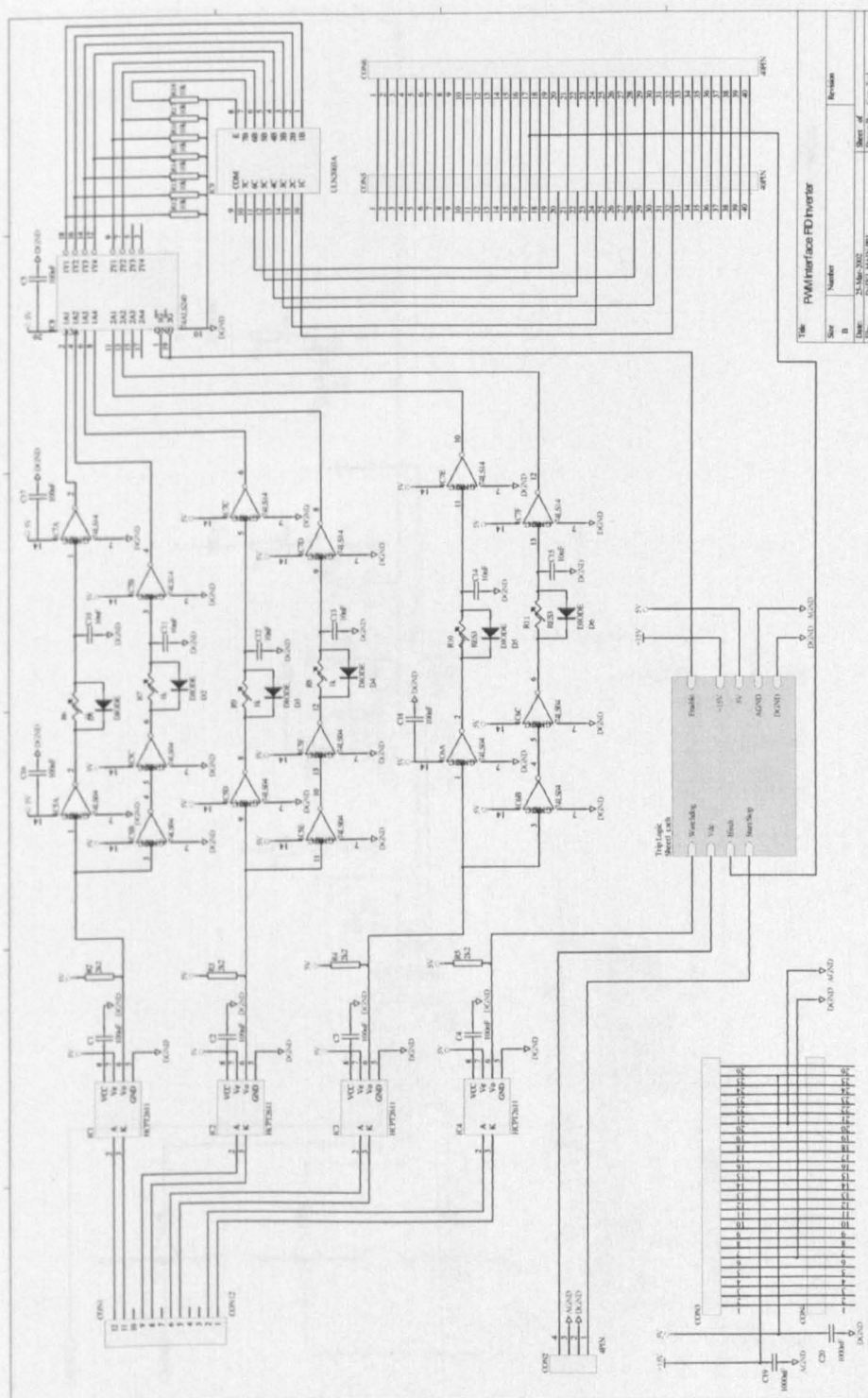
## D.2 Eurotherm Inverter – Trip Circuit



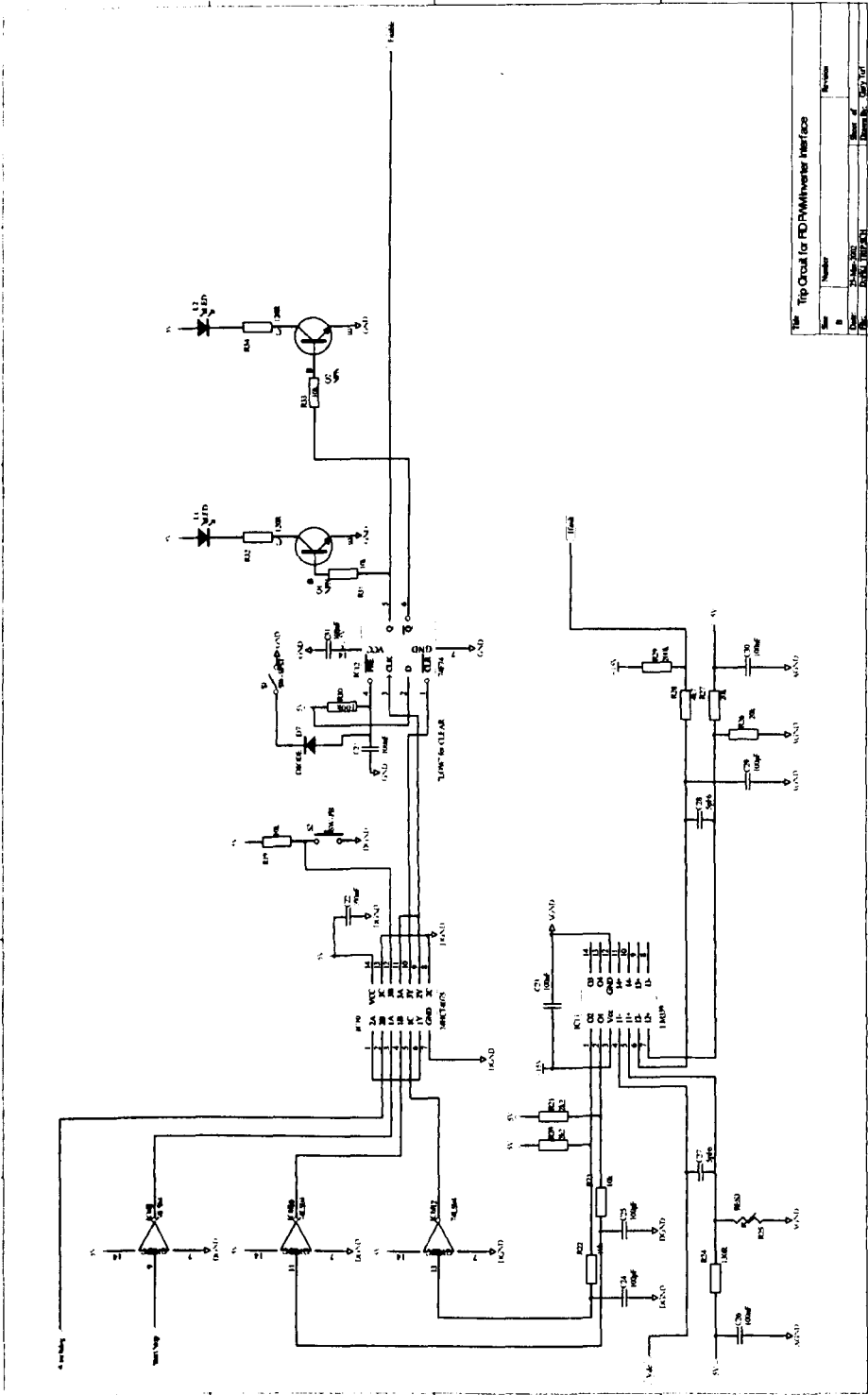
**Title:** Trip Circuit for Eurotherm Inverter Interface

Site	Project	Section	Sheet of
2		2 (Gary Fort)	

### D.3 FKI Industrial Drives Inverter - Interface Circuit



D.4 FKI Industrial Drives Inverter - Trip Circuit





---

## APPENDIX E Derivation of the AFO/ASO Equations

---

### E.1 The Stator Current Dynamic Equation

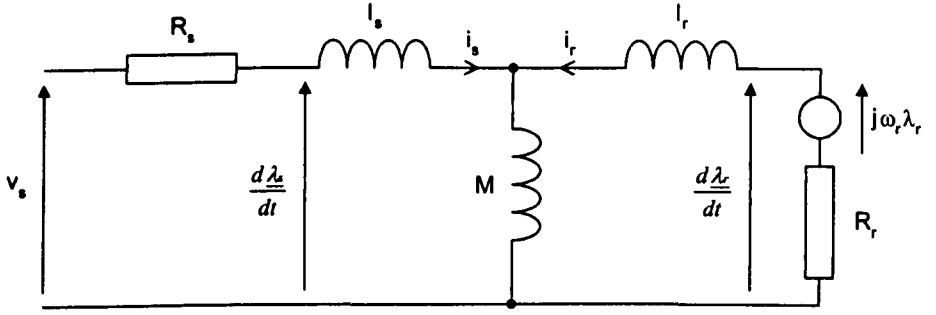


**Fig E.1. The induction motor dynamic model in the fixed stator frame**

From figure E.1, an expression for the stator voltage  $v_s$  can be derived

$$\begin{aligned}
 \underline{v}_s &= R_s \underline{i}_s + \frac{d\lambda_s}{dt} \\
 &= R_s \underline{i}_s + l_s \frac{d\underline{i}_s}{dt} - l_r \frac{d\underline{i}_r}{dt} - R_r \underline{i}_r + j\omega_r \underline{\lambda}_r
 \end{aligned}
 \tag{E.1}$$

The following equation can be used to substitute for  $\underline{i}_r$  in equation E.1

$$\underline{i}_r = \frac{\underline{\lambda}_r - M \underline{i}_s}{L_r}
 \tag{E.2}$$

This gives a new expression for  $v_s$

$$\underline{v}_s = R_s \underline{i}_s + l_s \frac{d\underline{i}_s}{dt} - l_r \frac{d}{dt} \left( \frac{\underline{\lambda}_r - M \underline{i}_s}{L_r} \right) - R_r \left( \frac{\underline{\lambda}_r - M \underline{i}_s}{L_r} \right) + j\omega_r \underline{\lambda}_r
 \tag{E.3}$$

Multiplying out equation E.3 gives a differential term for  $\lambda_r$  and the following expression can be used to substitute for this variable

$$\frac{d\lambda_r}{dt} = j\omega_r \lambda_r - R_r i_r \quad (E.4)$$

The expression for  $v_s$  is now as shown below in equation E.5

$$v_s = R_s i_s + l_s \frac{di_s}{dt} - j \frac{l_r}{L_r} \omega_r \lambda_r + \frac{l_r}{L_r} R_r i_r + \frac{l_r M}{L_r} \frac{di_s}{dt} - \frac{R_r}{L_r} \lambda_r + \frac{M}{L_r} R_r i_s + j\omega_r \lambda_r \quad (E.5)$$

Equation E.2 is used again to substitute for  $i_r$ , and the equation for  $v_s$  becomes as below

$$\begin{aligned} v_s &= R_s i_s + l_s \frac{di_s}{dt} - j \frac{l_r}{L_r} \omega_r \lambda_r + \frac{l_r}{L_r^2} R_r \lambda_r - \frac{l_r M}{L_r^2} R_r i_s + \frac{l_r M}{L_r} \frac{di_s}{dt} - \frac{R_r}{L_r} \lambda_r + \frac{M}{L_r} R_r i_s + j\omega_r \lambda_r \\ &= R_s i_s - \frac{l_r M}{L_r T_r} i_s + \frac{M}{T_r} i_s + l_s \frac{di_s}{dt} + \frac{l_r M}{L_r} \frac{di_s}{dt} - \frac{l}{T_r} \lambda_r + \frac{l_r}{L_r^2} R_r \lambda_r + j\omega_r \lambda_r - j \frac{l_r}{L_r} \omega_r \lambda_r \end{aligned} \quad (E.6)$$

Requiring a dynamic equation for stator current, the following relationship is used

$$\left( l_s - \frac{l_r M}{L_r} \right) \frac{di_s}{dt} = \sigma L_s \frac{di_s}{dt} \quad (E.7)$$

The dynamic equation for stator current is therefore shown in equation E.8

$$\begin{aligned} \frac{di_s}{dt} &= -\frac{R_s}{\sigma L_s} i_s + \left( \frac{l_r M}{\sigma L_s L_r T_r} - \frac{M}{\sigma L_s T_r} \right) i_s + \left( \frac{l}{\sigma L_s T_r} - \frac{l_r}{\sigma L_s L_r T_r} \right) \lambda_r + j \left( \frac{l_r}{\sigma L_s L_r} \omega_r - \frac{\omega_r}{\sigma L_s} \right) \lambda_r + \frac{l}{\sigma L_s} v_s \\ &= -\frac{R_s}{\sigma L_s} i_s - \frac{(l - \sigma)}{\sigma T_r} i_s + \frac{M}{\sigma L_s L_r T_r} \lambda_r - j\omega_r \frac{M}{\sigma L_s L_r} \lambda_r + \frac{l}{\sigma L_s} v_s \end{aligned} \quad (E.8)$$

This is the stator current dynamic equation, the 1<sup>st</sup> equation in the Kubota observers

## E.2 The Rotor Flux Dynamic Equation

Again from figure E.1, and as shown in equation E.4, the rotor flux dynamic equation can be expressed

$$\frac{d\lambda_r}{dt} = j\omega_r \lambda_r - R_r i_r \quad (E.9)$$

Equation E.10 below is used to substitute for  $i_r$ ,

$$i_r = \frac{\lambda_r - M i_s}{L_r} \quad (E.10)$$

The dynamic equation for rotor flux, forming the 2<sup>nd</sup> equation in the Kubota flux and speed observer, becomes as shown below in equation E.11

$$\begin{aligned} \frac{d\lambda_r}{dt} &= j\omega_r \lambda_r - \frac{R_r}{L_r} \lambda_r + \frac{M}{L_r} R_r i_s \\ &= \frac{M}{T_r} i_s - \frac{1}{T_r} \lambda_r + j\omega_r \lambda_r \end{aligned} \quad (E.11)$$

---

## APPENDIX F Speed Controller Design

---

### F.1 Speed Controller Design – Rig A

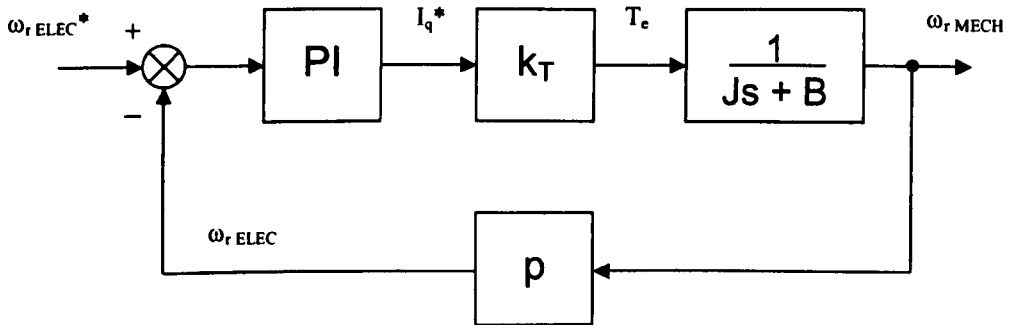


Fig F.1. Structure of the speed control loop

The structure of the speed control loop is shown in figure F.1.

The s-domain transfer function for the PI controller is

$$PI(s) = \frac{k_c(s + a_c)}{s} \quad (\text{F.1})$$

The characteristic equation for the above speed control loop is solved for  $1 + G(s)H(s) = 0$ . This is where  $J = 0.3$ ,  $B = 0.02$ ,  $k_T = 7.55$ ,  $p = 2$  (ignoring units).

$$\begin{aligned}
 0 &= s^2 + \left( \frac{B + 2k_c k_t}{J} \right) s + \frac{2k_c k_t a_c}{J} \\
 &= s^2 + \left( \frac{0.02 + 15.1k_c}{0.3} \right) s + \frac{15.1k_c a_c}{0.3}
 \end{aligned} \quad (\text{F.2})$$

The coefficients in the above equation are equated with those in the following equation, which defines the desired closed loop dynamics, thus solving for  $k_c$  and  $a_c$ . This is with  $\zeta = 0.707$ ,  $\omega_0 = 10\text{rad/s}$

$$\begin{aligned} 0 &= s^2 + 2\zeta\omega_0 s + \omega_0^2 \\ &= s^2 + 14.14s + 100 \end{aligned} \tag{F.3}$$

Thus

$$\begin{aligned} k_c &= \frac{(0.3 \times 14.14) - 0.02}{15.1} = 0.2796 \\ \therefore a_c &= \frac{(0.3 \times 100)}{(0.2796 \times 15.1)} = 7.1057 \end{aligned} \tag{F.4}$$

The PI transfer function is therefore

$$PI(s) = \frac{0.2796(s + 7.1057)}{s} \tag{F.5}$$

The speed loop sample frequency is  $100\text{Hz}$ , such that  $T = 0.01\text{s}$ . The PI law can be discretised using the bilinear transform.

$$s = \frac{2(z-1)}{T(z+1)} \tag{F.6}$$

Substituting the above equation into equation F.5 results in the sampled digital control law shown below.

$$\begin{aligned} u(k) &= u(k-1) + \frac{2k_c + k_c a_c T}{2} e(k) - \frac{2k_c - k_c a_c T}{2} e(k-1) \\ &= u(k-1) + 0.2895e(k) - 0.2687e(k-1) \end{aligned} \tag{F.7}$$

## F.2 Speed Controller Design – Rig B

The characteristic equation for rig B, with  $J = 0.12$ ,  $B = 0.01$ ,  $k_T = 7.5$ ,  $p = 2$  (ignoring units) is

$$\begin{aligned} 0 &= s^2 + \left( \frac{B + 2k_c k_i}{J} \right) s + \frac{2k_c k_i a_c}{J} \\ &= s^2 + \left( \frac{0.01 + 15k_c}{0.13} \right) s + \frac{15k_c a_c}{0.13} \end{aligned} \quad (F.8)$$

Equate coefficients with the following, where  $\zeta = 0.707$ ,  $\omega_0 = 10 \text{ rad/s}$

$$\begin{aligned} 0 &= s^2 + 2\zeta\omega_0 s + \omega_0^2 \\ &= s^2 + 14.14s + 100 \end{aligned} \quad (F.9)$$

Thus

$$\begin{aligned} k_c &= \frac{(0.13 \times 14.14) - 0.01}{15} = 0.122 \\ \therefore ac &= \frac{(0.13 \times 100)}{(0.122 \times 15)} = 7.104 \end{aligned} \quad (F.10)$$

The PI transfer function is therefore

$$PI(s) = \frac{0.122(s + 7.104)}{s} \quad (F.11)$$

The speed loop sample frequency is  $100 \text{ Hz}$ , such that  $T = 0.01 \text{ s}$ . The PI law can be discretised using the bilinear transform. The sampled digital control law is

$$\begin{aligned} u(k) &= u(k-1) + \frac{2k_c + k_c a_c T}{2} e(k) - \frac{2k_c - k_c a_c T}{2} e(k-1) \\ &= u(k-1) + 0.126e(k) - 0.118e(k-1) \end{aligned} \quad (F.12)$$

---

## APPENDIX G Current Controller Design

---

### G.1 Current Controller Design – Rig A

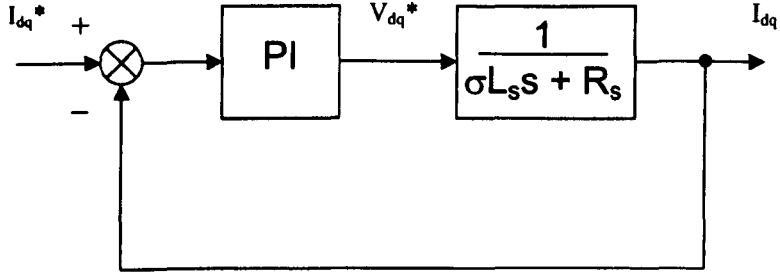


Fig G.1. Structure of the current control loop

The reduced structure of the current control loop is shown in figure G.1

The s-domain transfer function for the PI controller is

$$PI(s) = \frac{k_c(s + a_c)}{s} \quad (G.1)$$

The characteristic equation for the above current control loop is solved for  $1 + G(s)H(s) = 0$ . This is where (ignoring units)  $\sigma = 0.11$ ,  $L_s = 0.64$ ,  $R_s = 5.32$

$$\begin{aligned} 0 &= s^2 + \left( \frac{R_s + k_c}{\sigma L_s} \right) s + \frac{k_c a_c}{\sigma L_s} \\ &= s^2 + \left( \frac{5.32 + k_c}{0.0704} \right) s + \frac{k_c a_c}{0.0704} \end{aligned} \quad (G.2)$$

The coefficients in the above equation are equated with those in the following equation, which defines the desired closed loop dynamics, thus solving for  $k_c$  and

$a_c$ . This is where  $\zeta = 0.707$ ,  $\omega_o = 100\text{Hz} = 628.32\text{rad/s}$

$$\begin{aligned} 0 &= s^2 + 2\zeta\omega_o s + \omega_o^2 \\ &= s^2 + 888.44s + 394784 \end{aligned} \quad (\text{G.3})$$

Thus

$$\begin{aligned} k_c &= (0.0704 \times 888.44) - 5.32 = 57.226 \\ \therefore a_c &= \frac{(0.0704 \times 394784)}{(57.226)} = 485.67 \end{aligned} \quad (\text{G.4})$$

The PI transfer function is therefore

$$PI(s) = \frac{57.226(s + 485.67)}{s} \quad (\text{G.5})$$

The current loop sample frequency is  $4\text{kHz}$ , such that  $T = 250\mu\text{s}$ . The PI law can be discretised using the bilinear transform

$$s = \frac{2(z-1)}{T(z+1)} \quad (\text{G.6})$$

Substituting the above equation into equation G.5 results in the digital control law shown below

$$\begin{aligned} u(k) &= u(k-1) + \frac{2k_c + k_c a_c T}{2} e(k) - \frac{2k_c - k_c a_c T}{2} e(k-1) \\ &= u(k-1) + 60.69e(k) - 53.75e(k-1) \end{aligned} \quad (\text{G.7})$$



## G.2 Current Controller Design – Rig B

The characteristic equation for the rig B, where  $\sigma = 0.12$ ,  $L_s = 0.56$ ,  $R_s = 5.9$  (ignoring units).

$$\begin{aligned} 0 &= s^2 + \left( \frac{R_s + k_c}{\sigma L_s} \right) s + \frac{k_c a_c}{\sigma L_s} \\ &= s^2 + \left( \frac{5.9 + k_c}{0.0672} \right) s + \frac{k_c a_c}{0.0672} \end{aligned} \quad (G.8)$$

Equate coefficients with the following,  $\zeta = 0.707$ ,  $\omega_o = 100\text{Hz} = 628.32\text{rad/s}$

$$\begin{aligned} 0 &= s^2 + 2\zeta\omega_o s + \omega_o^2 \\ &= s^2 + 888.44s + 394784 \end{aligned} \quad (G.9)$$

Thus

$$\begin{aligned} k_c &= (0.0672 \times 888.44) - 5.9 = 53.803 \\ \therefore a_c &= \frac{(0.0672 \times 394784)}{(53.803)} = 493.09 \end{aligned} \quad (G.10)$$

The PI transfer function is therefore

$$PI(s) = \frac{53.803(s + 493.09)}{s} \quad (G.11)$$

The current loop sample frequency is  $4\text{kHz}$ , such that  $T = 250\mu\text{s}$ . The PI law can be discretised, resulting in the following sampled digital control law.

$$\begin{aligned} u(k) &= u(k-1) + \frac{2k_c + k_c a_c T}{2} e(k) - \frac{2k_c - k_c a_c T}{2} e(k-1) \\ &= u(k-1) + 57.12e(k) - 50.49e(k-1) \end{aligned} \quad (G.12)$$

APPENDIX H AFO Encoded Results from Rig B

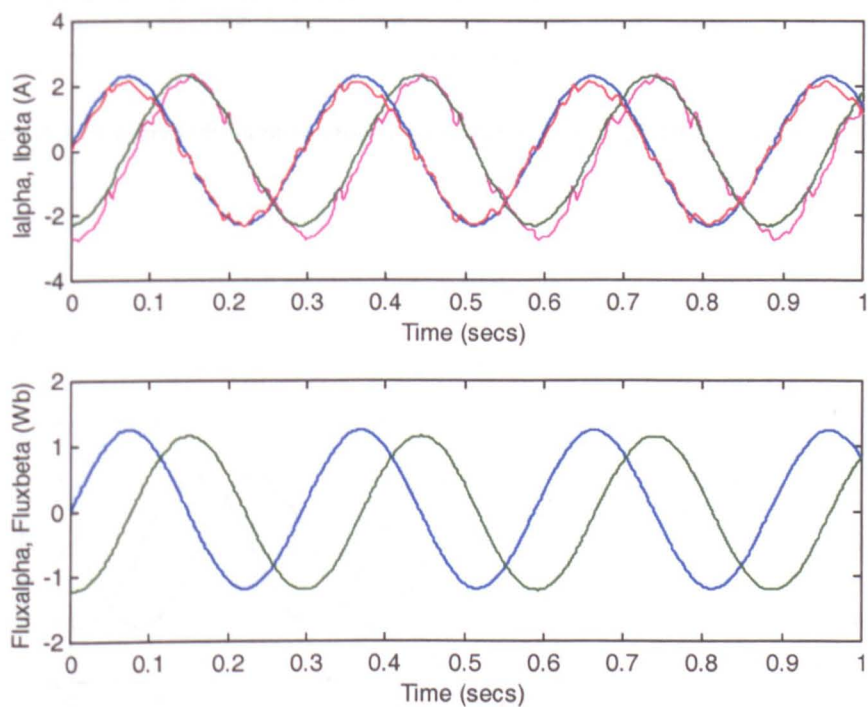


Figure H.1. Measured and observed  $\alpha\beta$  currents and observed  $\alpha\beta$  flux from the AFO with  $k=1.0$   
This drive is operating under encoded IRFO at 100rpm with no load (rig B)

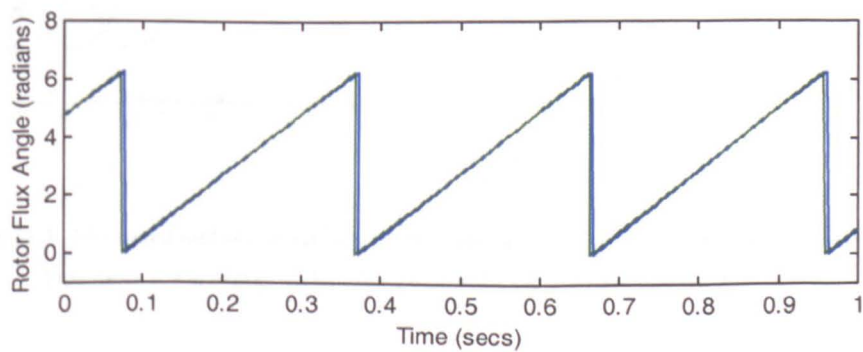


Figure H.2. Imposed rotor flux orientation angle and that measured by the AFO (rig B)

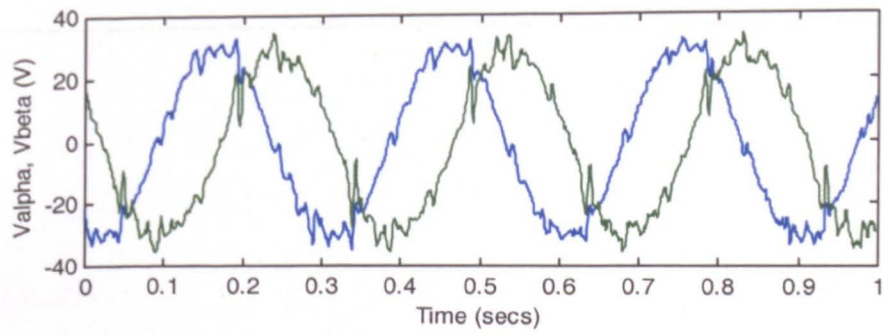


Figure H.3 Measured  $\alpha\beta$  stator voltages from the IRFO scheme at 100rpm with no load (rig B)

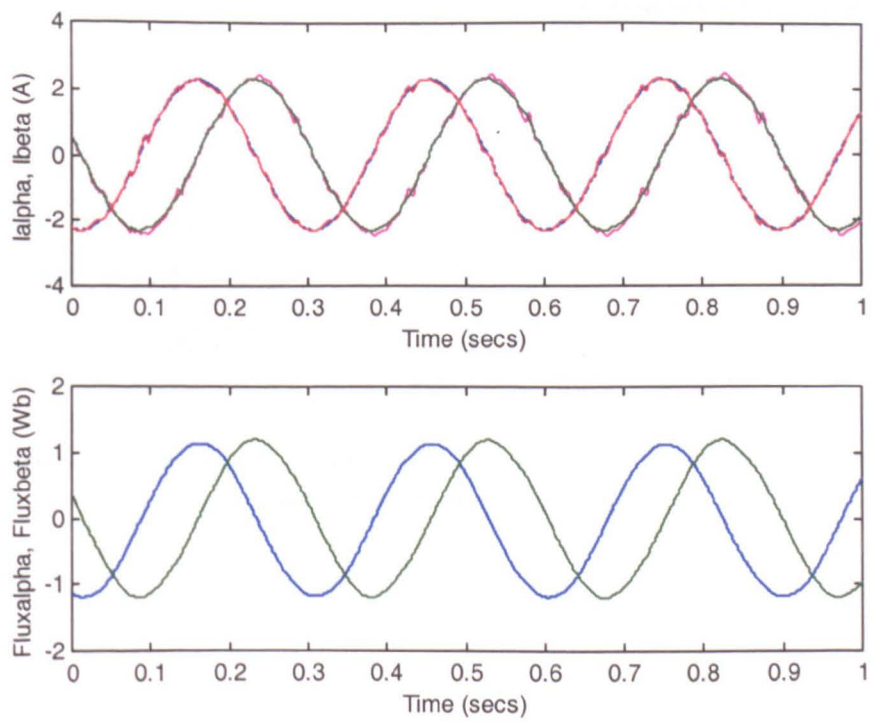


Figure H.4. Measured and observed  $\alpha\beta$  currents and observed  $\alpha\beta$  flux from the AFO with  $k=3.0$   
This drive is operating under encoded IRFO at 100rpm with no load (rig B)

# APPENDIX I ASO Encoded Results from Rig B

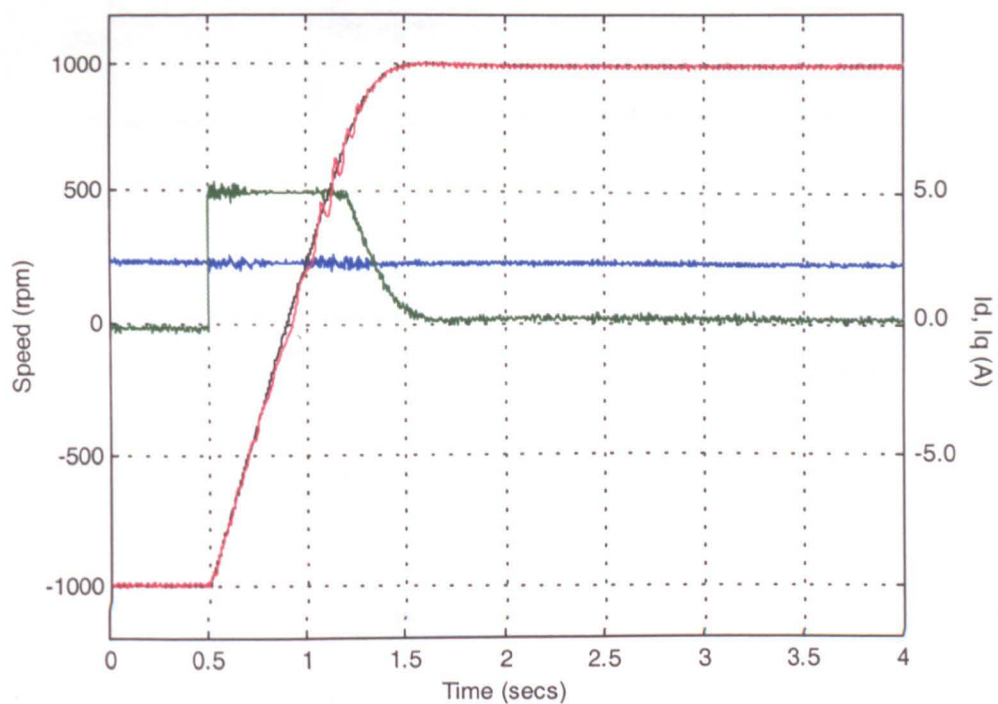


Figure I.1. Measured speed and ASO speed estimate for  $\pm 1000$ rpm no-load speed reversal  
Drive running encoded IRFO (rig B)

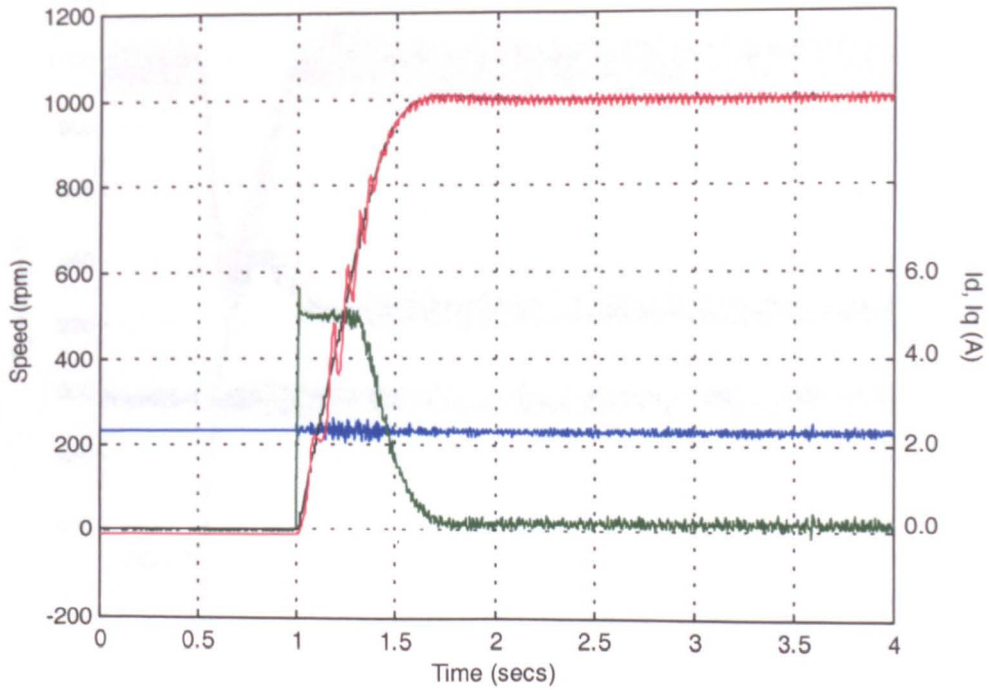


Figure I.2. Measured speed and ASO speed estimate for 1000rpm no-load speed transient  
Drive running encoded IRFO. Start-up conditions - inverter power up (rig B)

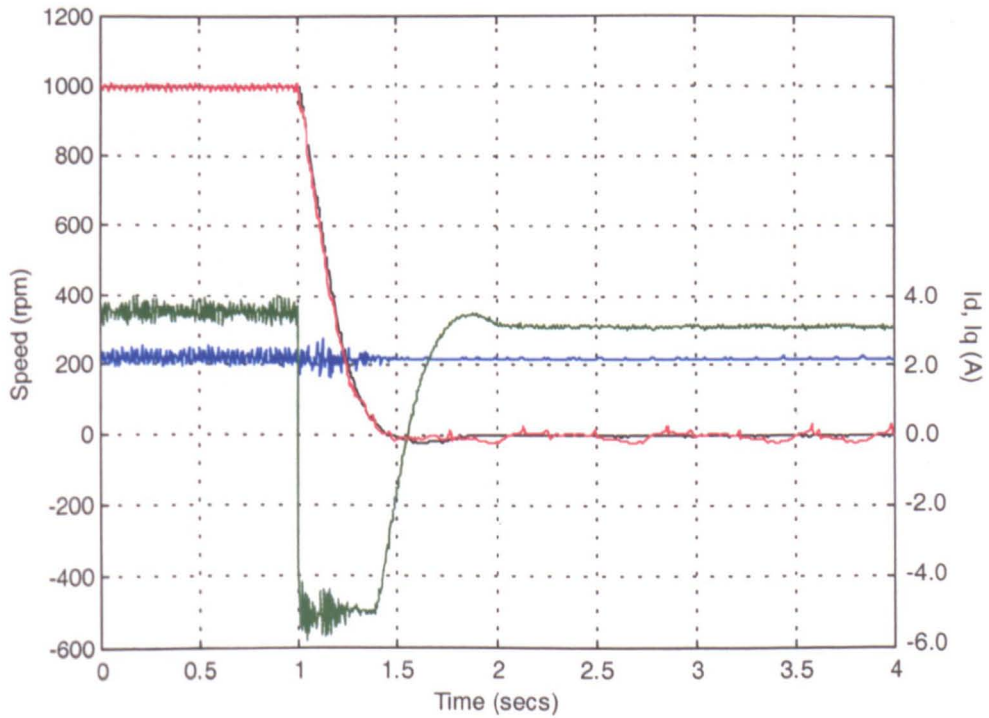


Figure I.3. Measured speed and ASO speed estimate during 1000rpm deceleration to standstill  
Drive running encoded IRFO -full rated load (rig B)



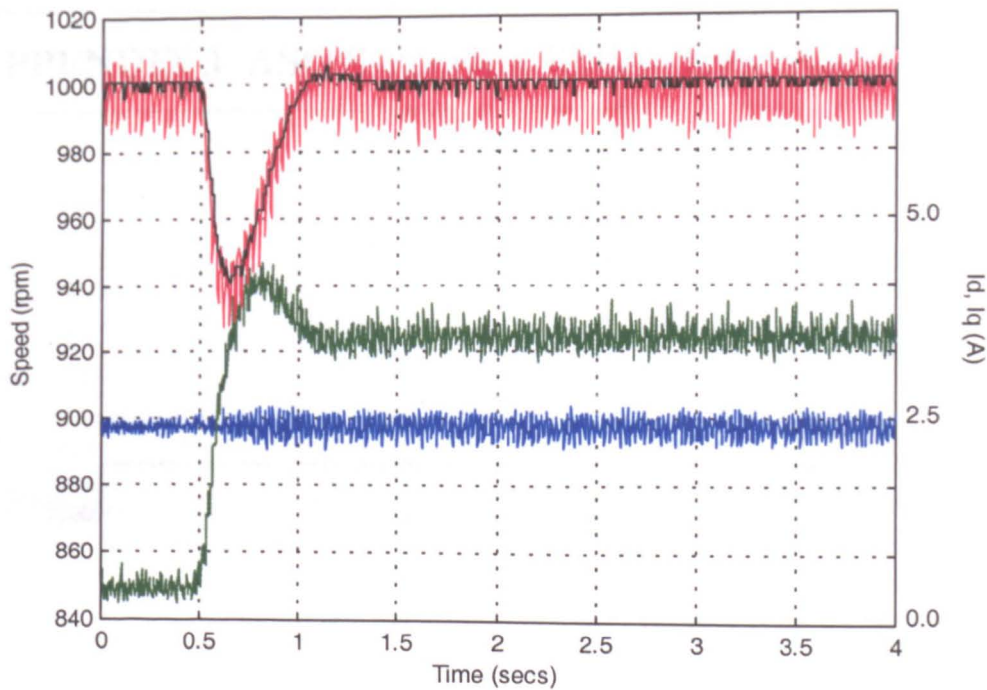


Figure I.4. Measured speed and ASO speed estimate during full-load torque impact at 1000rpm  
Drive running encoded IRFO (rig B)

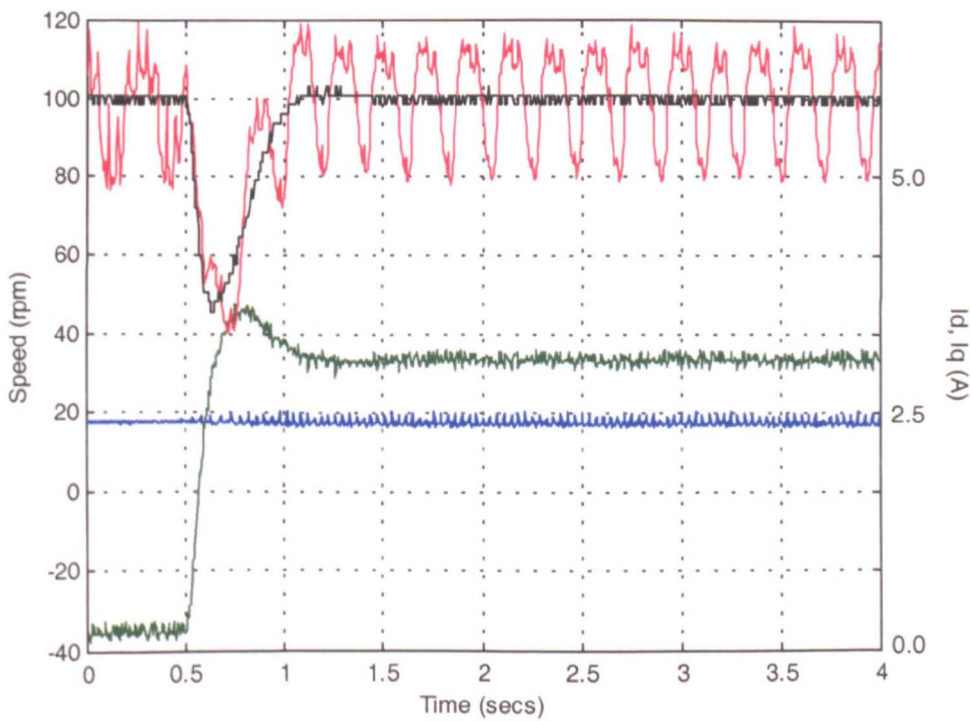


Figure I.5. Measured speed and ASO speed estimate during full-load torque impact at 100rpm  
Drive running encoded IRFO (rig B)

# APPENDIX J ASO Sensorless Results from Rig B

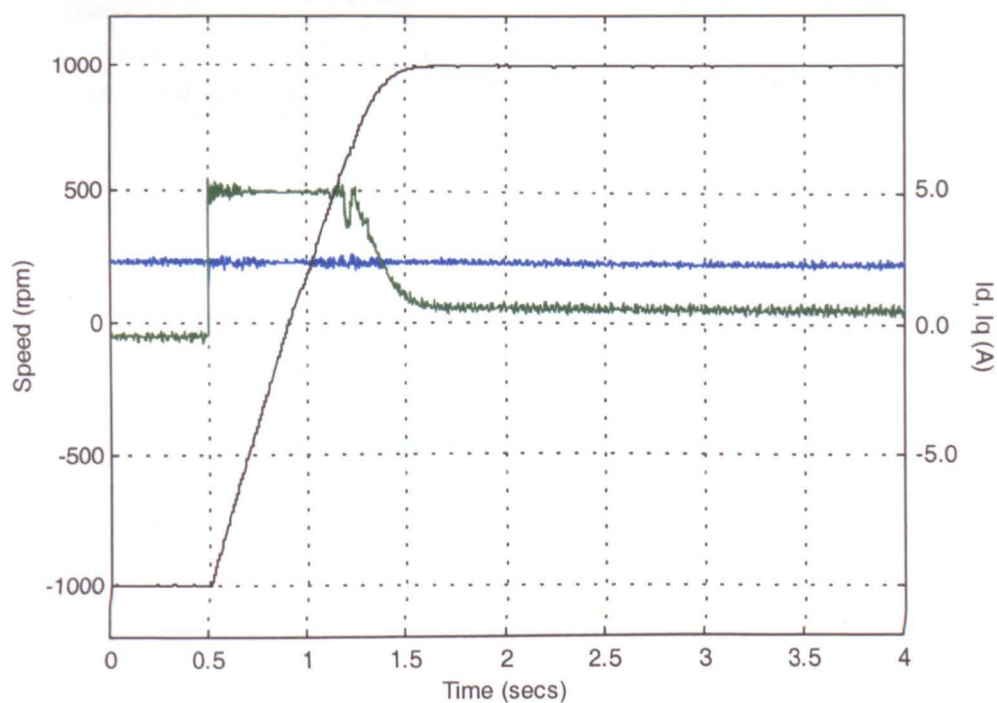


Figure J.1. Measured speed for  $\pm 1000$ rpm no-load speed reversal  
Drive is running sensorless DRFO (rig B)

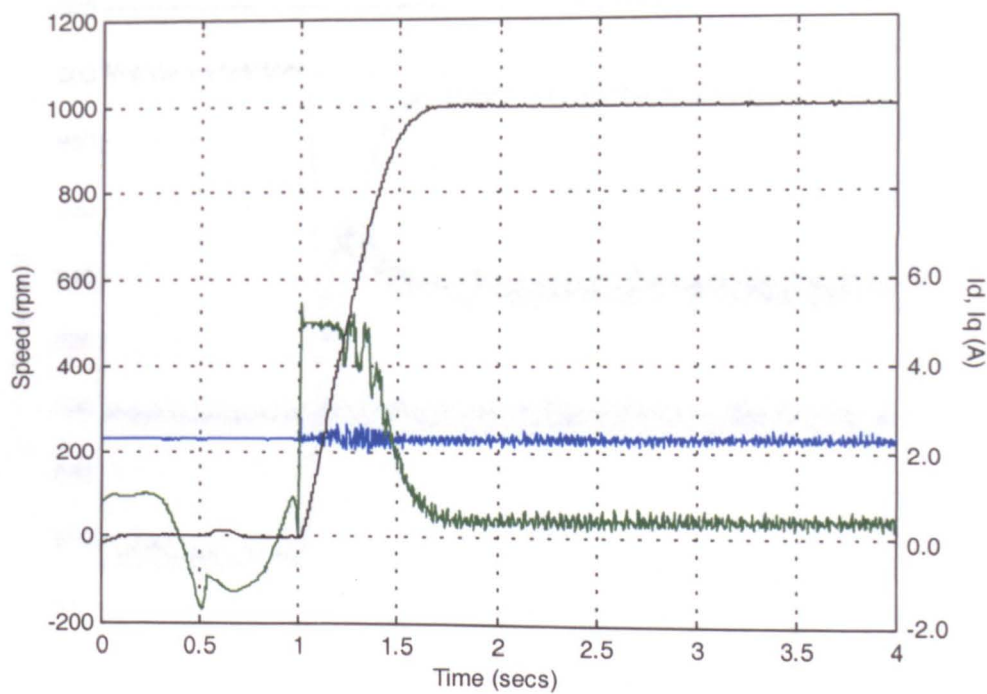


Figure J.2. Measured speed for 1000rpm no-load speed transient  
Drive is running sensorless DRFO. Start up conditions – inverter power up (rig B)

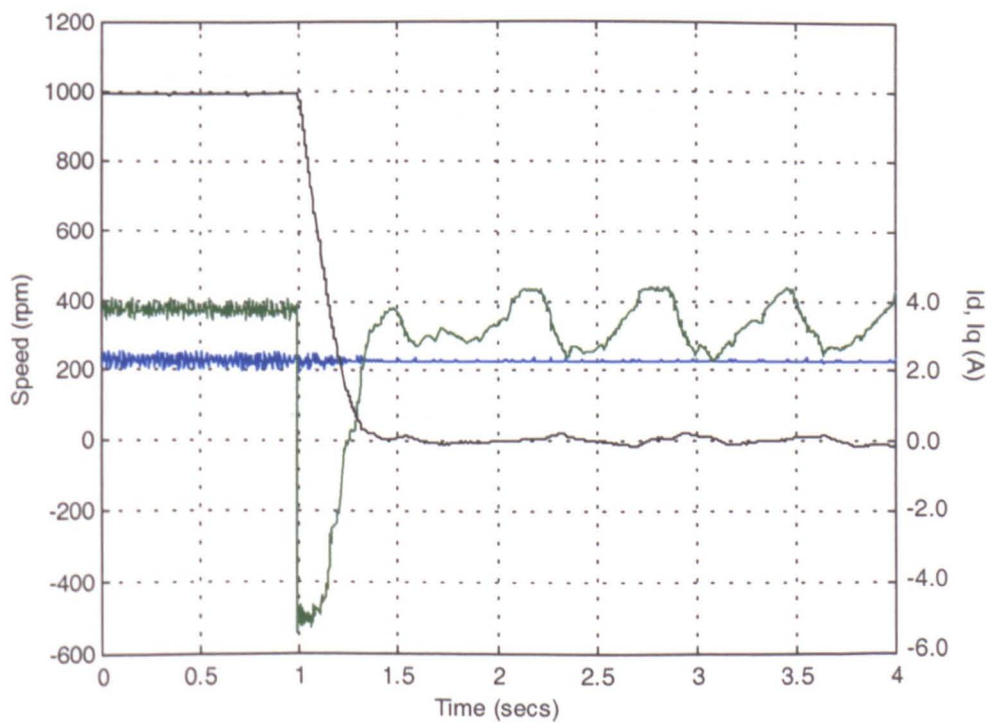


Figure J.3. Measured speed during 1000rpm deceleration to standstill  
Drive running sensorless DRFO – full rated load (rig B)



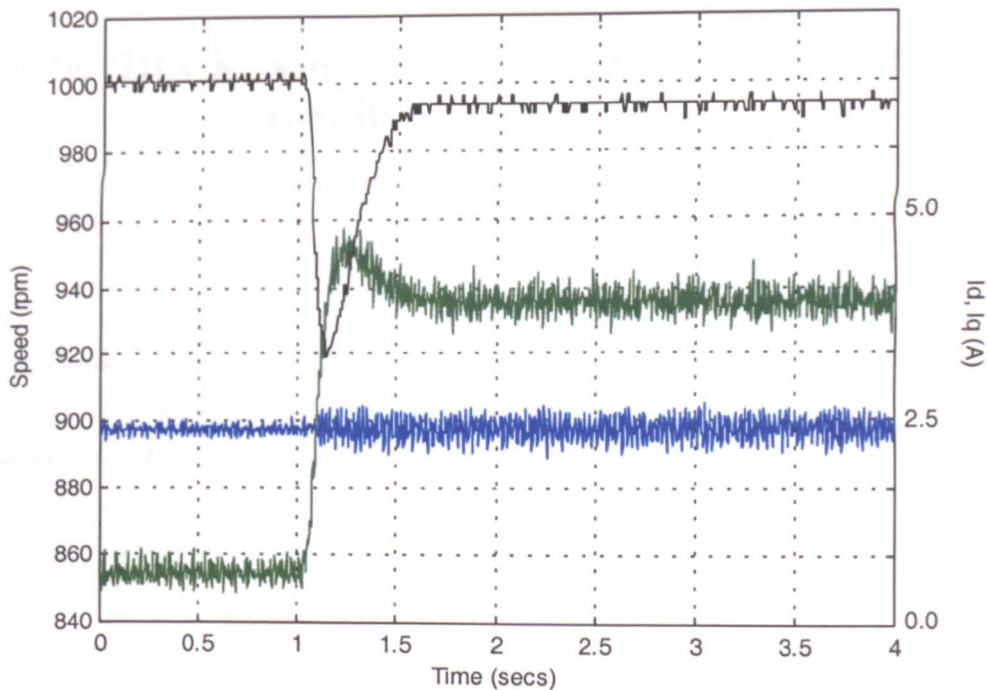


Figure J.4. Measured speed during full load torque impact at 1000rpm  
Drive running sensorless DRFO (rig B)

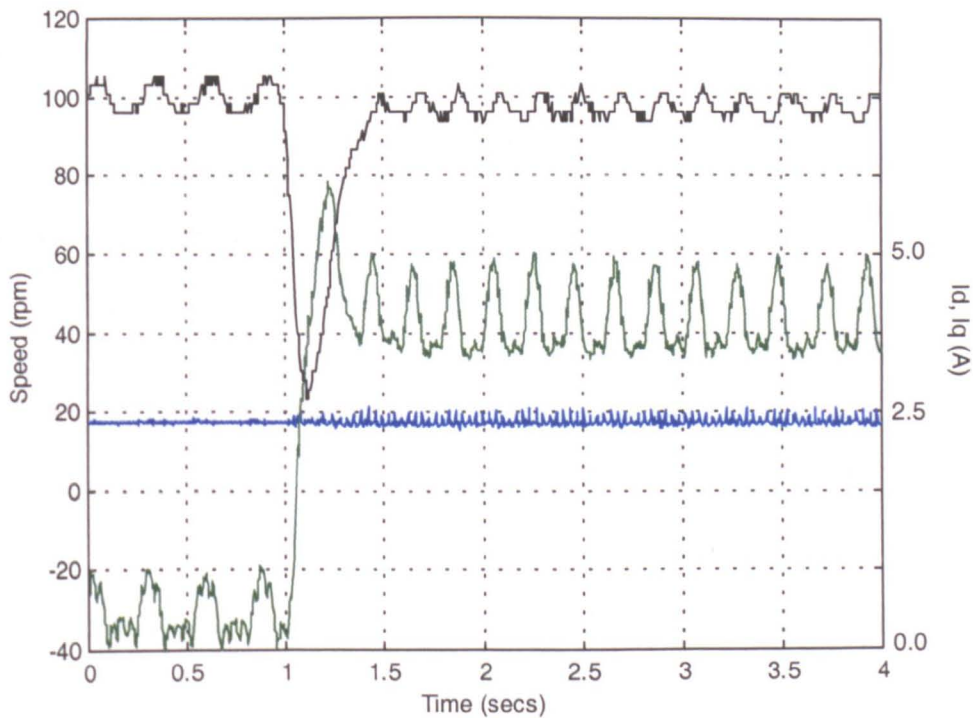


Figure J.5. Measured speed during full-load torque impact at 100rpm  
Drive running sensorless DRFO (rig B)

# APPENDIX K Sensorless Master/Slave Cross-Coupled Results

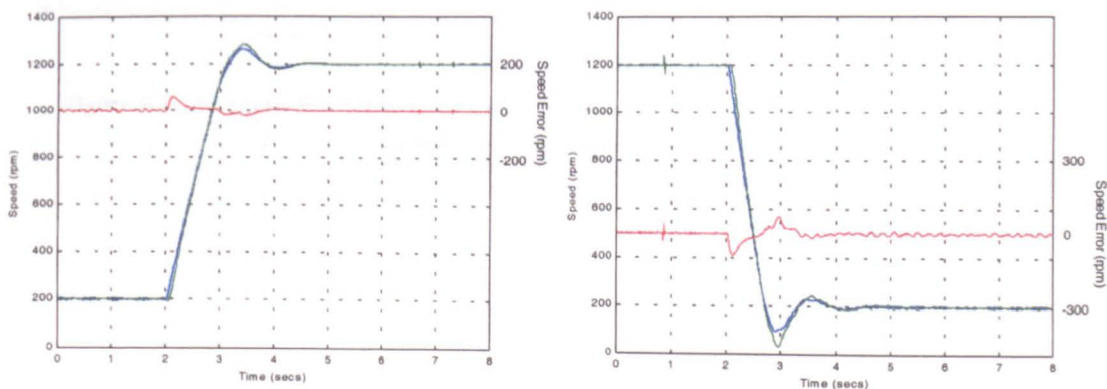


Figure K.1. Response of the sensorless cross-coupled master/slave scheme to step changes in reference command

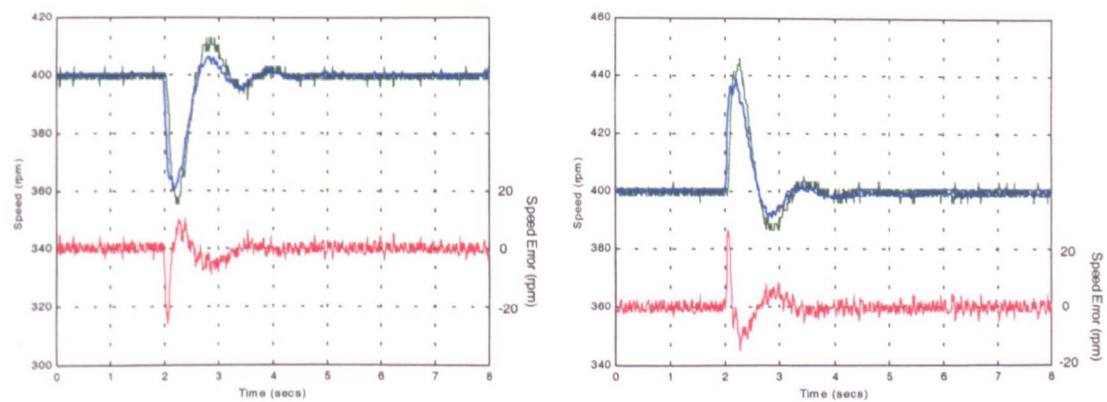


Figure K.2. Response of the sensorless cross-coupled master/slave scheme to large and sudden variation in load torque – Rig A

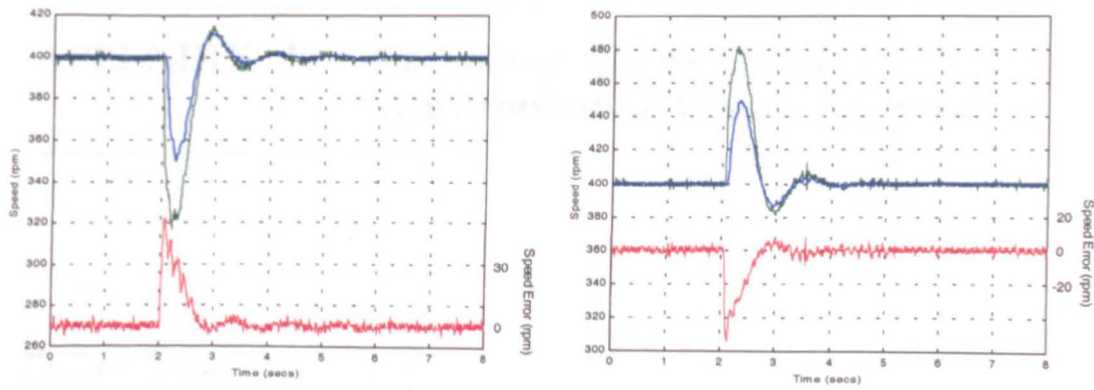


Figure K.3. Response of the sensorless cross-coupled master/slave scheme to large and sudden variation in load torque – Rig B

# APPENDIX L    Encoded Cross-Coupled Position Synchronisation Results for Rig B

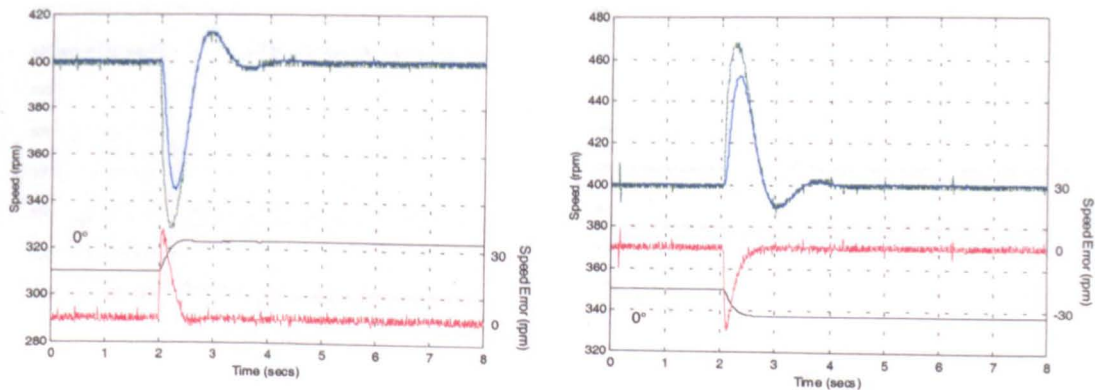


Figure L.1. Response of the encoded cross-coupling scheme to large and sudden variation in rig B load torque. Relative position error is shown in black and positional correction is not included

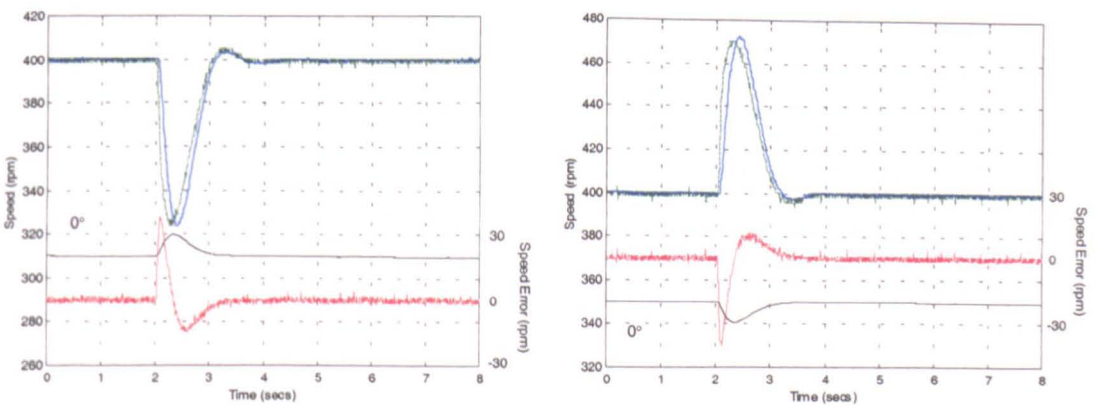


Figure L.2. Response of the encoded cross-coupling scheme to large and sudden variation in rig B load torque. Relative position error is shown in black and positional correction is included

---

# APPENDIX M    Sensorless Cross-Coupled Position Synchronisation Results for Rig B

---

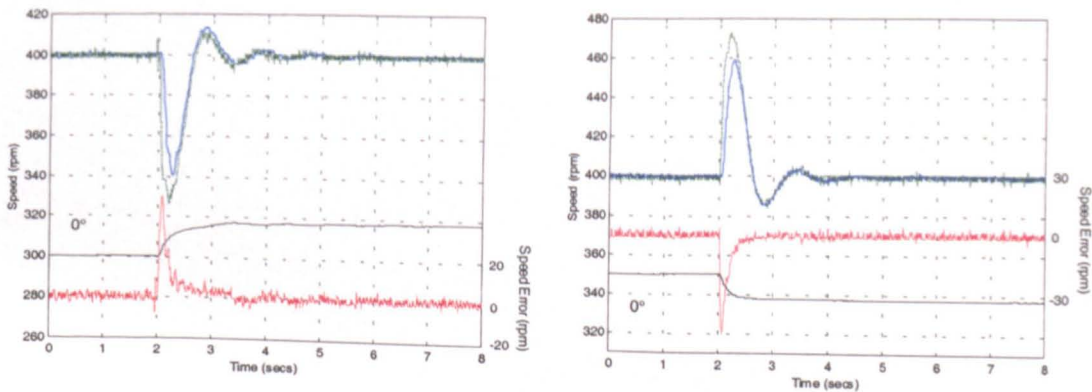


Figure M.1. Response of the sensorless cross-coupling scheme to large and sudden variation in rig B load torque. Relative position error is shown in black and positional correction is not included

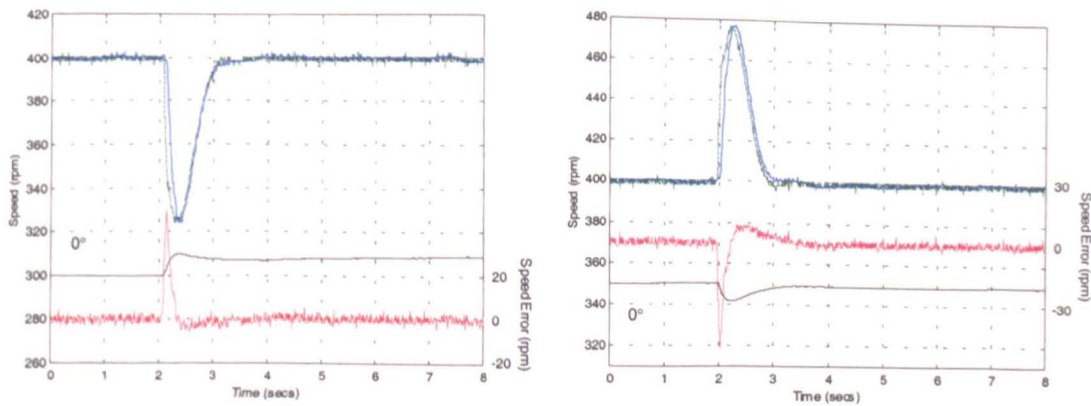


Figure M.2. Response of the sensorless cross-coupling scheme to large and sudden variation in rig B load torque. Relative position error is shown in black and positional correction is included